Multiscale simulation of extrusion growth and fatigue crack propagation in the near threshold regime : application to face-centered cubic metals and alloys

Eyouileki Awi

SORBONNE UNIVERSITÉ

THÈSE

présentée en vue de l'obtention du grade de

Docteur de Sorbonne Université

Ecole doctorale : ED 391 - SMAER
Sciences Mécaniques, Acoustique, Electronique & Robotique de Paris

Spécialité : Mécanique des solides

Multiscale simulation of extrusion growth and fatigue crack propagation in the near threshold regime: application to face-centered cubic metals and alloys

Par

Eyouléki AWI

Directeur de thèse : **Maxime Sauzay**
Co-encadrant de thèse : **Laurent van Brutzel**

Soutenue le 31 mars 2021 devant un jury composé de :

M. David L. McDowell,	Regents' Professor, Georgia Institute of Technology	Rapporteur
M. Derek H. Warner,	Associate Professor, Cornell University	Rapporteur
M. Gilbert Hénaff,	Professeur des universités, ISAE-ENSMA Poitiers	Membre
M. Philippe Vermaut,	Maître de conférences HdR, Sorbonne Université	Membre
M. Maxime Sauzay,	Directeur de recherche, SRMA, CEA Saclay	Membre
M. Laurent van Brutzel,	Chercheur, SCCME, CEA Saclay	Membre
M. Olivier Hardouin Duparc,	Chargé de rercherche HdR, École Polytechnique	Membre
M. Emmanuel Fessler,	Ingénieur de recherche, Safran Aircraft Engines	Membre

Commissariat à l'Énergie Atomique et aux Énergies Alternatives
Centre de recherche de Saclay
Route de Saclay, D36, F-91191 Gif-sur-Yvette, France

THIS PAGE INTENTIONALLY LEFT BLANK

Abstract

Predicting the lifetime of metals and alloys subjected to cyclic loading requires an understanding of the fatigue crack initiation and propagation mechanisms. In this Ph.D. thesis we are interested on the one hand in the extrusion formation and growth preceding fatigue crack initiation in metals and alloys and on the other hand in the mechanisms of fatigue crack propagation in ductile metals and alloys under an inert environment. The Persistent Slip Bands (PSBs) are modeled using a crystal plasticity constitutive law with thermal elastic plastic computations to simulate the extrusion formation and growth. The stress fields induced by the extrusions are estimated and the likelihood of fatigue cracks initiation is discussed in the light of the assessed stress fields. The propagation of fatigue cracks has been investigated using molecular dynamics computations with Embedded Atom Method (EAM) interatomic potentials. The simulations revealed a mechanism of fatigue crack propagation by dislocation emission and slip irreversibility. The various dislocation barriers, junctions between dislocations and other lattice defects as well as the cross-slip are identified as the origins of this plastic irreversibility. The weak influence of temperature generally observed in experiments and the effect of stacking fault energy could be explained, or at least partially, thanks to the dislocation microstructures observed around crack-tip. The propagation of fatigue cracks under mixed mode is also studied.

Key words : Fatigue, extrusion growth, crack initiation and propagation, slip irreversibility, temperature, stacking fault energy, crystal plasticity finite element, Molecular dynamics.

THIS PAGE INTENTIONALLY LEFT BLANK

Résumé

La prédiction de la durée de vie des métaux et alliages soumis à des sollicitations cycliques nécessite la compréhension des mécanismes d'initiation et de propagation des fissures de fatigue. Dans cette thèse de doctorat, nous nous intéressons d'une part à la croissance d'extrusion des bandes de glissement précédant l'initiation des fissures de et d'autre part aux mécanismes de propagation des fissures de fatigue dans les métaux et alliages ductiles sous environnement inerte. Les bandes de glissement sont modélisées via une loi de plasticité cristalline et des calculs thermoélastoplastiques permettent de simuler l'extrusion des bandes de glissement. Les champs de contraintes induits par l'extrusion des bandes de glissement sont évalués et l'initiation des fissures de fatigue est discutée à la lumière des champs de contraintes évalués. D'un autre côté, la propagation des fissures de fatigue a été étudiée grâce aux calculs de dynamique moléculaire avec des potentiels interatomiques de type EAM (Embedded Atom Method). Les simulations ont mis en évidence un mécanisme de propagation des fissures par émission des dislocations et irréversibilité du glissement plastique. Les différentes jonctions entre dislocations et les autres défauts cristallins de même que le glissement dévié sont identifiés comme origine de cette irréversibilité plastique. La faible influence de la température généralement observée dans les expériences et l'influence de l'énergie de faute d'empilement ont pu être expliquées ou du moins partiellement grâce aux microstructures de dislocations observées en pointe de fissure. La propagation des fissures de fatigue en mode mixte est également étudiée.

Mots clés : Fatigue, croissance des extrusions, initiation et propagation des fissures, irreversibilité plastique, temperature, énergie de faute d'empilement, éléments finis cristallins, dynamique moléculaire.

THIS PAGE INTENTIONALLY LEFT BLANK

To my father, my mother and all my family...

THIS PAGE INTENTIONALLY LEFT BLANK

Acknowledgements

The adventure began on Friday September 1, 2017 when I joined the Department of Nuclear Materials / Section for applied metallurgy research of the CEA - *Commissariat à l'Energie Atomique et aux Energies Alternatives (The French Atomic Energy and Alternative Energies Commission)* where I was going to carry out my research work for at least 3 years. It was probably one of my best experiences with all the difficulties that were attached to it. This work and the thesis defense have been made possible by a number of people to whom I would like to express my gratitude.

First of all, I would like to thank the supervisory team, in particular my thesis supervisor Dr. Maxime Sauzay and the co-supervisor Dr. Laurent van Brutzel for the trust they have placed in me and for their advice. Mechanical Engineer by training, I started this thesis with a master's degree in solid mechanics and thanks to this thesis, I was able to broaden my field of expertise to materials science and engineering (in particular metallurgy) and solid-state physics. Thank you.

I would also like to thank Professors David McDowell (Georgia Tech, USA) and Derek Warner (Cornell University, USA) for having accepted to review this thesis. It was an honor for me to discuss with you during the defense. Your comments, suggestions and advice have enriched my scientific background and I will be always grateful to you. I would also like to thank Professor Gilbert Hénaff (ISAE-ENSMA, France) for having chaired the defense jury as well as the other jury members: Dr. Philippe Vermaut (Sorbonne Université, France), Dr. Olivier Hardouin Duparc (Ecole Polytechnique, France), Dr. Emmanuel Fessler (Safran Aircraft Engines, France) for their participation in the jury.

I would also like to express my gratitude to Dr. Laurence Portier (Head of the Section for Applied Metallurgy Research), Dr. Jérôme Canel (Deputy Head of the Section for Applied Metallurgy Research) and Dr. Ludovic Vincent (Head of the Laboratory of the Mechanical Behavior of Materials) for their support. Thanks also to Laurent Dupuy who was kind enough that I assist him and with whom I took my first steps in higher education as teaching assistant at the INSTN - *Institut National des Sciences et Techniques Nucléaires (National Institute for Nuclear Science and Technology)*. I also thank Dr. Paul Fossati for his help in

the analysis of crystal defects especially vacancies, with the *acme* code as well as Dr. Philippe Zeller for the creation of the computer accounts on *Tintin* and *Blake* clusters. I also offer my sincere gratitude to my colleagues, engineers, interns, technical and administrative staff with whom I had contact at a given time: Dr. Bertrand Sicaud, Dr. Jérôme Hazan, Dr. Elric Barbe, Dr. Sicong Ren, Dr. Yanjun Wang, Dr. Yang Li, Dr. Zhengxuan Fan, Thomas Doger de Spéville, Adrien, Sara Chakibi, Clémentine Piotrowicz, Jihane Mkadmi, Dr. Diogo Gonçalves, Dr. Liang Huang, Dr. Malik Shukeir, Dr. Wassim Kassem, Louis Ziolek, Nicolas Boudier, Cathy Vidal, Nathalie Palayan, Stessy Loreto.

I do not forget some friends and colleagues for their support: Dr. Ibishola Santos, Bernus Kouevidjin. I apologize to people I did not mention here but may be sure that their contribution and encouragements are recognized.

Thank you all of you!

Joinville-le-Pont, April 28, 2021

Dr. Eyouiléki AWI

This research project was funded by the CEA - Commissariat à l'Energie Atomique et aux Energies Alternatives (the French Atomic Energy and Alternative Energies Commission) through a flagship thesis grant (excellence grant). The computing times were provided by the CCRT - Centre de Calcul pour la Recherche et la Technologie (Computing Center for Research and Technology) thanks to the "Cobalt", "Irene" and "Curie" supercomputers and by the CINES - Centre Informatique National de l'Enseignement Supérieur (National Computer Center for Higher Education) thanks to the supercomputer "Occigen".

THIS PAGE INTENTIONALLY LEFT BLANK

Articles to be submitted for publication

Some chapters of this thesis constitute the bases of a certain number of articles which will be enriched and submitted for publication.

1. E. Awi, M. Sauzay, L. van Brutzel. Physically-based simulation of extrusion growth in cyclically strained metals ans alloys. To be submitted to *Materials Science and Engineering A*

2. E. Awi, L. van Brutzel, M. Sauzay. Atomistic-based study of cyclic plastic deformation and underlying crystal defects in FCC single crystals. To be submitted to *Journal of the Mechanics and Physics and Solids*.

3. E. Awi, L. van Brutzel, M. Sauzay Slip irreversibility induced fatigue crack growth in FCC single crystals: The role of dislocation microstructures and crystal defects. To be submitted to *Acta Materialia*

4. E. Awi, L. van Brutzel, M. Sauzay. Influence of temperature on cyclic plastic deformation and fatigue crack growth in copper single crystals: A Molecular dynamics based investigation. To be submitted to *Engineering Fracture Mechanics*

5. E. Awi, L. van Brutzel, M. Sauzay. Fatigue crack propagation in FCC metals: An insight into the effect of stacking fault energy via Molecular dynamics simulations. To be submitted to *International Journal of Fatigue*

THIS PAGE INTENTIONALLY LEFT BLANK

Oral communications in conferences

1. E. Awi, M. Sauzay, L. van Brutzel, Z. Fan, O. Hardouin Duparc. Simulation de la propaation des fissures par dynamique moléculaire. *Matériaux 2018, Strasbourg, France, 2019*

2. E. Awi, M. Sauzay, L. van Brutzel, Z. Fan, O. Hardouin Duparc. Atomistic-based Analysis of Fatigue Crack Propagation Mechanisms in FCC Metals, *TMS* 148^{th} *Annual Meeting and Exhibition - TMS 2019, San Antonio, USA, 2019*

3. E. Awi, M. Sauzay, J. Hazan, Simulation of Extrusion Growth and Micro-crack Initiation for Type A and type B Persistent Slip Bands, *TMS* 148^{th} *Annual Meeting and Exhibition - TMS 2019, San Antonio, USA, 2019*

4. E. Awi, M. Sauzay, L. van Brutzel, Z. Fan, O. Hardouin Duparc. Simulations atomistiques de la propagation des fissures de fatigue sous environnement inerte, *Congrès Français de Mécanique 2019, Brest, France 2019*

5. E. Awi, J. Hazan, M. Sauzay, L. van Brutzel, Simulation par éléments finis de l'initiation des fissures de fatigue le long des bandes de glissement persistantes. *Congrès Français de Mécanique - CFM 2019, Brest, France, 2019*

6. E. Awi, L. van Brutzel, M. Sauzay, Molecular dynamics based study of fatigue crack growth in ductile crystals under inert environment: application to face-centered cubic (FCC) metals. *International Congress of Theoretical and Applied Mechanics - ICTAM 2020+1, Milan, Italy* (Postponed due to Covid-2019)

7. E. Awi, L. van Brutzel, M. Sauzay. Large scale molecular dynamics simulation of fatigue crack propagation in ductile metals, *Multiscale Materials Modelling - MMM 2019, Baltimore, USA* (Postponed due to Covid-19)

THIS PAGE INTENTIONALLY LEFT BLANK

Contents

THIS PAGE INTENTIONALLY LEFT BLANK

List of Figures

THIS PAGE INTENTIONALLY LEFT BLANK

List of Tables

Chapter 1

Context and motivation

La diversité de nos opinions ne vient pas de ce que les uns sont plus raisonnables que les autres, mais de ce que nous conduisons nos pensées par diverses voies et ne considérons pas les mêmes choses. Car ce n'est pas assez d'avoir l'esprit bon, mais l'essentiel est de l'appliquer bien. Les plus grandes âmes sont capables des plus grands vices aussi bien que des plus grandes vertus [...] Pour moi, je n'ai jamais présumé que mon esprit fût en rien plus parfait que ceux du commun: même j'ai souvent souhaité d'avoir la pensée aussi prompte, ou l'imagination aussi nette et distincte, ou la mémoire aussi ample, ou aussi présente que quelques autres.

René Descartes, *Discours de la méthode* .

Abstract

In this chapter, we explain the reasons which motivate this research project. First, we recall the importance of the study of fatigue damage in general. Secondly, we introduce fatigue in nuclear components while explaining our motivations.

Contents

1.1 Introduction

Fatigue is a damage mechanism of materials and structures subjected to time-varying loading. It is characterized by microstructural evolutions leading to the initiation of cracks, their propagation and then final failure of mechanical devices. It is estimated that 80% of structural failures are linked to this damage mechanism and costs 4% of the gross domestic product (GDP) of industrialized countries. As a general rule, structures are designed in such a way that the nominal stresses they undergo do not exceed the elastic limit of the materials used for their design. While this ensures that no ductile fracture related to the applied loading will be triggered, failure due to cyclic loading, generally resulting in cumulative damage, is not ruled out as evidenced by the various accidents that occurred throughout history, mainly in the field of transportation.

One of the accidents that led to an increased study of the phenomenon of fatigue was the derailment of the Paris-Versailles train at Meudon on May 8, 1842. This accident occurred because of the fracture of an axle and caused more than 200 deaths and one hundred serious injuries. The Scottish engineer William Rankine, by studying the fracture surfaces of the axle, shows that the failure of the axle was the result of a new mode of failure, now known as "fatigue failure". On April 28, 1988, the Boeing 737-200 of U.S. Aloha Airlines Flight 243 lost the upper portion of its fuselage (Fig. 1-1). According to the NTSB report, a crack in the aircraft fuselage was located adjacent to the left front door. The crack was likely caused by stresses applied to the alloy after the 89 090 compressions and decompressions. This was also the case for the DC10 of United Airlines Flight 232 on July 19, 1989. An expert report established that the failure occurred as a result of a fatigue crack in the alloys of one of the turbine blades. Other accidents related to this phenomenon of fatigue damage were also reported.

Although fatigue damage was already known by 19^{th} century scientists and engineers, including the German mining engineer Wilhelm August Julius Albert (1787-1846) who described it as "a mysterious phenomenon", important developments took place in the second half of the 20th century. In the aftermath of the Meudon accident, the first milestones in the study of the fatigue of materials were laid down. Since then, significant progress have been made. However, there are still some unknowns that do not allow the full and clear understanding of this phenomenon. Some of the fatigue phenomena still remain partly unexplained today and require dedicated and in-depth studies in order to update knowledge in a field where many factors such as those related to material (in particular microstructure) [Suresh, 1998, McDowell and Dunne, 2010, Castelluccio et al., 2016, Laird, 1967b] and environmental parameters [Hénaff et al., 2007, Petit et al., 2003, Bilotta et al., 2017] and also structure effects can very quickly become determining factors.

Fatigue damage occurs in different sectors such as transportation area (aeronautics, automotive, railways, etc.), the energy area, in machine tools, etc. In the aeronautics area, turbine blades, for example, are subjected to variations in me-

Figure 1-1: Remaining fuselage of Boeing 737-297 of Aloha Airlines Flight 243, after explosive decompression. The NTSB (United States National Transportation Safety Board) investigation report concluded that the accident was caused by metal fatigue exacerbated by crevice corrosion (Source: Wikipedia)

chanical stresses during take-off and landing phases. In the railway area, the train/rail contacts at each pass of a train are sources of cyclic stresses that can lead to fatigue failure. In the automotive sector, vibrations of engine block components are, for example, possible causes of fatigue failure. Fatigue occurs also in nuclear plants. In nuclear reactors, the reactor start-up and shutdown cycles are sources of fatigue loading as well as the circulation of hot and cold fluids which can cause thermal fatigue problems. The vibrations may be also sources of stress variations.

1.2 Fatigue in nuclear components: industrial context of the study

1.2.1 Operating principle of a nuclear plant

There are different nuclear reactor technologies. In France, the most widespread technology is the pressurized water reactor (PWR). Research has been underway for several years to develop the ASTRID (Advanced Sodium Technological Reactor for Industrial Demonstration) reactor, which is an industrial demonstrator of a sodium-cooled fast neutron reactor (FNR-Na). Fig. 1-2 and Fig. 1-3 show schematic diagrams respectively of a PWR and a FNR-Na. Whether the reactor is pressurized water or fast neutron, the basic principle is the same. The fission of a nuclear fuel (Uranium 235 in the case of a PWR, or Uranium 238+Plutonium mixture in the case of FNR-Na/He) produces heat. This heat is transported by a heat transfer fluid (water in the case of PWRs and Na/He in the case of FNR-Na/He) in a closed circuit (primary circuit) and transmitted via a heat exchanger to a closed secondary circuit (secondary circuit) in which liquid Na/He gas (in the case of FNR-Na/He), or water (in the case of PWRs) circulates. In the case of PWRs, the water in the secondary circuit is transformed into steam, which during its expansion activates a turbine coupled to a generator that produces electricity. In the case of FNR-Na, the sodium circulating in the secondary circuit transmits its heat to the tertiary circuit (where the sodium/gas conversion takes place) via a sodium/gas heat exchanger (SGHE). As before, the gas activates the turbine, which produces electricity. At the end of the chain, there is a cooling circuit in which water and/or air circulates to cool the steam leaving the turbine and transform it into water (via a condenser) and returned to the steam generator.

1.2.2 Fatigue of nuclear components

Reactor start-up and shut-down cycles are a source of cyclic loading that can lead to fatigue damage of individual components. The circulation of fluids at different temperatures in the piping system also causes fatigue damage. Various incidents have already been reported in nuclear power plants in different com-

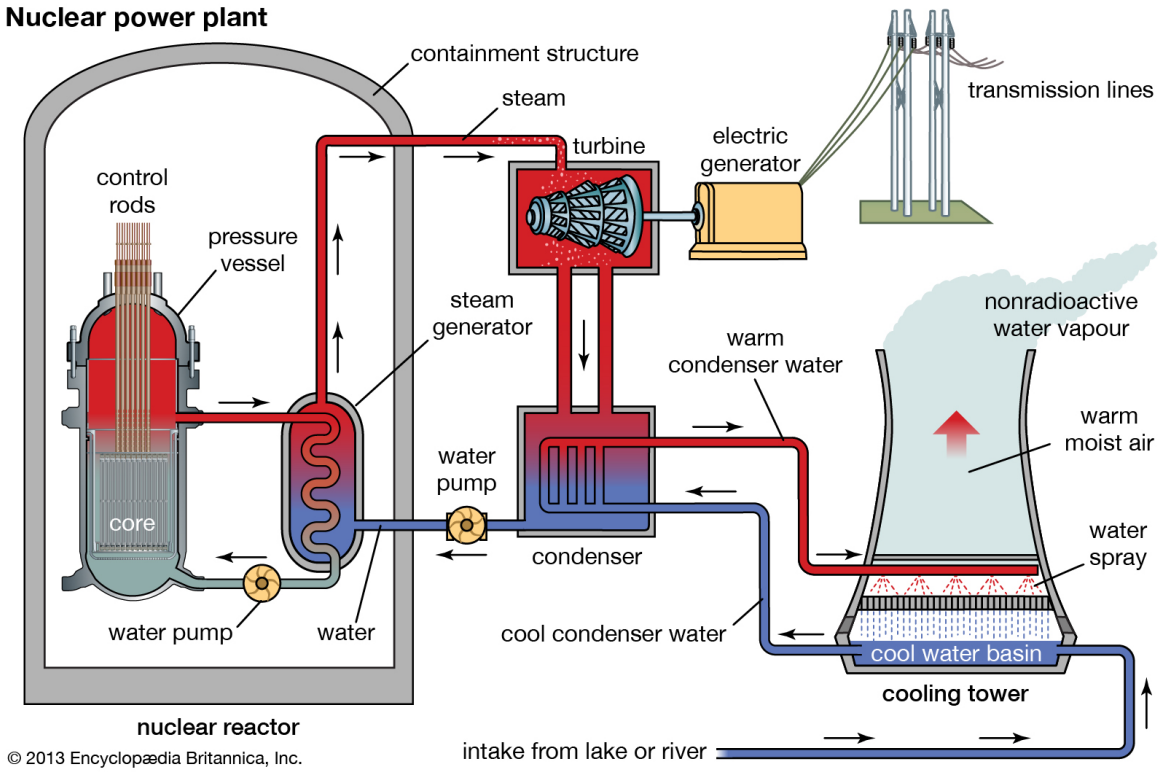

Figure 1-2: Schematic diagram of a pressurized water reactor and the whole nuclear power plant

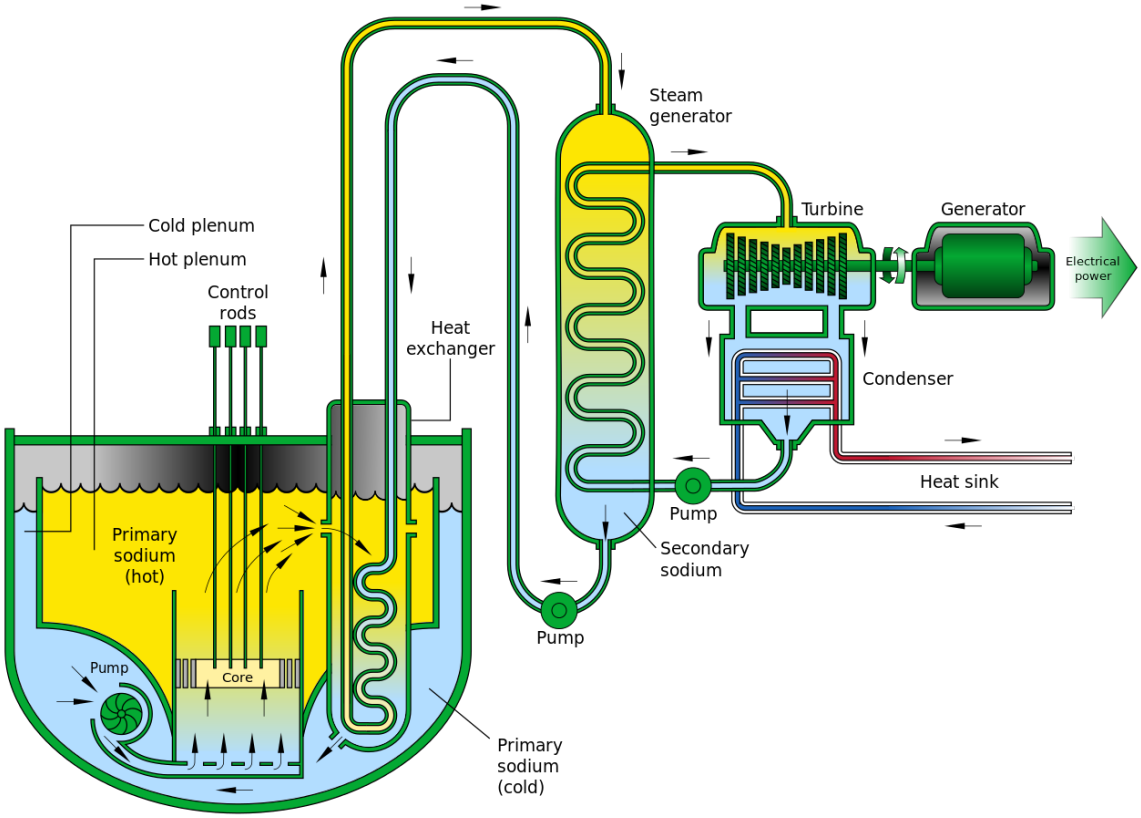

Figure 1-3: Schematic diagram of a sodium-cooled fast neutron reactor

ponents: manifold, steam generator, primary pump, piping, valves, turbines,... [Osterstock, 2013]. The Civaux incident is at the origin of many studies at CEA, EDF, IRSN and different universities. It also motivates this work and occurred on May 12, 1998 at the Civaux power plant. A leak of $30\ \mathrm{m^3/h}$ was detected in the reactor cooling system when the reactor was shut-down, after only 1500 hours of operation. From then on, metallurgical and mechanical studies have been carried out to determine the cause of the leak as well as thermal hydraulics and experimental ones. Expertise operations reveal a traversing crack of length $180\ \mathrm{mm}$ long in the outer skin and $250\ \mathrm{mm}$ long in the inner skin along a longitudinal weld in an AISI 304L austenitic stainless steel bend (Fig. 1-4, [Maillot, 2003]). Thermal crack networks were also observed in the vicinity of the mixing tee. In fact, the turbulences induced by the mixing of hot and cold fluids cause temperature variations of up to $150\ ^\circ\mathrm{C}$ in the internal part of the pipe walls, as can be observed in Fig. 1-5 obtained by thermohydraulic simulation. A temperature gradient is established in the thickness of the pipe. The hot zones deform independently of the cold zones inducing deformation incompatibilities. Strain compatibility is restored by the creation of elastic strains and then internal stresses (Fig. 1-6). These thermally-induced stresses, which vary over time in the same way as temperature varies, characterizes a complex fatigue loading. Following the Civaux incident, all bends in the French nuclear fleet were replaced by components accounting for geometric modifications to limit turbulence in the mix. In spite of this, fatigue cracks were still detected recently on pipes in the secondary circuit of some PWRs.

In addition, in the FNR-Na technology, a Sodium/Gas Heat Exchanger (SGHE) is planned. This heat exchanger, consisting of several modules (Fig. 1-7) inside which liquid sodium and nitrogen under pressure circulate, is made of 316L(N) austenitic stainless steel using the hot isostatic pressing process of millimeter thick plates. Due to the manufacturing process, grain size up to a few hundred microns are achieved for component thicknesses of around $1\ \mathrm{mm}$. This induces specific problems with regard to the fatigue strength of these SGHE components and, above all, with regard to their design. In fact, space separation is no more guarantied in such structure.

It is true that the discussion relates to the thermomechanical fatigue. But our aim is to treat the initiation of fatigue cracks by reducing to mechanical loading at constant temperature.

As we have just seen, fatigue is a phenomenon present in all areas of industry (aeronautics, railways, automotive, energy, manufacturing, etc.).

More research in this field especially at low scale may make it possible to better control this damage mechanism by understanding the fundamental mechanisms of fatigue crack initiation and propagation. The effect of crystal orientation, the influence of temperature and stacking fault energy and the effect of loading mode are the questions to which we will attempt to provide partial answers through our present contribution.

In chapter 2, we present the state of the art on the initiation and propagation

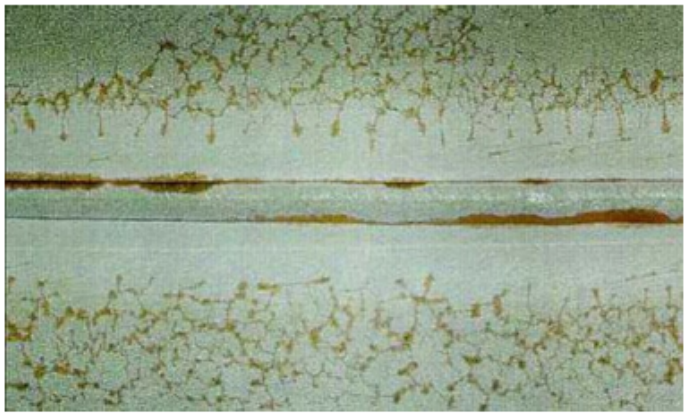

Figure 1-4: Long Crack and crack networks along a weld of the Civeaux power plant [Maillot, 2003]

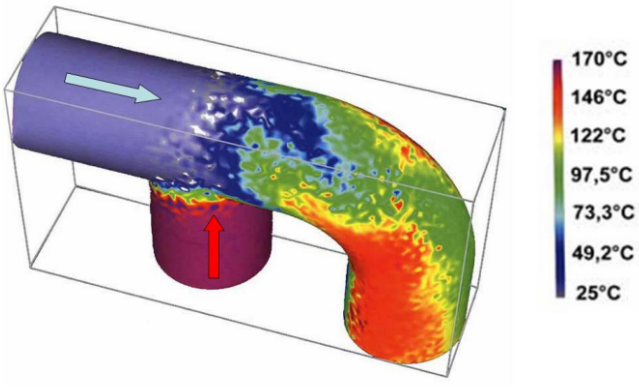

Figure 1-5: Temperature distribution at a given time in the bend of a pipe of the Civeaux power plant [Osterstock, 2013]

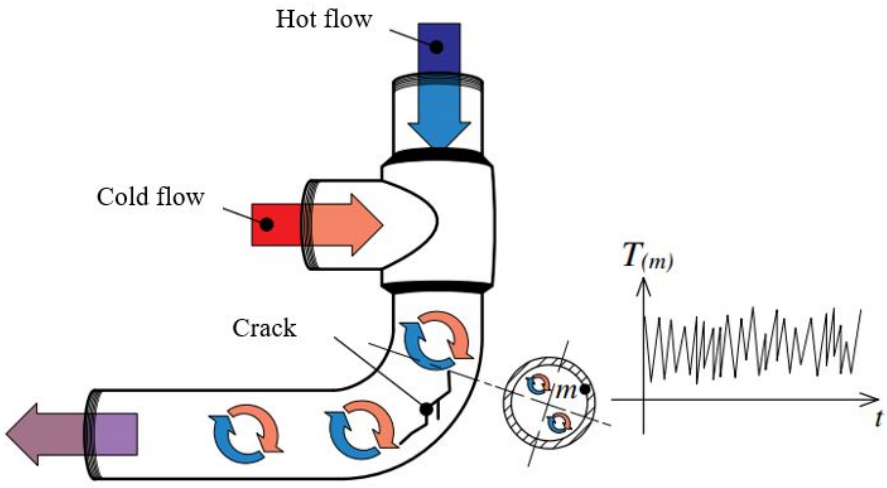

Figure 1-6: Mechanism of internal stresses production: a temperature gradient is established in the wall of thickness (i). If the hot and cold zones expand independently, this leads to a strain incompatibility (ii) which are restored by the creation of elastic strains and then internal stresses (iii) [Déprés, 2004]

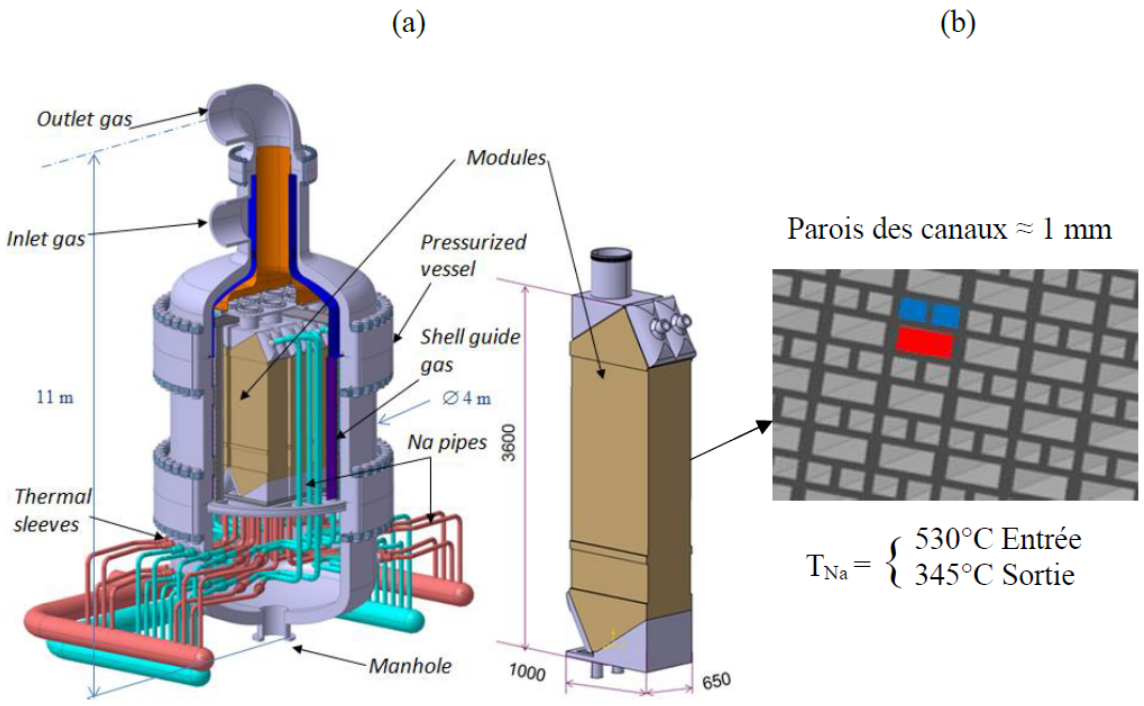

Figure 1-7: (a) Schematic representation of sodium-nitrogen heat exchanger [Cachon et al., 2015] and (b) sectional view of a module of the exchanger [Hazan, 2019]

of fatigue cracks in metals and alloys and we note the shortcomings of the state of the art in fatigue modelling and lack of consensus regarding fatigue mechanisms while indicating the outlines of this manuscript.

Chapter 2

State of the art

Ceux qui sont férus de pratique sans posséder la science sont comme le pilote qui s'embarque sans timon ni boussole et ne saurait jamais avec certitude où il va.

Leonard de Vinci

Abstract

A short review of fatigue of materials is provided in the following lines. First, a review of the fundamental concepts of fracture mechanics and fatigue of materials is presented: the stress concentration, stress singularity, the stress intensity factor, loading modes, fatigue life approaches (S-N curves, strain-life approach, fracture mechanics approach). Secondly, a literature review on extrusion growth and fatigue cracks initiation sites (persistent slip bands, twin boundaries, grain boundaries) and mechanisms is displayed followed by a review on fatigue crack propagation in particular fatigue crack growth mechanisms (blunting-resharpening, void coalescence) and the effect of environment.

Contents

2.1 Fatigue of metallic materials: background information and theory

2.1.1 Fundamental concepts of Fracture Mechanics

Fracture mechanics is concerned by stress concentrators and fracture modes. The fracture can occur from a pre-existing flaw. Considering a plate pierced with a hole of elliptical section, the Fracture Mechanics shows that with such a defect, the stress distributions are inhomogeneous and lead to stress concentrations in the vicinity of the flaw. The stress concentration factor K_t is then defined as the ratio of the maximum stress reached in the vicinity of the flaw and the nominal stress applied to the plate.

$$K_t = \frac{\sigma_{max}}{\sigma_{nom}} \tag{2.1}$$

This parameter therefore provides an idea of the local stresses prevailing in the vicinity of a flaw with regard to the macroscopic applied stresses. The value of the stress concentration coefficient varies according to the geometry of the defect. In the case of an elliptical defect with major axis $2a$ and minor axis $2b$, the stress concentration coefficient is given by:

$$K_t = 1 + 2\frac{a}{b} \tag{2.2}$$

By assimilating a perfect crack to a infinitely flattened elliptical defect ($b \ll a$), one notices that K_t tends towards infinity and therefore such approach does not allow to characterize the local fields in the vicinity of the defect. The introduction of the stress intensity factor (SIF) by Irwin [Irwin, 1957] following the investigations of Westergaard [Westergaard, 1939] made possible the characterization of the distribution of mechanical fields in the vicinity of a crack within the framework of linear elastic fracture mechanics (LEFM). Indeed, with the asymptotic development of the stress field in the vicinity of the crack one can write:

$$\sigma_{ij}(r,\theta) = \frac{K}{\sqrt{2\pi r}} f_{ij}(\theta) \tag{2.3}$$

where K is the SIF, r the position of a point M (Fig. 2-1) with respect to the crack tip and $f_{ij}(\theta)$ an angular distribution function which depends on the loading mode.

The different loading modes are (see Fig. 2-2):

- Mode I or opening mode, characterized by an opening of crack lips in the normal direction to the crack plane.
- Mode II or shear mode characterized by in-plane shearing of crack lips, in the direction normal to the crack front

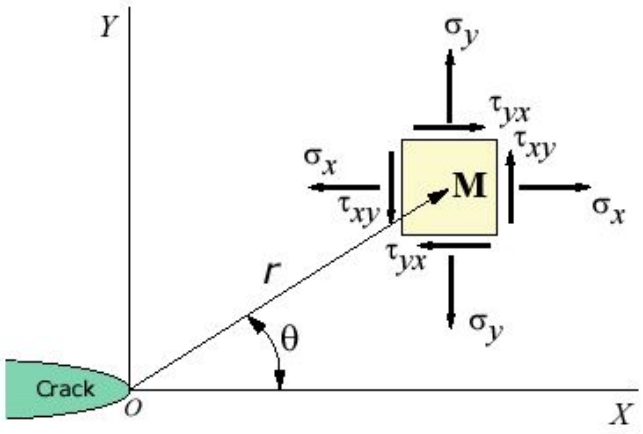

Figure 2-1: Stress fields near crack-tip

- Mode III or anti-plane shear mode characterized by the shearing of crack lips in the direction parallel to the crack front.

Another way to characterize the stress singularity near crack tip is the use of contour integrals including the Rice integral. The latter is defined by:

$$J = \int_{\Gamma} \left(wdy - T\frac{\partial u}{\partial x} \right) dS \tag{2.4}$$

with Γ an integration contour surrounding the end of the crack (Fig. 2-3), T and u denotes the stress and displacement vectors in a point of Γ. w is the strain energy density. The J-integral is path-independent in plastic materials provided that there is no non-proportional loading. Considering that the J-integral allows the characterization of the singularity of stresses at crack-tip as well as the stress intensity factor, it is shown that in LEFM framework, there exists a relation between the integral J and the stress intensity factor. For an isotropic material, one can write:

$$J = \frac{K_I^2}{E^*} \tag{2.5}$$

with $E^* = E$ under plane stress conditions and $E^* = E/(1-\nu^2)$ for plane strain condition. The Young's modulus is denoted by E and ν denotes the Poisson ratio.

2.1.2 Fundamentals of fatigue of materials

2.1.2.1 Fatigue loading

There are different fatigue loading paths. In this thesis, we will limit ourselves to constant amplitude loading. Various parameters allow the characterization of this type of loading namely:

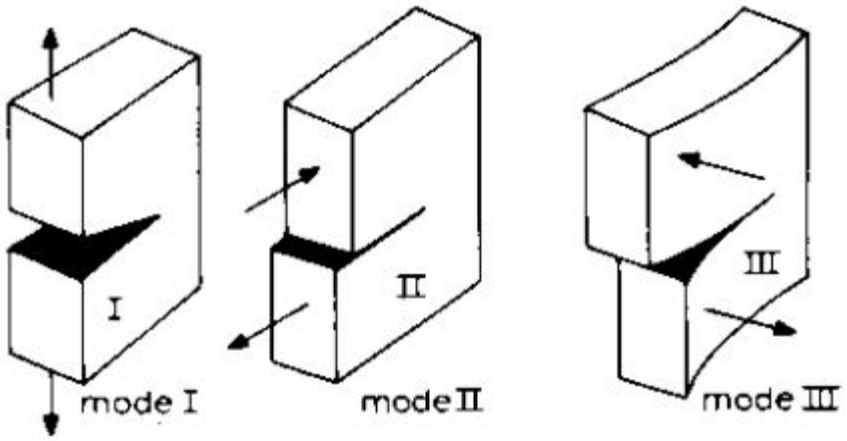

Figure 2-2: Schematic representation of different loading modes

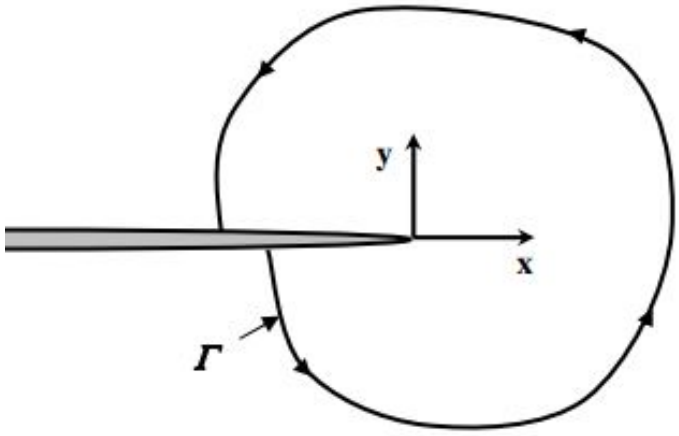

Figure 2-3: Arbitrary contour around the end of a crack

- The form of the loading: For a sinusoidal loading with constant amplitude, the applied stress obeys the following mathematical formulation:

$$\sigma_{ij}(t) = \sigma_{a,ij} \sin(\omega t) + \sigma_{m,ij} \tag{2.6}$$

where σ_a is the amplitude of the stress and σ_m is the mean stress. $f = \omega/2\pi$ is the loading frequency. The amplitude of the applied stress and the mean stress are calculated respectively by Equation 2.7 and Equation 2.8:

$$\sigma_{a,ij} = \frac{1}{2}\left[\max(\sigma_{ij}(t)) - \min(\sigma_{ij}(t))\right] \tag{2.7}$$

$$\sigma_{m,ij} = \frac{1}{2}\left[\max(\sigma_{ij}(t)) + \min(\sigma_{ij}(t))\right] \tag{2.8}$$

- Load ratio: The stress ratio can be defined as:

$$R_\sigma = \frac{\sigma_{min}}{\sigma_{max}} \tag{2.9}$$

According to the value of the loading ratio, one distinguishes the alternating loading (for which the load ratio is equal to -1), the repeated loading (for which the load ratio is 0). Another type of load ratio conventionally used for fracture analysis of cracked bodies (and also used in this work) is the one based on stress intensity factors and defined by:

$$R_K = \frac{K_{min}}{K_{max}} \tag{2.10}$$

During cyclic loading, the properties of metallic materials are modified. Microdamage accumulates may becomes fatal. In practice, the fatigue of materials is approached in two different ways: the recording of the Wöhler curves (S-N curves) and the measurement of the crack growth rates.

2.1.2.2 Fatigue life approaches

S-N Curves The S-N curve or Wöhler curve is a curve that allows the evaluation of the lifetime of a material (in terms of the number of cycles to failure) as a function of the magnitude of the applied stresses. It is also called the endurance curve. Fig. 2-4 shows an example of the Wöhler curve. An increase in the lifetime when the magnitude of the applied stresses decreases is observed. We can split this curve into three zones:

- Low cycle fatigue zone (zone 1) for which the applied stresses are higher than the yield stress of the material. This zone is also called the oligocyclic plastic fatigue zone. In this area the fracture occurs after a small number of cycles (few cycles to approximately 10^4 cycles)

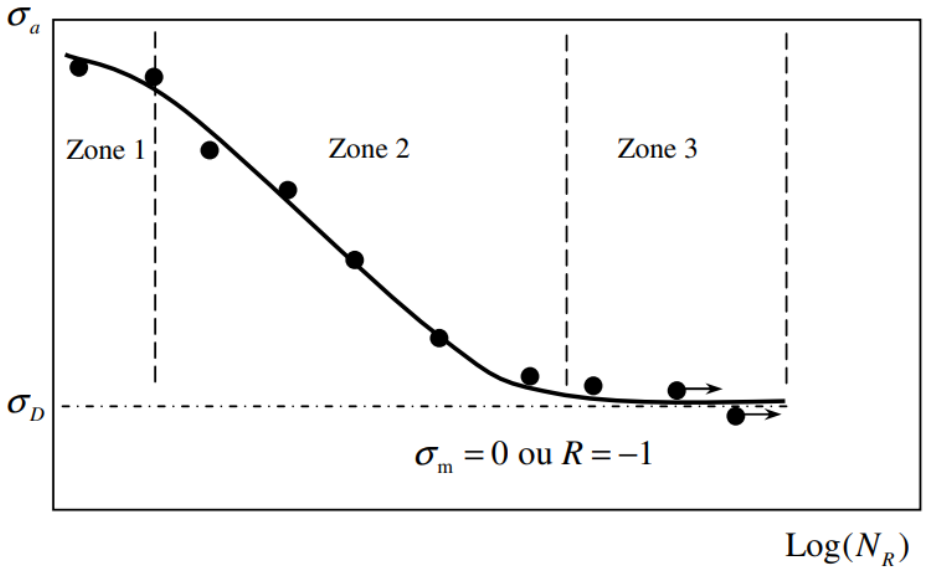

Figure 2-4: Schematic representation of a S-N curve

- Zone of limited endurance (zone 2) for which failure occurs after a large number of cycles but limited (fatigue life between 10^5 and 10^6 cycles)
- Zone of fatigue limit or safety zone (zone 3) which corresponds to low stress loads. In this zone, it is estimated that the fracture cannot occur before a higher number of cycles: 10^6- 10^7 cycles. However, gigacyclic fatigue tests question the existence of this limit ([Mughrabi, 1999, Mughrabi, 2006, Stanzl-Tschegg et al., 2007])

Strain-life approach In addition to S-N curves, strain-life approaches (Fig. 2-5) are also often used to estimated fatigue crack initiation. In this case, the total strain is used instead of the stress as in the case of S-N curves. The total strain amplitude $\Delta\epsilon/2$ is defined as:

$$\frac{\Delta\epsilon}{2} = \frac{\Delta\epsilon_e}{2} + \frac{\Delta\epsilon_p}{2} \tag{2.11}$$

with $\Delta\epsilon_e/2$ and $\Delta\epsilon_p/2$ the amplitude of elastic and plastic strain respectively.

Fracture mechanics approach Another way to study fatigue life of materials consists in measuring cyclic crack propagation rates as function of the stress intensity factor (SIF) amplitude. Fig. 2-6 shows a schematic representation of a traditional plotting of fatigue crack growth rate as function of SIF. One can distinguish along this curve three main domains:

- Regime A where the propagation rate is very low with significant effects of microstructure, environment and mean stress. The propagation rates

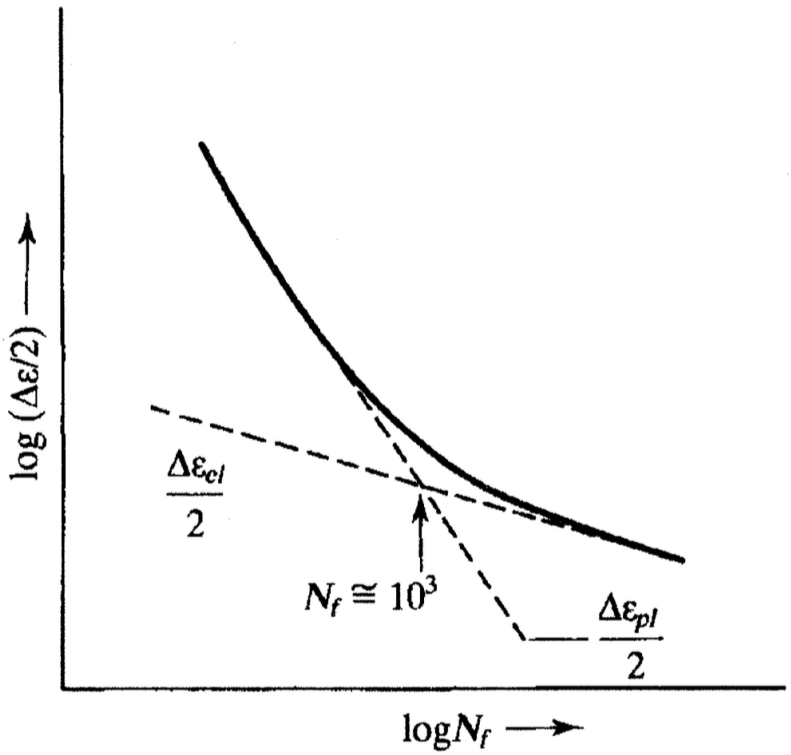

Figure 2-5: Schematic representation of a Strain-N curve

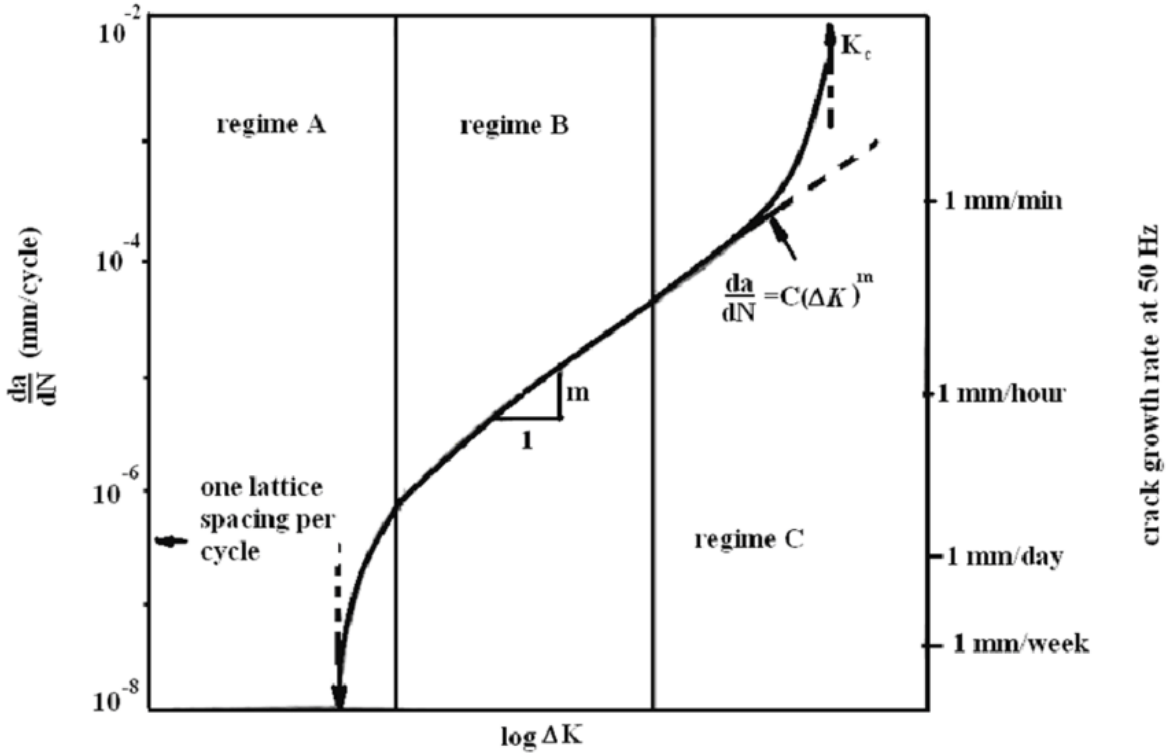

Figure 2-6: Schematic representation of the dependence of crack growth on stress intensity factor

measured in this regime are generally between 10^{-12} and 10^{-10} m/cycle.

- Regime B where prevail not only microstructure effects but also combined effects of environment and loading frequency. In this area, the measured propagation rates are often between 10^{-9} m/cycle and 10^{-6} m/cycle.
- Regime C corresponds to the abrupt failure regime with an effect of microstructure, maximum applied stress intensity factor K_{max}, as well as geometry, as in static overload fracture. But it depends little on environment.

2.2 Literature review on fatigue crack initiation

2.2.1 Cyclic slip localization and PSB formation

Predicting the lifetimes of metallic materials and structures subjected to fatigue first requires the understanding of the physical mechanisms of damage evolution during cyclic loading. Whatever the fatigue crack initiation site, it always involves the localization of plastic deformation in the form of Persistent Slip Bands (PSBs) which are formed in transition fatigue of metals and metal alloys. The pioneering work of Ewing and Humfrey [Ewing and Humfrey, 1903]

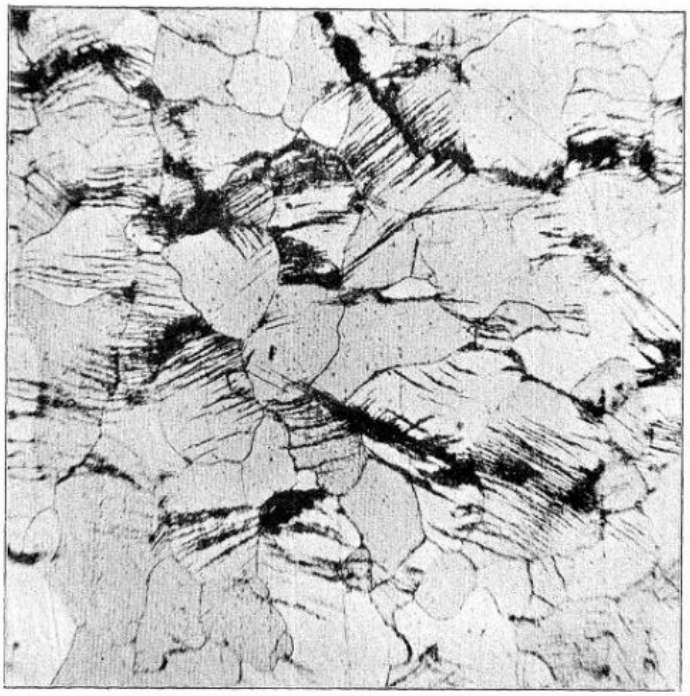

Figure 2-7: Cyclic slip localization in surface grains of a polycrystalline Swedish iron cyclically deformed up to 60000 *cycles* [Ewing and Humfrey, 1903]

allow for the first time the observation of possible localized cyclic slip and fatigue crack initiated within the rough surface relief in surface grains of a polycrystalline Swedish iron cyclically deformed during a rotating bending test (Fig. 2-7). Indeed, as a result of the accumulation of loading cycles, defects like dislocations multiply and accumulate, leading to an increase in the dislocation density [Polák, 1970, Polák, 1987] within the material. Some believe that in order to minimize the energy of the system, these dislocations are arranged in specific structure [Basinski and Basinski, 1992a], thus causing the location of the plastic slip in the form of what is called "slip bands". The "persistent" character of slip bands induced by fatigue loading was first revealed by Thompson and co-workers [Thompson et al., 1956] who showed that the slip bands are persistent in the sens that they always reappear at the same location after electropolishing and recycling operations. Since then, it was widely accepted that, the localization of cyclic plastic deformation in persistent slip bands is the first step in the damage evolution leading to crack initiation in fatigued crystalline materials. Many studies dedicated to PSBs were first carried out in copper crystals [Basinski et al., 1969, Basinski et al., 1983, Finney and Laird, 1975, Finney and Laird, 1982, Watt et al., 1968, Winter, 1973] and later on nickel crystals [Hollmann et al., 2000, Holste, 2004, Mecke and Blochwitz, 1982, Weidner et al., 2008b] and allowed the understanding of their formation, structure and behaviour. Many years after the pioneering works of Ewing and Humphrey [Ewing and Humfrey, 1903] many other authors enriched

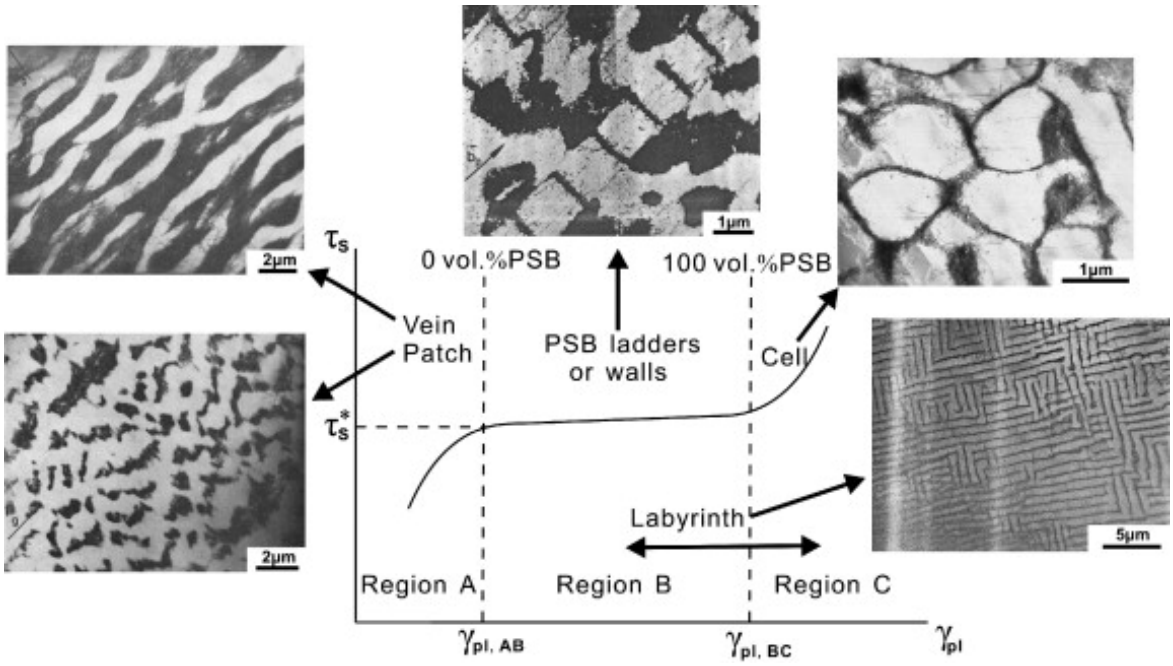

Figure 2-8: Cyclic stress–strain (CSS) curve and dislocation patterns with three regions of copper single crystal oriented for single slip. [Li et al., 2011]

the knowledge on slip localization and PSB formation through the proposed mechanism of PSB formation. That involves dislocations which slip is responsible for the plastic deformation. Many studies suggest the existence of a PSB threshold under which the microscopic structure contains relatively few dislocations and is rather homogeneous (Fig. 2-8). Above this threshold which is established at about 6×10^{-5} according to Mughrabi and co-workers [Mughrabi, 1978, Wang and Mughrabi, 1984b] or 10^{-4} according to Bily [Bílý, 1993] in copper, the formation a PSBs occurs. Previous works showed that dislocation structures in PSBs are different from those observed in the surrounding material generally called "matrix" and consist in a ladder-like structures [Lukáš et al., 1968, Woods, 1973, Katagiri et al., 1977, Winter, 1980, Winter et al., 1981, Rasmussen and Pedersen, 1980, Liu et al., 1994, Holzwarth and Essmann, 1994, Li et al., 2009, Petrenec et al., 2006, Polák et al., 2017, Mughrabi, 1984] as illustrated in Fig. 2-9. The internal structure of PSBs consists of walls of high dislocation density, mainly edge dipole dislocations that are almost immobile, and channels of low dislocation density, in which the screw dislocations glide. Despite the ladder-like structure is the widely observed dislocation structure type in PSBs, the ladder-like structure is not the only structure type that characterizes PSBs as pointed out by Man et *al.* [Man et al., 2009b]. According to the authors, in some cases, the internal structure of PSBs is, so far, unresolved. During loading, the volume fraction of the PSB increases up to 100% when the amplitude of the plastic slip reaches $\gamma^p_{PSB} = 7.5 \times 10^{-3}$ [Mughrabi, 1978, Wang and Mughrabi, 1984b] which

is the level of saturation generally reported in literature for copper for example. This saturation level is approximately 10^{-2} for 316L SS or Ni [Hazan, 2019]. Therefore, the amplitude of the total plastic slip can be calculated through the mixture law as proposed by Winter *et al.* [Winter et al., 1981].

$$\gamma^p = f\gamma^p_{PSB} + (1-f)\,\gamma^p_M \tag{2.12}$$

where γ^p is the remote plastic slip, γ^p_{PSB} is the plastic slip within PSBs and γ^p_M the plastic slip within the matrix. f denotes the volume fraction of PSBs. Beyond the the PSB plateau, the formation of dislocation cells and labyrinth structures is observed (Fig. 2-8) with an increase in resolved shear stress (RSS).

It should be kept in mind that there exist two types of slip bands depending on the orientation angle between the slip vector and the normal with respect to the free surface. Brown and Miller [Brown and Miller, 1973] classified SBs into two types: type A and type B SBs (Fig. 2-10). As illustrated in Fig. 2-10, for type B PSBs, the slip occur through the free surface while for type A PSBs, the slip occurs in the free surface.

2.2.2 Extrusions and intrusions formation

PSBs are volumes of intense plastic activity and the plastic strain localization within PSBs leads generally to the formation of surface persistent slip markings [Polák et al., 2017] leading to fatigue crack initiation. For a long time, and until today, extrusions and intrusions have been the object of many studies, both qualitatively and quantitatively. The development of experimental techniques and theoretical approaches have made it possible to shed light on the mechanisms of formation of these extrusions and intrusions. Their shape, their heights and width can be now measured accurately by AFM (Atomic Force Microscopy) and using FIB (Focussed ion Beam) cutting. Nowadays, these extrusions/intrusions continue to hold the attention of researchers throughout the world because of their role in fatigue crack initiation in single and polycrystals of numerous metals and alloys subjected to fatigue loading. A non-exhaustive study of the experimental techniques that allowed or still allow the study of these extrusions and intrusions is presented in the review of Man et *al.* [Man et al., 2009b].

The EGM I model is the first theory which provide a physically based explanation for the formation of extrusions. This model explains in fact that the extrusion of PSBs throughout the free surface is the result of the production of vacancies inside the PSB following the interactions between dislocations. Indeed, Essmann and Mughrabi [Essmann and Mughrabi, 1979] and Essmann et *al.* [Essmann et al., 1981] showed that in a copper cyclically strained at RT, two edge dislocations of opposite signs which encounters will spontaneously annihilate if the distance between their slip planes is lower than a characteristic distance of 1.6 nm and this annihilation leads to the production of vacancies. Also, as we will see in chapter 4 and 6, vacancies can be also produced by jog dragging. This process of mutual annihilation of dislocations and jogs dragging induces the

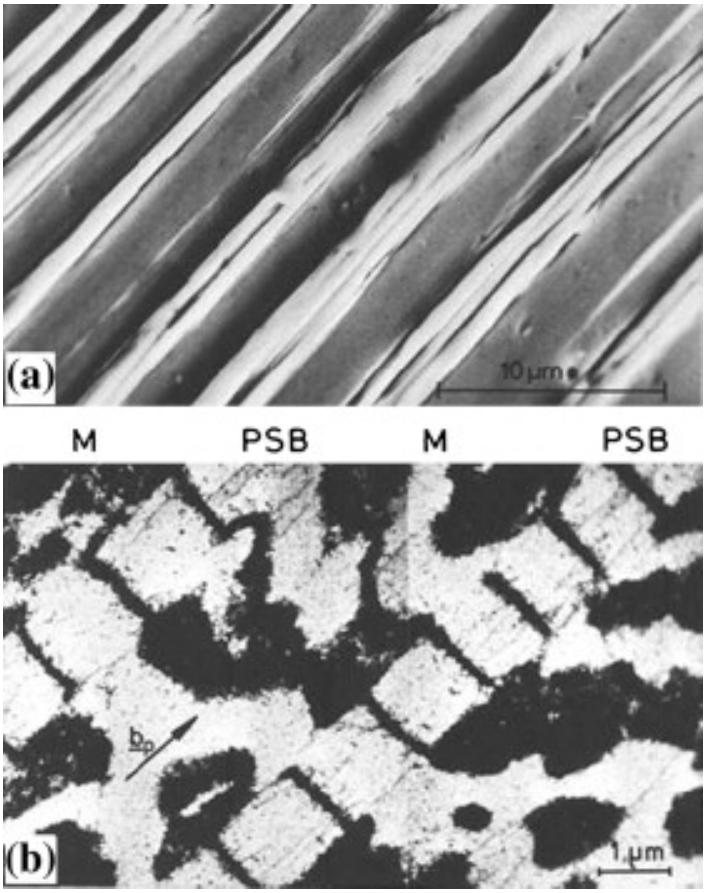

Figure 2-9: Persistent slip bands in fatigued copper single crystal (a) surface relief observed by SEM (b) TEM picture showing PSBs with a ladder-liked structure and matrix with a vein structure between PSBs. Quoted from [Li et al., 2011, Mughrabi, 1985]

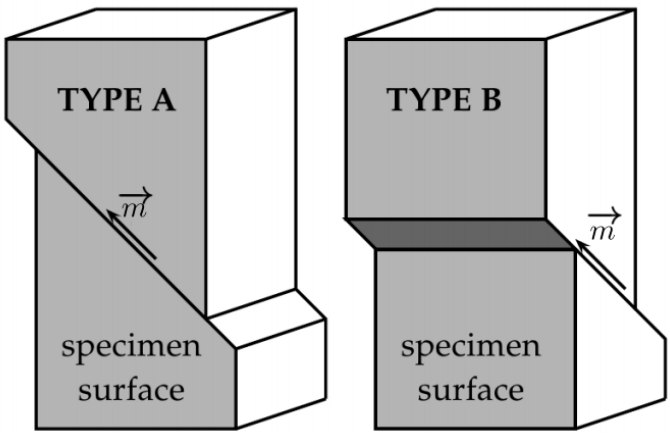

Figure 2-10: Different types of slip bands. $\vec{m}$ is the sip direction. For type A SBs, slip occurs in the free surface while for type B SBs, slip occurs through free surface. Quoted from [Agbessi, 2013].

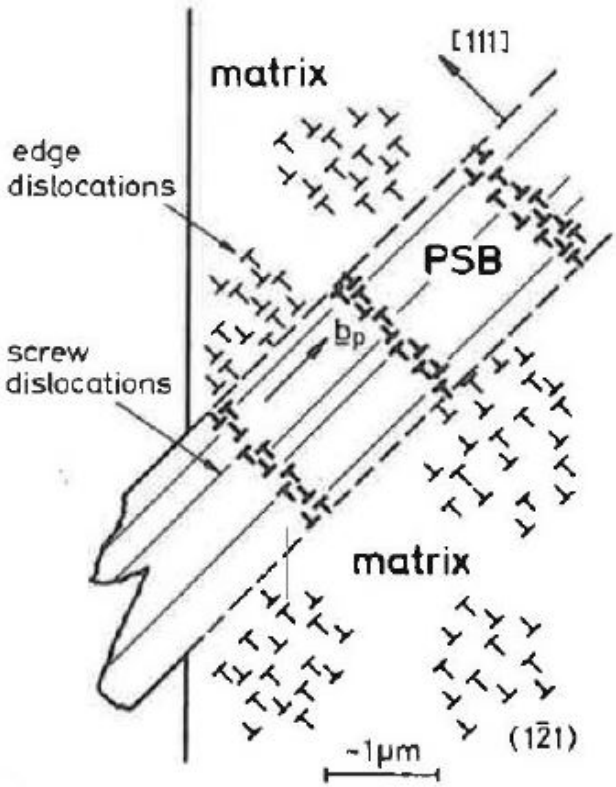

Figure 2-11: Shematic representation of a PSB emerging on the free surface, embedded in a quasi-elastic matrix (The PSB is composed of zones saturated with edge dislocations arranged in very dense clusters and zones with very low dislocations) [Essmann et al., 1981].

production of vacancies, the production of which leads to a free expansion of the PSB and consequently a rapid extrusion of the PSB throughout the free surface.

The EGM II (EGDM) model proposed by Differt et *al.* [Differt et al., 1986] tries to explain the surface roughness by the plastic irreversibility following the mechanism of annihilation of edge and screw dislocations. Considering screw dislocations only, Differt et *al.* [Differt et al., 1986] evaluated the irreversibility factor to be approximately 0.6 in copper at RT while this irreversibility factor drops to 0.3 when edge dislocations are taken into account. The slip irreversibility factor is characterized by the fraction p of irreversible plastic slip per cycle compared to the total plastic slip ($p = \Delta\gamma_{pl,irr}/\Delta\gamma_{pl}$). The MD investigations by Fan et *al.* [Fan et al., 2016] provided slip irreversibility factor ranging between 0.35 and 0.725 while the experimental investigations via AFM by Weidner and coworkers [Weidner et al., 2011] provided a cyclic slip irreversibility of 0.8 in nickel. The irreversibility factor allowed the authors to predict the evolution of surface relief. The surface roughness in EGM II is defined as the average value of the difference between the greatest positive and negative displacements parallel to the effective slip vector and is given by:

$$\frac{h}{b} = \sqrt{f\left(4\ N\ p\ \gamma^{p}_{PSB}\frac{t}{b}\right)} \tag{2.13}$$

where p is the slip irreversibility factor, t, the PSB thickness, b the Burgers vector, f the Schmid factor, γ^{p}_{PSB} the plastic slip amplitude within the PSB and N the number of cycles.

Considering typical values for copper, Equation 2.13 leads to:

$$h = 1.5 \times 10^{-3}\sqrt{N}\ \ [\mu m] \tag{2.14}$$

An illustration of surface relief is shown in Fig. 2-11 according to EGM I and II models. As depicted on Fig. 2-11, the surface relief formation begins by an early rapid growth of extrusion followed by a slow roughening during cyclic loading due to slip irreversibility.

The model proposed by Polàk [Polák, 1987] as an extension of the EGM II model suggests not only vacancy production and annihilation within PSB but also the migration of steadily produced point defects at temperatures at which they are mobile. These vacancies at high temperatures can migrate from channels to the surrounding matrix. The steady production of vacancies and their diffusion lead to the dynamic extrusion growth and to the production and deepening of intrusions at the PSB/matrix interface. The first analytical model of the coupled diffusion-plasticity was proposed by Polàk and Sauzay [Polák and Sauzay, 2009]. These intrusions are considered by the author to be the source of fatigue crack initiation.

2.2.3 Fatigue crack initiation sites

Different fatigue crack initiation sites may be observed, namely: (i) initiation along persistent slip bands (PSBs), (ii) initiation along twin boundaries parallel to PSBs, and (iii) intergranular initiation. It should be noted that in the case of hard steels containing second phase particles, initiation can take place either inside or at the interfaces of inclusions. Fatigue crack initiation sites generally depend on the environment in which tests are performed. Indeed, at a plastic amplitude of $\Delta\epsilon_p/2 = 2\times10^{-3}$, according to the experimental work of Mineur et *al.* [Mineur et al., 2000], 73% of fatigue microcracks are initiated along PSBs in air environment, while the intergranular initiation and initiation along twin boundaries represent respectively 20% and 7%. Under vacuum, intragranular initiation along PSBs represents only 33% while intergranular initiation accounts for 57% and initiation along twin boundaries constitutes 10% of fatigue cracks initiation. Furthermore, Chan and co-workers [Chan et al., 2009, Chan, 2010] showed a strain amplitude dependence of fatigue crack initiation site. Indeed, the authors reported that, the percentage of fatigue cracks initiated along PSBs decreases and the GB cracks one increases when increasing plastic strain amplitudes.

Numerous studies investigated fatigue crack initiation along PSBs in ductile metals and alloys. Almost all of these studies emphasize the importance of extrusions and intrusions in the initiation of fatigue crack. Using Focused ion beam (FIB) technique and some advanced microscopy techniques, Man *et al.* [Man et al., 2012] studied the microstructural evolution that precedes fatigue crack initiation in nickel and 316L steel cyclically deformed at constant plastic strain amplitude ($\epsilon_{ap} = 10^{-3}$). Fig. 2-14 shows an extrusion and a fatigue crack initiated from the intrusion in 316L SS after $3800\ cycles$ ($8.3\%\ N_f$). Polak *et al.* [Polák et al., 2017] studied the role of extrusions and intrusions in fatigue crack initiation in a polycrystalline copper of 99% of purity, 316L SS and highly alloyed Sanicro 25 austenitic steel. The specimen were cyclically strained at a constant strain rate of $5 \times 10^{-3}\ s^{-1}$ up to $5000\ cycles$ for copper and $9250\ cycles$ for Sanicro 25. The authors were able to observe and well document the initiation of fatigue fatigue cracks from the tip of intrusions.

The initiation of fatigue cracks along grain boundaries is also the result of a process involving PSBs. Indeed, the initiation of fatigue cracks along the grain boundaries results from the interaction between a PSB and a GB. The impingement of a PSB on a GB leads to strain incompatibilities inducing stress concentrations which may lead to the initiation of a fatigue crack. Therefore, the initiation of a fatigue crack along a grain boundary will depend on a number of factors such as grain size, grain boundary structure, disorientation from neighboring grains, the nature and geometry of the grain boundary. Some authors pointed out the ability of the grain boundary to promote slip transfer as an important factor that can influence the initiation of a fatigue crack since this ability to slip transfer depends on the nature and geometry of the GB. Fig. 2-16 shows an exam-

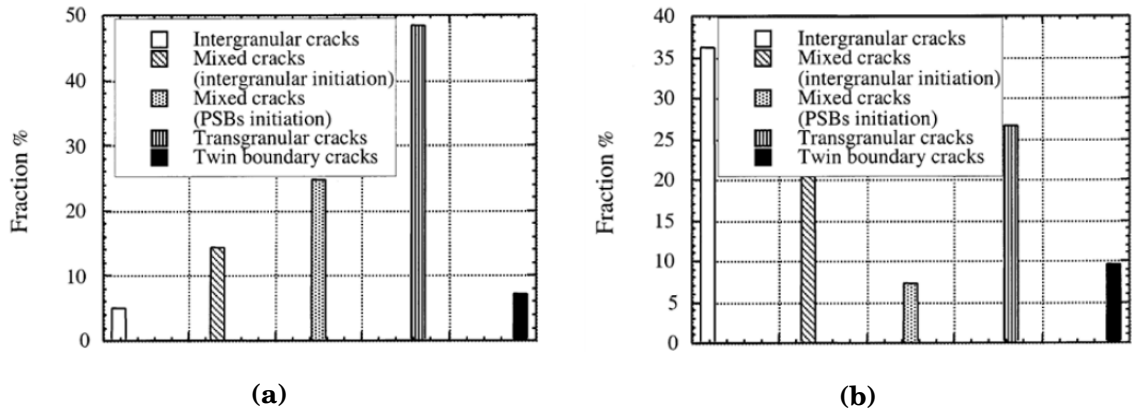

Figure 2-12: Fatigue crack initiation sites in a 316L Stainless Steel (316L SS) under (a) air environment (b) vacuum after 5000 cycles [Mineur et al., 2000]

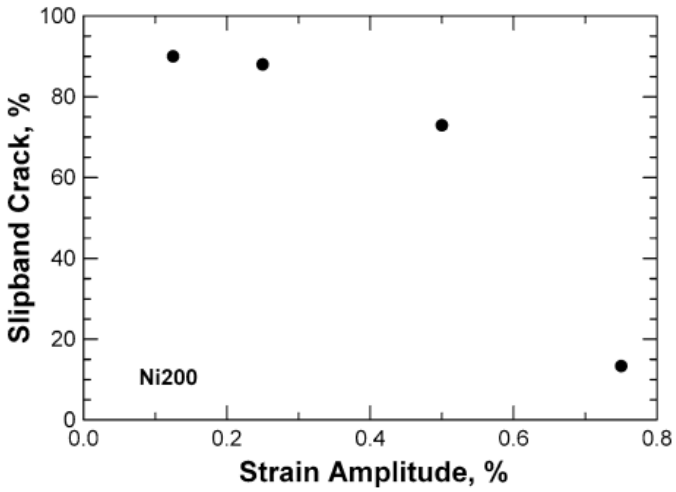

Figure 2-13: Percentage of fatigue cracks parallel to PSBs normalized by the sum of cracks parallel to PSBs and GB cracks in Ni200 as a function of strain amplitude [Chan et al., 2009]

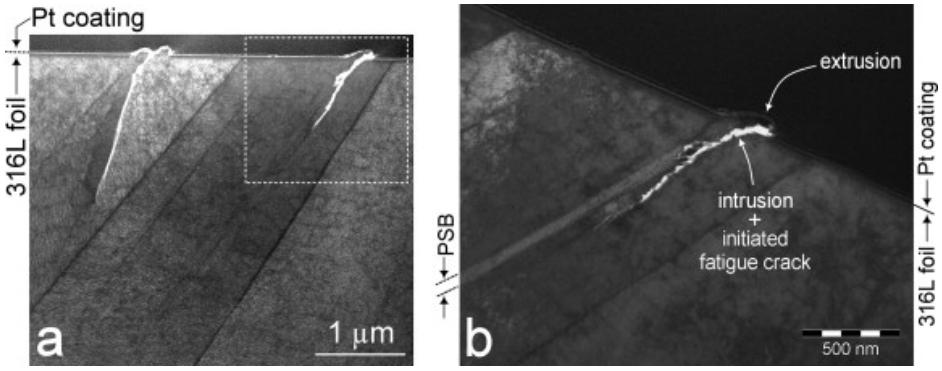

Figure 2-14: (a) Overview observation and (b) detailed observation of an extrusion and a short fatigue crack initiated from an intrusion in 316L SS after 8300 cycles (8.3% N_f). Applied constant plastic strain: $\Delta\epsilon_p/2 = 10^{-3}$ [Man et al., 2012]

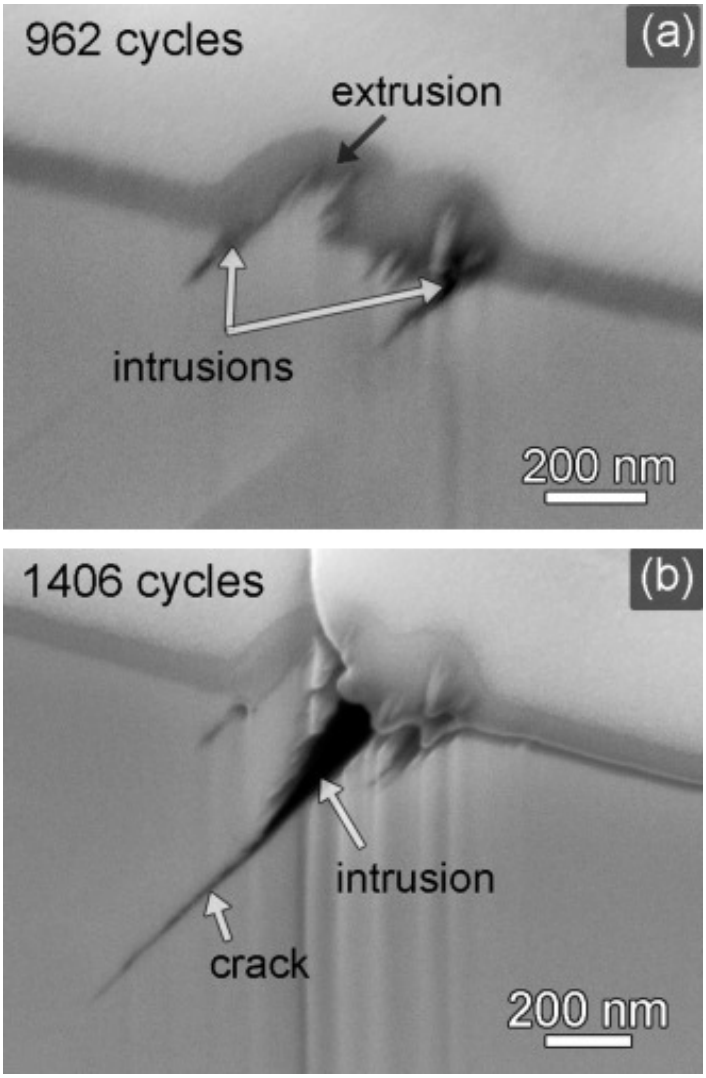

Figure 2-15: Extrusion-intrusion profile and fatigue crack initiation in Sanicro 25 during cyclic loading at constant amplitude strain 3.5×10^{-3} (a) $962\ cycles$ (b) $1406\ cycles$ [Polák et al., 2017]. One can observe a crack initiated from the tip of one of the two intrusions.

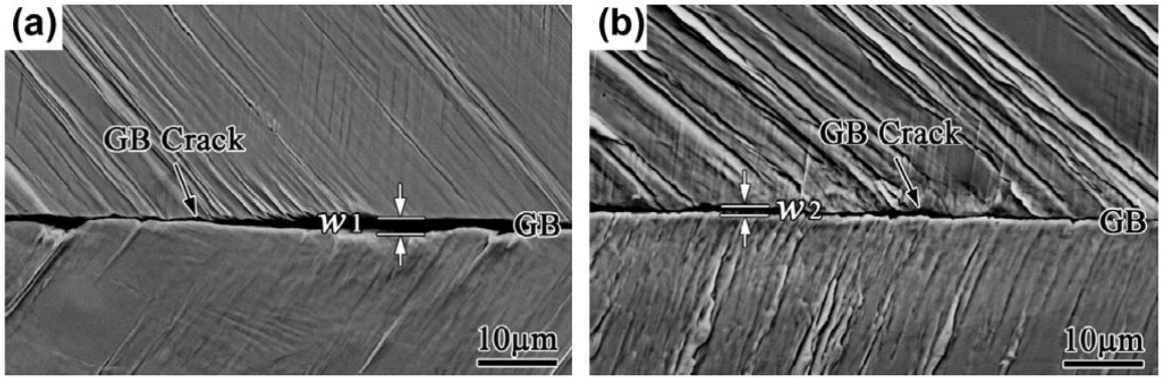

Figure 2-16: Fatigue crack initiated along grain boundaries in copper bi-crystals [Li et al., 2013]. One can observe the slip bands impingement on grain boundaries.

ple of fatigue cracks initiated at grain boundaries. Some authors such as Eshelby et *al.* [Eshelby et al., 1951] earlier or more recently Guo et *al.* [Guo et al., 2014], Sauzay and co-authors [Sauzay and Vor, 2013, Sauzay and Moussa, 2013] under monotonous loading, Hazan [Hazan, 2019] for cyclically deformed FCC metals and alloys and Sicaud [Sicaud, 2020] for irradiated FCC metals and alloys attempted to predicted stress concentration resulting from the interaction between a SB and a GB. Sangid et *al.* [Sangid et al., 2011a, Sangid et al., 2011b] proposed a microstructure based model with pile-up theory for the prediction of fatigue crack initiation in Udimet 720 Ni-based superalloy whereas Hazan [Hazan, 2019] proposed a model of fatigue crack initiation for FCC metals based on point defect production and continuum crystal plasticity. It should also be noted that fatigue cracks do also form along crystallographic planes that intersect disrupted grain boundaries. This mechanism is also known as Zener-Stroh mechanism.

The initiation of fatigue cracks along twin boundaries (TB) has also been reported in the literature. In general, the cracks are initiated when PSBs develop parallel to TBs [Favier et al., 2016]. The mechanism of initiation of these fatigue cracks is the formation of PSBs along the TBs. Indeed according to the works of Neumann and co-workers *al.* [Heinz and Neumann, 1990, Neumann and Tönnessen, 1987, Neumann, 1999] and Blochwitz et *al.* [Blochwitz et al., 2008, Blochwitz and Richter, 1999, Blochwitz et al., 1997, Blochwitz and Tirschler, 2003], the stress concentration in the vicinity of an emerging TB, close to the free surface, combined with the shear stress promote the activation of local plasticity within the TBs resulting in a localization of the plastic deformation and the formation persistent slip bands along the TBs since TBs in FCC metals run also along the $\{1\,1\,1\}$ planes. This will be followed by the initiation and propagation of fatigue cracks as in the case of initiation along PSBs without TBs or GBs. This mechanism has been validated experimentally by the investigations of Man *et al.* [Man et al., 2012]. Some authors have observed cracks not directly along

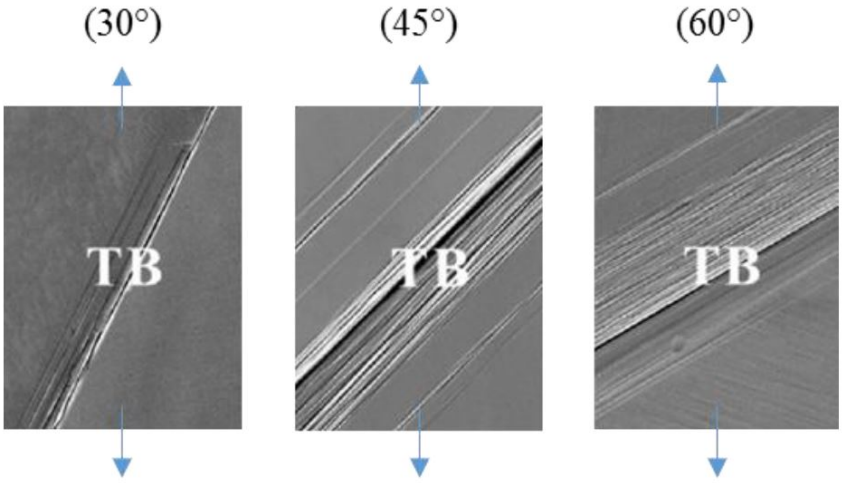

Figure 2-17: Fatigue crack initiated along TBs oriented at different angles with respect to the loading axis [Hazan, 2019, Zhang et al., 2017]. One can observe PSBs parallel to TBs whatever the orientation.

twin boundary but parallel to the twin boundary at some distance away (about 30 to 50 nm) as shown by Miao *et al.* [Miao et al., 2012], Castellucio and McDowell [Castelluccio and McDowell, 2013]. The investigations of Zhang *et al.* [Zhang et al., 2017] shed light on the crystallographic configurations favorable to the formation of PSBs parallel to TBs. It has been found that in the majority of cases, the PSBs are produced parallel to TBs inclined at $45°$ with respect to the loading axis (see Fig. 2-17). In the case of TBs inclined at $30°$ and $60°$, the PSBs intersect TBs, then PSBs also form along these TBs and the initiation of fatigue cracks follows along TBs. The orientations that favors the initiation of fatigue cracks along TBs are therefore the TBs oriented at $30°$, $45°$ and $60°$ (see Fig. 2-17). For TBs oriented at 0 and $90°$, the initiation of fatigue cracks occurs late. More generally, many studies have looked at the role of TBs in fatigue crack initiation, particularly in pure copper [Ma, 2006, Ma, 2007, Qu et al., 2008, Zhang et al., 2008], and copper alloys [Qu et al., 2008, Zhang et al., 2008]. Studies show that the frequency of fatigue cracking along TBs increases as the magnitude of strain decreases. The orientation and misorientation distributions were also found to play an important role on the density and the propagation of TB cracks. Some authors observed fatigue crack initiation

2.3 Literature review on fatigue crack propagation

2.3.1 Fatigue crack propagation stages, effect of environment

It is generally admitted that fatigue crack propagation (FCP) occurs into two main stages: stage I and stage II. Fig. 2-18 shows an illustration of these stages. Stage I corresponds to the short crack propagation after its initiation. As discussed above, fatigue cracks are generally initiated along PSBs and they propagate along these slip bands in a mixed mode manner, along the primary slip plane and in the direction of primary burgers vector. It is shown that during stage I, crack growth rates are very slow [Sauzay and Liu, 2014]. According to Kaplan [Kaplan, 1967], the propagation of fatigue cracks in stage I is characterized by the coplanar glide of dislocations. During loading, as the stress intensity factor increases, multiple slip occurs at a crack-tip initiating stage II crack propagation during which, fatigue crack propagates perpendicular to the loading axis (Fig. 2-18). To these stages, a stage III can be added which is associated with an unstable crack propagation for stress intensity factors close to K_{IC} and which generally leads to a sudden failure. Neumann's tests on $[1\,0\,0]$ (stress axis) oriented single crystals show that under air, stage I crack propagation takes place for any crack length provided the loading level is low enough to induce a propagation rate of less than $10\ \mathrm{nm/cycle}$ [Neumann et al., 1978]. Neumann did not observe stage I crack growth under vacuum. Wang and Mughrabi [Wang and Mughrabi, 1984a] in their tests on copper single crystal oriented for a single slip revealed that stage I crack propagation takes place either under air or under vacuum. The absence of stage I crack propagation under vacuum in Neumann experiments would be linked to the crystal orientation. This orientation favors a symmetric multiple slip and therefore is not suitable to a stage I crack propagation. Additionally, the crack plane is perpendicular to the $[1\,0\,0]$ direction which does not correspond to stage I crack propagation plane. Even if stage I crack growth has been observed in a variety of ferrous, aluminum and titanium alloys for crack length values substantially larger than the grain size [Suresh, 1998], cracks generally undergo a transition from stage I to stage II during which cracks grow along a macroscopic plane perpendicular to the loading axis. As reported by Wang and Mughrabi [Wang and Mughrabi, 1984a], the transition from stage I to stage II could occur at arbitrary crack length by a suitable increase or reduction in load amplitude whatever the environment. They stated that the higher the stress on the secondary slip system compared to that on the primary slip system, the sooner the transition from stage I to stage II will take place.

The environment was shown to play an important role in fatigue crack growth. For example, Neumann et *al.* [Neumann et al., 1978] showed that at

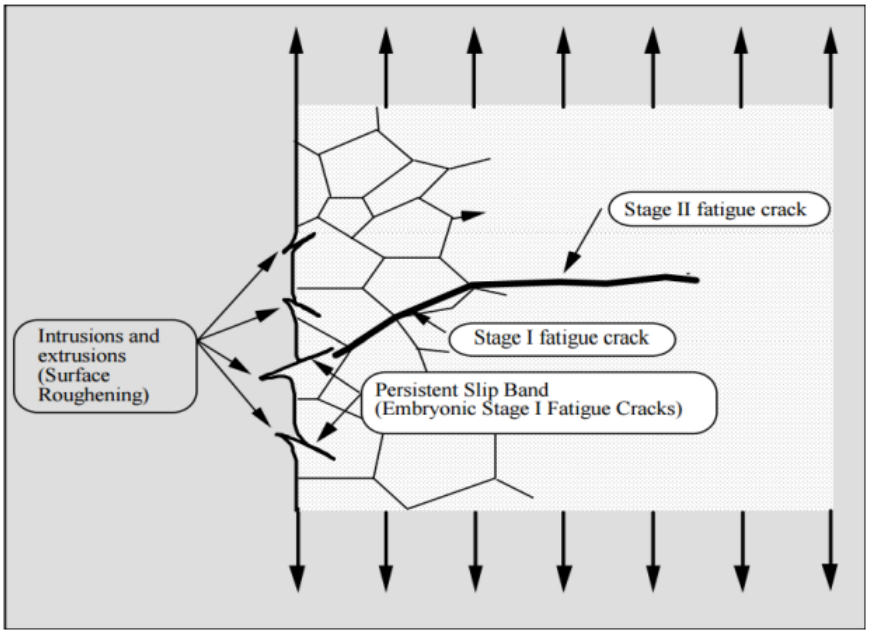

Figure 2-18: Fatigue crack propagation stage I and stage II. Quoted from [Fan, 2016]

.

a low load amplitude, the propagation rate in air could be ten times higher than that measured in vacuum. Wang et *al.* [Wang et al., 1984] show that fatigue life of copper single crystals cyclically deformed under vacuum could be 15-30 times longer than under air environment. As the authors did not observed significant differences in terms of microstructure, they suggest that the difference in fatigue life should be due to the reduced fatigue crack growth rate under vacuum in stage I. This is in agreement with their stage I vs stage II growth rate measurement under vacuum and air.

2.3.2 Fatigue crack propagation models

Two main models of fatigue crack propagation are highlighted in literature: the void coalescence model and the blunting-resharpening model.

2.3.2.1 Void coalescence model

Void absorption model suggests that fatigue crack grows by the cavity nucleation, growth and coalescence ahead of the crack tip. Voids growth under monotonous and cyclic loading have been extensively studied in the literature ([Benzerga and Leblond, 2010, Benzerga et al., 2016, Monchiet and Kondo, 2013, Morin and Michel, 2018, Lacroix et al., 2016, Devaux et al., 1997, Potirniche et al., 2006]). This crack propagation mechanisms is generally encountered in hard steels containing second phase particles. These cavities are produced due to the localization of plastic deformation around

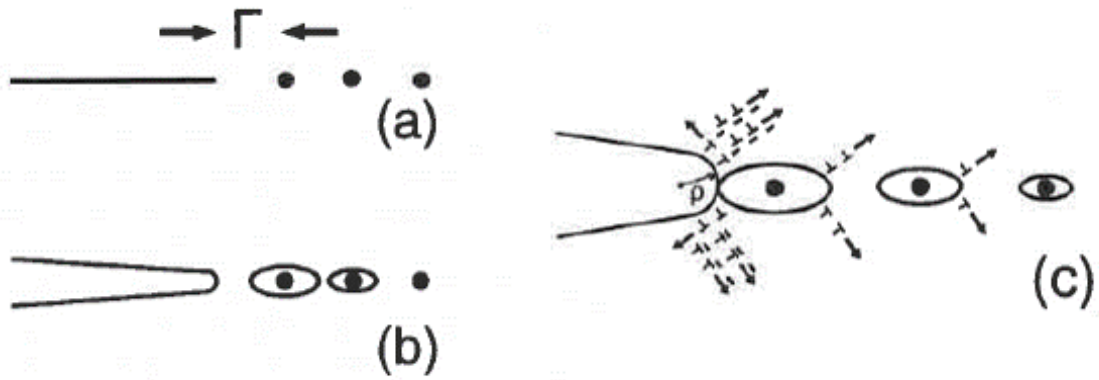

Figure 2-19: Schematic illustration of void absorption model. (a) crack tip with non coherent particles separated by distance Γ before loading. (b) Cavity nucleation at particles after loading application. (c) Cavity coalescence with blunted crack-tip. Quoted from [Weertman, 1996]

second phase particles, impurities,...Since pure metals does not contain second phase particles or may contain low impurities, it will be difficult to encounter this mechanism in pure metals.

2.3.2.2 Blunting resharpening model

This model was first proposed by Laird and Smith [Laird and Smith, 1962]. The blunting resharpening model suggests that fatigue crack tip blunts during tension phase and during unloading or compression, the crack-tip resharpens with the reversal slip (Fig. 2-20). Experimental investigations carried out by Neumann [Neumann, 1974, Neumann et al., 1978] on copper single crystals evidenced clearly this mechanism. This mechanism allow to explain the striations generally observed on fatigue crack surfaces.

However, the fundamental mechanisms governing fatigue cracks propagation remained unclear. To achieve this objective, some previous atomistic studies attempted to shed light on these fundamental mechanisms and have reported observations that are at odds with experimental observations. Indeed, many studies such as [Horstemeyer et al., 2001, Potirniche et al., 2005, Farkas et al., 2005, Wu et al., 2015] reported that the mechanism of fatigue crack propagation in ductile single crystals was cavities nucleation and coalescence ahead of crack-tip (Fig. 2-21). Other atomistic investigations reported fatigue crack growth by cleavage ([Horstemeyer et al., 2010, Potirniche et al., 2005]). These mechanisms are not in agreement with the experiments carried out on pure single crystals and alloys ([Neumann, 1974, Neumann et al., 1978] which reported mainly fatigue crack propagation by plastic blunting. In addition, FE computations by Hutar and Sauzay [Hutar and Sauzay, 2006] showed a ratchet effect around fatigue crack-tip. This ratchet effect should play an important role in fatigue crack propagation.

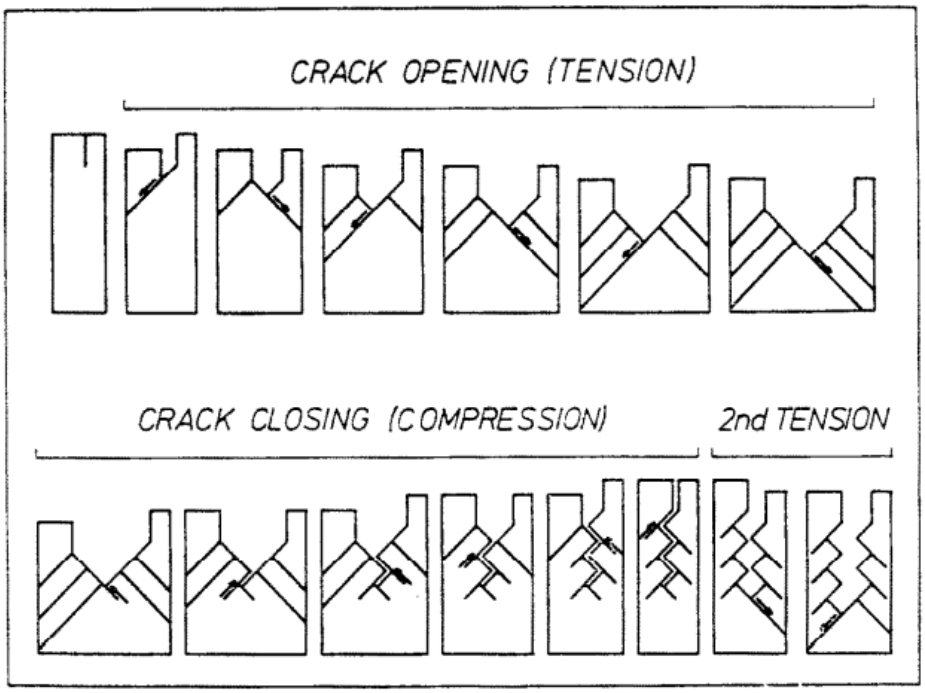

Figure 2-20: Schematic illustration of the blunting resharpening model. Crack tip blunting occurs during tension with plastic slip activity and the resharpening occurs during compression with reversal slip. Due to the non full reversibility of the plastic slip, the crack propagates [Neumann, 1974]

Otherwise, some experimental investigations reported on the one hand, a weak influence of temperature on fatigue crack propagation under inert environment [Sarrazin et al., 1997, Cotterill and Knott, 1992] and on the other hand, a more or less important effect of stacking fault energy on fatigue crack propagation [Miller, 1966, Ishii and Weertman, 1971a]. But to the author's knowledge, no extensive study at nanoscale have been carried out in order to shed light on the effect of temperature and stacking fault energy on fatigue crack propagation.

In this investigation, we tries to bring our contribution by answering partially these questions via molecular dynamics computations: fatigue crack (long crack) propagation mechanisms in the near threshold regime and in the framework of small scale yielding; the effect of temperature and stacking fault energy. Due to the limitations of such approach we are not interested in the effect of loading history. However before that, a chapter is devoted to the simulation of extrusions growth which precede the formation of fatigue cracks, via crystal plasticity finite element computations. The kinetics of extrusion growth is studied as well as stress fields induced by the extrusion growth and the relative likelihood of crack formation process.

This Ph.D. thesis manuscript is structured around eight chapters. In chapter 1 the reasons motivating this Ph.D. thesis are discussed. Then followed by chapter 2 providing short state of the art on fatigue crack initiation and propagation. Chapter 3 is devoted to the study of extrusion growth preceding fatigue crack initiation in cyclically deformed FCC metals and alloys. Based on the experimental observations of persistent slip bands (PSBs), and by the means of crystal plasticity finite element computations, we simulate the extrusion growth in crystals subjected to cyclic loading. The extrusion growth induced by vacancy production induces internal stresses along persistent slip bands. Chapter 4 deals with the plastic deformation mechanisms occurring near fatigue crack tip loaded under mode I and the subsequent lattice defects. Chapter 5 presents the results in terms of fatigue crack propagation in copper single crystals while in chapter 6 we assess the influences of temperature and stacking fault energy on crack-tip deformation and extension by fatigue, by considering different FCC single crystals Ag, Al, Cu, Ni. Chapter 7 is dedicated to the investigation of fatigue crack growth mechanisms under mixed mode loading. A general summary and future research directions extending this PhD thesis research works are provided in chapter 8.

2.4 Conclusion

In this chapter, after a review of the fundamental concepts of fracture mechanics and fatigue of materials, we are interested in the literature on the initiation of fatigue cracks. A state of the art on the surface relief of fatigued ductile metals as well as different sites and mechanisms of fatigue crack initiation was presented. The third and last part was devoted to the review on fatigue crack propagation,

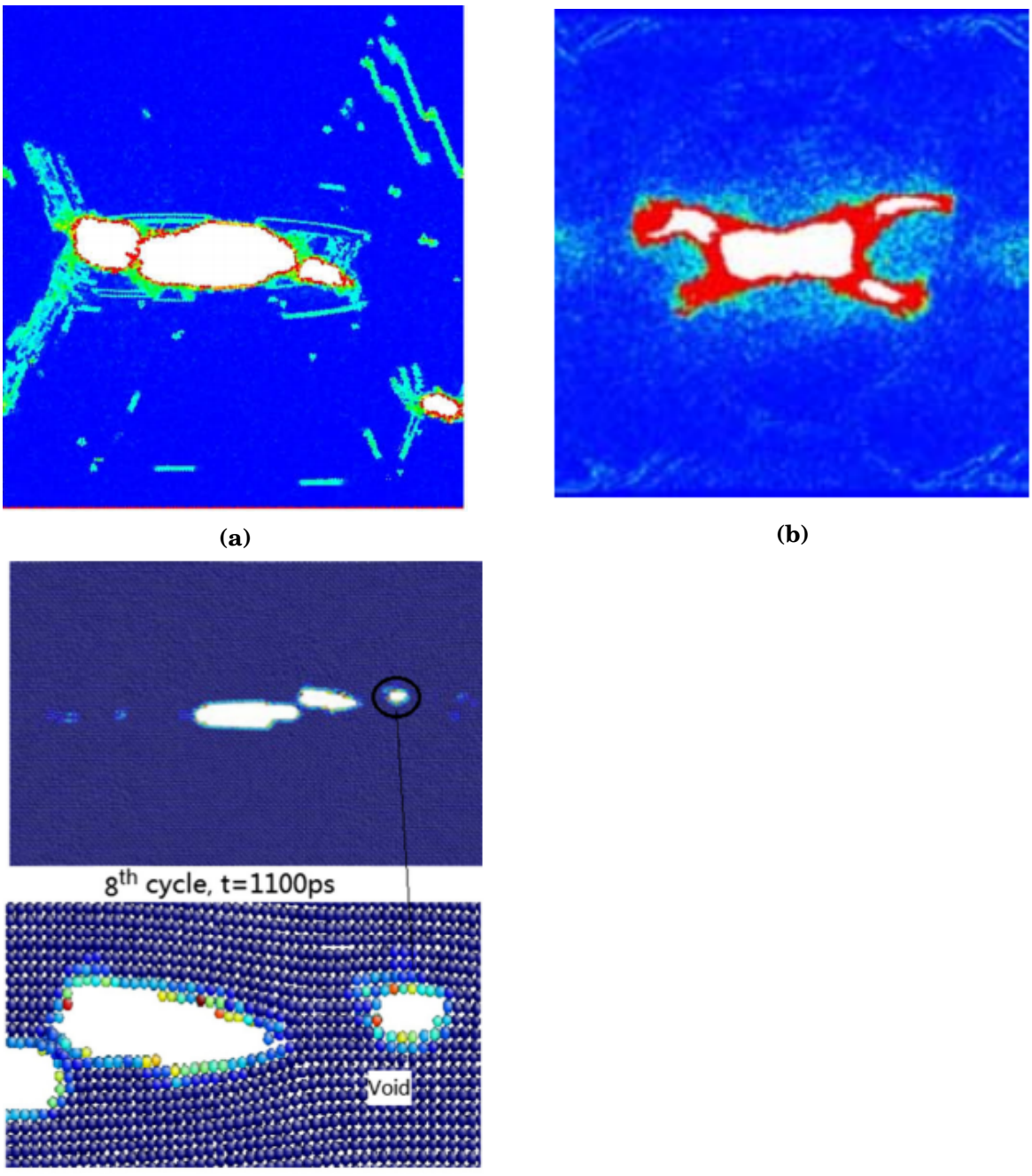

(a) **(b)** **(c)**

Figure 2-21: Fatigue crack propagation by cavities coalescence as reported by (a) Horstemeyer *et al.* [Horstemeyer et al., 2010] in copper single crystal (b) Potirniche *et al.* [Potirniche et al., 2005] in nickel single crystal and (c) Wu *et al.* [Wu et al., 2015] in nickel single crystal.

in particular the various crack propagation mechanisms reported in literature as well as the effect of the environment.

As previously stated, before addressing the propagation of fatigue cracks at the nanoscale, we will first study the events preceding the fatigue crack initiation and propagation, in particular the extrusions growth.

In the following chapter, we investigate by the means of crystal plasticity finite element method (CPFEM) the extrusion growth in fatigued crystalline materials on the basis of the experimental observations which have been updated in the present state of the art.

Chapter 3

Growth of extrusions in cyclically deformed f.c.c. metals and alloys

No generalization is wholly true - not even this one.

Oliver Wendell Holmes Jr.

Abstract

In this chapter, the extrusion growth in metals and alloys subjected to cyclic loading is studied. In accordance with the experimental observations and through crystal plasticity finite element computations, we simulate the extrusion of both type A and type B persistent slip bands (PSBs). The extrusion growth is found to be linear with the number of cycle and the extrusion height for type B PSBs is higher than that for type A PSBs, in agreement with experimental observations. The influence of the different parameters (PSBs length and thickness , PSB inclination angle) is evaluated and close-form expression are proposed the describe the extrusion height. In general, the results are found to be in agreement with the experimental observations and measurements. In the last part, the induced stress fields are analyzed and fatigue cracks initiation is discussed in relation with the assessed stress fields.

Contents

3.1 Introduction

The formation of persistent slip bands (PSBs) in face-centered cubic (FCC) ductile metals and alloys under cyclic loading generally precedes fatigue crack nucleation. During cyclic loading, under the effect of a certain number of mechanisms (production and diffusion of vacancies, plastic slip and dislocation irreversibility), extrusions of these PSBs through the free surface of single and poly crystals (surface grains) occurs. Since the first evidence of slip localization by Ewing and Humfrey [Ewing and Humfrey, 1903], who showed the existence of a surface reliefs on a polycristalline Swedish iron cyclically deformed, important development have been carried out and shed light on the mechanisms of these surface relief formation, shape and growth. Numerous studies (see for example [Man et al., 2002, Man et al., 2003, Forsyth, 1953, Polák et al., 2003, Weidner et al., 2008a] highlighted the formation and growth of extrusion (and intrusions sometimes) in single and polycrystalline materials under cyclic loading.

A few well-established models in the literature attempt to explain the mechanisms of extrusion formation and growth. Among these models, one can cite the well-known EGM I model by Essman *et al.* [Essmann et al., 1981] and EGM II model by Differt *et al.* [Differt et al., 1986], Polàk [Polák, 1987] which leads to improvements [Polák and Sauzay, 2009, Polák et al., 2017, Polák and Man, 2014b, Polák et al., 2013, Polák et al., 2009, Polák and Man, 2014a, Polák, 2020, Polák et al., 2017]. The EGM I model explains the PSB extrusion by vacancies production, due to the interactions between dislocations. Such vacancy production leads to the formation of a rapid static extrusion while the EGM II model tries to explain some observed surface reliefs, by the irreversibility of dislocations glide crossing the free surface. Fatigue crack initiation in this model is assumed to occur due to stress concentration induced by stress raisers. The EGM model considers two types of stress raisers: the slip offsets at the PSB/matrix interface (type I stress raiser) and the roughness of the surface of the cyclically deformed specimen which is made of notches valley (type II stress raiser) from which crack can initiate (Fig. 3-1).

Polàk model assumes a steady vacancies production in PSBs as well as their annihilation and diffusion. This results in an extrusion, not only static but also dynamic, and the formation of intrusions at the interfaces between the PSB and the remaining material, due to vacancy diffusion. In this model, these intrusions constitute the origin of fatigue crack nucleation which occurs along individual PSBs in single crystals and polycrystals and along macro-PSBs in single crystals. Polàk considers that fatigue cracks initiate in the continuity of intrusions (unlike the EGM I and EGM II models which does not consider the formation of intrusions). And cracks can be considered as initiated when the rate of new surface formation due to stress concentration at intrusion tips or due to slipping-unslipping, is higher than the intrusion growth rate (change of mechanism).

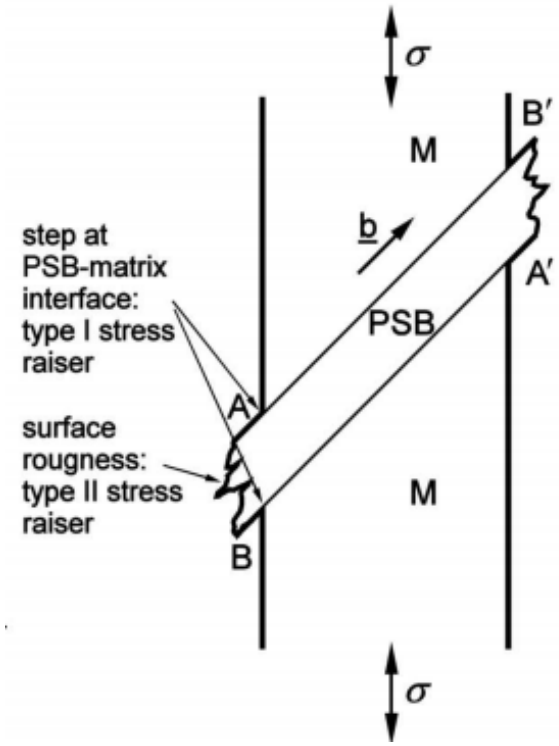

Figure 3-1: Different types of stress raisers according to EGM models. Quoted from [Man et al., 2009b]

Through the development of experimental techniques, the study of extrusion has progressed rapidly throughout history. From the first observations of Ewing and Humphrey [Ewing and Humfrey, 1903] using optical microscopy to the most modern techniques such as TEM, FEG-SEM, AFM, FIB (allowing to reach high resolutions and thus to catch details at the nanometer scale concerning the morphology of surface relief and the measurement of extrusion heights and intrusion depths), the advances in the study of PSBs have been considerable. For example, the work of Man *et al.* [Man et al., 2002] on 316L steel polycrystals highlighted the dependence of the extrusion height with respect to its thickness, to the grain size (or PSB length) and to the PSB inclination with respect to the tension-compression axis. The authors also showed that the extrusion height increases linearly with respect to the number of cycles.

On the modelling point of view, Repetto and Ortiz [Repetto and Ortiz, 1997] performed 2D finite element (FE) simulation of extrusion growth in a fcc single crystal. They consider dislocation annihilation and point defect production and their migration towards free surface. But the extrusion growth kinetics was found to be unrealistic considering experimental results.

Considering the internal structure of a PSB, Brown and co-workers ([Brown, 1977, Brown, 1981, Brown, 1990, Brown and Nabarro, 2004, Brown and Ogin, 1985]) concluded that the whole PSBs is subjected to tensile

strain in the direction of the Burgers vector. The authors indeed showed that whatever the strain level, the stress fields along the interfaces between the matrix and the PSB displays a logarithmic singularity. Theses high stresses near free surface should be according to the authors, responsible for decohesion of the PSB from matrix and fatigue crack initiation.

Using Discrete Dislocation Dynamics simulations, Déprés *et al.* [Déprés et al., 2006] simulated surface relief formation in early fatigue damage in surface grains of 316L steel. Only dislocation slip was accounted for point defect production was not taken into account. PSBs thicknesses of approximately 200-500nm was obtained from their computations Based on their investigation using discrete dislocation dynamics, Déprés et al. [Déprés et al., 2004, Déprés et al., 2006] predicted fatigue crack initiation along individual PSBs both in single crystals and polycrystals. Intrusions accompanying extrusions were found to be the fatigue crack initiation site and according to the authors, fatigue crack initiation occurs when a critical value of local dislocation distortion energy within PSBs channels is reached due to stress triaxiality. By the means of dislocation dynamics, Brinckmann and Van der Giessen [Brinckmann and Van der Giessen, 2003, Brinckmann and Van der Giessen, 2004] studied stress profiles near the surface but their computation did not reveal the logarithmic singularities predicted by Brown and co-workers investigations based on purley thermoelastic computations.

Previous studies allowed important progress in our understanding of the fatigue crack initiation mechanisms. However, from a modeling point of view, significant progress remains to be made in order to predict the initiation of fatigue cracks, in particular by taking into account in the modelling, the experimental observations.

In the present study, based on previous experimental observations, we carry out extensive simulations of extrusion growth in FCC metals and alloys, via crystal plasticity finite element computations. The effect of the PSB thickness and length is studied as well as the PSBs inclination with respect to the tension-compression axis. The results are compared with experimental observations and measurements. Finally, an analysis of surface stresses and normal stress fields along persistent slip bands is detailed as well as a discussion on fatigue crack initiation in the light of the stress fields computed.

3.2 Constitutive equations

3.2.1 Elasticity

In this study, single crystals of metals and alloys with face-centered cubic structure (FCC) are considered. These single crystals generally obey cubic elasticity, which is fully characterized by three parameters (the elasticity constants C_{11},

C_{12} and C_{44}). Anisotropy in cubic elasticity can be evaluated with the anisotropy coefficient, a, defined by:

$$a = \frac{2C_{44}}{(C_{11} - C_{12})} \tag{3.1}$$

The elasticity constants of the materials under study and their relative anisotropy coefficients are provided in table 3.1.

Table 3.1: Cubic and isotropic elasticity parameters for copper, nickel and 316L [Huntington, 1958, McClintock and Argon, 1966]

Material	**Cubic elasticity**				**Isotropic elasticity**	
	C_{11} (GPa)	C_{12} (GPa)	C_{44} (GPa)	a	E (GPa)	ν
Cu	168.4	121.4	75.4	3.2	130	0.35
Ni	246.5	147.3	124.7	2.5	230	0.3
316L(Feγ)	197.5	125	122	3.4	200	0.33

In order to evaluate the effect of using isotropic elasticity instead of anisotropic cubic elasticity, some calculations are carried out by considering isotropic elasticity defined by only two parameters: the Young's modulus, E, and the Poisson's ratio, ν. The isotropic elasticity parameters used herein are also provided in table 3.1 for the different materials studied, considering polycrystals with no texture.

3.2.2 Crystal plasticity

3.2.2.1 (Visco)plastic flow rule and isotropic hardening law

The plastic flow rule governing the evolution of viscoplastic slip rate on each slip system, s, is given by:

$$\dot{\gamma_s}^p = A_p \left[\sinh\left(\frac{\tau_s}{\tau_s^c}\right)\right]^{\frac{1}{m}} \operatorname{sgn}(\tau_s) \tag{3.2}$$

with A_p and m parameters (shown in table 3.2) chosen to avoid the viscosity effect. In metals and alloys with a face-centered cubic structure, there are 12 slip systems ($\mathbf{n_s}$, $\mathbf{m_s}$) where $\mathbf{n_s}$ is the normal to the slip plane ($\mathbf{n_s} = 1/\sqrt{3}\{1\,1\,1\}$) and $\mathbf{m_s}$ is the slip vector ($\mathbf{m_s} = 1/\sqrt{2}\langle 1\,1\,0\rangle$).

The shear stress on each slip system is computed by:

$$\tau_s = \mathbf{m_s}^T \sigma \mathbf{n_s} \tag{3.3}$$

with σ, the local stress tensor and s ranging from 1 to 12. The Schmid law is used as criterion for the activation of plastic slip on slip systems when the shear stress $|\tau_s|$ reaches the critical value $\tau_{c,s}$ and the plastic activity of each slip system

is described by the linear hardening law defined by:

$$\begin{aligned} |\tau_s| &= \tau_{c,s} \\ \dot{\tau}_{c,s} &= H_0 \sum_{j=1}^{12} d_{ij} \left|\dot{\gamma}_j^p\right| \\ d_{ij} &= 1 \text{ for } i = j \end{aligned} \tag{3.4}$$

where H_0 is the linear hardening slope, d_{ij} the components of the interaction matrix between the twelve slip systems and q the latent hardening coefficient.

Table 3.2: Plastic flow rule and isotropic hardening law parameters

A_p (s^{-1})	$\frac{1}{m}$	q	H_0 (MPa)
2×10^{11}	47.6	10^8	1

3.2.2.2 Kinematic hardening law

The Amstrong-Frederick kinematic hardening law defined in equation 3.5 is used because it allows a fair reproduction of the experimental hysteresis loops of various single crystals. This law, which only takes into account the recent history of the material, describes fairly the saturated state of a single crystals.

$$\delta x_s = C \left(\frac{2}{3} A \delta \gamma_s^p - x_s \delta \gamma_{cum,s}^p \right) \tag{3.5}$$

with s ranging from 1 to 12. The s^{th} kinematic hardening stress is denoted x_s whereas δx_s is the s^{th} increment of kinematic hardening stress, $\delta \gamma_s^p$, the s^{th} increment of plastic slip and $\delta \gamma_{cum,s}^p$ the s^{th} cumulative plastic slip. The C and A are parameters adjusted.

These different laws were implemented in a UMAT procedure, which has been used and validated through different studies [Sauzay, 2007, Sauzay and Liu, 2014, Hazan, 2019]. The adjusted parameters are taken from [Hazan, 2019] (Fig. 3-2) and reported in the table 3.3.

Table 3.3: Kinematic hardening law fitting parameters

Material	τ_0(MPa)	A (MPa)	C	τ_{PSB}(MPa)	γ_{PSB}^p
Cu	16	17.8	450	28	0.0075
Ni	32	25	600	48	0.01
316L	50	12.5	3500	57	0.01

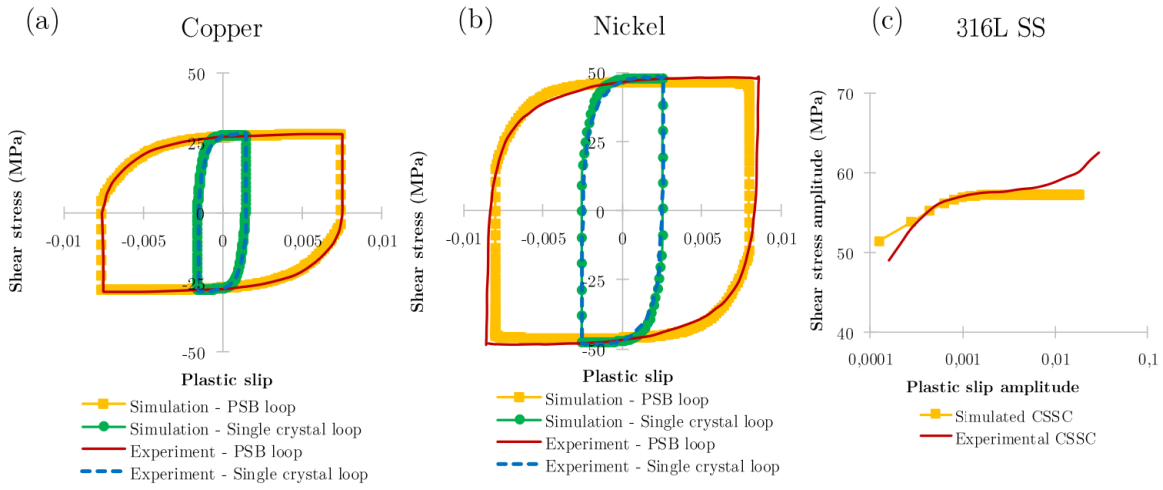

Figure 3-2: Adjustement of kinematic hardening law parameters. Quoted from [Hazan, 2019]

3.3 Modelling hypotheses

3.3.1 Modeled microstructures

We intend to investigate the influence of PSB thickness and length on both type A and type B PSB extrusions (Fig. 2-10). For this purpose, different microstructures are generated using Cast3M finite element computation software [CEA, 2000]. The computations are carried out under the assumptions of plane strain conditions and finite strain framework. The Cauchy stress tensor and Green-Lagrange strain tensor definition were used. The effect of the finite element (FE) size has been checked. The FE size is small enough to have reach numerical convergence with respect to it. The Following the investigations of Hunsche and Neumann [Hunsche and Neumann, 1986] on FCC single crystals and Man *et al.* [Man et al., 2002] on FCC polycrystals different PSBs thicknesses ($0.2\ \mu\text{m}$ - $10\ \mu\text{m}$) and different PSBs lengths are considered. The PSBs are inclined by an angle α_{SB} (Fig. 3-4) with respect to the loading axis and is embedded in a homogeneous purely elastic matrix. This allows us to simulate the almost elastic vein matrix of single crystals and less rigorously the behaviour of the other grains of the polycrystal. Numerous studies in the literature, notably those of Mughrabi [Mughrabi, 1988] and Man *et al.* [Man et al., 2002] reported that the PSBs are observed for the most part in grains oriented for single slip (maximum Schmid factor, $f = 0.5$). In this investigation, orientations corresponding to single slip are under focus. This is why in this study, considering $\mathbf{n}$ as the unit vector normal to the slip system and the $\mathbf{m}$ as the slip vector, these vectors are oriented at $45°$ with respect to the stress axis in order to maximize the Schmid factor since the latter is given by:

$$f = \cos(\alpha_{SB}) \sin(\alpha_{SB}) \tag{3.6}$$

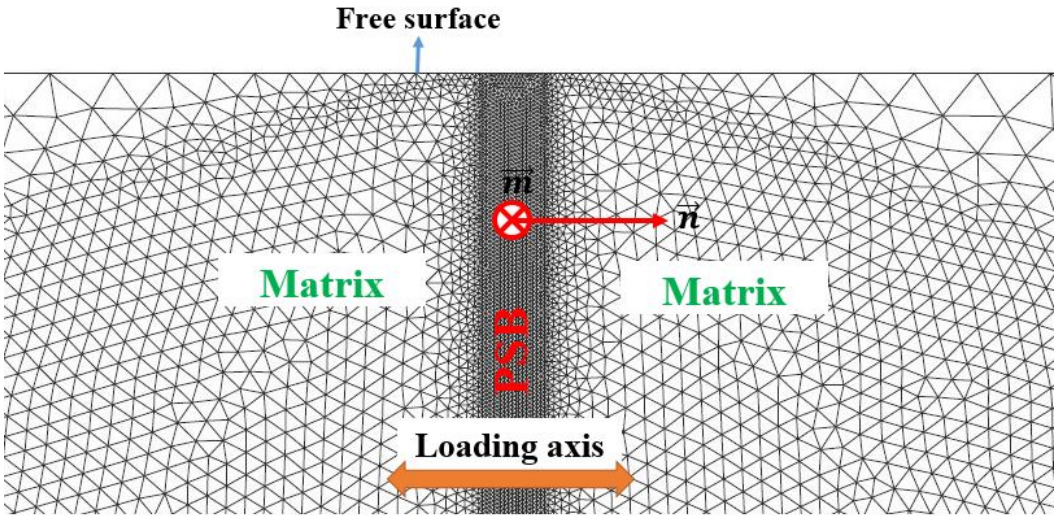

Figure 3-3: Mesh used for computations for type A PSBs.

However, in polycrystals, some surface grains of various crystal orientation with lower Schmid factors may contain slip bands [Sauzay and Jourdan, 2006, Sauzay and Moussa, 2013]. To take this fact into account, and assess the influence on PSBs extrusions, we consider different PSBs orientations i.e. α_{SB} (between $30°$-$60°$ (corresponding to Schmid factor ranging between 0.43 and 0.5) in order to keep only one slip system active).

3.3.2 Loading conditions

The loading applied in this study is an imposed displacement. However, this imposed displacement is called upon to reproduce a certain number of phenomena observed experimentally. Indeed, according to the experimental results of Mugrabi [Mughrabi, 1978, Mughrabi, 1979], Essmann *et al.* [Essmann et al., 1981], during the cyclic loading, the PSBs occupy the entire volume of the sample when the plastic slip reaches $\gamma^p_{PSB} = 7.5 \times 10^{-3}$ for copper, or even 10^{-2} in the case of nickel or 316L SS [Hazan, 2019]. By considering that all the plastic strain is localized in the PSB, and by using the mixture law of Winter *et al.* [Winter et al., 1981], (Equation 2.12), an appropriate displacement is imposed to reproduce the appropriate plastic slip in the PSB, knowing that the one of the matrix is considered to be zero. The PSB extrusion induced by the production and annihilation of vacancies is simulated by imposing an equivalent free thermal expansion. Indeed, Polak and Sauzay [Polák and Sauzay, 2009] estimated the vacancy production rate per cycle to be approximately $P_{PSB} = 3.1 \times 10^{-7}\text{cycle}^{-1}$ in copper single crystal. The effect of this production of vacancies in PSBs is simulated by imposing thermal strain ϵ_{th} given by:

$$\epsilon_{th} = P_{PSB} \times N \tag{3.7}$$

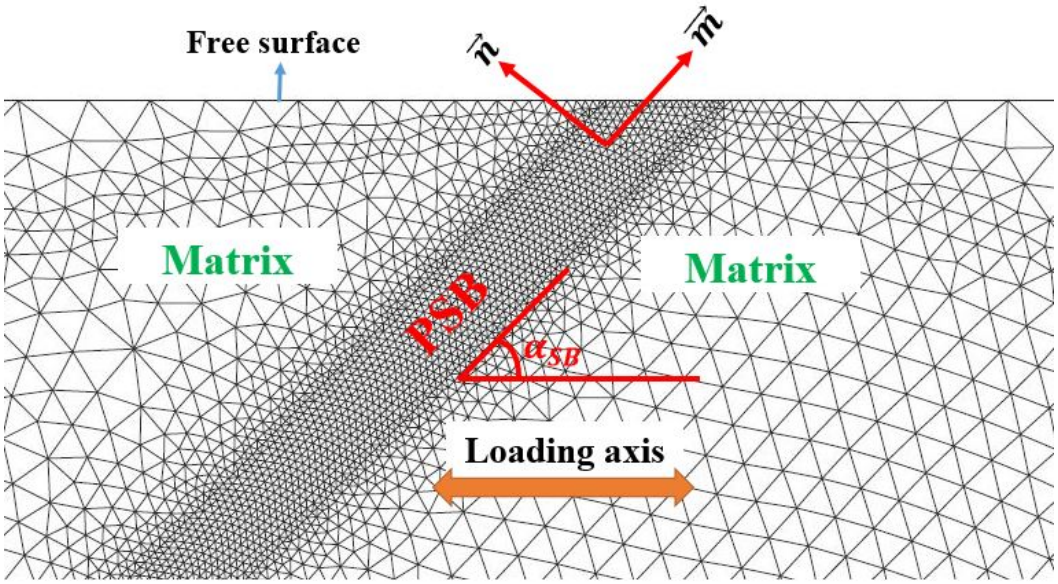

Figure 3-4: Mesh used for computations for type B PSBs.

with N, the number of cycles. Due to the fairly large number of cycles necessary to produce a visible effect of thermal expansion, and taking into account the large computation times that it should require, the number of cycles applied has been reassessed in terms of blocks. This involves applying N_v blocks of N_b cycles, that can reproduce the effect of certain number of real cycles, N. The blocks of cycles are defined as follows:

$$N_v = \frac{N}{N_b} \tag{3.8}$$

with N_b representing the number of real cycles contained in one virtual cycle N_v. The vacancy production term depends on the real number of cycles applied:

$$\epsilon_{th} = P_{PSB} \times N = \alpha_{th} \times N_v \times \Delta T \tag{3.9}$$

with ΔT the temperature increment applied during each virtual cycle N_v and α_{th} the thermal expansion coefficient. This reassessment of the number of cycles to be imposed has no effect on the mechanical behavior since the constitutive equations are adjusted to reproduce the stabilized mechanical behavior in particular (i) the saturated isotropic hardening (friction stress) (ii) the non-linear kinematic hardening (backstress) (CSSC plateau). In the following, blocks containing 250 real cycles are used. It has been shown in [Liu, 2013] that with $N_b = 250$, the same results are obtained as considering $N_b = 1$. The computations are carried out under the assumptions of plane strain conditions within finite strain framework and Cauchy stress definition.

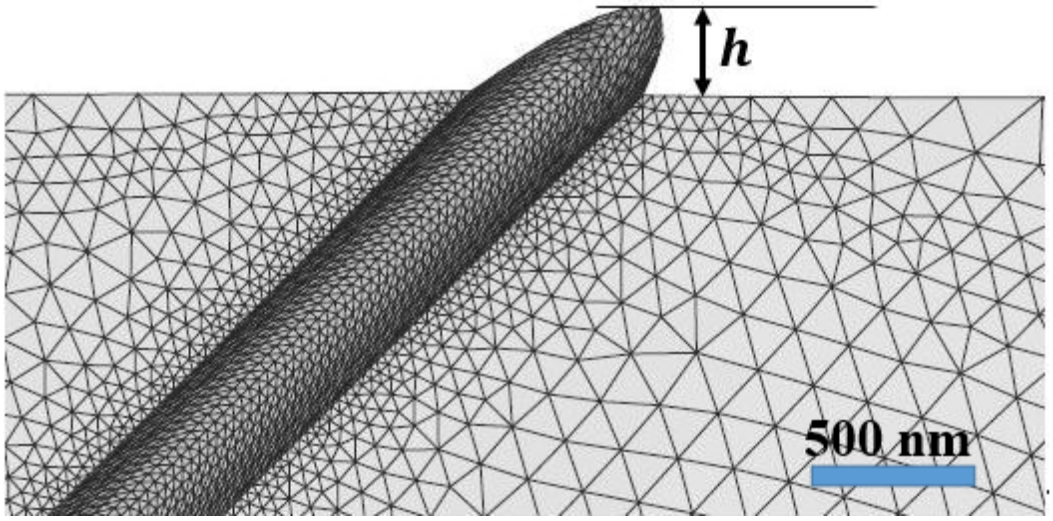

Figure 3-5: Extrusion shape of copper cyclically deformed at RT, $N = 10000$ cycles, $t = 0.424$ μm, $L = 17$ μm. Displacements amplified by a factor of 10.

3.4 Prediction of extrusion growth

The extrusion heights are predicted for both type A and type B PSBs. Based on the simplified 2D meshes displayed in Fig. 3-3 and 3-4, the PSB extrusion height have been computed. Fig. 3-5 shows an example of extrusion shape obtained and Fig. 3-6 shows the extrusion heights measured for type A and B PSBs.

Two observations emerge through these results: the linearity of the extrusion height with the number of cycles regardless of the type the PSB and the fact that the extrusion height of a type B PSB is higher than that of a type A PSB.

On the one hand, the linearity of the extrusion height observed in this study, resulting from the thermal strain applied, agrees with the experimental results of Man *et al.* [Man et al., 2003], which showed thanks to tests carried out on a 316L SS polycrystal that the extrusion height increases linearly with respect to the number of cycles. (Fig. 3-7). On the other hand, this linearity of the extrusion height contradicts the theories EGM models in the sense that if the extrusion mechanism was that proposed by the EGM models (EGM I+II), after the static extrusion, the dependence of the extrusion height, with respect to the number of cycles, should be a square root type (Equation 2.13). The linearity of the extrusion height with the number of cycles indicates not only the appropriateness of the vacancy production model but it also indicates that the production, annihilation and diffusion of vacancies is more efficient than plastic irreversibility in the extrusion formation and growth.

It can also be noticed in Fig. 3-6 that the extrusion height of the type B PSB is much higher than the type A PSB one. While the type B PSB extrusion grows at a rate of about 0.0027 nm/cycle for a PSB thickness of $t = 0.424$ μm and a PSB length of about $L = 17$ μm in copper, the type A PSB extrusion grows at a rate

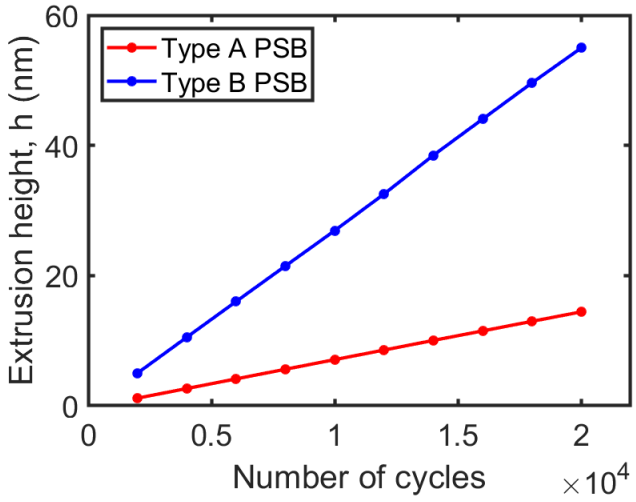

Figure 3-6: Extrusion heights as function of number of cycles for type A and type B PSBs in copper cyclically deformed at RT. $t = 0.424\ \mu m,\ L = 17\ \mu m$

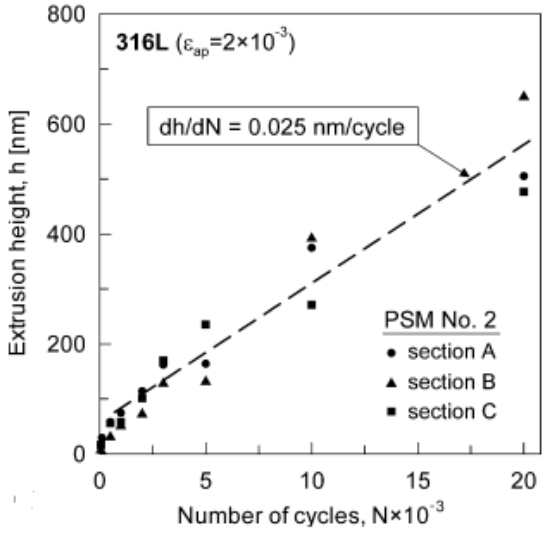

Figure 3-7: Extrusion height vs. the number of cycles N in 316L SS. Mean grain size : $120\ \mu m,\ t = 0.5\ \mu m$,. Quoted from Man *et al.* [Man et al., 2003]

of about 0.0007 nm/cycle. This is 4 times lower than the type B PSB extrusion growth rate. This fact can be explained by an easier plastic relaxation in the direction of Burgers vector in the case of type B PSB than in the case of type A PSB. Indeed, as a reminder, type A PSBs correspond to slip taking place in the free surface of the crystal i.e. parallel to the free surface. This means that the vectors **n** (normal to the slip plane) and **m** (slip direction) are coplanar with the free surface. In the case of type B PSBs, slip takes place across the free surface and the vectors **n** and **m** are inclined at $45°$ with respect to the vector normal to the free surface. The Burgers vector is oriented towards the free surface and according to the work of Sauzay and Gilormini [Sauzay and Gilormini, 2002], the plastic slip of type B slip bands is higher than that of type A slip bands. Slip is therefore found to be easier in the case of type B band than in the case of type A band. This numerical result is also in agreement with the experimental observations of Holste and Schwab [Holste and Schwab, 2006] and Obrtlik *et al.* [Obrtlík et al., 1997]. Indeed, Hoslte and Schwab [Holste and Schwab, 2006] found that the slip traces on the side face of Al-Ni alloy single crystal (corresponding to type A) are rather smooth, whereas on the top face (corresponding to type B) the authors observed high extrusions. Obrtlik *et al.* [Obrtlík et al., 1997] who worked on copper single crystals, plotted the extrusion heights as a function of the angle ϕ defined, as shown in the Fig. 3-8. The measurements show that the extrusions corresponding to type B PSBs ($\phi = 0°, 180°$) are higher than those corresponding to type A PSBs ($\phi = -90°, 90°$).

Whether the PSB is of type A or type B, its characteristic dimensions (thickness and length) affect the PSB extrusion height [Man et al., 2002, Hunsche and Neumann, 1986]. The following section is dedicated to the assessment of the influence of these characteristic dimensions.

3.4.1 Effect of PSB thickness and length

In order to evaluate the influences of the characteristic lengths (PSB thickness and length), we carry out a parametric study by varying the thickness of the slip band at a fixed PSB length and vice-versa. The PSB thicknesses considered are in agreement with the experimental observations. Indeed, the work of Man *et al.* [Man et al., 2002] showed that the thicknesses of the PSBs vary between 0.15 and 1.15 μm in 316L steel (Fig. 3-9). The investigations of Hunsche and Neumann [Hunsche and Neumann, 1986] on copper single crystals provided typical value of $0.5 - 2.5$ μm with additionally macro-bands which can reach 70 μm. In agreement with these experimental observations and taking into account the computational time, different thicknesses and lengths of PSBs are considered.

Fig. 3-10 shows the evolution of type A PSB extrusion height as a function of the PSB thickness (Fig. 3-10a) and as function of PSB length (Fig. 3-10b). In general, it can be observed that the extrusion height increases with PSB thickness and with PSB length. However, the dependence of the extrusion height on PSB thickness or on PSB length are not the same. Even though the two de-

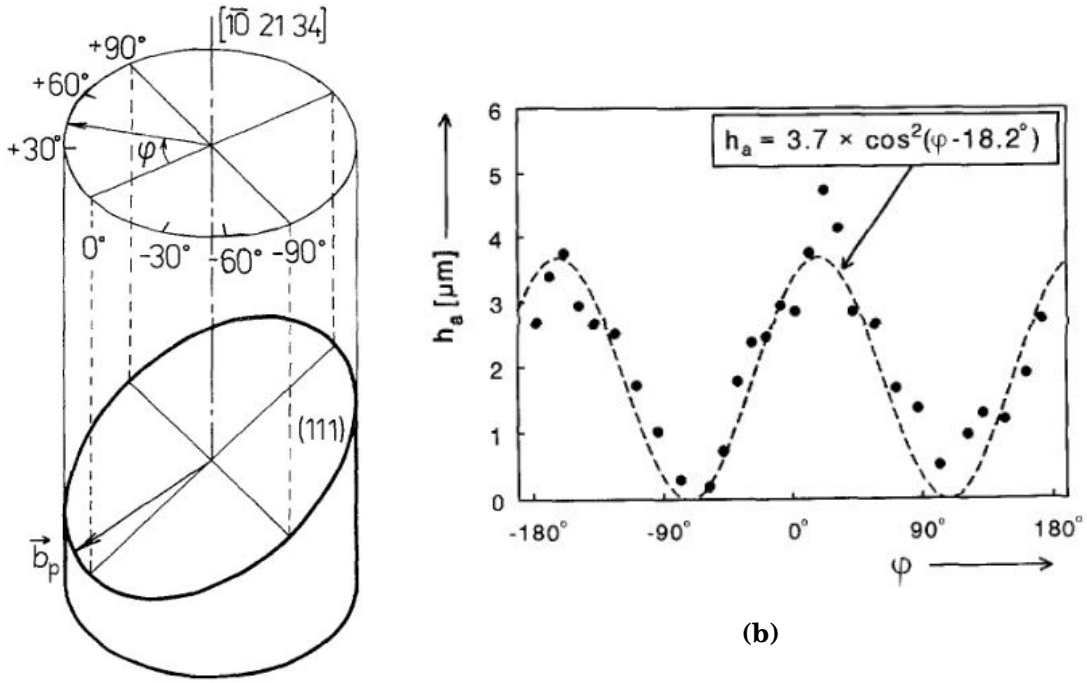

Figure 3-8: (a) Schematic picture of the single crystal geometry with the angle ϕ definition (b) Average extrusion height as function of the angle ϕ. Quoted from Obrtlik et al. [Obrtlík et al., 1997].

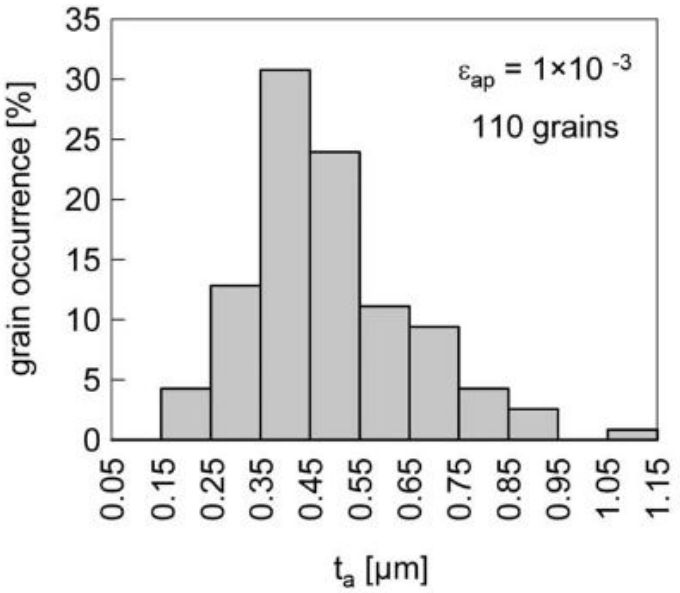

Figure 3-9: Occurrence of grains containing the PSB of the average thickness t_a for a set of 110 grains. Quoted from Man *et al.* [Man et al., 2002]

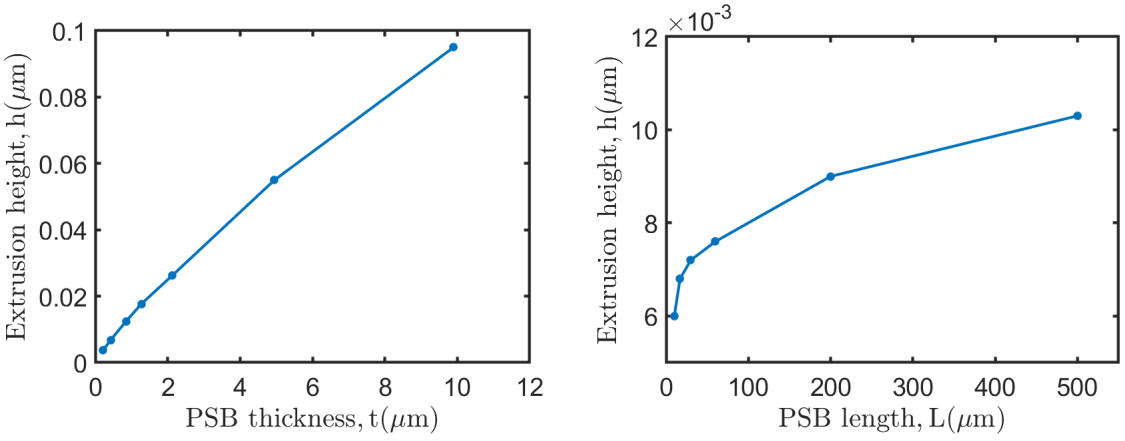

(a) **(b)**

Figure 3-10: Effect of PSB characteristic lengths on type A PSB extrusion in copper. (a) Effect of PSB thickness (N = 10000 cycles, L = 17 μm). (b) Effect of PSB length (N = 10000 cycles, t = 0.424 μm).

pendencies are of power law type, the dependence on PSB thickness is stronger than that on PSB length. Therefore, to describe the influence of PSB thickness and PSB length on the extrusion height, an analytic expression is proposed in Equation 3.10:

$$h = A \times N \times p \times t^{\alpha} \times L^{(1-\alpha)} \tag{3.10}$$

This law is obviously a function of the characteristic dimensions of the PSB (thickness t and length L), of the number of cycles N and of the vacancy production rate, p. The remaining dimensionless prefactor A and the exponent α are material-dependent and are adjusted on the FE computations as shown in Fig. 3-11a and Fig. 3-11b and the values are summarized in table 3.4.

Table 3.4: Adjusted parameters of Equation 3.10 for type A PSBs in copper.

Parameters	A	α
Value	2.91	0.85

Fig. 3-12 shows the evolution of type B PSB extrusion height as a function of the PSB thickness (Fig. 3-12a) and PSB length (Fig. 3-12b) in copper single crystal. As noticed previously, for type A PSB extrusions, the general trend for type B PSBs suggest also that the extrusion height increases with the PSB thickness. These results show two domains in the dependence of the extrusion height as a function of the PSB thickness. The first domain extends from t = 0.2 μm to around t = 2 μm and the second domain extends from t = 2 μm up to the maximum thickness tested (i.e.10 μm). Even if each of these domains exhibit different behavior, they can be described analytically by a combination of a power and an

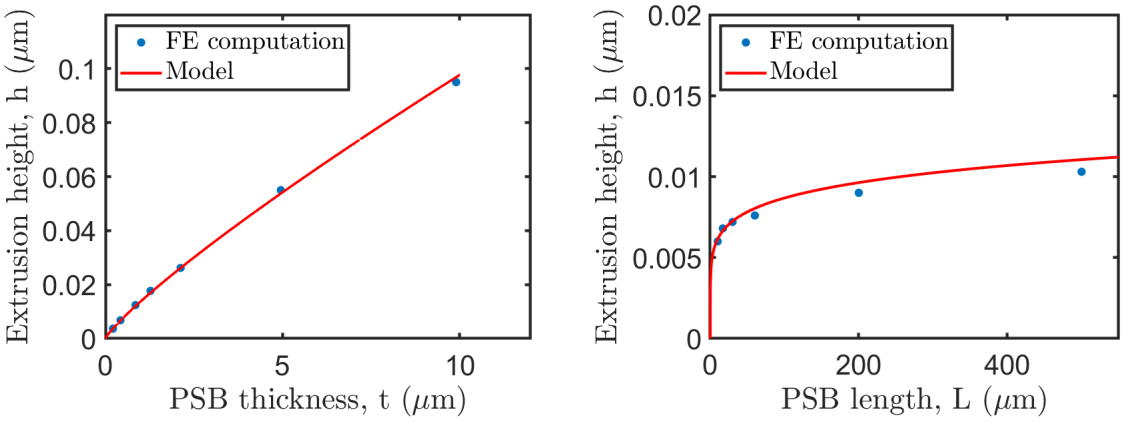

Figure 3-11: Adjustment of the parameters of the proposed model on type A PSB extrusion heights computed via FE in Copper. (a) Effect of PSB thickness (N = 10000 cycles, L $= 17\mu$m). (b) Effect of PSB length (N = 10000 cycles, $t = 0.424\ \mu m$).

exponential law. As for the evolution of the PSB extrusion with respect to its thickness, we notice also two domains in the extrusion height evolution with respect to PSB length. It can be observed in Fig. 3-12b that, the PSB extrusion height increases with the PSB length between L $= 10\ \mu$m and L $= 100\ \mu$m up to a saturation value. Beyond L $= 100\ \mu$m, the extrusion height does not vary. The dependence of the PSB extrusion with respect to its length can be also described by an combination of a power and an exponential law. Finally, a model describing the effect of the PSB characteristic lengths on the extrusion height for type B PSBs is also proposed in Equation 3.11:

$$h = N \times p \times t^{\alpha} \times L^{1-\alpha} \times \left(A_1 \times e^{B_1(t/L)} + A_2 \times e^{B_2(t/L)}\right)\left(1 - e^{-B_3(L/t)}\right) \tag{3.11}$$

with $A_1,\ A_2,\ B_1,\ B_2,\ B_3,\ \alpha$ adjusted and dimensionless parameters. As previously, N and p denotes respectively the number of cycles and the vacancy production rate. Fig. 3-13 shows the adjustment of the previous parameters in copper (Table 3.5) using FE computations.

Table 3.5: Adjusted parameters of Equation 3.11 for copper

A_1	A_2	B_1	B_2	B_3	α
211.4	-188.7	1.01	1.00	0.025	0.92

3.4.2 Effect of material

The computations carried out previously for copper are also carried out in nickel and 316L steel. To the author's knowledge, no measurement of the vacancy pro-

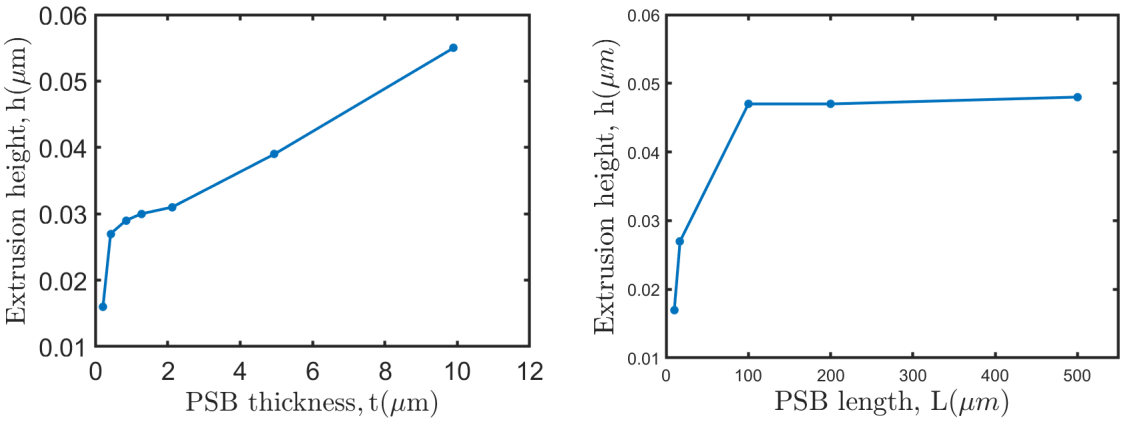

(a) **(b)**

Figure 3-12: Effect of PSB characteristic dimensions on type B PSB extrusion in copper. (a) Effect of PSB thickness. (b) Effect of PSB length

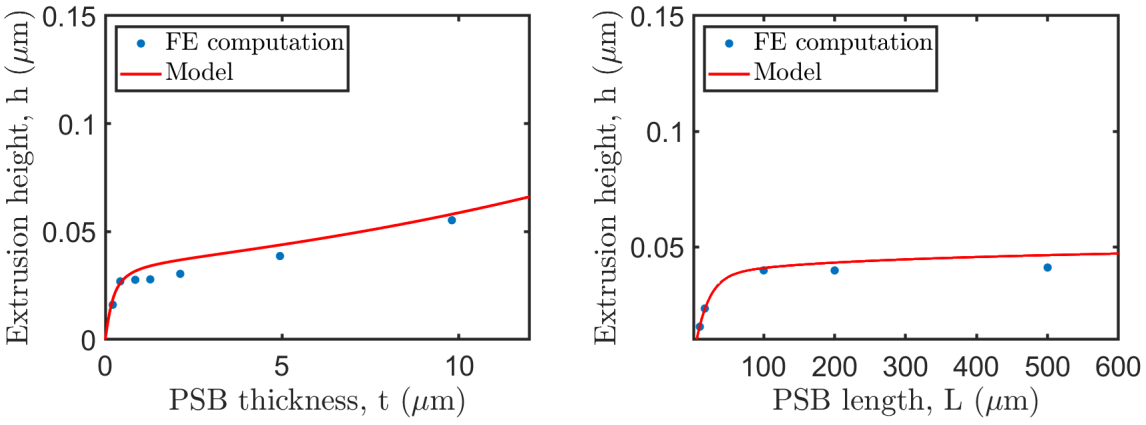

(a) **(b)**

Figure 3-13: Adjustment of the parameters of the proposed model on type B PSB extrusion heights computed via FE in copper. (a) Effect of PSB thickness (N = 10000 cycles, $\mathrm{L} = 17\ \mu\mathrm{m}$). (b) Effect of PSB length (N = 10000 cycles, $t = 0.424\ \mu m$).

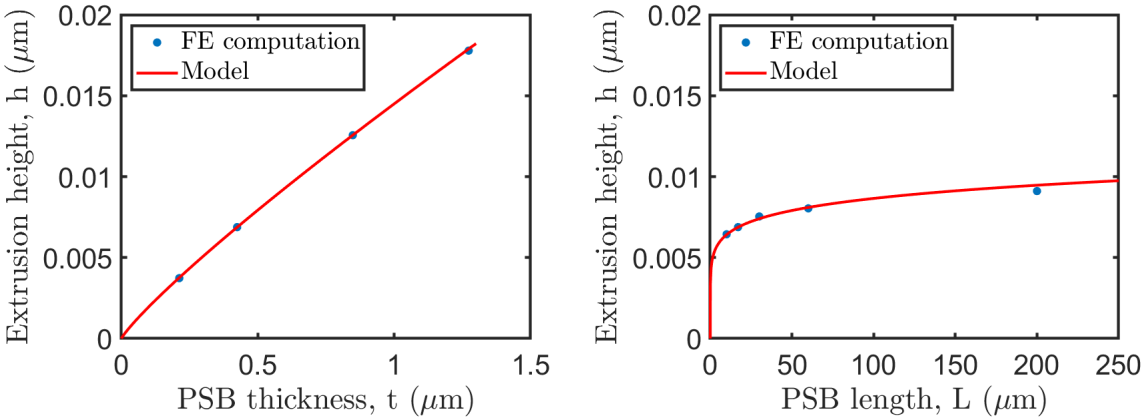

Figure 3-14: Adjustment of the parameters of the proposed model for type A PSB extrusion computed via FE computations in Nickel. (a) Effect of PSB thickness (N = 10000 cycles, L = 17 μm). (b) Effect of PSB length (N = 10000 cycles, $t = 0.424\ \mu m$).

duction rate in PSB for nickel or 316L has been published yet. By using as first approximation the vacancy production rate measured in copper by Polak and Sauzay [Polák and Sauzay, 2009], and taking into account the elastic-plastic parameters of each of these materials, an investigation similar to that carried out in copper is carried out in nickel and 316L steel as well. In general, as in the previous case of copper, we observe that the extrusion height increases with the PSB thickness and length in the same manner. Fig. 3-14 shows the evolution of the extrusion height as a function of the thickness (Fig. 3-14a) and the the PSB length (Fig. 3-14b) in nickel for type A PSBs. The simulations results are used to adjust the proposed extrusion height model (Equation 3.10). The adjusted parameters are provided in table 3.6. Still concerning the type A PSBs, the simulation results in 316L steel (Fig. 3-15) are also used to adjust the Equation 3.10 parameters, which can be found in the table 3.6.

Table 3.6: Adjusted parameters of Equation 3.10 for nickel and 316L.

	A	α
Nickel	3.23	0.87
316L	2.92	0.88

Fig. 3-16 and Fig. 3-17 show the simulation results for type B PSBs for respectively nickel and 316L steel. The evolution is similar to that observed in the case of type B PSB in copper for both materials. Therefore, the six parameters of the extrusion height model proposed in Equation 3.11 for type B PSBs, is adjusted for nickel and 316L steel. All these adjusted parameters can be found in table 3.7.

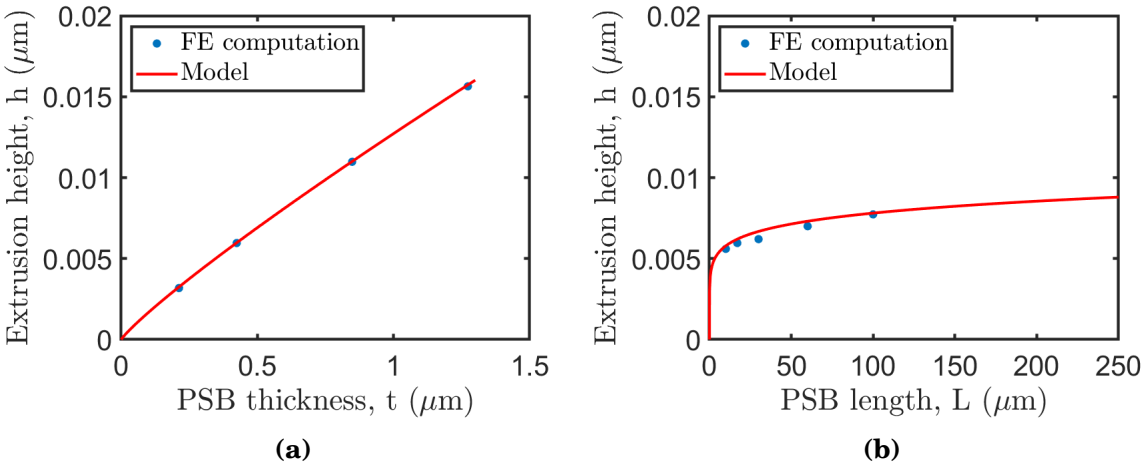

Figure 3-15: Adjustment of the parameters of the proposed model on type A PSB extrusion computed via FE in 316L. (a) Effect of PSB thickness (N = 10000 cycles, L $= 17$ μm). (b) Effect of PSB length (N = 10000 cycles, $t = 0.424$ μm).

Table 3.7: Adjusted parameters of Equation 3.11 for nickel and 316L.

	A_1	A_2	B_1	B_2	B_3	α
Nickel	354.1	−324.2	1.22	1.20	0.021	0.88
316L	208.1	−188.1	1.01	1.00	0.025	0.92

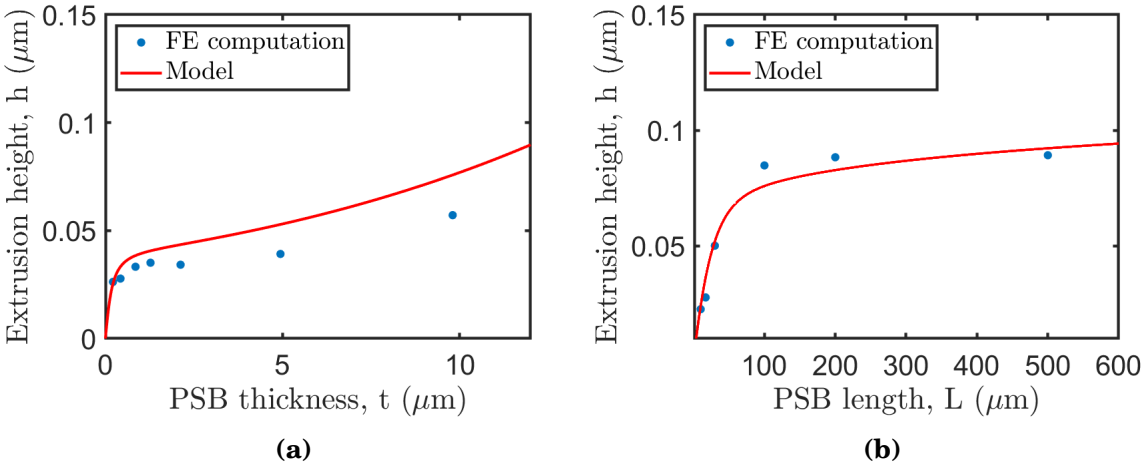

Figure 3-16: Adjustment of the parameters of the proposed model on type B PSB extrusion computed via FE in nickel. (a) Effect of PSB thickness (N = 10000 cycles, $\mathrm{L} = 17\ \mu\mathrm{m}$). (b) Effect of PSB length (N = 10000 cycles, $t = 0.424\ \mu m$).

It emerges from these simulations that the PSBs extrusion height in copper and in 316L steel are similar both qualitatively (dependence on the characteristic lengths) and quantitatively (close values of extrusion height) while the extrusion height in nickel seems to be a little higher than in the other two materials.

3.4.3 Effect of PSB inclination

The experimental investigations of Man *et al.* [Man et al., 2002] have shown that the inclination of the PSB affects the extrusion height. To check that point, we have assessed the influence of the inclination by choosing 5 inclination angles of the PSB (α_{SB}) with respect to the loading axis ($30°, 37.5°, 45°, 52.5°, 60°$). The simulations are carried out on type B PSB, during 10000 cycles in copper with a PSB thickness of $0.424\ \mu\mathrm{m}$. The simulation results in terms of $\mathrm{h/L}$ are presented in Fig. 3-18. We can indeed observe that the normalized height $\mathrm{h/L}$ increases linearly with the sine of the PSB inclination angle. This result is in agreement with the experimental observations of Man *et al.* [Man et al., 2002] (Fig. 3-19), who showed that on a polycrystal of 316L steel cyclically deformed, the normalized extrusion height h/L increases linearly with the sine of the angle of inclination of the PSB with respect to the loading axis. One can deduce from the work of Man *et al.* [Man et al., 2002] a slope of about 0.0024 (Fig. 3-19). In this study, the slope obtained is approximately 0.0022 which is therefore in agreement with the experimental measurements [Man et al., 2002].

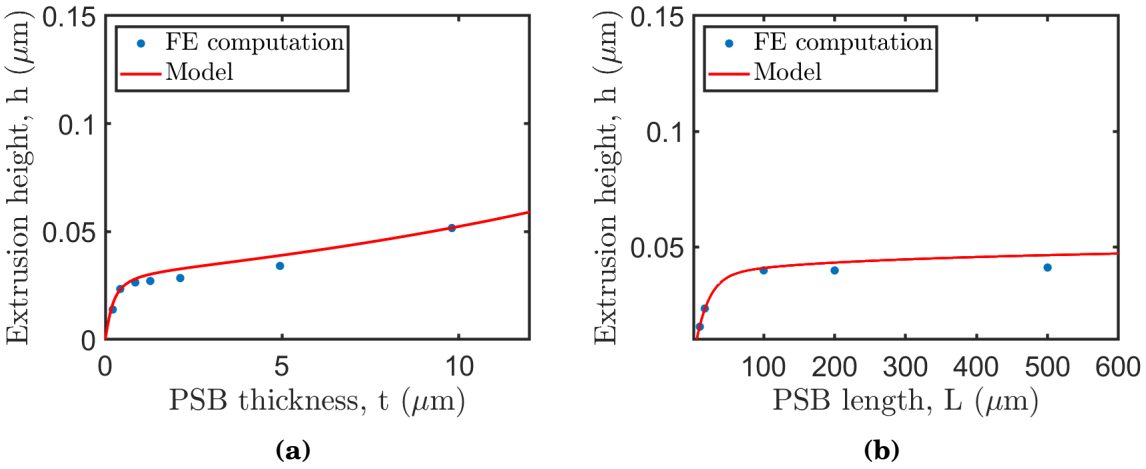

Figure 3-17: Adjustment of the parameters of the proposed model on type B PSB extrusion computed via FE in 316L SS. (a) Effect of PSB thickness (N = 10000 cycles, L = 17 μm). (b) Effect of PSB length (N = 10000 cycles, $t = 0.424$ μm).

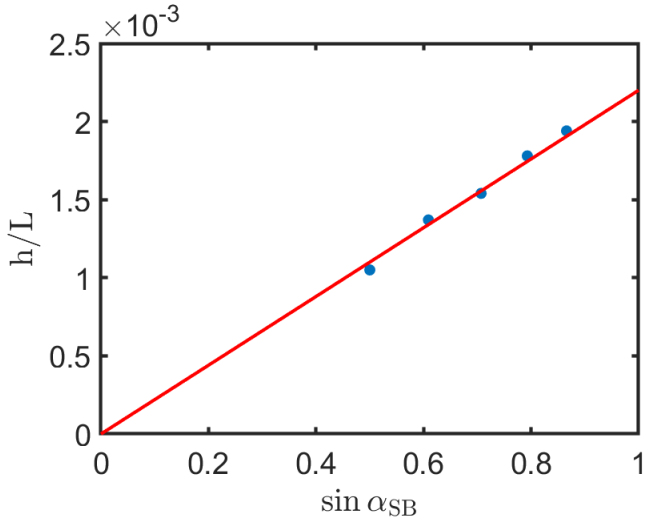

Figure 3-18: Effect of PSB inclination angle on extrusion height in copper (t = 0.5 μm).

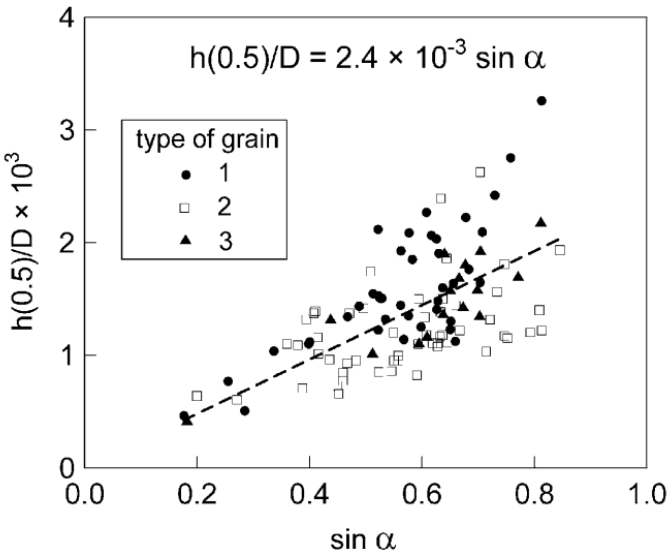

Figure 3-19: Normalized extrusion height h/L in dependence on the sine of the angle α. Quoted from [Man et al., 2002].

3.4.4 Effect of crystal elasticity anisotropy, lattice rotation and finite displacements

The previous computations have been carried out under certain hypotheses (anisotropic elasticity (cubic elasticity), finite displacements, lattice rotation). The aim of this section is to evaluate the influence of these assumptions on the measured extrusion heights. Thus, initially the assumption of isotropic elasticity is made and the predictions are compared with the anisotropic case. Then, we assume that the hypothesis of small displacements is valid. And finally, we do not use the lattice rotation during the FE computations. The computations are carried out for copper with a type PSB B thickness of $0.424\ \mu\mathrm{m}$ and length of $\mathrm{L} = 17\ \mu\mathrm{m}$. The different results are shown in Fig. 3-20, Fig. 3-21 and Fig. 3-22.

Using isotropic elasticity hypothesis instead of cubic elasticity is found to have practically no effect on extrusion height even if on can mention a very slight effect with increasing number of cycles (see Fig. 3-20). Fig. 3-21 shows the effect of the small displacement hypothesis on extrusion height. We can observe in Fig. 3-21 that the effect is very weak, or almost non-existent. It is the same story in Fig. 3-22 where we investigate the influence of the lattice rotation. As before, only a very weak effect is also observed in Fig. 3-22. It is also important to specify that no effect of these different assumptions on the shape of the extrusion can be reported.

3.4.5 Comparison with experimental data

Some experimental investigations in the literature have attempted to describe quantitatively the PSBs extrusion heights. We can cite the work of Man *et al.*

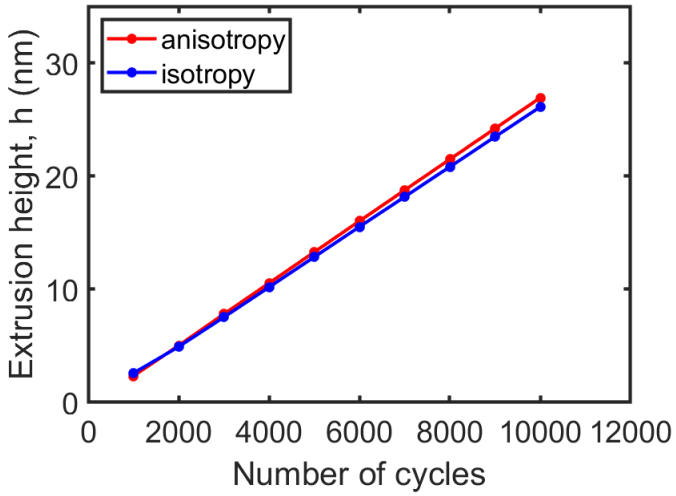

Figure 3-20: Effect of isotropy/anisotropy (cubic elasticity) hypothesis on extrusion growth in copper ($\mathrm{t} = 0.424\ \mu\mathrm{m}, \mathrm{L} = 17\ \mu\mathrm{m}$)

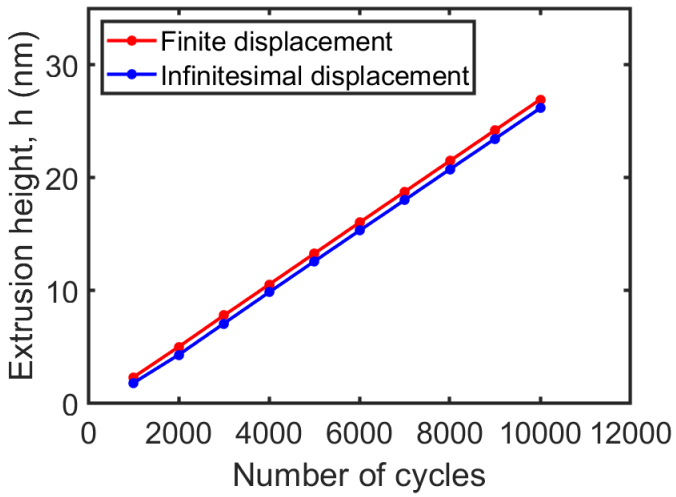

Figure 3-21: Effect of small/finite displacements hypothesis on extrusion growth in copper ($\mathrm{t} = 0.424\mu\mathrm{m}, \mathrm{L} = 17\ \mu\mathrm{m}$)

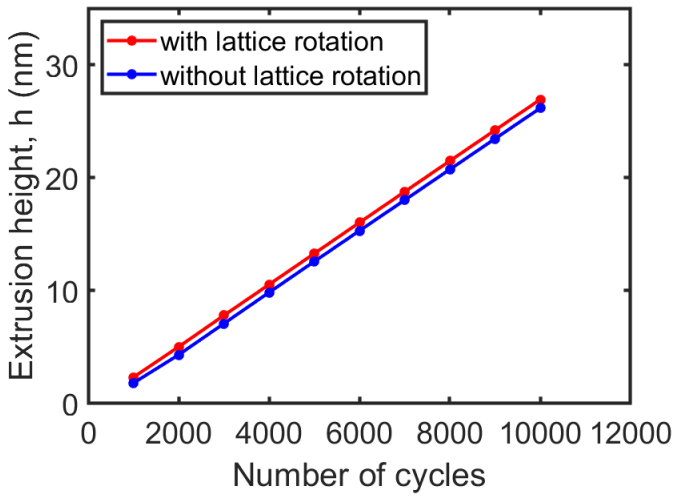

Figure 3-22: Effect of lattice rotation on extrusion growth in copper ($\mathrm{t} = 0.424\ \mu\mathrm{m}, \mathrm{L} = 17\ \mu\mathrm{m}$)

[Man et al., 2002] in 316L SS polycrystals or the work of Hunsche and Neumann [Hunsche and Neumann, 1986] in copper single crystals. In this section, we will compare the predictions of the proposed model (especially for type B PSBs) with these experimental measurements.

Fig. 3-23 shows the comparison between the predictions obtained by the proposed model for type B PSBs and the experimental measurements carried out by Hunsche and Neumann [Hunsche and Neumann, 1986] in copper single crystals. These measurements show the variation of the extrusion height with the protrusion thickness after 60000 fatigue loading cycles. One can notice in Fig. 3-23 the predictions of the proposed model are in fair agreement with the experimental data.

Fig. 3-24 shows the extrusion heights measured experimentally in polycrystals of a 316L steel with an average grain size of $120\ \mu\mathrm{m}$ after 30000 cycles by Man *et al.* [Man et al., 2002]. The results are presented as a function of the PSB thickness and as can be noticed, the agreement between the model predictions are also in fair agreement with the experimental measurements.

Similarly, in Fig. 3-25, Man *et al.* [Man et al., 2002], present the results of extrusion heights measured experimentally in 316L steel polycrystals after 30000 cycles depending on the grain size. The average PSB thickness amounts to $0.5\ \mu\mathrm{m}$. The agreement between the proposed model and the experimental measurements is rather mixed. Agreement seems to be fairly reached in a given domain (for grain size up to $100\ \mu\mathrm{m}$) but the general trend does not seem to be reproduced by the model.

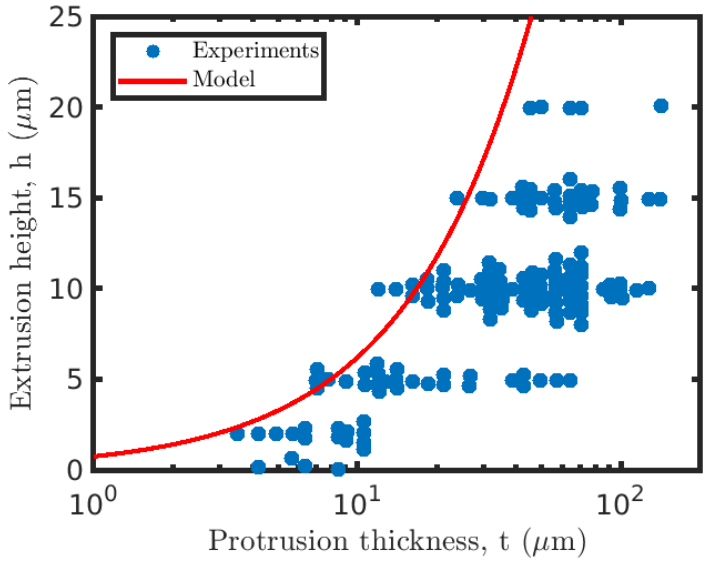

Figure 3-23: Comparison between the proposed model (Equation 3.11) predictions and experimental data of Hunsche and Neumann [Hunsche and Neumann, 1986] experiments on copper single crystals. N = 60000 cycles

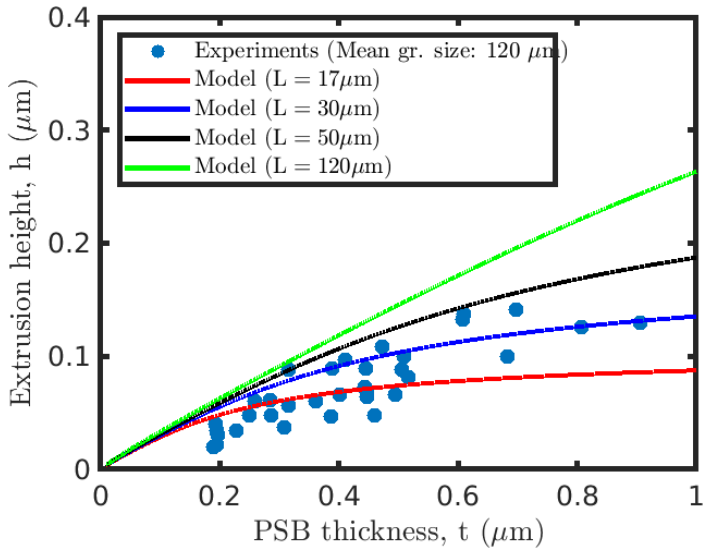

Figure 3-24: Comparison between the model predictions and the experimental results of Man *et al.* [Man et al., 2002] on 316L SS polycrystals. $N = 30000$ *cycles*, Mean grain size : 120 μm.

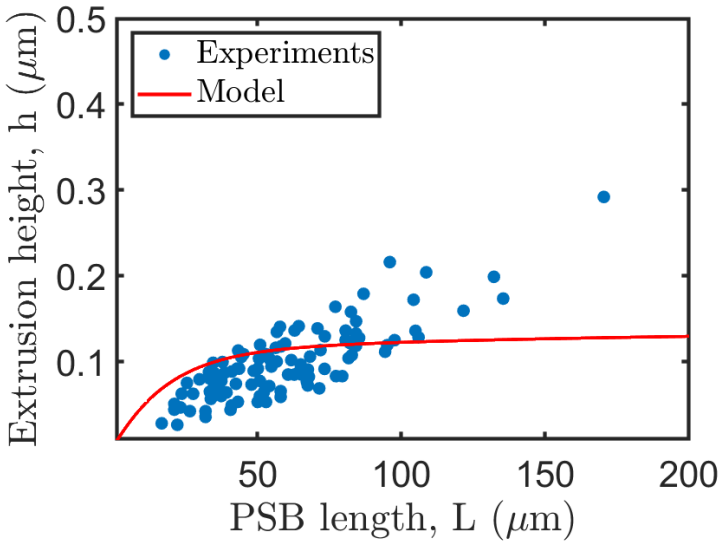

Figure 3-25: Comparison between the model predictions and the experimental results of Man *et al.* [Man et al., 2002] on 316L SS polycrystals. N = 30000 cycles, PSB thickness : $t = 0.5\ \mu$m.

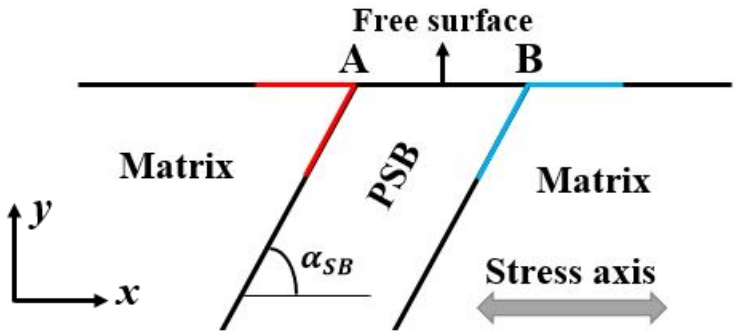

Figure 3-26: Figure showing the lines along which the stresses are assessed

3.5 Stress field analysis and fatigue crack initiation

The extrusion of PSBs induces internal stresses which can contribute to the initiation of fatigue cracks along PSBs.

Numerous studies in the literature such as those of [Laufer and Roberts, 1966, Lukáš and Klesnil, 1971, Katagiri et al., 1977, Hahn and Duquette, 1978, Basinski and Basinski, 1984, Polák et al., 1985, Hunsche and Neumann, 1986, Ma and Laird, 1989, Mughrabi, 2009], etc. have discussed the initiation of cracks along PSBs. These studies in their almost totality show that the initiation of cracks occurs preferentially along the interface between the PSB and the elastic matrix even if some

authors such as Mughrabi [Mughrabi, 2009], pointed out the possibility for crack initiation to occur in the sharp valleys of the roughness profile of the PSB. But such observations is rather rare. Some experimental investigations ([Hunsche and Neumann, 1986, Laufer and Roberts, 1966, Mughrabi et al., 1983, Boettner and McEvily, 1965, Lukáš and Klesnil, 1971], for example) and theoretical studies ([Brown and Ogin, 1985]) went even further by specifying the preferential site (A or B, as defined in Fig. 3-26) for crack initiation. Moreover, the need or not for intrusions for fatigue cracks initiation remains unresolved since some authors such as Mughrabi supports that fatigue crack could be initiated without intrusions whereas Polák supports that fatigue crack initiation occurs always in the continuity of an intrusion.

The EGM I and EGM II models explain that fatigue cracks are initiated along PSBs thanks to the stress concentrations produced in the vicinity of the point where the PSB emerges on the surface (point A or B as defined in Fig. 3-26). Considering the internal structure of the PSB, Brown and co-authors suggested that the whole PSB was subjected to tensile strains which induce a surface stress characterized by a logarithmic singularity (Equation 3.12. Therefore, for even small strain, the logarithmic singularity leads to high stresses that may induce crack nucleation.

$$\sigma_{xx}(r) \propto \log\left(\frac{\sqrt{2}r}{t}\right) \tag{3.12}$$

(with r the distance from the singularity point A (see Fig. 3-26), t the PSB thickness).

A thermoelastic simulation carried out on copper with a thermal expansion $\epsilon_{th} = 0.0031$ in the PSB while neglecting the plastic behavior of the PSB, effectively revealed a logarithmic singularity of surface stress in the vicinity of points A and B ($r \ll t$) as shown in Fig. 3-27a. One can observe that stresses on the left side (side A) of the PSB are tensile ones while the stresses on the right side (B) are compressive stresses.

The normal stresses along the PSB/matrix interface show also the same characteristic (Fig. 3-28). As shown in Fig. 3-28, the normal stresses along the PSB/matrix interface on the left side (A) over a small distance from the singularity point A are tensile tresses while those on the right side (side B) along the interface with reference to point B are compressive ones.

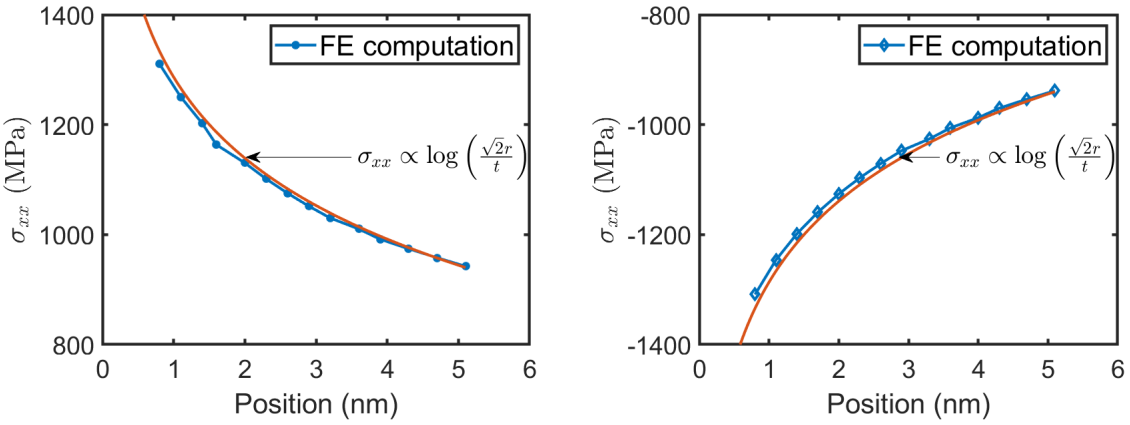

Figure 3-27: Surface stress σ_{xx} as a function of the position along the free surface with respect to (a) point A (red line on the surface, Fig. 3-26) and (b) point B (blue line on the surface, Fig. 3-26). One can observe tensile stress on the left side of PSB (side A) and compressive stresses at the right side of the PSB (side B). $\mathrm{N} = 10000$ cycles, $t = 0.424\ \mu m$, $L = 17\ \mu m$ (Thermoelastic FE computations carried out in copper).

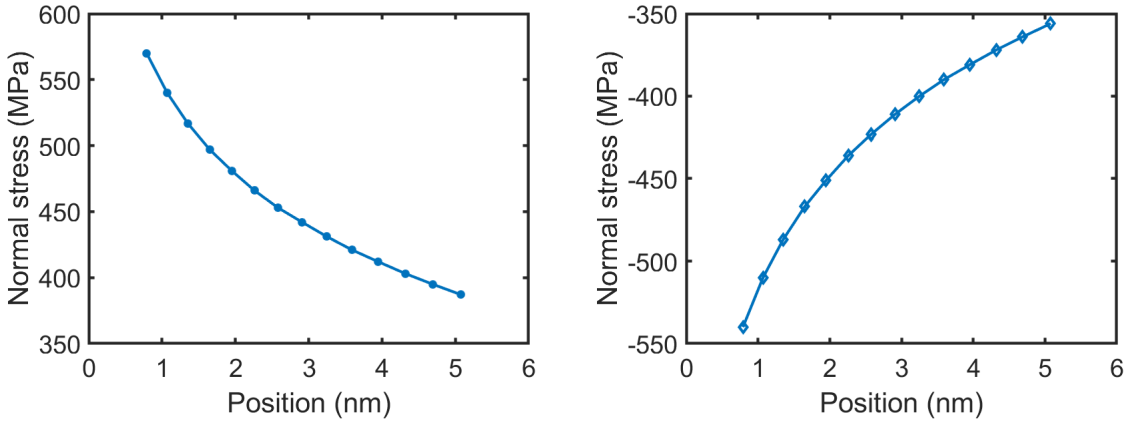

Figure 3-28: Normal stresses as a function of the position along PSB with respect to (a) point A (red line on the left side along the PSB) and (b) point B (blue line on the right side along the PBS) (Fig. 3-26). One can observe tensile stress on the left side of PSB (side A) and compressive stresses at the right side of the PSB (side B) as in the case of surface stress σ_{xx}. $\mathrm{N} = 10000$ cycles, $t = 0.424\ \mu m$, $L = 17\ \mu m$ (Thermoleastic FE computations carried out in copper)

However, by considering the real behavior of the PSB (elastoplastic behavior), we notice that there is no longer any logarithmic singularity as already pointed out by Brinckmann and van der Giessen [Brinckmann and Van der Giessen, 2003] who came to the same conclusion by using dislocation dynamics computations. Moreover the authors show that the surface stress profile does not resemble to that was predicted by Brown and Ogin [Brown and Ogin, 1985]. Fig. 3-30 shows the surface stress σ_{xx} on the left side (A) and on the right side (B) computed assuming elastic-plastic behaviour of PSB. The surface stresses computed on the left side are low compared to that was predicted by thermoelastic computations whereas surface stresses at the right side are compressive ones. Fig. 3-31, shows the normal stresses computed along the PSB/matrix interface on the left side (A) over a distance of 5 nm from point A. As can be noticed, the normal stresses along the interface increase with the number of cycles. It is also observed that the normal stresses vary with the PSB thickness and length as shown in Fig. 3-32 and Fig. 3-33.

One can realize also that, contrary to surface stresses, the normal stresses along PSB/matrix interface on the right side (B) are tensile stresses and increase with PSB thickness (Fig. 3-33a). However, their values remain low compared to the normal stresses assessed along PSB/matrix interface on the left side (A) (Fig. 3-32a). Also, the normal stresses along PSB/matrix interface on the right side (B) decrease as PSB length increases, with the occurrence of compressive normal stresses (Fig. 3-33b). On the left side (A), normal stresses along PSB/matrix interface was found to vary a little with respect to the PSB length (Fig. 3-32b).

In summary, for computations taking into account the elastic-plastic behavior of the PSB contrary to Brow and Ogin computations [Brown and Ogin, 1985], the surface stresses do not show logarithmic singularity as suggested by Brown and Ogin. Even more, the surface stresses do not seem to present any singularity on the left side (A) (Fig. 3-30). The normal stresses computed along PSB/matrix interfaces remain low and cannot induce fatigue crack initiation along PSBs.

Indeed, considering the ideal tensile strength of 7.5 GPa of copper along $\langle 1\,1\,1 \rangle$ direction computed by *ab initio* ([Pokluda et al., 2015, Černý and Pokluda, 2009] or even the ideal measured experimentally (1.5 GPa) on whiskers ([Kobayashi and Hiki, 1973, Macmillan, 1983]), it seems obvious that the stresses predicted by our computations are not sufficient to induce an initiation of fatigue crack along PSB after the 10000^{th} cycle. Experimentally, some authors reported fatigue cracks initiation after only 500 cycles ([Kwon et al., 1989a]) in air environment and after 1000 cycles ([Kwon et al., 1989a]) in inert environment on copper single crystals. In polycrystals, Known *et al.* [Kwon et al., 1989b] observed crack initiation after 1000 cycles, 10000 cycles depending on the grain size and the environment. Kim *et al.* [Kim et al., 1991] reported fatigue crack initiation after 3500 cycles in polycristalline copper in air environment. Other authors such as Polák *et al.* [Polák et al., 2009, Polák et al., 2013] observed crack initiation after 500 cycles and 3800 cycles depending on the grain size.

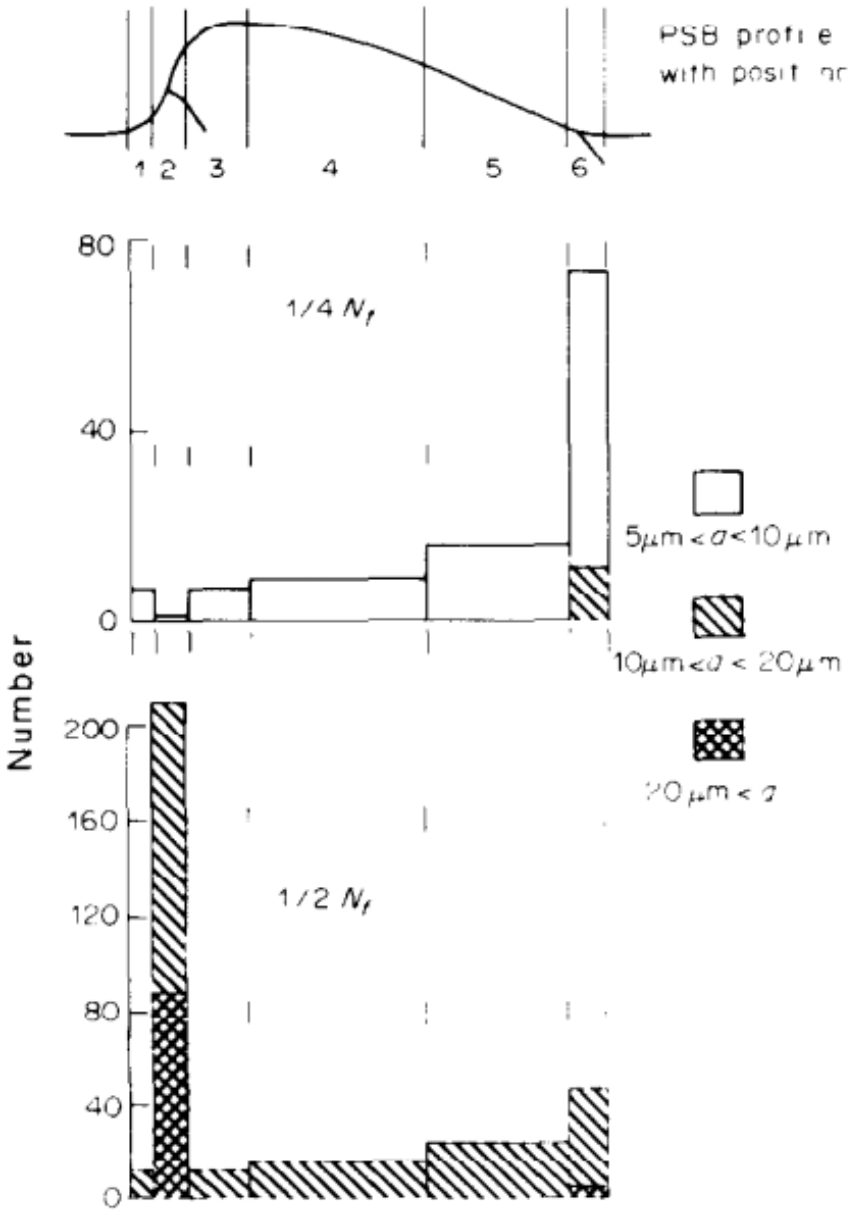

Figure 3-29: Number of cracks at various locations within PSB ($N_f = 120000$ cycles). Quoted from [Hunsche and Neumann, 1986].

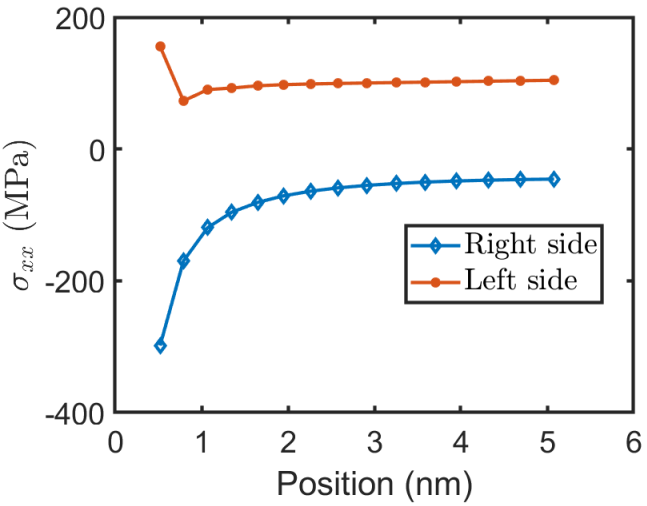

Figure 3-30: Surface Stress σ_{xx} at left side (surface red line in Fig. 3-26) and at right side (surface blue line in Fig. 3-26). $t = 0.424\mu m$, $L = 17\mu m$, $N = 10000$ cycles (Thermoelastic-plastic computations)

Under these conditions, the need for a stress raisers other than that induced by PSB extrusion through free surface becomes a necessity to initiate short fatigue cracks along PSBs.

The formation of intrusions as suggested by Polák and co-authors would maybe lead to much higher stress concentrations. They may be high enough to reach the tensile strength along an interface segment of reasonable length and lead to the initiation of short fatigue cracks along PSB/matrix interfaces. Stresses computed in this study suggest that fatigue crack initiation should always occur on the left side (A) of the PSB (since stresses on this side (A) are tensile stresses and the ones at the right side (B) are compressive stresses). This could indeed explain, or at least partially, the observations of Hunsche and Neumann [Hunsche and Neumann, 1986], who showed that a large proportion of short cracks originated from the side A (Location 6 in Fig. 3-29) while the other side was the location of only a few initiated short cracks after $1/4\ N_f = 30000$ cycles ($N_f = 120000$ cycles). Nevertheless, this cannot explain the change in the proportion of cracks initiation between sides A and B (Locations 6 and 1 respectively, in Fig. 3-29) after $1/2\ N_f = 60000$ cycles as shown in Fig. 3-29. This also cannot explain the fact that some authors ([Boettner and McEvily, 1965, Laufer and Roberts, 1966, Basinski and Basinski, 1989] observed nucleation of fatigue cracks only on the right side (B) where stresses was found to be compressive ones.

But with the formation of companion intrusions on the right side (B) of the PSB, the normal stress fields on this side could become tensile stresses as the intrusions depth increases. And this may lead to fatigue crack initiation on side B. This could also explain the observations of some authors who observed cracks

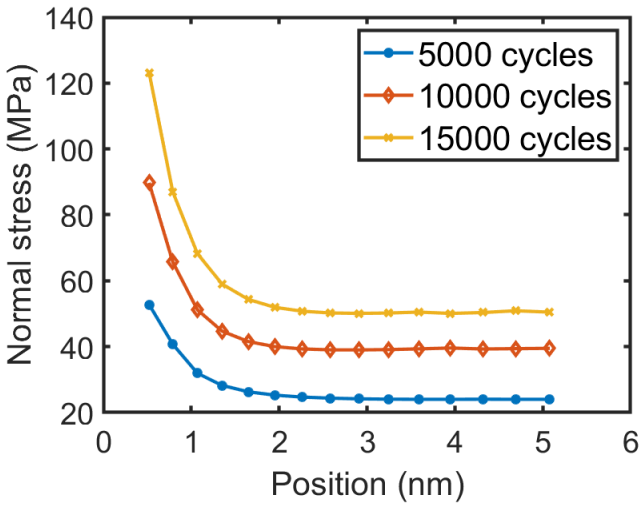

Figure 3-31: Effect of number of cycles on normal stresses along PSB/matrix interface ($t = 0.424\ \mu m,\ L = 17\ \mu m$) for different number of cycles (Thermoelastic-plastic computations). Side A

located only on side B. Indeed authors such as [Man et al., 2009a] observed intrusions growing at both sides (A and B) and, some observed intrusions only on side B ([Man et al., 2009a, Man et al., 2012]).

3.6 Conclusion

Cyclic straining of metals and alloys generally leads to the localization of plastic deformation in PSBs at the surface of which extrusions grow. In this chapter, through crystal plasticity finite element computations and a basic modelling of production and annihilation of vacancies, we simulated the extrusion of PSBs in FCC metals and alloy (Cu, Ni, 316L). The influence of a number of parameters has been investigated. Firstly, significant differences between type A and type B PSBs is observed as also shown by Stopka and McDowell [Stopka and McDowell, 2020] in a recent study based on crystallographic slip contraints near free surface without consideration of PSB modelling. Indeed, the results show a linear increase of the extrusion height with respect to the number of cycles, whatever the type of PSB considered (type A or type B). This is in agreement with the experimental measurements of Man et *al.* [Man et al., 2002] and Hunsche and Neumann [Hunsche and Neumann, 1986]. This contradicts the EGM I model and EGM II model for which the dependence of the extrusion height on the number of cycles should be of square root type. Furthermore, the results also show that the extrusion height of type B PSBs is higher than that of type A PSBs; a result in agreement with the experimental observations of Obrtlik et *al.* [Obrtlík et al., 1997] in copper single crystals and Holste and Schwab [Holste and Schwab, 2006] in single crystals of Ni-Al alloy. This tendency of

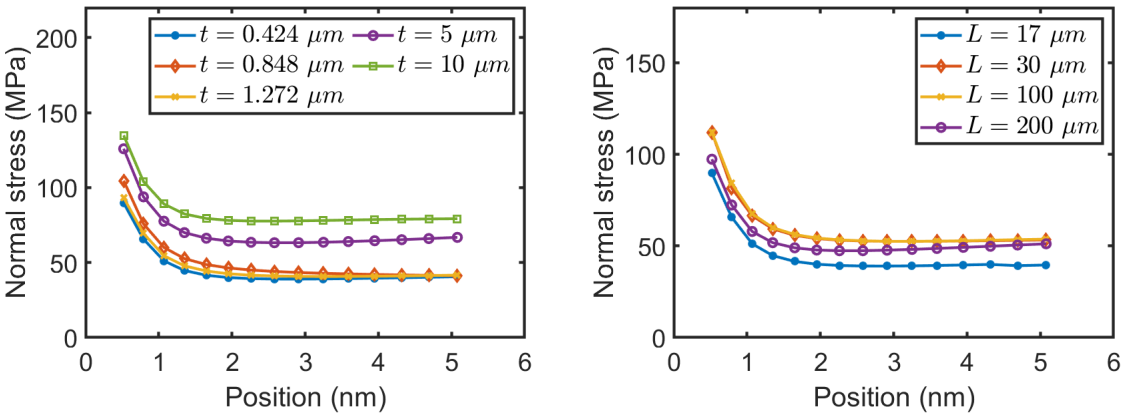

Figure 3-32: Normal stresses along side A PSB/matrix interface. (a) Effect of PSB thickness ($\mathrm{L} = 17\mu\mathrm{m}$), (b) Effect of PSB length ($\mathrm{t} = 0.424\mu\mathrm{m}$).

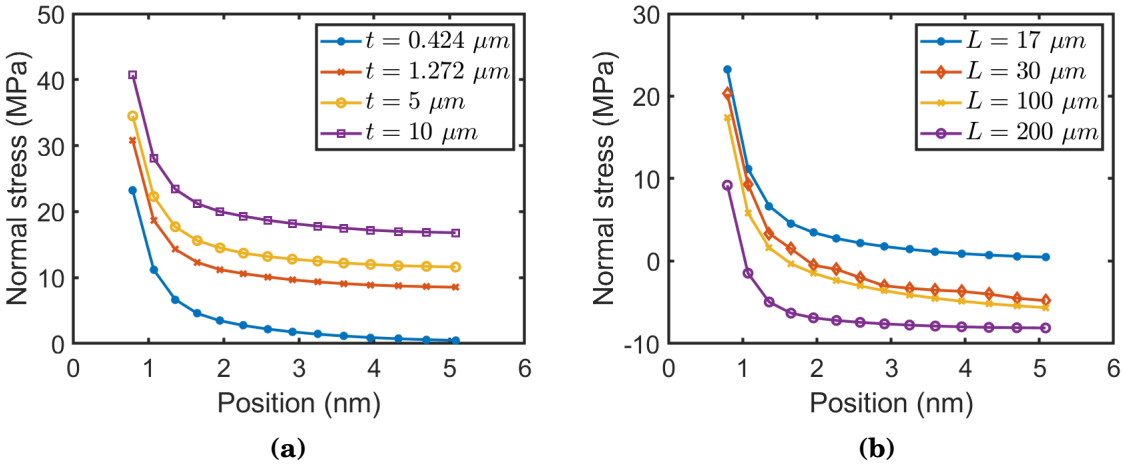

Figure 3-33: Normal stresses along side B PSB/matrix interface. (a) Effect of PSB thickness ($\mathrm{L} = 17\mu\mathrm{m}$), (b) Effect of PSB length ($\mathrm{t} = 0.424\mu\mathrm{m}$).

type B PSBs to extrude faster than type A PSBs can be explained by an easy plastic accommodation in the direction of the Burgers vector for type B PSBs. The dependence of extrusion height on PSB thickness and length is highlighted whatever the type of PSB. Analytical expressions have thus been proposed to describe the influence of the characteristic dimensions of the PSB on the extrusion height. Their predictions are compared with the various experimental measurements found in the literature and a quite good agreement is observed. The dependence of the extrusion height on the PSB inclination angle with respect to the loading axis is also investigated. The simulations showed that the normalized extrusion height h/L increased linearly with the sine of the inclination angle as observed experimentally on 316L steel polycrystals [Man et al., 2002]. The slope measured experimentally (approximately $0.0025\ \mu\mathrm{m}$) is similar to the slope computed by finite element method ($0.0022\ \mu\mathrm{m}$). Finally, the influence of the modelling assumptions (large displacements/small displacements, lattice rotation or not, isotropy/anisotropy) is studied. The results show at this level a very weak effect of the modelling hypotheses both on extrusion heights and profiles.

An analysis of the stress fields shows an increase in stresses with the number of cycles. Thermoelastic computations show a logarithmic singularity as predicted by Brown and Ogin [Brown and Ogin, 1985]. However, by assuming that the PSB is elastic-plastic, the stress fields exhibit no more logarithmic singularity. The normal stresses computed along PSB/matrix interfaces are found to be very low compared to the theoretical or experimental cleavage strength (on a $\{1\,1\,1\}$ plane) and therefore seem no to be sufficient to induce the initiation of short cracks along PSBs. Intrusion-type stress raisers would therefore be necessary in order to increase the stress concentrations and reach the cleavage strength. This could also allow a better understanding of certain experimental observations especially the crack site location on the surface. Then the solving of the diffusion equation together with the equations of the presented model can allow the prediction of the evolution and shape and depth of intrusions. Finally, extracting displacement fields computed by FE method and applying these displacement fields to a MD simulation box containing the intrusion shape can allow us to check if crack initiation at the bottom of the intrusions takes place by cleavage or by blunting-resharpening (chapter 7). These two intrinsic crack initiation mechanisms compete together and such MD simulations weakly coupled with FE computations may be able to show which mechanism is the most prone to lead to crack initiation and further intrinsic propagation.

As mentioned previously, after fatigue crack initiation, the propagation occurs first in stage I along the slip planes then in stage II. Before addressing stage I crack propagation where the latter takes place in mixed mode manner (chapter 7), we first investigate in chapter 4 and chapter 5, the fatigue crack-tip deformation and extension by fatigue under under mode I loading (stage II) in copper single crystals.

THIS PAGE INTENTIONALLY LEFT BLANK

Chapter 4

Plastic deformation and underlying crystal defects in the vicinity of fatigue crack-tip

Nichts Großes auf der Welt wurde jemals ohne Leidenschaft erreicht.

Georg Wilhelm Friedrich Hegel in *Vorlesungen über die Philosophie der Geschichte.*

Abstract

In this paper, we study the crack-tip plastic deformation for various orientations of copper single crystals containing a crack loaded under mode I. The results show that depending on the crack orientation, different strain localization patterns are predicted by molecular dynamics (MD) simulations. These predictions are in agreement with the different experimental observations available. On the other hand the different plastic deformation mechanisms are analyzed. It appears that depending on the crack orientation, plastic deformation can be accommodated either by emission and gliding of dislocations at the crack-tip or by a mixture of emission and gliding of dislocations and mechanical twinning. The various lattice defects generated during cyclic loading are also analyzed, in particular dislocations, but also all point defects such as vacancies, the density of which is evaluated and found to be in the same orders of magnitude as the experimentally reported values in the case of severe plastic deformation as observed at the crack-tip or as in the case of cyclically deformed copper single crystals. In addition, the different dislocation structures such as Lomer-Cottrell locks, Hirth lockes, jogs are also analyzed as well as the stacking defect tetrahedra observed in the present simulations also in agreement with the experimental observations. The plastic irreversibility at the crack-tip which was shown to be a consequence of different dislocation interactions was analyzed and the irreversibility factors were computed for different crystal orientations. Finally internal stresses due to the remaining dislocations at crack-tip have also been studied.

Contents

4.1 Introduction

Fatigue is one of the most damaging mechanism for materials and structures. For a long time, fatigue of metals and alloys has been a very active field of research. Despite many advances accomplished in this area, some aspects including the exact mechanisms of initiation and propagation of fatigue cracks remain unclear especially when the environment, the microstructure and/or crystallography effects occur. This seems to be due to certain mechanisms occurring at the atomic scale, which govern the initiation and propagation of the crack at various scales. These mechanisms at the atomic scale are not easily accessible by experimental means and hence render difficult the understanding and the modeling of fatigue phenomenon. Atomistic simulation techniques such as molecular dynamics (MD) provide today opportunities for studying and understanding phenomena occurring at the atomic scale and governing the multiscale behavior of materials and structures. On the modelling point of view, finite element computations and experimental investigations have contributed greatly to the understanding of fatigue crack initiation and propagation mechanisms; microstructure evolution during fatigue and life prediction under cyclic loading. One can point some representative references [Basinski and Basinski, 1992b, Basinski et al., 1983, Cheng and Laird, 1981, Cheng and Laird, 1983, Essmann et al., 1981, Essmann and Mughrabi, 1979, Hunsche and Neumann, 1986, Neumann, 1974, McDowell and Dunne, 2010, Polák and Sauzay, 2009, Repetto and Ortiz, 1997, Vehoff and Neumann, 1979, Hénaff et al., 2002]. Nevertheless, there is a real need to get an insight on the atomic scale mechanisms of the fatigue since these phenomena are those which govern the multiscale behavior of fatigued materials. As indicated by Horstemeyer *et al.* [Horstemeyer et al., 2010], macroscale fatigue models, particularly ones with microstructural sensitive do not cover the atomic scale. To obtain predictive tools that perform well on a macroscopic scale, it is important to conduct studies at the atomic scale for better understanding of crystalline orientation and then latter grain boundary effects, temperature, stacking fault energy, etc. However, several researchers have reported some interesting investigations on fatigue crack behavior via molecular dynamics simulations [Fan et al., 2016, Fan et al., 2017, Farkas et al., 2005, Nishimura and Miyazaki, 2004, Potirniche et al., 2005, Potirniche and Horstemeyer, 2006, Baker and Warner, 2014, Wu et al., 2015].

Today it is widely accepted that the propagation of fatigue cracks is largely influenced by crack-tip phenomena, in particular crack-tip plasticity in ductile metals and alloys. In order to better understand the propagation of fatigue cracks, it is therefore important to understand how plastic deformation proceeds at the crack-tip as well as its impact on the propagation. It is generally admitted that in the case of FCC single crystals under mechanical loading, plastic deformation proceeds by two main mechanisms: dislocation gliding and mechanical twinning. Although dislocation slip is the most reported plastic deformation

mechanism, some previous studies have nevertheless reported mechanical twinning and/or crack tip twinning [Adamesku et al., 1994, English and Chin, 1965, Fortes and Ralph, 1970]. Molecular dynamics simulations performed on nickel single crystal by Zhang and Ghosh [Zhang and Ghosh, 2013] under tensile loading evidenced an orientation dependence of the deformation mechanisms at crack-tip while Warner *et al.* [Warner et al., 2007] show a rate dependence of crack-tip deformation mechanisms.

The first studies on the nature of the stress and strain fields in the vicinity of crack-tips were conducted by Pan [Pan, 1986] assuming an elastic ideally plastic behavior. Later Rice [Rice, 1987] proposed the first solution for crack-tip stress field in FCC and BCC crystals, followed by an extension of this solution to HCP crystals by Gupta [Gupta, 1993]. Kysar and Bryant [Kysar and Briant, 2002] carried out an experimental study of crack-tip deformation fields in aluminum single crystals subjected to tensile loading. Their observations provide evidence of some features of the deformation fields that were predicted by the Rice analytical solution for an elastic ideally plastic single crystal. One of these features consists in kink bands. Shield [Shield, 1996], Crone and co-workers ([Crone and Shield, 2001, Crone and Shield, 2003, Crone et al., 2004]) investigated experimentally the plastic deformation features around a notch tip within ductile single crystal of copper and copper-beryllium alloy by the means of Moiré Microscopy and compared their observations to both analytical solutions and finite element computations. These investigations showed strain localization patterns similar to that ones predicted by Rice for the same orientation. But the authors did not observe kink bands at 90° with respect to the notch axis, as predicted by Rice.

A similar orientation was used by Van der Gissen *et al.* [Van der Giessen et al., 2001], in discrete dislocation dynamics computations and came to the same conclusion as before.

Flouriot *et al.* [Flouriot et al., 2003] studied experimentally and numerically under tensile loading, the strain localization at a crack-tip in a nickel base superalloy single crystal. The computations were carried out in the framework of standard continuum crystal plasticity for different crack orientations with a focus on the differences between the plastic strain fields at free surface and in the mid-section of the specimen. The numerical result were compared to the experimental ones and a good agreement was found for orientation $(1\,1\,0)[\bar{1}\,1\,0]$ ($(1\,1\,0)$ is the crack plane and $[\bar{1}\,1\,0]$ is the crack front) as strain localization bands were concerned. The existence of kink bands for this orientation has been confirmed.

The investigations carried out by Potirniche *et al.* [Potirniche G.P et al., 2006] and by Horstemeyer *et al.* [Horstemeyer et al., 2010] via MD simulations on FCC bi-crystals under cyclic loading reveal the formation of slip bands and dislocation vein structures in the vicinity of crack tip. Void formation was also observed and was thought to be the main fatigue crack propagation mechanism.

However, unlike these MD simulations, the experimental studies by Awatani

et al. [Awatani et al., 1978] did not show the formation of such voids. Indeed, the authors investigated the dislocation structures around propagating fatigue cracks in iron via TEM. Their observations reveal dislocation cell structures with the interior of the cells showing relatively low density of dislocations. But the authors added: "any crack supposed to be formed by linking of voids was not found".

The investigations of Dewald *et al.* [Dewald et al., 1990] show that under mode I loading, the crack-tip dislocation structures are not a simple linear array of dislocations. Indeed, the authors reported a complex configuration of crack-tip dislocations. Cracks were found to propagate with the emission of dislocations from both crack-tip and nearby sources.

The aim of the present investigation is to get insight in the deformation nature and processes at crack-tip, at atomic scale under cyclic loading via molecular dynamics simulations. The computations are carried out on copper single crystals at room temperature (RT). First of all, the crack-tip dislocation emission is analyzed according to the different crystal orientations. We then study the mechanisms of plastic deformation at crack-tip as well as slip traces patterns for different crystalline orientations. The interactions between dislocations are studied as well as the junctions and vacancy type defects resulting from these interactions.

4.2 Computational method

For this study, classical molecular dynamics simulations using empirical potentials are performed. Simulations are carried out with the LAMMPS (Large scale Atomic/Molecular Massively Parallel Simulator) software developed at Sandia National Laboratories [Plimpton, 1995].

4.2.1 Interatomic potentials

Interatomic potentials are functional relationships that describe the interaction energy between atoms that composed the considered physical system. These functional relationships are adjusted to experimental and/or *ab initio* data. Therefore, the reliability of classical MD simulations depends on the accuracy of the interatomic potentials for a given set of particles. In this study, the Embedded Atom Method (EAM) type potentials are used. Originally developed by Daw and Baskes [Daw and Baskes, 1983], these potentials, which are many-body potential function, are designed to compute metals and metal alloys interactions. Since mechanism of crack growth in FCC ductile metals seems to involve plastic deformation, it is necessary that the potentials predicts both reliable elastic constants, stacking fault energies, surface energies, vacancy formation and migration energies. Therefore, we chose to use the EAM interatomic potential proposed by Mishin *et al.* [Mishin et al., 2001], which fulfills these requirements.

The total potential energy in this formalism is given by:

$$E_{tot} = \sum_i F\left(\bar{\rho}_i\right) + \frac{1}{2}\sum_{ij} V(r_{ij}) \tag{4.1}$$

where $V\left(r_{ij}\right)$ is the pair potential; r_{ij} is the distance between the atoms i and j; F is the embedding energy as a function of the host electron density $\bar{\rho}_i$ induced at site i by all the surrounding atoms within a sphere of a radius corresponding to the interaction cut-off distance. This electron density is given by the following expression:

$$\bar{\rho}_i = \sum_{j \neq i} \rho\left(r_{ij}\right), \tag{4.2}$$

where $\rho\left(r_{ij}\right)$ is the electron density function. For the selected potential [Mishin et al., 2001], the electron density obeys the following analytic expression:

$$\rho(r) = \left[a\exp(-\beta_1(r - r_0^{(1)})^2 + \exp(-\beta_2(r - r_0^{(2)}))\right]\psi\left(\frac{r - r_c}{h}\right) \tag{4.3}$$

where a, $r_0^{(1)}$, $r_0^{(2)}$, β_1, β_2, r_c and h are adjusted parameters. ψ is the cutoff function and is given by:

$$\psi(x) = \begin{cases} 0 & \text{if } x \geqslant 0 \\ \frac{x^4}{1+x^4} & \text{if } x < 0 \end{cases} \tag{4.4}$$

The pair interaction function is adjusted as:

$$\begin{aligned} V\left(r\right) = &\left[E_1 M(r, r_0^{(1)}, \alpha_1) + E_2 M(r, r_0^{(2)}, \alpha_2) + \delta\right]\psi\left(\frac{r - r_c}{h}\right) \\ &- \sum_{n=1}^{3} H\left(r_s^{(n)} - r\right) S_n \left(r_s^{(n)} - r\right)^4 \end{aligned} \tag{4.5}$$

where M is a Morse function given by

$$M(r, r_0, \alpha) = \exp\left[-2\alpha(r - r_0)\right] - 2\exp\left[-\alpha(r - r_0)\right] \tag{4.6}$$

and $H(x)$ is a unit step function.

The embedding function is represented by:

$$F\left(\bar{\rho}\right) = F^{(0)} + \frac{1}{2}F^{(2)}\left(\bar{\rho} - 1\right)^2 + \sum_{n=1}^{4} q_n \left(\bar{\rho} - 1\right)^{n+2} \tag{4.7}$$

for $\bar{\rho} < 1$

$$F\left(\bar{\rho}\right) = \frac{F^{(0)} + \frac{1}{2}F^{(2)}(\bar{\rho}-1)^2 + q_1(\bar{\rho}-1)^3 + Q_1(\bar{\rho}-1)^4}{1 + Q_2\left(\bar{\rho} - 1\right)^3} \tag{4.8}$$

for $\bar{\rho} > 1$

with $\bar{\rho}$ the host electron density given by:

$$\bar{\rho}_i = \sum_{j \neq i} \rho\left(r_{ij}\right) \tag{4.9}$$

E_1, E_2, $r_0^{(1)}$, $r_0^{(2)}$, α_1, α_2, δ, r_c, h, $\left(r_s^{(n)}, S_n\right)_{n=1,2,3}$, Q_i and q_i are adjusted parameters. The value of the adjusted parameters can be found in [Mishin et al., 2001].

4.2.2 Simulation setup

4.2.2.1 Model and boundary conditions

The simulation model used consists in a parallelepiped box containing atoms placed in a face-centered cubic (FCC) lattice. Different lattice orientations are considered. In this investigation, seven systems corresponding to different crystal orientations (crack surface and crack front) are investigated for which the loading axis is parallel to the y direction (see Fig. 4-1 and Table 4.1). For instance, the first system coined A1 is oriented along the $[1\,0\,0]$; $[0\,1\,0]$ and $[0\,0\,1]$ directions. The crack plane is the $(0\,1\,0)$ plane and the crack front is along the $[0\,0\,1]$ direction. The initial dimensions of this simulation box are $93 \times 124 \times 20$ nm^3 in the x, y and z directions respectively. All the features of the seven simulation boxes are summarized in Table 4.1. Each of the seven simulation boxes contains approximately 17 to 20 million atoms. To the author's knowledge, such large simulation boxes have never been carried out to study fatigue mechanisms in MD. The surfaces of the simulation box perpendicular to the x and y directions are free surfaces. But atoms near these free surfaces are frozen. Therefore, these surfaces do not behave as real free surfaces and it blocks the transmission of dislocation. It leads to the pile-up of dislocations at the boundaries of the simulation box (approximately 2 to 3 dislocation loops) which can serve to produce backstresses within the domain. To check this effect, backstresses due to the dislocation pile-up were estimated and it was found that these backstresses were significantly low (less than 50 MPa$\sqrt{\text{m}}$) compared to the stresses observed around crack-tip ($2 - 6$GPa). Also, a computation carried out on a less wide box (80 nm $\times$ 80 nm $\times$ 20 nm) shows that the dislocation structures were almost the same. Periodic boundary conditions are applied in the z direction along crack front and as it can be seen on the 3D sketch of Fig. 4-1, an initial edge crack of $a_i = 10$ nm long and approximately 3 nm opening is modeled. It must be beard in mind that this edge crack represents only a small region of the entire crack.

Compared to previous atomistic modeling of fatigue, the simulation box thickness used herein is larger ($\text{L}_\text{z} \approx 20$ to 22 nm) than the thickness of previous atomistic studies which ranges from about 2 to 6 nm [Horstemeyer et al., 2010, Farkas et al., 2005, Potirniche et al., 2005, Potirniche and Horstemeyer, 2006, Zhou et al., 2015]. This size was necessary because as pointed out by Hirth and Lothe [Hirth and Lothe, 1992] and Zhang and Ghosh [Zhang and Ghosh, 2013],

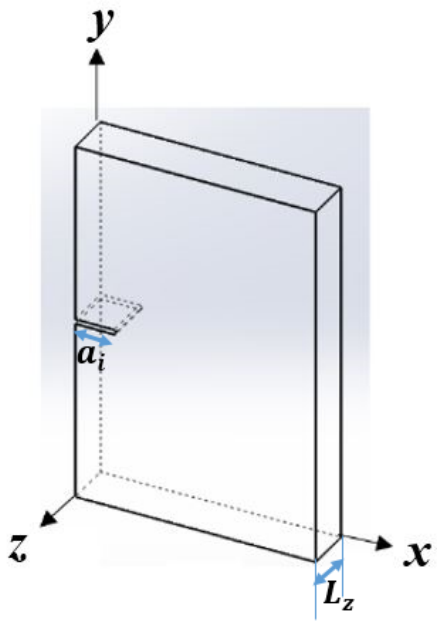

Figure 4-1: Simulation box geometry.L_z is the simulation box thickness (≈ 20 nm) and a_i is the initial crack length (≈ 10 nm). The initial crack opening is about 3 nm. The displacement fields (LEFM fields) are applied around the simulation box to mimic the crack-tip field for a long crack.

the interaction between a dislocation and its image scales with the thickness as:

$$f_{image} = \propto \left(\frac{1}{L_z}\right) \tag{4.10}$$

where f_{image} is the force between a dislocation and its image; and L_z is the thickness of the simulation box. Therefore, for small thicknesses, these interactions become very strong and can suppress dislocation nucleation and gliding because of the strong bias introduced by the periodic boundary conditions along the z axis. For larger L_z, the interactions between a dislocation and its image are reduced. Zhang and Ghosh [Zhang and Ghosh, 2013] showed that there is a trend convergence in the evolution of dislocation density from a thickness of 18.75 nm. The preliminary tests we have carried out confirm this trend.

4.2.3 Loading conditions

Atomistic simulations of fatigue crack propagation described in literature used different methods that affect the simulation results. For example, the use of center-crack tension specimen impedes the application of the linear elastic fracture mechanics (LEFM) formalism. Therefore, number of publications in literature, used uniform displacement, deformation or force loading. In a recent review on atomistic modeling of fracture, Andric and Curtin [Andric and Curtin, 2018] pointed out that except in explicit problem of

Table 4.1: Orientations and features of the three simulation boxes. a_0 corresponds to the lattice parameter.

	x	y	z	Crack plane	Crack front direction	Box dimension	Number of atoms
A1	$[1\,0\,0]$	$[0\,1\,0]$	$[0\,0\,1]$	$(0\,1\,0)$	$[0\,0\,1]$	$93 \times 124 \times 20$ nm^3	19 501 832
A2	$[0\,\bar{1}\,1]$	$[1\,0\,0]$	$[0\,1\,1]$	$(1\,0\,0)$	$[0\,1\,1]$	$95 \times 124 \times 21$ nm^3	20 135 360
A3	$[0\,\bar{1}\,2]$	$[1\,0\,0]$	$[0\,2\,1]$	$(1\,0\,0)$	$[0\,2\,1]$	$93 \times 124 \times 21$ nm^3	20 336 836
B1	$[\bar{1}\,1\,0]$	$[1\,1\,0]$	$[0\,0\,\bar{1}]$	$(1\,1\,0)$	$[0\,0\,\bar{1}]$	$103 \times 103 \times 21$ nm^3	18 206 769
B2	$[0\,0\,\bar{1}]$	$[\bar{1}\,1\,0]$	$[1\,1\,0]$	$(\bar{1}\,1\,0)$	$[1\,1\,0]$	$103 \times 103 \times 21$ nm^3	18 230 640
C1	$[\bar{1}\,1\,0]$	$[1\,1\,1]$	$[1\,1\,\bar{2}]$	$(1\,1\,1)$	$[1\,1\,\bar{2}]$	$82 \times 125 \times 22$ nm^3	18 974 000
C2	$[1\,1\,\bar{2}]$	$[1\,1\,1]$	$[1\,\bar{1}\,0]$	$(1\,1\,1)$	$[1\,\bar{1}\,0]$	$83 \times 124 \times 21$ nm^3	17 551 920

nanoscale materials and structures, the default analysis of atomic scale fracture mechanics is the LEFM. Our aim in these atomistic simulations is to reveal the complex mechanism at the crack-tip in the high stress region. Under a macroscopic loading, phenomena at crack-tip are governed by the high local stresses. To simulate, the crack-tip behavior under cyclic loading, we used systems with edge pre-cracks. The pre-crack in MD simulation box represents the very crack-tip region of an entire crack. Therefore, we apply as loading, a displacement field drawn from the LEFM formalism The loading variable is the stress intensity factor that controls the displacement applied. However in this study, since simulations are carried out on copper single crystals, which anisotropy of cubic elasticity is high, the displacement fields drawn from the LEFM formalism should take into account the anisotropic nature of crystal elasticity.

Therefore, the displacement field applied at the boundary of the MD simulation box (Fig. 4-2) is [Sih et al., 1965]:

$$\begin{cases} u_x = K_I\sqrt{\dfrac{2r}{\pi}}\Re\left[\dfrac{1}{a_1-a_2}\left(a_1p_2\sqrt{\cos\theta+a_2\sin\theta}-a_2p_1\sqrt{\cos\theta+a_1\sin\theta}\right)\right] \\ u_y = K_I\sqrt{\dfrac{2r}{\pi}}\Re\left[\dfrac{1}{a_1-a_2}\left(a_1q_2\sqrt{\cos\theta+a_2\sin\theta}-a_2q_1\sqrt{\cos\theta+a_1\sin\theta}\right)\right] \end{cases} \tag{4.11}$$

where K_I is the stress intensity factor in mode I and p_1, q_1, p_2, q_2 depend on the material elasticity compliance constants (s_{ij}) and are given by:

$$p_1 = s^p_{11}a_1^2 + s^p_{12} - s^p_{16}a_1 \tag{4.12}$$

$$p_2 = s^p_{11}a_2^2 + s^p_{12} - s^p_{16}a_2 \tag{4.13}$$

$$q_1 = s^p_{12}a_1 + \frac{s^p_{22}}{a_1} - s^p_{16} \tag{4.14}$$

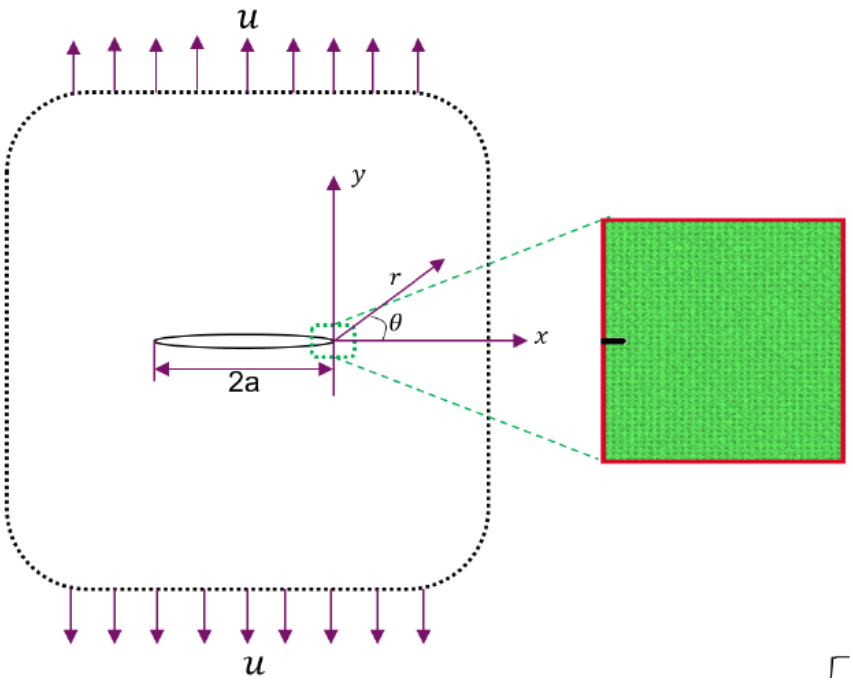

Figure 4-2: Representation of the whole solid subjected to any loading conditions and the embedded MD simulation box located in the vicinity of the crack-tip. The LEFM displacement field is applied at the boundaries of this MD simulation box (The red zones at the boundaries).

$$q_2 = s_{12}^p a_2 + \frac{s_{22}^p}{a_2} - s_{26}^p \tag{4.15}$$

and a_1 and a_2 are solutions of the following characteristic equation:

$$s_{11}^p a^4 - 2s_{16}^p a^3 + (2s_{16}^p + s_{44}^p)a^2 - 2s_{26}^p a + s_{22}^p = 0 \tag{4.16}$$

with :

$$s_{ij}^p = s_{ij} - \frac{s_{i3}s_{3j}}{s_{33}} \tag{4.17}$$

The crack is loaded under mode I and the analysis is made in the framework of plane strain conditions. One of the important considerations in MD simulations is the applied strain rate. Some studies [Horstemeyer et al., 2001, Warner et al., 2007, Zhang and Ghosh, 2013] attempted to capture the effect of the strain rate on crack-tip processes. Various studies such as the ones of Zhang *et al.* [Zhang and Ghosh, 2013] suggested that for strain rates less or equal to 10^8 s^{-1}, the stress–strain response tends toward a stabilized quasi-static response. Due to time limitations, previous MD studies used short fatigue period. This can lead to high stresses and can introduce a bias In this investigation, taking into account the computational time, a period of $\Delta t = 500\,\text{ps}$ is applied. For this period, the preliminary tests show that the dislocation structures were

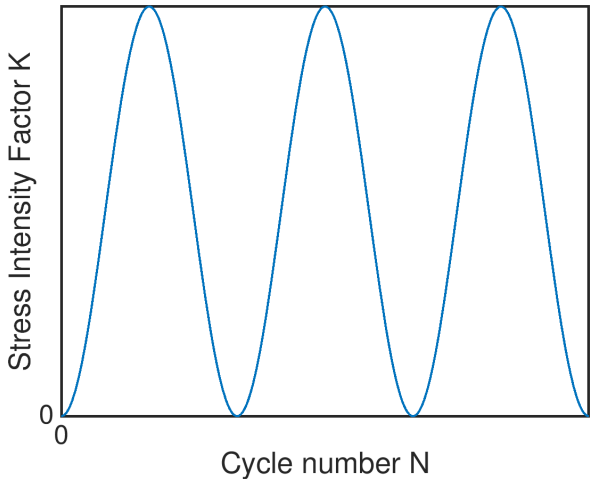

Figure 4-3: Loading geometry : waveform. The loading vary each cycle from 0 to a maximum loading, The minimum load is $\mathrm{K_{min}} = 0$ ($\mathrm{R} = 0$).

almost the same as those observed at higher periods (1 ns and 2 ns). The loading evolution is displayed on Fig. 4-3. As can be noticed in Fig. 4-3, the cyclic loading evolution has a waveform varying from 0 to a maximum load K_{max}. Therefore, the stress intensity factor during one loading cycle can be computed via Equation 4.18:

$$K = K_{max}\left(1 - \cos\left(\frac{2 \times \pi \times dt \times N_{st}}{\Delta t}\right)\right) \tag{4.18}$$

dt is the time step duration ($dt = 1 \times 10^{-15}$ s), N_{st} the number of steps and Δt is the period duration.

Except where otherwise mentioned, the loading ratio in the following is set to 0, meaning that the minimum load value is always equal to 0 ($K_{min} = 0\,\mathrm{MPa}\sqrt{\mathrm{m}}$).

4.2.3.1 Simulation process

The simulation boxes are loaded under various stress intensity factor levels according the following procedure. After the simulation box is generated, a conjugate gradient is applied to minimize the total energy of the system by adjusting atomic positions at $0\,\mathrm{K}$. Then, initial velocities are randomly assigned to each atom with a Gaussian distribution to apply a temperature of $300\,\mathrm{K}$. Thereafter, isobaric-isothermal relaxation is run during $10\,\mathrm{ps}$ at 0 GPa using Parrinello-Rahman algorithm while maintaining temperature at $300\,\mathrm{K}$ with the Nosé-Hoover thermostat. Subsequently, the mechanical displacement field is imposed on the atoms embedded in a layer of 10 Å ($\approx 2 \times r_c$, with r_c the cut-off radius of the interatomic potential) at the boundaries perpendicular to the x and y directions of the simulation box. Depending on the applied maximum loading, the boundary atoms are displaced according to the LEFM displacement field in the x and y directions. The dynamics of these boundary atoms is frozen. Mean-

while, the positions of the inner atoms are updated by integrating the motion equations of the Newtonian dynamics under canonical ensemble.

4.2.4 Post-processing

The visualization of the simulation snapshots is made by the means of the Open Visualization Tool (OVITO) developed by Stukowski [Stukowski, 2009]. In this study, the Common Neighbor Analysis (CNA) is used to identify stacking faults. Indeed, this algorithm is used to identify atoms in particular environment such as FCC (face centered cubic), BCC (Body centered cubic), HCP (Hexagonal close-packed) or icosahedral [Faken and Jónsson, 1994]. The CNA analyzes requires a cut-off radius and can be sensitive to it. This cut-off depends on the crystal structure. For FCC crystals, which are of interest in this paper, the cutoff radius is:

$$R_c = \frac{a_0}{2}\left(\frac{\sqrt{2}}{2} + 1\right) \tag{4.19}$$

with a_0 the lattice parameter of the material considered. Dislocation lines identification is made possible by the dislocation extraction algorithm (DXA). Proposed by Stukowski *et al.* [Stukowski and Albe, 2010, Stukowski et al., 2012], it provides a robust method for identifying dislocation lines within a crystal. DXA can identify dislocations lines, their type (edge or screw), length and Burgers vector. It can also distinguish twin boundary from intrinsic stacking fault. Other metrics such as microrotation metric proposed by Tucker and co-workers [Tucker et al., 2011, Tucker et al., 2012] can also classify these stacking faults and defect types as well.

The atomic stress tensor is computed using the virial theorem. According to this theorem, the stresses in a physical system can be computed by the relation:

$$\sigma_{ij} = \frac{1}{V}\left(-\sum_{i}^{N}(m\mathbf{v_i}\otimes\mathbf{v}_i) + \frac{1}{2}\sum_{i,j\neq i}^{N}\mathbf{f}_{ij}\otimes\mathbf{r}_{ij}\right) \tag{4.20}$$

where V is the volume of a cell containing a large number of atoms; $\vec{f_{ij}}$ is the interatomic force applied by an atom j on an atom i; $\mathbf{r}_{ij}$ ($\mathbf{r}_{ij} = \mathbf{r}_j - \mathbf{r}_i$) is the relative position; and $\mathbf{v}_i$ denotes the velocity of an atom i.

To characterize the path of moving dislocations during cyclic loading, the slip vector is computed. This vector provides information on how much slip happens in crystals. The slip vector was originally outlined by Zimmerman *et al.* [Zimmerman et al., 2001] and defined as:

$$\mathbf{S}_i = \sum_{j\neq i}^{n_{nn}}(\mathbf{x_{ij}(t)} - \mathbf{X_{ij}(0)}) \tag{4.21}$$

with n_{nn} the number of nearest neighbors to atom i; $\mathbf{x}_{ij}(t)$ and $\mathbf{X}_{ij}(0)$ are the

vector differences of atoms i and j current and reference positions, respectively. The reference configuration is the arrangement of atomic positions associated with zero mechanical stresses. As noted in [Zimmerman et al., 2001], the Burgers vector can be estimated from the slip vector by dividing the slip vector by the number of slipped neighbors across the plane. In the case of FCC crystals, this number is equal to 3. To evaluate the slip amount and the plastic irreversibility in the crystal, we computed the "plastic slip distance" defined by:

$$d_{slip} = \sum_{i}^{N_s} \|S_i\| = \sum_{i}^{N_s} \left\| \sum_{j \neq i}^{n_{nn}} (\mathbf{x}_{ij}(t) - \mathbf{X}_{ij}(0)) \right\| \tag{4.22}$$

where N_s is the number of slipped atoms.

4.3 Dislocation emission from crack-tip and plastic deformation localization

4.3.1 Dislocation nucleation from crack-tip

At the beginning of the loading, the system undergoes an elastic deformation. The stresses at the crack-tip increase up to a critical stress intensity factor above which plastic deformation occurs by dislocation emission and gliding or by mechanical twinning. The emission of crack-tip dislocations has been the subject of some investigations in the literature, including the investigations of Rice [Rice, 1992, Rice and Beltz, 1994, Rice and Thomson, 1974] and more recently by [Andric and Curtin, 2017, Warner and Curtin, 2009, Yamakov et al., 2014]. The investigations of Rice allow the determination of the exact solution for the dislocation emission criterion at crack-tip when the crack is loaded under mode II. Under mode I loading, an approximate solution of the emission criterion of the dislocation based on the concept of effective shear stress intensity factor is given by Rice [Rice, 1992]. Indeed, Rice's theory suggests that under mode II loading, the J-integral along crack face contour can be computed by:

$$J = -\int_0^{\infty} \tau \frac{\partial \delta}{\partial x} dx = \int_0^{\delta_{tip}} \tau d\delta \equiv \Phi(\delta_{tip}) \tag{4.23}$$

where $\tau = \tau(\delta)$ is the shear stress, $\Phi(\delta)$ is the energy associated with slip discontinuity δ. Since the J-integral far from the crack-tip is given by:

$$J = G = \frac{(1-\nu)K_{II}^2}{2\mu_{slip}}, \tag{4.24}$$

where G denotes the energy release rate and μ_{slip} the shear modulus defined by $\mu_{slip} = (C_{11} - C_{12} + C_{44})/3$ on a $\{1\,1\,1\}$ plane.

The path independence of the J-integral leads to :

$$G \equiv \frac{(1-\nu)K_{II}^2}{2\mu_{slip}} = \Phi(\delta_{tip}). \tag{4.25}$$

According to Rice [Rice, 1992], the dislocation emission at crack-tip occurs when the slip discontinuity at crack-tip, δ_{tip}, reaches a critical position at which the energy associated with the slip discontinuity reaches the unstable stacking fault energy γ_{us}. Therefore, the critical Stress Intensity Factor (SIF) required for dislocation emission at crack-tip reads:

$$K_{IIe} = \sqrt{\frac{2\mu_{slip}\gamma_{usf}}{1-\nu}} \tag{4.26}$$

For mode I loading, Rice assumes the same slip profile along the slip plane as in mode II. Thanks to the concept of effective shear SIF [Rice, 1992], and within isotropic elasticity, one can estimate the mode I criterion for crack-tip dislocation emission as follows:

$$K_{Ie} = \sqrt{\frac{2\mu_{slip}\gamma_{usf}}{1-\nu}} \frac{1}{\cos^2\left(\frac{\theta}{2}\right)\sin\left(\frac{\theta}{2}\right)} \tag{4.27}$$

with θ, the slip plane angle.

Later, Andric and Curtin [Andric and Curtin, 2017] proposed a modified formulation based on the idea that the dislocation emission from crack-tip during mode I loading is accompanied by a surface step creation. Andric and Curtin recompute the energy release rate and proposed the following formulation:

$$G_{Ie} = 0.145\gamma_s + 0.5\gamma_{usf}, \gamma_s > 3.45\gamma_{usf} \tag{4.28}$$

$$G_{Ie} = \gamma_{usf}, \gamma_s < 3.45\gamma_{usf} \tag{4.29}$$

where γ_s denotes the surface energy. Therefore, the previous formulation for the critical SIF for dislocation nucleation from crack-tip for a mode I loading becomes:

$$K_{Ie} = \sqrt{\frac{2\mu_{slip}G_{Ie}}{1-\nu}} \frac{1}{\cos^2(\theta/2)\sin(\theta/2)} \tag{4.30}$$

In our investigation, we compute K_{Ie} for the different crack orientations described in section 4.2.2 from atomistic simulation and compare them with those derived from Rice [Rice, 1992] and Andric and Curtin [Andric and Curtin, 2017] criteria. The dislocation emission is determined with the help of the DXA analysis of the OVITO tools. When dislocation appears, the corresponding K_{Ie} is recorded.

Fig. 4-4 shows the predictions of the MD simulations and the predictions of

the Rice [Rice, 1992] and Andric and Curtin [Andric and Curtin, 2017] criteria. As can be noticed in Fig. 4-4, the predictions of the MD simulations are in fair agreement with the predictions of the different criteria, in particular with the improved criterion of Andric and Curtin [Andric and Curtin, 2017]. Apart from orientations A1 and B1 for which strong deviations are observed between MD simulations and different criteria, the agreement are reasonable for other crack orientations. For example, the deviation for orientations A1 and B1 from Andric-Curtin criterion is estimated at about 24.7% and 17.7% respectively. For orientation C1, the deviation is 1.6%. For other orientations, the deviations varies between 10% and 11.5%.

The strong deviations for orientations A1 and B1 can be explained on the one hand by the fact that, the original Rice works considered a crack configuration in which the crack plane intersect the slip plane, therefore, the crack front lie in the slip plane In this study for orientations A1 and B1, the crack front ($[0\,0\,1]$ for orientation A1 and $[0\,0\,\bar{1}]$ for orientation B1) does not lie in the slip plane. On the other hand, the different formula used in this study are drawn in the framework of isotropic elasticity. Taking into account the anisotropic nature of the crystal elasticity should enhance the predictions.

Based on our computations, for the same loading axis, the critical SIF for dislocation emission at the crack-tip varies according to the crack front direction. For instance, for orientations A1, A2 and A3 with the same loading axis ($\langle 1\,0\,0\rangle$), the critical values of SIF are numerically estimated to be about 0.752, 0.633 and 0.515 $\mathrm{MPa}\sqrt{\mathrm{m}}$ respectively. For orientations B1 and B2 both having a $\langle 1\,1\,0\rangle$ axis as the "macroscopic" loading axis, the critical SIF values are 0.692 $\mathrm{MPa}\sqrt{\mathrm{m}}$ and 0.515 $\mathrm{MPa}\sqrt{\mathrm{m}}$, respectively. Finally, the critical SIF for orientations C1 and C2 (with a $\langle 1\,1\,1\rangle$ as load axis) are estimated to be about 0.516 $\mathrm{MPa}\sqrt{\mathrm{m}}$ and 0.47 $\mathrm{MPa}\sqrt{\mathrm{m}}$, respectively.

Table 4.2: Deviations between MD predictions and Rice and Andric and Curtin criteria (A-C)

Orientation	A1	A2	A3	B1	B2	C1	C2
From Rice crit.	39.5%	28.2%	11.7%	33.0%	9.7%	16.9%	8.7%
From A-C. crit.	24.7%	10.6%	10.0%	17.7%	10.5%	1.6%	11.5%

4.3.2 Strain localization at crack-tip

During cyclic loading, and even after the first loading cycle, all slip planes near crack-tip experienced plastic slip whatever the orientation. But depending on the orientation, the plastic activity could be reduced on some slip planes. Theoretically, for a crystal without crack with a stress axis of the $\langle 1\,0\,0\rangle$ type (homogeneous loading), 8 active slip systems with a Schmid factor of about 0.408 (the resolved shear stress of the four other systems are equal to zero) are expected

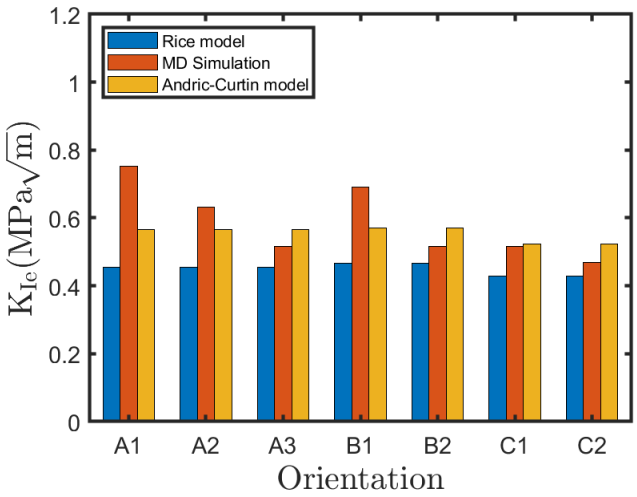

Figure 4-4: Critical stress intensity factors for dislocation emission from crack-tip for different crack orientations in copper at RT

whereas for crystals loaded along $\langle 1\,1\,0\rangle$, only 4 active systems with the same Schmid factor (0.408) are expected. For a crystal loaded along the $\langle 1\,1\,1\rangle$ axis, one expects 6 active systems with a Schmid factor of 0.272. However, at a crack-tip, because of the complex mechanical fields which prevail there before the emission of dislocations, many and strong deviations from the previous ideal symmetric activation may be expected. Indeed, even for a homogeneous macroscopic loading, the stress fields at the crack-tip are strongly heterogeneous. Equation 4.31 provides the stress fields at the crack-tip in a an anisotropic body [Sih et al., 1965] before dislocation emission:

$$\begin{cases} \sigma_{xx} = \dfrac{K_I}{\sqrt{2\pi r}} \Re\left[\dfrac{a_1 a_2}{a_1 - a_2}\left(\dfrac{a_2}{\sqrt{\cos\theta + a_2 \sin\theta}} - \dfrac{a_1}{\sqrt{\cos\theta + a_1 \sin\theta}}\right)\right] \\ \sigma_{yy} = \dfrac{K_I}{\sqrt{2\pi r}} \Re\left[\dfrac{1}{a_1 - a_2}\left(\dfrac{a_1}{\sqrt{\cos\theta + a_2 \sin\theta}} - \dfrac{a_2}{\sqrt{\cos\theta + a_1 \sin\theta}}\right)\right] \\ \sigma_{xy} = \dfrac{K_I}{\sqrt{2\pi r}} \Re\left[\dfrac{a_1 a_2}{a_1 - a_2}\left(\dfrac{1}{\sqrt{\cos\theta + a_1 \sin\theta}} - \dfrac{1}{\sqrt{\cos\theta + a_2 \sin\theta}}\right)\right] \\ \sigma_{zz} = \dfrac{1}{s_{33}}\left(s_{13}\sigma_{xx} + s_{23}\sigma_{yy} + s_{26}\sigma_{xy}\right) \\ \sigma_{xz} = \sigma_{yz} = 0 \end{cases} \tag{4.31}$$

With dislocation emission and interactions, additional internal stresses with relaxation can occur. The emission and gliding of dislocations induce strain localization near crack-tip zones that will be analyzed in the next subsections. To study the slip traces, the equivalent von Mises shear strain was computed after the first cycle and compared to slip trace patterns available in the literature for

different crack configurations.

4.3.2.1 Crack configurations A1, A2, A3

Fig. 4-5, Fig. 4-6 and Fig. 4-7 show the strain localization pattern at crack-tip from MD simulation of orientation A1, A2 and A3. In Fig. 4-5, one can observe the comparison between the slip traces predicted by MD simulation (Fig. 4-5a) and experimental study (Fig. 4-5b) carried out by Fouriot *et al.* [Flouriot et al., 2003] for a similar crack configuration. Fig. 4-6 displays the comparison between the strain localization patterns obtained from MD computations (Fig. 4-6a) and the experimentally observed strain localization patterns (Fig. 4-6b, [Crone and Shield, 2001]). As observed, the slip traces obtained by MD simulation agree well with the SEM micrographs. Slip traces observed at surface (a V-shape as observed experimentally by Fouriot *et al.* [Flouriot et al., 2003] and Neumann *et al.* [Neumann, 1974]) are inclined at about $\pm 45°$ to the crack axis (axis [OX), Fig. 2-1) as found experimentally ($39-47°$). The slip traces inclined at $+45°$ correspond to the $(1\,\bar{1}\,\bar{1})$ and the $(1\,\bar{1}\,1)$ planes while traces inclined at $-45°$ correspond to the $(1\,1\,\bar{1})$ and the $(1\,1\,1)$ slip planes. For crack configuration A2, two sets of slip traces are observed from both MD simulations and experiments [Crone and Shield, 2001], as depicted in Fig. 4-6a and Fig. 4-6b. The slip traces of the first type are orientated at $0°$ (or $180°$) with respect to the crack axis and correspond to the $(\bar{1}\,\bar{1}\,\bar{1})$ and the $(1\,\bar{1}\,\bar{1})$ planes. In contrast, traces observed at $+54°$ (respectively $-54°$ or $125°$) correspond to the $(\bar{1}\,\bar{1}\,1)$ (respectively the $(1\,\bar{1}\,1)$) planes. The crack configuration A3 exhibits two types of slip traces: at $\pm 25°$ and $\pm 54°$. Traces inclined at $+25°$ (respectively at $-25°$ correspond to the $(\bar{1}\,1\,1)$ plane (respectively the $(1\,1\,1)$ plane) while traces oriented at $+54°$ (respectively $-54°$) correspond to the $(\bar{1}\,\bar{1}\,1)$ plane (respectively the $(1\,\bar{1}\,1)$ plane).

4.3.2.2 Crack configurations B1 and B2

Strain localization patterns of configurations B1 and B2 are depicted in Fig. 4-8 and Fig. 4-9 respectively. Fig. 4-8 and Fig. 4-9 show the localization patterns around the crack-tip for respectively configurations B1 and B2 and the comparison with experimentally observed slip localization. For crack configuration B1, the localization patterns predicted by MD simulation (Fig. 4-8a) are in good agreement with experimental pattern observed by Vinogradov *et al.* [Vinogradov et al., 1995] (Fig. 4-8b). Two type of traces are observed: at $0°$ (corresponding to the $(\bar{1}\,\bar{1}\,1)$ and the $(\bar{1}\,\bar{1}\,\bar{1})$ planes) and at $\pm 90°$ (corresponding to the $(\bar{1}\,1\,\bar{1})$ and the $(\bar{1}\,1\,1)$ planes) with respect to the crack axis. For crack configuration B2, one can also notice the good agreement between MD simulations (Fig. 4-9a) and experiments carried out by Flouriot *et al.* [Flouriot et al., 2003] (Fig. 4-9b). Traces inclined at $35°$ correspond to the $(1\,\bar{1}\,\bar{1})$ slip plane and the ones at $-35°$ correspond to the $(\bar{1}\,1\,\bar{1})$ plane. The two other slip planes $(1\,1\,\bar{1})$ and $(1\,1\,1)$ are represented by traces oriented at $0°$ or $180°$ with respect to crack axis.

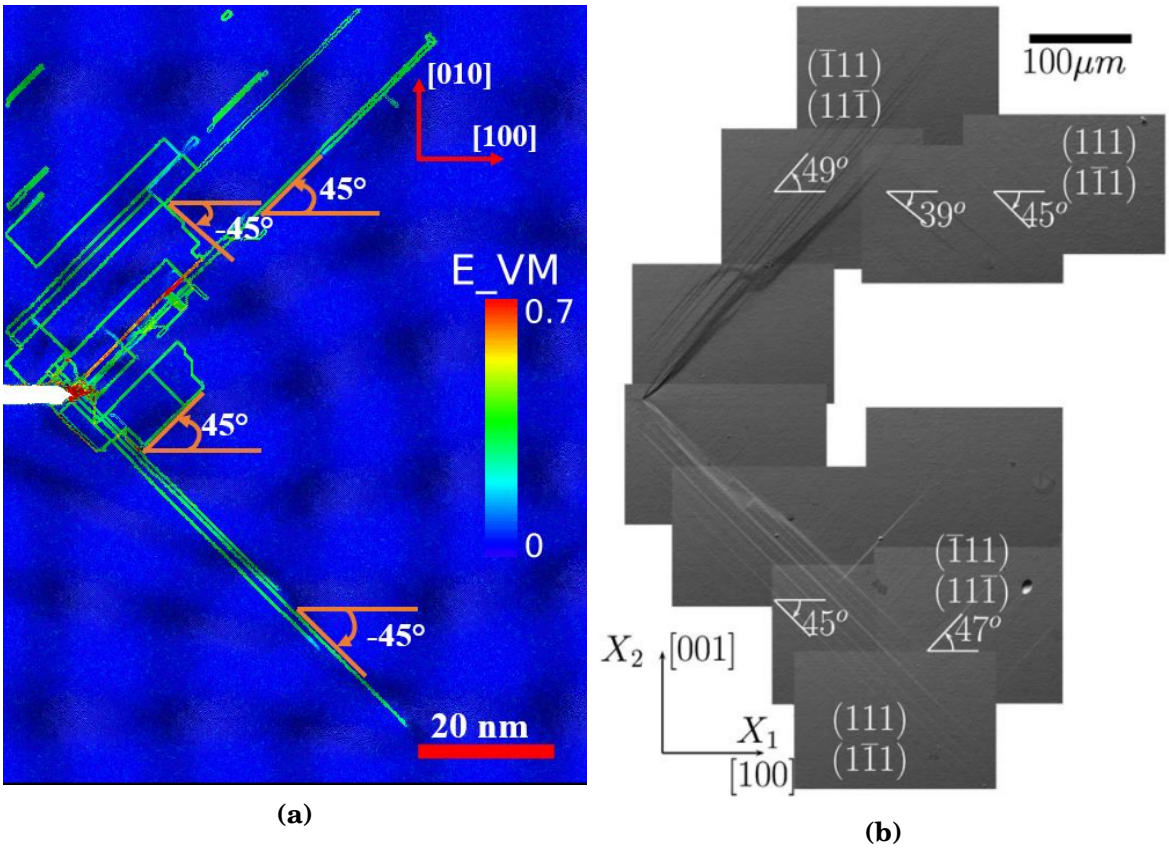

Figure 4-5: Slip traces pattern around crack-tip (a) MD simulations for crack configuration A1 (010)[001] showing the slip traces inclined at an angle of $\pm 45°$ to the crack axis (b) SEM micrograph of the crack-tip region for (001)[010] crack configuration with identification of slip lines inclined to $\pm 39 - 47°$ with respect to the crack axis [Flouriot et al., 2003].

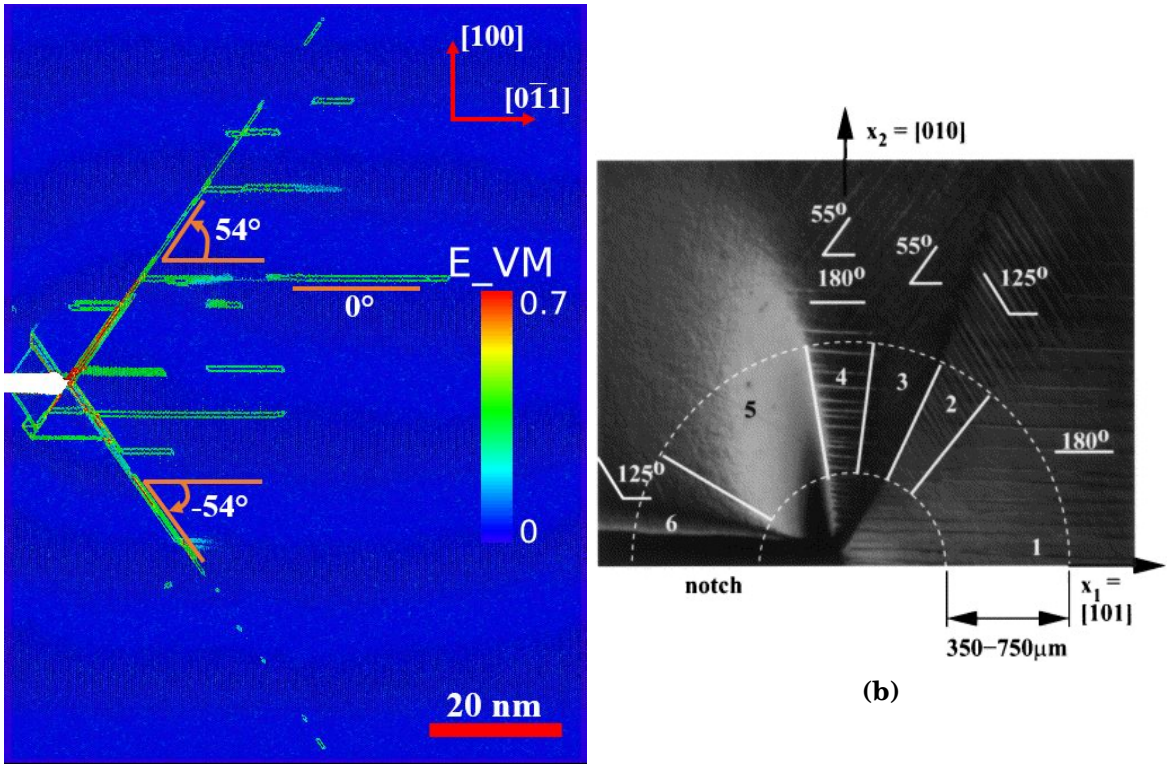

Figure 4-6: Slip traces patterns around crack-tip (a) MD simulation of crack configuration A2 $(1\,0\,0)[0\,1\,1]$ showing in $(0\,1\,1)$ plane the slip traces inclined at an angle of $\pm 54°$ and $0°$ (or $180°$) with respect to the crack axis. (b) Experimental observations of strain localization pattern for a similar crack orientation $((0\,1\,0)[1\,0\,1]$ [Crone and Shield, 2001]. The slip traces inclined at $125°$ with respect to the crack axis correspond to those inclined at $-54°$ obtained from MD simulations.

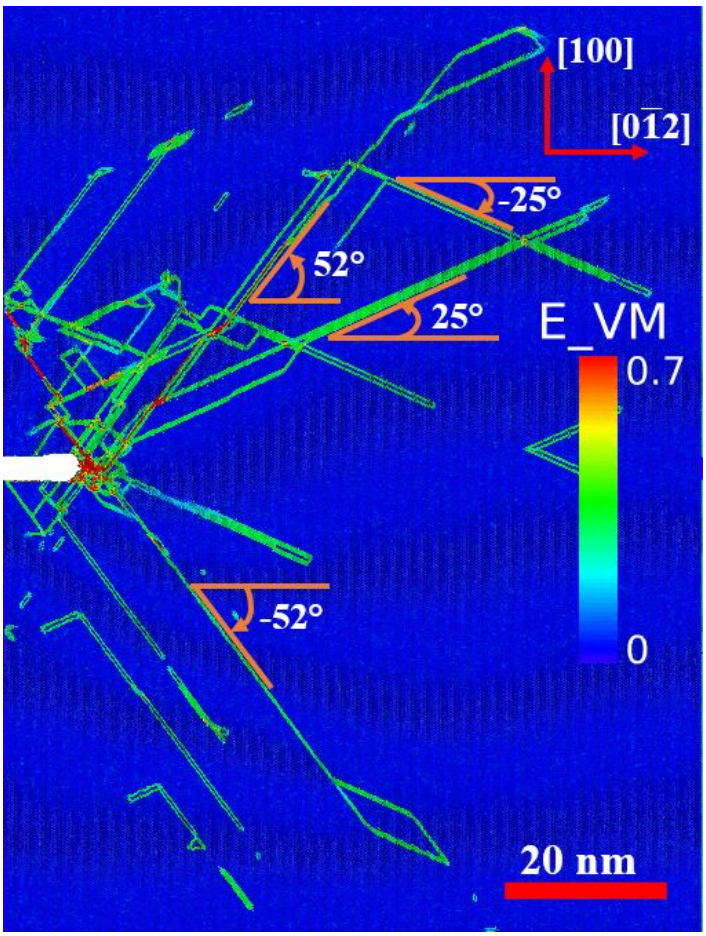

Figure 4-7: Slip traces pattern for crack configuration A3 $(1\,0\,0)[0\,2\,1]$ showing slip traces in $(0\,2\,1)$ plane inclined at $\pm 25°$ and $\pm 52°$ with respect to the crack axis.

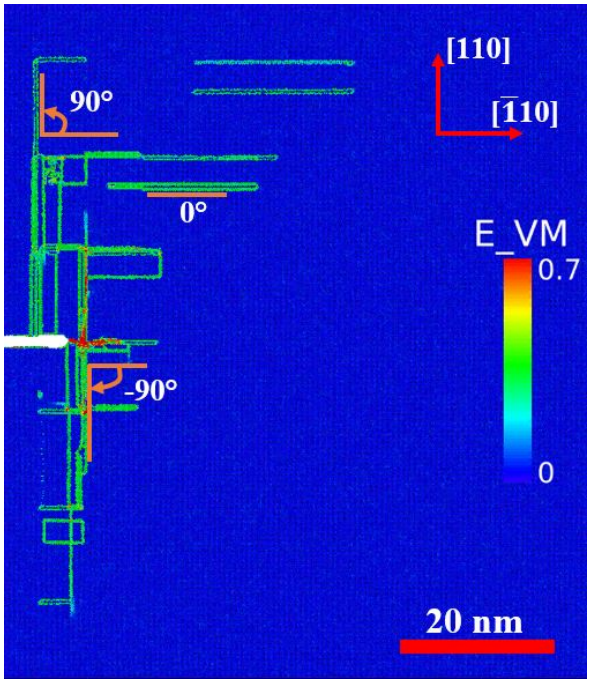

(a)

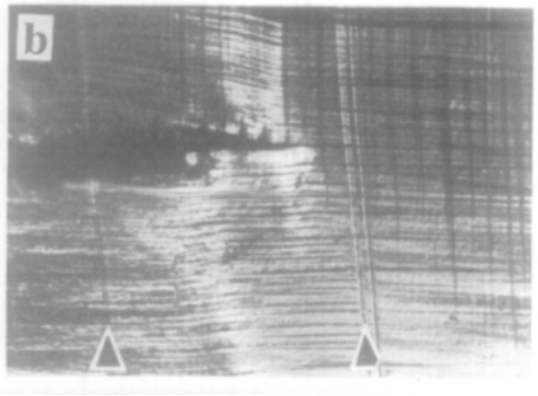

(b)

Figure 4-8: Strain localization aroun the crack-tip (a) MD simulation for crack configuration B1 $(1\,1\,0)[0\,0\,\bar{1}]$ showing the slip traces inclined at an angle of $0°$ and $\pm 90°$ to the axis of the crack in the $(0\,0\,\bar{1})$ plane. (b) SEM micrograph of the crack-tip region for $(1\,1\,0)[0\,0\,\bar{1}]$ crack orientation with identification of slip traces inclined at about $0°$ and $\pm 90°$ with respect to the crack axis [Vinogradov et al., 1995].

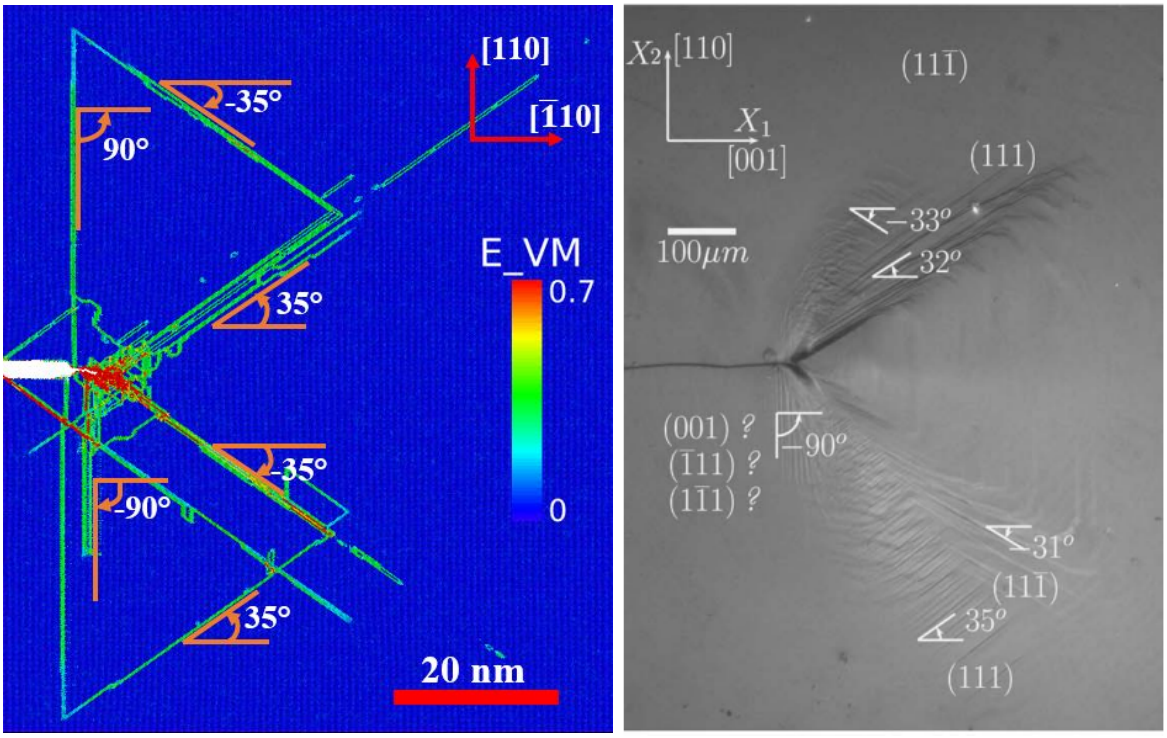

(a) **(b)**

Figure 4-9: Strain localization around crack-tip (a) MD simulation of crack orientation B2 $(\bar{1}\,1\,0)[1\,1\,0]$ showing the slip traces inclined at an angle of $\pm 35°$ and $\pm 90°$ to the crack axis in the $(1\,0\,0)$ plane. (b) SEM micrograph of the crack-tip region for $(1\,1\,0)[\bar{1}\,1\,0]$ crack configuration with identification of slip traces inclined to about $\pm 35°$ and $\pm 90°$ to the crack axis [Flouriot et al., 2003].

4.3.2.3 Crack orientation C1 and C2

The strain localization patterns for configurations C1 and C2 are displayed in Fig. 4-10. Fig. 4-10a shows slip traces oriented at $0°$ and $\pm 70°$. The $0°$ lines correspond to the $(\bar{1}\,\bar{1}\,1)$ and the $(1\,1\,1)$ planes while the $+70°$ (and $-70°$ respectively) correspond to the $(\bar{1}\,1\,\bar{1})$ plane (respectively the $(\bar{1}\,1\,1)$ plane). Fig. 4-10b displays the plastic patterns observed around crack-tip of C2 configuration $(1\,1\,1)[1\,\bar{1}\,0]$. Three sets of slip traces are observed: traces oriented at $0°$ corresponding to the $(1\,1\,1)$ planes, $58°$ corresponding to the $(\bar{1}\,1\,\bar{1})$ and the $(1\,\bar{1}\,\bar{1})$ planes and finally traces at $70°$ corresponding to the $(1\,1\,\bar{1})$ one.

4.4 Plastic deformation mechanisms and lattice defects

4.4.1 Plastic deformation mechanisms

The onset of plasticity at crack-tip is accompanied by the emission of dislocations. The emitted dislocations are Shockley partials. The gliding of a Shockley partial causes a modification of the stacking of the atomic planes. Usually, the issuance of a first Shockley partial called *leading partial* will often be followed by the issuance of a second partial called *trailing partial* on the same slip plane. The latter rearranges the stack of atomic planes during its glide reconstructing a perfect but slipped FCC lattice with a Burgers vector of the type $1/2\langle 1\,1\,0\rangle$. Therefore, slip occurs on different $\{1\,1\,1\}\langle 1\,1\,0\rangle$ slip systems.

The deformation microtwinning occurs when the leading partial is followed by another partial of the same Burgers vector on the adjacent plane. This microtwin is likely to expand under the effect of the emission of other twin partials on adjacent planes. The formation of deformation twins in metals is often associated with the low Stacking Fault Energy (SFE) of the metal. It is generally admitted that the lower the stacking fault energy of the metal, the more likely plastic deformation occurs by mechanical twinning. For example, experimental studies have shown the deformation twining and/or crack-tip twining in Silver [English and Chin, 1965]. However, some experimental observations showed that deformation twinning is possible at the crack-tip in some cases even in materials with high SFE such as iridium ([Fortes and Ralph, 1970, Adamesku et al., 1994]) provided that the stress concentration is sufficient and that the crystal orientation is favorable. This prompted Tadmore and Hai [Tadmor and Hai, 2003] to propose a deformation twinning criterion that predicts crack-tip deformation twinning in all FCC metals (regardless of SFE) for a class of ductile orientations.

In this study, deformation twinning is observed for some crack configurations (A2, B2 and C2). In these cases, during loading half cycle, association between dislocation slip process and deformation twinning process occurs with

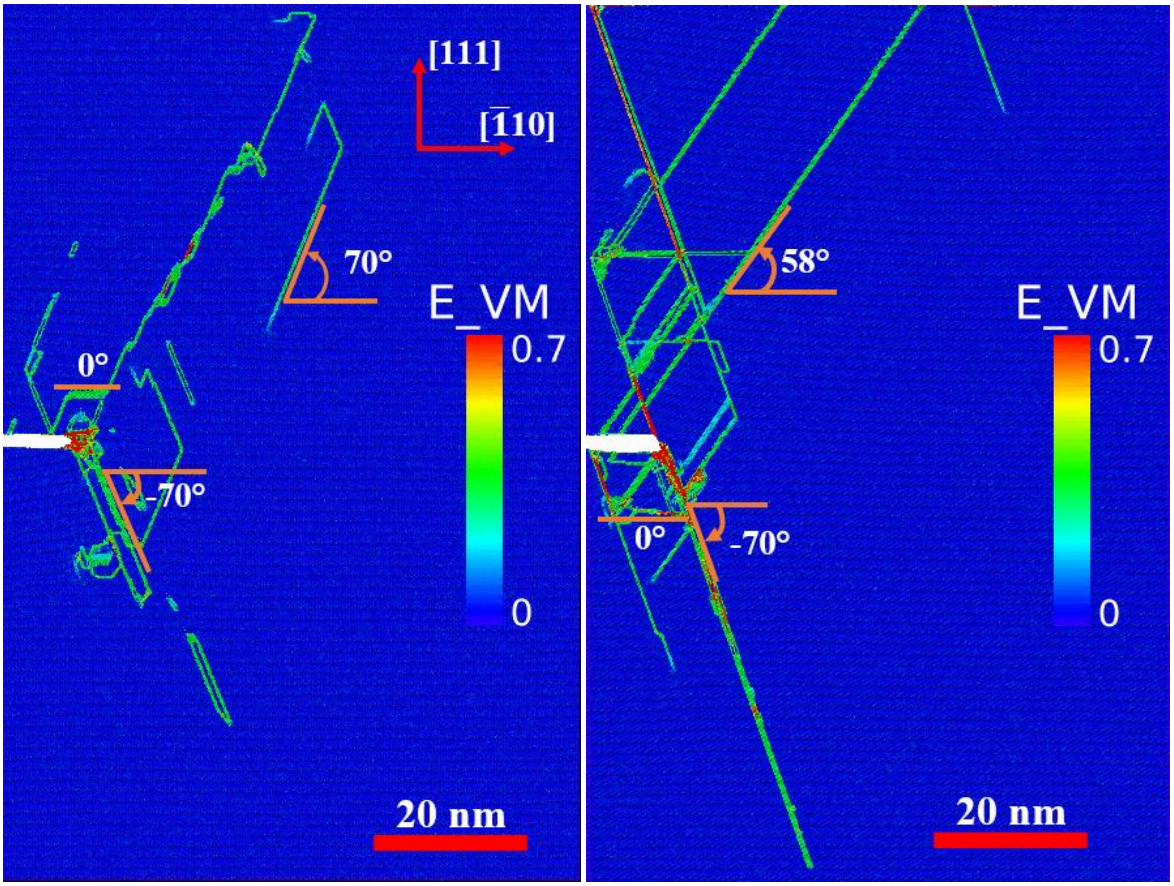

(a) **(b)**

Figure 4-10: Strain localization patterns around crack-tip (a) MD simulation for crack configuration C1 $(1\,1\,1)[1\,1\,\bar{2}]$ showing the lines inclined at an angle of 0° and $\pm 70^\circ$ with respect to the crack axis viewed in the $(1\,1\,\bar{2})$ (b) MD simulation of crack orientation C1 $(1\,1\,1)[1\,\bar{1}\,0]$ showing the lines inclined at an angle of 0° 58° and -70° with respect to the crack axis viewed in the $(1\,\bar{1}\,0)$.

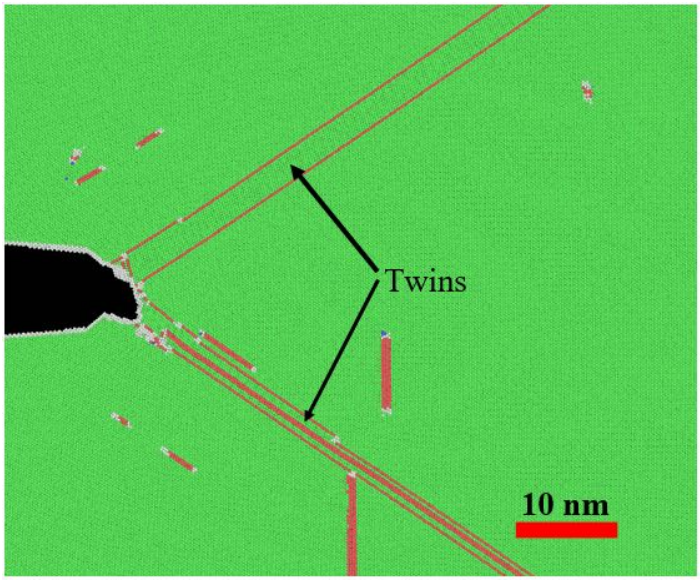

Figure 4-11: Example of deformation twining observed in MD simulations for crack configuration B2 $(1\,1\,0)$[-110]. The red lines are the twin boundaries

a domination of dislocation slip process. Fig. 4-11 shows an example of deformation twining observed during the first loading cycle for crack orientation B2. These three crack configurations have in common the initial crack front parallel to a $\langle 0\,1\,1 \rangle$ direction. Both mechanisms occur simultaneously during cyclic loading even if slip process dominates. However, after unloading, the twins formed during the loading half cycle disappear. As cyclic loading proceeds, a twinning-detwinning process takes place and the amount of twins decreases gradually, giving way to dislocation slip processes which become the only plastic deformation mechanism. This confirms the transition from crack-tip twinning at short times to dislocation slip process at long times reported by Warner *et al.* [Warner et al., 2007] and therefore, it is thought that deformation twinning observed in crack configurations A2, B2 and C2 during the first cycles, is an artefact due to the high strain rates (also shown by [Warner et al., 2007, Baker and Warner, 2012]), combined with initially perfect crack-tip conditions: no initial defects ([Zepeda-Ruiz et al., 2017]) and geometry [Tadmor and Hai, 2003] . For other orientations (orientation A1, A3, B1 and C1), only dislocation slip process was observed as unique plastic deformation mechanism. Table 4.3 summarizes the different plastic deformation mechanisms observed at the crack-tip as a function of crack configuration. One can notice in Table 4.3 that slip is a common mechanism for all crack configurations investigated while twinning appear for specific crack configurations with $\langle 1\,1\,0 \rangle$.

One of the consequences of the plastic deformation at crack-tip, is the so-called Crack-Tip Opening Displacement (CTOD). The accommodation of plastic deformation by dislocation emission and gliding or by twinning leads to a certain displacement at crack-tip that can be characterized by the CTOD. This quantity

Table 4.3: Plastic deformation mechanisms

Crack orientation	Plastic deformation mechanism
A1	dislocation slip
A2	dislocation slip
A3	dislocation slip and mechanical twinning
B1	dislocation slip
B2	dislocation slip and mechanical twinning
C1	dislocation slip
C2	dislocation slip and mechanical twinning

measures the resistance of a material to crack blunting and partially to propagation. In this MD investigation, we compute the evolution of CTOD at the first cycle during the loading half cycle. The procedure for defining the CTOD is shown in Fig. 4-12. Fig. 4-13a shows the evolution of the CTOD for different crack configurations as a function of the applied SIF.

Generally speaking, two regimes can be observed in the evolution of CTOD (Fig. 4-13b). The first regime is characterized by a slow evolution of the CTOD as a function of the applied SIF. This regime, which corresponds indeed to the elastic regime, is followed by another regime, after dislocations emission, which shows the acceleration in the the CTOD evolution (Fig. 4-13b). The acceleration of the CTOD increase is due to the onset of plastic deformation following the emission of dislocations and/or mechanical twinning. Furthermore, the CTOD values depend on the crack configuration. For example, it is noted that the value of the CTOD is the lowest in the case of B1 and C1 crack configurations while it is the highest for crack configuration A3. The amount of plastic slip and the plastic deformation mechanism can explain this differences. Indeed, apart from the A3 configuration for which the only plastic deformation mechanism observed is dislocation slip, it is observed that for the crack configurations with the same loading axis, the CTOD tends to be highest in cases where the accommodation of plastic deformation is ensured by both the dislocation slip and the mechanical twinning. Thus, it can be noted that the computed CTOD of crack configurations A2 and B2, are respectively slightly higher than those computed for crack configurations A1 and B1. Nevertheless, crack configurations C1 and C2 exhibit almost the same value of CTOD. The particular case of orientation A3 can be explained by the quantity of dislocations emitted at the crack-tip. It is notably higher in the case of orientation A3 as shown in Fig. 4-15.

During cyclic loading, dislocations causing crack blunting increases within the crystal. Different interactions involving dislocations and point defects occurs. The following section focuses on the nature of crack-tip dislocation microstructures and dislocation interactions.

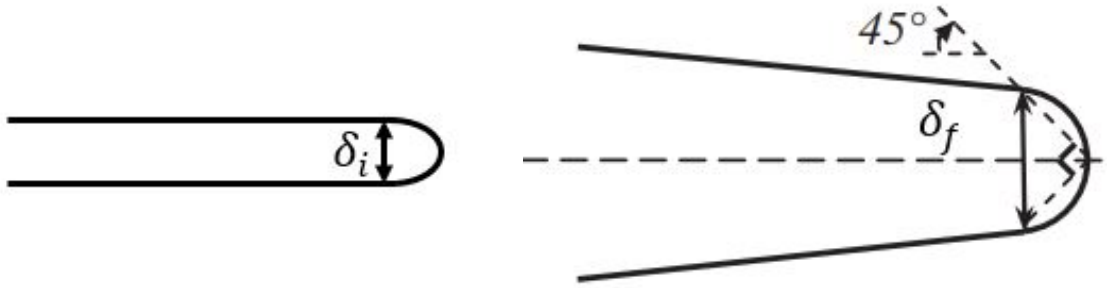

(a) **(b)**

Figure 4-12: Undeformed (a) and deformed (b) crack showing the procedure for defining the CTOD ($\mathbf{CTOD} = \delta_\mathbf{f} - \delta_\mathbf{i}$) with δ_i and δ_f the initial and final opening at crack-tip

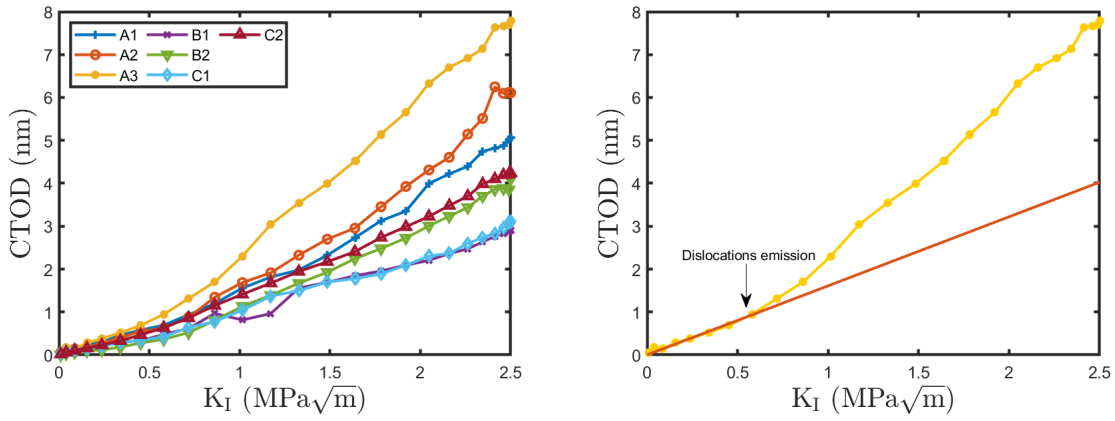

(a) **(b)**

Figure 4-13: (a) Evolution of CTOD during de first loading half cycle for different crack configurations. (b) Evolution of the CTOD of orientation A3 showing two regimes: a first regime from the beginning of loading until dislocation emission where the CTOD follows the red line and a second regime from dislocation emission and where the CTOD no longer follows the red line

4.4.2 Dislocation structures and lattice defects near crack-tip

During cycling, dislocations emitted from crack-tip are likely to multiply. Therefore, the dislocation density increases as the number of cycles increases as depicted in Fig. 4-15. Transition regime in dislocation density evolution can be pointed ou during the first cycles (1^{st}-5^{th} cycle approximately) . If we consider that the evolution of the dislocation density is almost linear from the 5th cycle, we can estimate the rate of increase in dislocation density. The dislocation density increased at a rate of approximately $10^{14}\ \mathrm{m}^{-2}\mathrm{cycle}^{-1}$ for crack configuration C2, $2\times10^{14}\ \mathrm{m}^{-2}\mathrm{cycle}^{-1}$ for crack configuration C1 and $4\times10^{14}\ \mathrm{m}^{-2}\mathrm{cycle}^{-1}$ for crack configuration A1. This rate is estimated at approximately $5\times10^{14}\ \mathrm{m}^{-2}\mathrm{cycle}^{-1}$ in the case of A2 and B1 crack configurations, while crack configurations A3 and B2 exhibit respectively rates of about $8\times10^{14}\ \mathrm{m}^{-2}\mathrm{cycle}^{-1}$ and $10^{15}\ \mathrm{m}^{-2}\mathrm{cycle}^{-1}$.

Fig. 4-14 shows dislocation microstructures around crack-tip at the 15th cycle for crack configuration A1 loaded at $\Delta K = 2\ \mathrm{MPa}\sqrt{\mathrm{m}}$. We can observe different types of dislocations such as Shockley partials (green lines), stair-rod partials (purple lines), Frank partials (sky blue), Hirth partials (yellow), perfect dislocations (blue lines). It can also be noted that whatever the crack configuration, Shockley partials represent the majority of crack-tip dislocations followed by stair-rod partials, Hirth partials, Frank partials and perfect dislocations. Fig. D-1 (in Appendix D) shows the proportion of each type of dislocation during cyclic loading for different crack configurations. We can observe in this figure a slight decrease in the proportion of Shockley partials and a slight increase in the proportion of stair-rod partials while the proportions of other types of dislocations remain almost constant during cyclic loading. The Shockley partials represent at the first loading cycle about 75% to 85% of the total dislocation density and is established at the 16th cycle at about 65% to 77% of the total dislocation density. The stair-rod partials represent about 20% to 30% of the dislocations at the end of the 16th cycle whereas they represented only about 10% to 20% at the end of the first cycle. The perfect dislocations and the Hirth partials remain between 1% and 3% while the Frank partials represent between 0.5% and 1% even if it is to be noted for the orientation B2 quite important oscillations during the cyclic loading with peaks reaching 2%.

The general trend suggests that, the proportion of Shockley will continue to decrease whereas the stair-rod partials proportion will keep on increasing. It should be noted that among the different types of dislocations observed, only the Shockley partials are mobile. The other types of dislocations resulting from the interactions between dislocations are mostly sessile. This will be discussed in the following later.

The numerous dislocations emitted from crack-tip will glide on different slip systems, meet, repel, attract, and interact. FCC metals such as copper, are characterized by 12 possible easy slip systems. And according to the activated slip systems, different interactions leading to the formation of different dislo-

cation substructures occur. Junctions between slip systems take place if the reaction is energetically favorable. Therefore, different dislocation locks can appear and act as barrier against dislocation forward and reverse slip. An illustration of the complexity of these dislocation substructures is depicted in Fig. 4-14. This figure shows dislocations network in orientation A1 at the end of 15th cycle. One can observe a complex dislocation network in the direct vicinity of the crack-tip made of dislocation tangles and various locks such as Lomer-Cottrell locks, Hirth locks. This complex dislocation network is in agreement with the experimental observations of Dewald *et al.* [Dewald et al., 1990], McEvily and Boettner [McEvily and Boettner, 1963a] Awatani *et al.* [Awatani et al., 1978], who observed a complex dislocation network made of tangles as in this study. Moreover, this complex network differs from the simple array of dislocations used in some models (Pippan *et al.* [Pippan et al., 2011], Riemelmoser *et al.* [Riemelmoser et al., 1997, Riemelmoser et al., 2001]) to explain the mechanisms of fatigue crack propagation.

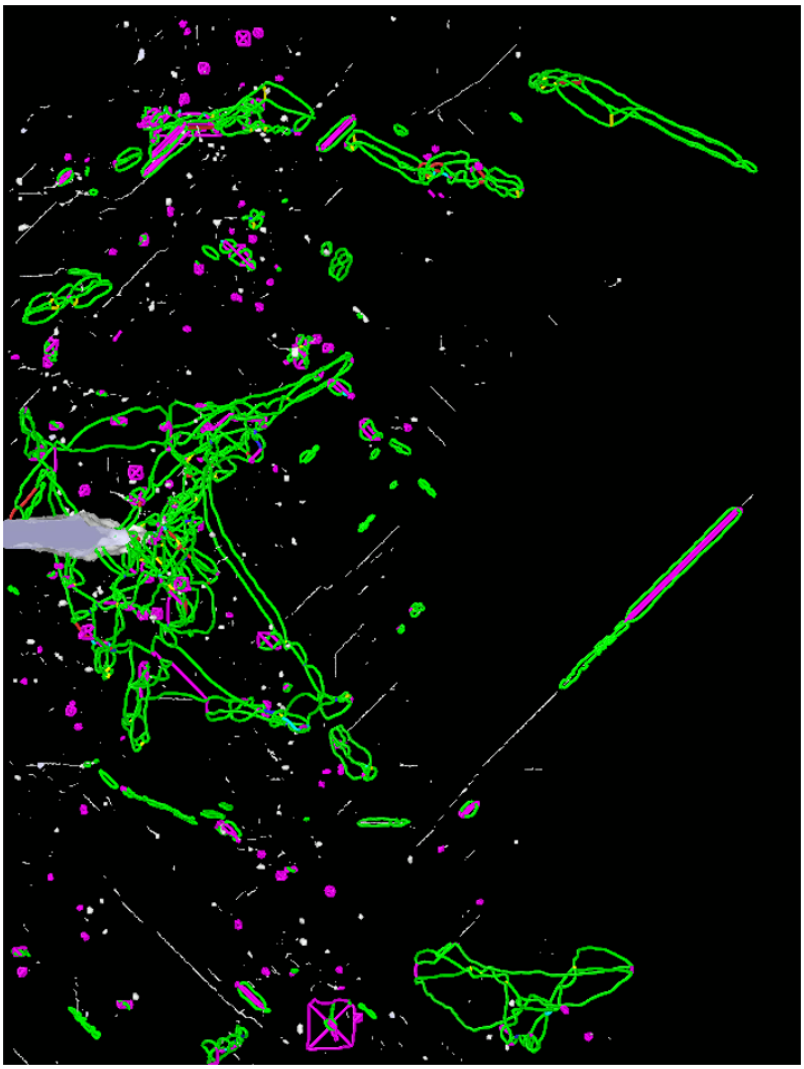

(a)

See the next page for complete description ...

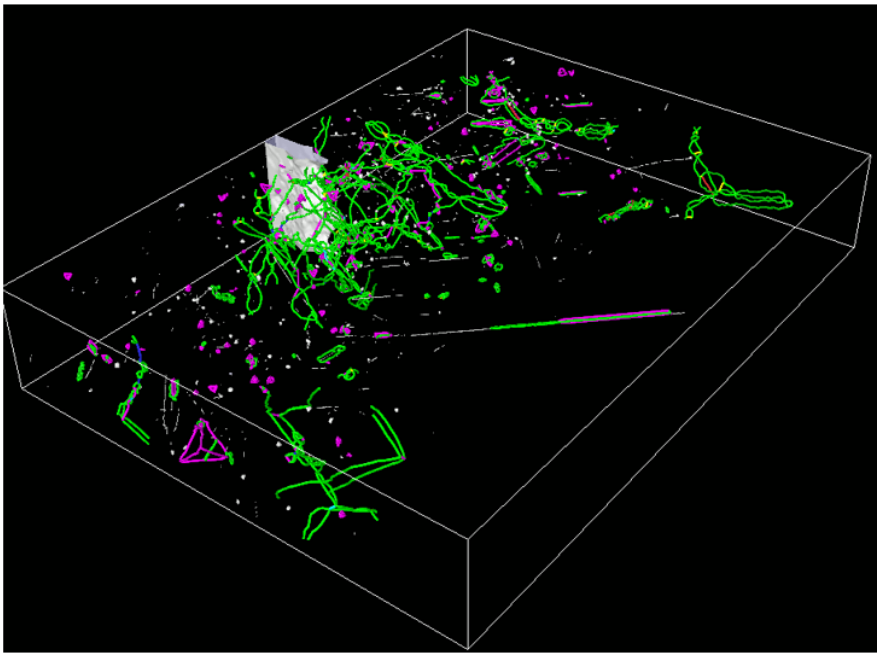

(b)

Figure 4-14: Dislocation network around crack-tip at the end of 15th cycle for $\Delta K = 2\ \mathrm{MPa}\sqrt{\mathrm{m}}$: (a) Top view (b) Perspective view. Green lines are Shockley partials, purple lines are stair-rod partials of the type $\frac{1}{6}\langle 1\,1\,0\rangle$, yellow lines are Hirth partials and other dislocation types involving stair-rod ones of the type $\frac{1}{6}\langle 3\,1\,0\rangle$ and $\frac{1}{3}\langle 1\,1\,0\rangle$.

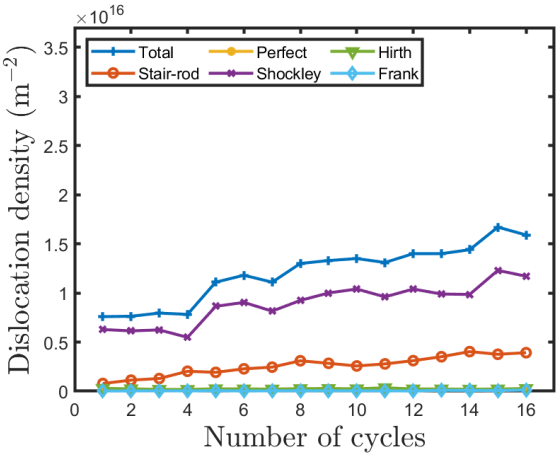

(a)

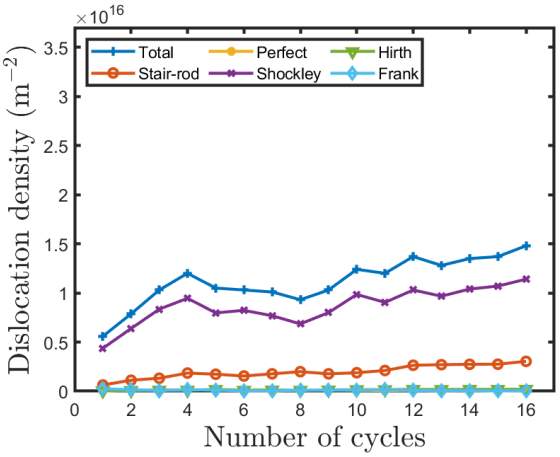

(b)

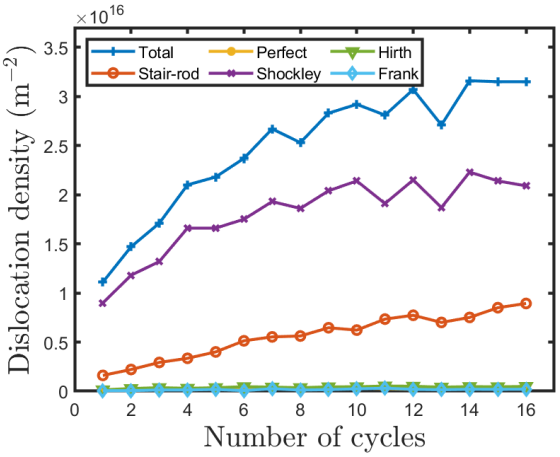

(c)

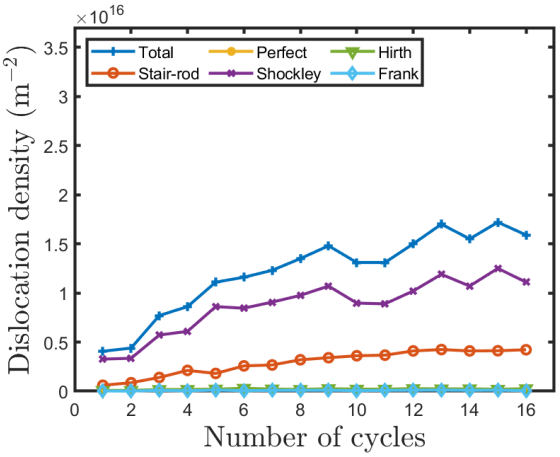

(d)

See the next page for complete description ...

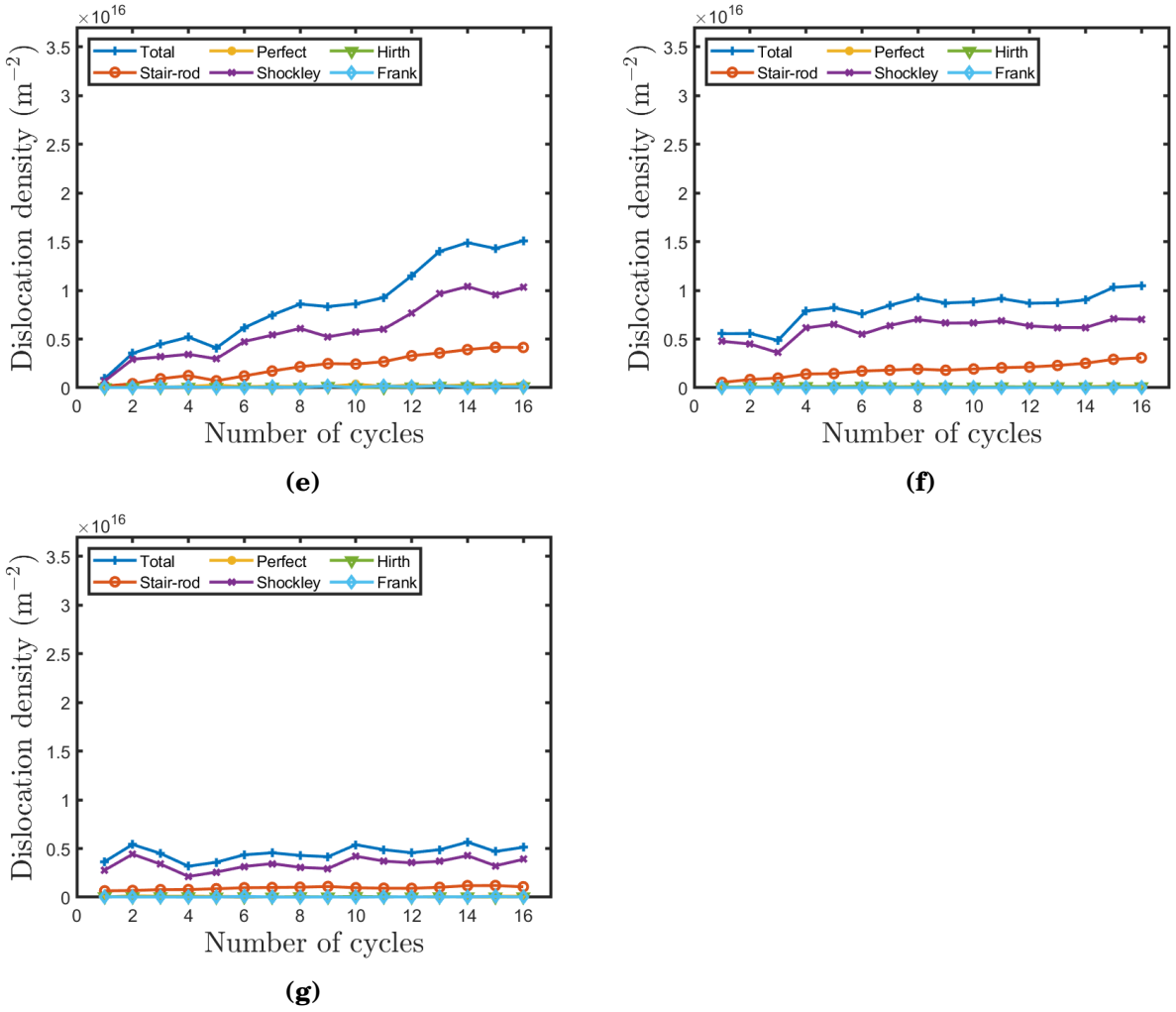

Figure 4-15: Evolution of dislocation density during cyclic loading for $\Delta K = 2\ \mathrm{MPa}\sqrt{\mathrm{m}}$ for orientations (a) A1, (b) A2, (c) A3, (d) B1, (e) B2, (f) C1, (g) C2. Figures display the evolution of the total dislocation density and the evolution of different dislocation type density.

4.4.2.1 Lomer-Cottrell locks

One of the well-known dislocation locks is the Lomer-Cottrell lock. Fig. 4-16a, Fig. 4-16b, Fig. 4-16c show close-up of this lock observed in our simulations. This lock is formed by the interaction between two Skockley partials gliding on two slip planes that intersect. As shown on Fig 4-16a , a new dislocation (a stair-rod one colored in purple) is formed at the intersection between the two slip planes along a $\langle 1\,1\,0\rangle$ direction according to the reaction :

$$\frac{1}{6}\langle \bar{1}\,2\,\bar{1}\rangle + \frac{1}{6}\langle 2\,\bar{1}\,1\rangle \rightarrow \frac{1}{6}\langle 1\,1\,0\rangle \tag{4.32}$$

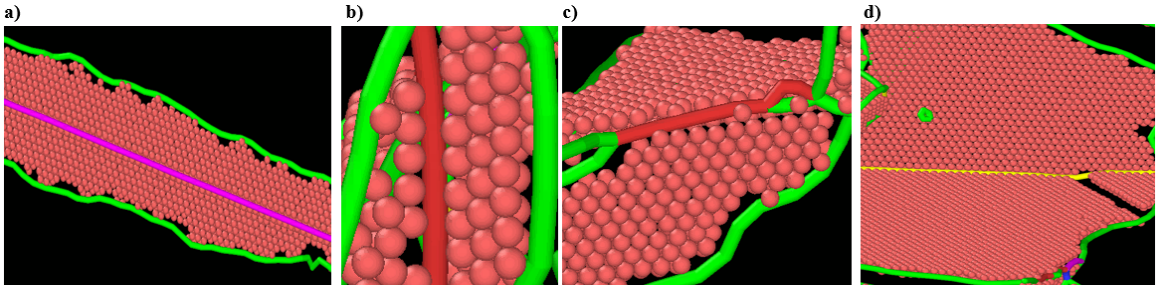

Figure 4-16: Close-ups of dislocation barriers formed by the reaction of two Shockley partials: (a) Lomer-Cottrell lock with a stair-rod dislocation (purple line) of $1/6\langle 1\,1\,0\rangle$ type (b) Lomer-Cottrell barrier with a stair-rod dislocation (red line) of the $1/6\langle 1\,1\,0\rangle$ type; (c) barrier with a stair-rod dislocation (red line) of the $1/3\langle 3\,1\,0\rangle$ type; (d) Hirth junction with a $1/3\langle 1\,0\,0\rangle$ Hirth partial (yellow line). The green lines represent Shockley partials and red spheres are atoms in the stacking fault plane

Alternatively, extensive studies reported in [Anderson et al., 2017] proposed other barriers by considering other stable stair-rod dislocations formed at the intersection of two slip planes by Shockley partial reactants. These barriers include inverted Lomer-Cottrell locks. Inverted Lomer-Cottrell locks are observed in our simulation and one example is displayed in Fig. 4-16b. Similarly to the Lomer-Cottrell locks, a partial stair-rod (red line in Fig. 4-16b) is formed along a $\langle 1\,1\,0\rangle$ direction, but for that case the Burgers vector is different, according to the following reaction :

$$\frac{1}{6}\langle 1\,1\,2\rangle + \frac{1}{6}\langle 1\,1\,\bar{2}\rangle \rightarrow \frac{1}{3}\langle 1\,1\,0\rangle \tag{4.33}$$

Other stable stair-rod dislocations along $\langle 3\,1\,0\rangle$ direction are observed as well in our study and displayed in Fig. 4-16c. They can be formed by Shockley partials according to the reaction:

$$\frac{1}{6}\langle 1\,2\,1\rangle + \frac{1}{6}\langle 2\,\bar{1}\,\bar{1}\rangle \rightarrow \frac{1}{6}\langle 3\,1\,0\rangle \tag{4.34}$$

Although these last two reactions are rare, even in our study, they are energetically favorable and its formation leads to a decrease in the energy of the system. However, the stair-rod dislocations do not glide, hence the Lomer-Cottrell lock acts as barrier that will impede the mobile dislocations gliding along the associated slip planes.

4.4.2.2 Hirth locks

Another type of locks observed as well herein is the Hirth ones. Hirth locks are the result of the interactions between slip systems which Burgers vectors are perpendicular to each other. By the same mechanism as above, Shockley partials coming from two slip planes interact along a $\langle 1\,0\,0\rangle$ direction to form a

Hirth partial according to the reaction:

$$\frac{1}{6}\langle 1\,2\,1\rangle + \frac{1}{6}\langle \bar{1}\,\bar{2}\,1\rangle \rightarrow \frac{1}{3}\langle 0\,0\,1\rangle \tag{4.35}$$

An example of this lock is displayed in Fig. 4-16d. The yellow line observed at the intersection of the two planes represents the Hirth partial of the $1/3\langle 1\,0\,0\rangle$ type. Since the Burgers vector of Hirth partials do not belong to easy slip planes, the Hirth locks act also as barriers to forward and reverse glide of mobile dislocations.

Other dislocation structures such as Frank partials ($1/3\langle 1\,1\,1\rangle$) or entanglements, multiple junctions, leading to a minimization of the energy of the system are also observed. These structures will act under certain conditions as sources of dislocations or as barriers that will impede the glide of mobile dislocations along certain easy slip planes, either during loading (forward glide) or during unloading (reverse glide).

4.4.2.3 Cross-slip

Because of the numerous obstacles produced around the crack-tip, cross slip is a possibility of movement by changing the slip plane, for dislocations with screw components. Indeed, cross slip is also observed in our simulations. Although due to the nature of the dislocations (Shockley partials) generally observed in our simulations, the cross slip mechanism may have been hindered. However, in our study the high stresses prevailing near crack-tip can facilitate cross-slip. Ishii and Weertman [Ishii and Weertman, 1971b] and McEvily and Boettner [McEvily and Boettner, 1963a] discussed the importance of this phenomenon in prior experiments carried out at RT. It should be recalled that the objective of our study is to reveal the complex response of atoms in regions of very high stress around the crack-tip where the phenomena are more governed by very high local stresses than by a thermal activation at RT [Sauzay and Kubin, 2011]. Fig. 4-17 shows an example of cross slip observed in our simulations. It can be observed in Fig. 4-17a a split of Shockley partials in the deviate plane $(\bar{1}\,1\,1)$ whereas the primary plane is a $(1\,1\,1)$ plane. In Fig. 4-17b, Shockley partials changing slip plane from a $(\bar{1}\,1\,1)$ to a $(1\,1\,\bar{1})$ plane are observed. These changes in slip planes by dislocations can and will have consequences on crack propagation as shown later in the manuscript.

4.4.2.4 Jogged dislocations

As cyclic plastic deformation proceeds, dislocation densities in the crystal increase. Dislocations gliding in a slip plane may intersect dislocations forest crossing this plane. Thus jogs and superjogs are formed as shown in Fig. 4-18 of our simulations. The left figure of Fig. 4-18a and 4-18b, respectively show a jog and a superjog. The formation of jogs and superjogs can induce locking

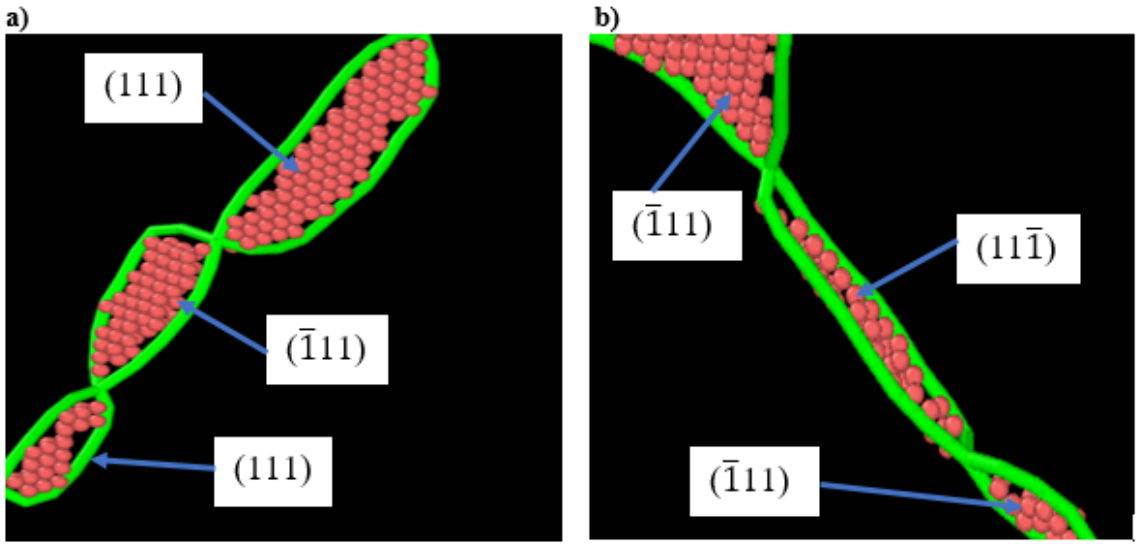

Figure 4-17: Example of the results of dislocation cross-slip. (a) the two parts of dissociated dislocations in the $(1\,1\,1)$ primary slip plane and another part in the deviate slip plane $(\bar{1}\,1\,1)$; (b) dissociated dislocations in the $(\bar{1}\,1\,1)$ primary slip plane and another part in the deviate slip plane.

phenomena hindering the gliding of dislocations. The presence of jogs on a dislocation can increase the friction forces exerted on dislocations and impede its glide. Also the presence of stair-rod partials or Hirth partials, which are sessile dislocations on superjogs will also impede the dislocation gliding. Under certain conditions like high stresses such as those experienced in the crack-tip region or due to close dislocations, jogs may move.

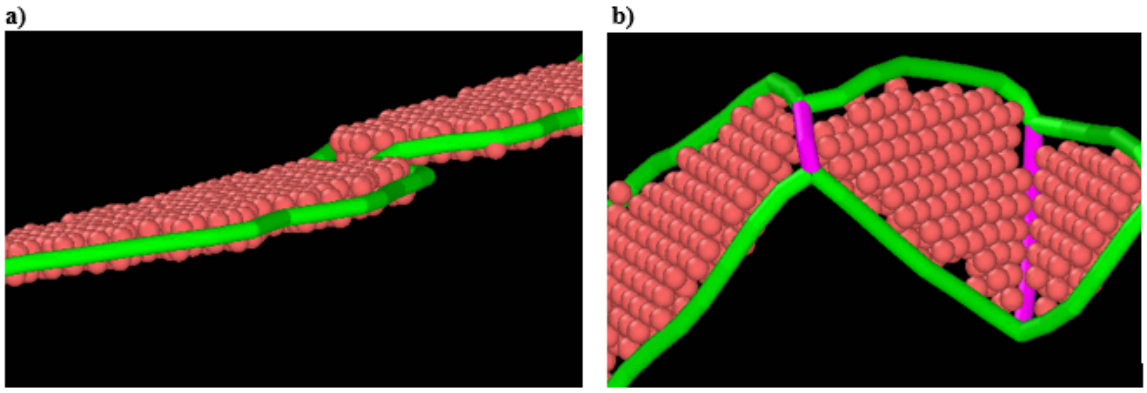

Figure 4-18: Example of (a) jogs ; (b) super-jog

4.4.2.5 Point defects

High densities of vacancies are produced during cyclic loading in our simulations. In fact, the plastic deformation causes a saturation of vacancies. As stated in [Hull and Bacon, 2001], there is a considerable body of evidence from measurement of physical properties such as electrical resistivity, that vacancies are generated by plastic deformation. Obviously, as cyclic plastic deformation proceeds, vacancy concentration increases as shown in Fig. 4-19 and Fig. 4-20 where vacancy distribution within the crystal is shown for the crack configuration A2 at different number of cycles (N= 5, 10). Fig. 4-19 shows the evolution of vacancy concentration at the end of each cycle for different crack configuration and for $\mathrm{K_{max}} = 2\ \mathrm{MPa}\sqrt{\mathrm{m}}$. Whatever the crack configuration, vacancy concentrations increase during cyclic loading. Typical values of $10^{-4}\ \mathrm{at}^{-1}$ are predicted in this MD study. These values are of the same order of magnitude with those reported experimentally by Polák [Polák, 1969] for cyclically deformed copper single crystals at $4\,\mathrm{K}$ and also with values generally reported in the case of a severe plastic deformation [Čížek et al., 2019].

There exist different mechanisms of vacancy production. In this study, vacancies are generated by jogs dragging. As stated previously, under certain conditions like high stresses such as those experienced by the crack-tip regions or due to close dislocations, jogs can move. This glide of jogged dislocation is non-conservative, thus the glide of jogged dislocations produces trails of point defects as shown in Fig. 4-20. Vacancy production can be higher in materials promoting cross-slip. In fact, during cross-slip, jogs can be generated on screw dislocations and during the dragging of these jog, vacancies will be produced. Vacancies are not only produced for crack configuration A2. Vacancies are also observed for all the crack configurations tested, but in different proportion as shown in Fig.4-19. Vacancy production around crack-tip were also observed experimentally (see for example [Kiritani et al., 1999]).

In our simulations, the evolution of the vacancy concentration during cyclic loading can be considered as linear, if we disregard the first five or six cycles. Thus, one can estimate the production rate of vacancies at about $2 \times 10^{-5}\ \mathrm{at}^{-1}\mathrm{cycle}^{-1}$ for crack configurations A1, A3 and B1; $10^{-5}\ \mathrm{at}^{-1}\mathrm{cycle}^{-1}$ for crack configurations A2, B2 and C2 and $8 \times 10^{-6}\ \mathrm{at}^{-1}\mathrm{cycle}^{-1}$ for orientation C1. Experimentally, the vacancy production rate reported by Polák and Sauzay [Polák and Sauzay, 2009] in persistent slip bands, is about $3.1 \times 10^{-7}\ \mathrm{at}^{-1}\mathrm{cycle}^{-1}$ for a tension-compression test. Our computed values are 10 to 100 times higher than their measured value. This is maybe due to the fact that their tests were carried out on crystal orientations which favor a single slip and therefore less interactions compared to the crystal orientations, which favor multiple slip. Finally, the introduction of a crack in our MD simulation lead to additional higher stresses in the vicinity of the crack-tip which can enhance vacancies production.

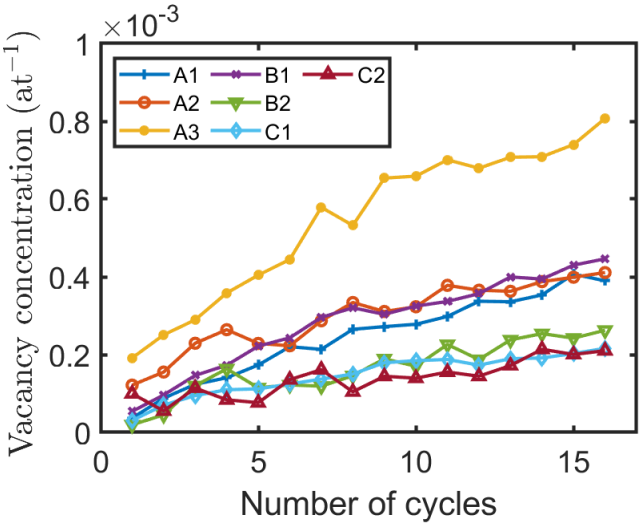

Figure 4-19: Evolution of vacancy concentrations during cyclic loading for different crack configurations.

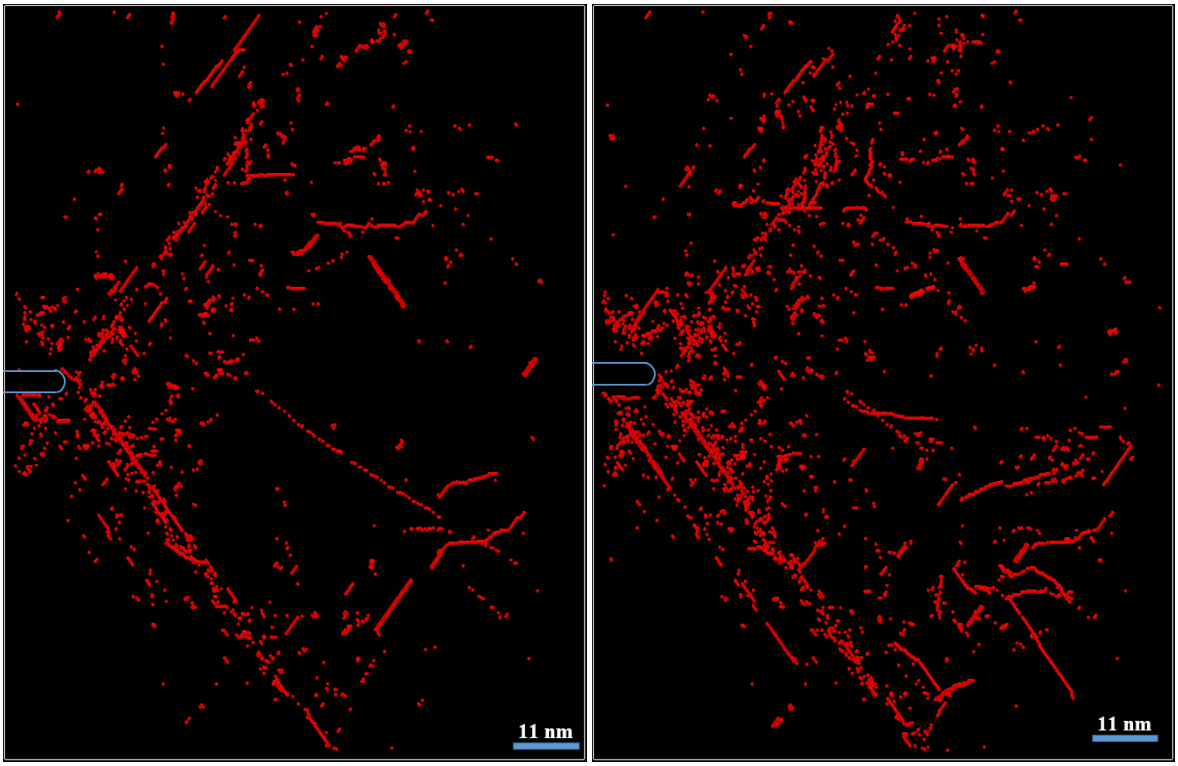

(a) **(b)**

Figure 4-20: Vacancies and vacancy clusters produced during cyclic loading at different number of cycles: (a) cycle 5, (b) cycle 10. Vacancy concentration increases with the number of cycle. Different structure of vacancies observed: single vacancies, bi-vacancies, rows of vacancy and 3D clusters. Blue lines indicates the location of crack.

4.4.2.6 Stacking fault tetrahedra

Stacking fault tetrahedra formation is the results of dislocation interactions. Fig. 4-21 shows stacking fault tetrahedra observed from our simulations. In Fig. 4-21a), the nucleation of a stacking fault tetrahedron. Fig. 4-21b) shows well-formed stacking fault tetrahedra and Fig. 4-21c) displays a stacking fault tetrahedron absorbing trail of vacancies. Experimental TEM observations showed small stacking fault tetrahedra near crack zones in Cu, Au, Ni, and Al, [Matsukawa et al., 2003a] which support the observations arising from our atomistic simulations. The mechanisms of formation of stacking fault tetrahedra have been widely studied. Some representative papers such as [Wang et al., 2011a, Wang et al., 2011b, Wirth et al., 2000a, Loretto et al., 1965] can be pointed out.

Interaction of stacking fault tetrahedra with a mobile dislocation have been also studied and successfully simulated at the atomic scale by MD. Wirth and co-wokers [Wirth et al., 2000b] carried out MD simulations to characterize the motion and velocity of edge dislocations at high strain rate and their interactions with stacking fault tetrahedra in Cu, using an EAM interatomic potential. Their results show that a perfect stacking fault tetrahedron acts as a hard obstacle for dislocation motion and, although the stacking fault tetrahedron is sheared by the dislocation passage, it remains largely intact [Wirth et al., 2000b]. Their simulations reveal also that an overlapping, truncated stacking fault tetrahedron is absorbed by the passage of an edge dislocation, resulting in dislocation climb and the formation of a pair of less mobile super-jogs on the edge dislocation. Chen *et al.* [Chen et al., 2019] studied the interaction of a screw dislocation and a stacking fault tetrahedron. Two types of interactions were studied: cross-slip and obstacle-cutting. It has been observed that a pinning SFT has an attractive interaction with a screw dislocation, resulting in a local trapping. This has the effect of locally reducing the separation distance between the leading partial and the trailing partial, thus promoting cross-slip. The competition between the cross-slip and obstacle-cutting was studied. For a fixed SFTs separation, the activation energy for cross-slip and obstacle-cutting decreases. For low resolved shear stresses (RSS) (≤ 100 MPa), it was shown that cross-slip is dominant, whereas for high RSS (≥ 100 MPa), obstacle-cutting dominates. The effect of SFT spacing was found to be weak on the activation energy. The effect of the SFT size on the cross-slip and on the obstacle-cutting was also studied by the authors. Their results showed that on the one hand, the smaller the size of the SFT, the greater the activation energy for cross-slip and on the other hand, the smaller the size of the SFT, the smaller the activation energy for the obstacle-cutting.

In our simulations it was also observed that, mobile dislocations whether its edge or screw dislocation, interact with stair-rod partials of a stacking fault tetrahedron and since stair-rod partials are sessile dislocations, it impedes the glide of these mobile dislocations.

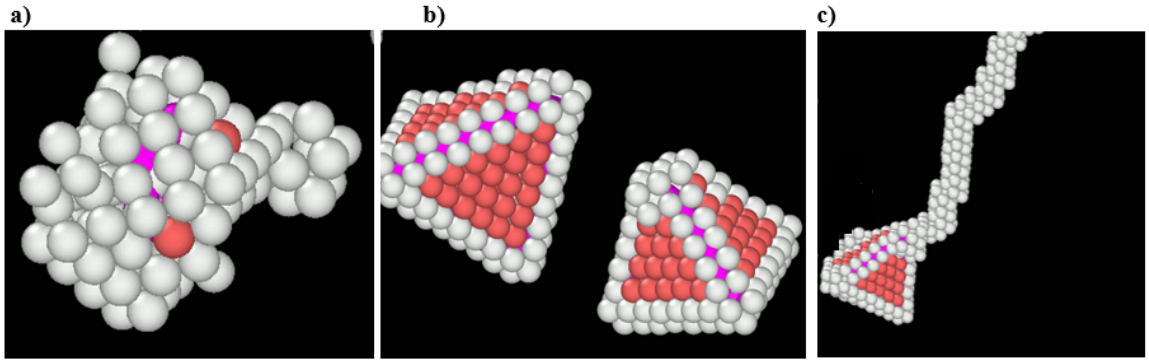

Figure 4-21: Close ups of stacking fault tetrahedra. (a) Cluster of vacancies at the beginning of the formation of a stacking fault tetrahedra; (b) Well-formed stacking fault tetrahedra; (c) stacking fault tetrahedron absorbing vacancies

4.5 Plastic irreversibility

Emission and gliding of dislocations induce in the regions close to the crack-tip plastic slip. Fig. 4-22 shows the evolution of the slip distance d_{slip} as computed by Equation 4.22. It is observed that during cyclic loading, the slip distance increases with the number of cycles. As we have noticed previously, not all dislocations emitted during loading glide back to the crack-tip. In the same way, the plastic slip induced by the gliding of dislocations during the loading half cycle is not totally reversible. We are then concerned with a cyclic irreversibility of the plastic slip. Fig. 4-22 shows the slip distance during loading at maximum and minimum loads. One can observe from Fig. 4-22 an increase in the cumulative slip distance both at maximum loading and at minimum loads. Apart from orientation B2 for which the evolution of the cumulative slip distance seems to be linear, the general trend suggests a power law evolution with an exponent ranging between 0.4 and 0.7. This exponent seems to be in agreement with the 3D discrete dislocation dynamics computations of Déprés *et al.* [Depres et al., 2015] who showed that the dependence of cumulative plastic slip on the number of cycle was of square root type. Fig. 4-23 displays the slip irreversibility factors computed for different crack configurations and for $\Delta K = 2\ \mathrm{MPa}\sqrt{\mathrm{m}}$. The slip irreversibility factor p is computed by:

$$p = \frac{d_{slip,irr}}{d_{slip}} \tag{4.36}$$

where $d_{slip,irr}$ is the irreversible slip distance after each cycle (the remaining slip distance after unloading). The evolution of the plastic irreversibility during cyclic loading is plotted in Fig. 4-23. As can be seen in Fig. 4-23a, the irreversibility factors fluctuate during cyclic loading around a mean value shown in Fig. 4-23b. This plastic irreversibility can be explained by the different interactions between dislocations inducing entanglement, dislocation locks, jogs, etc. that

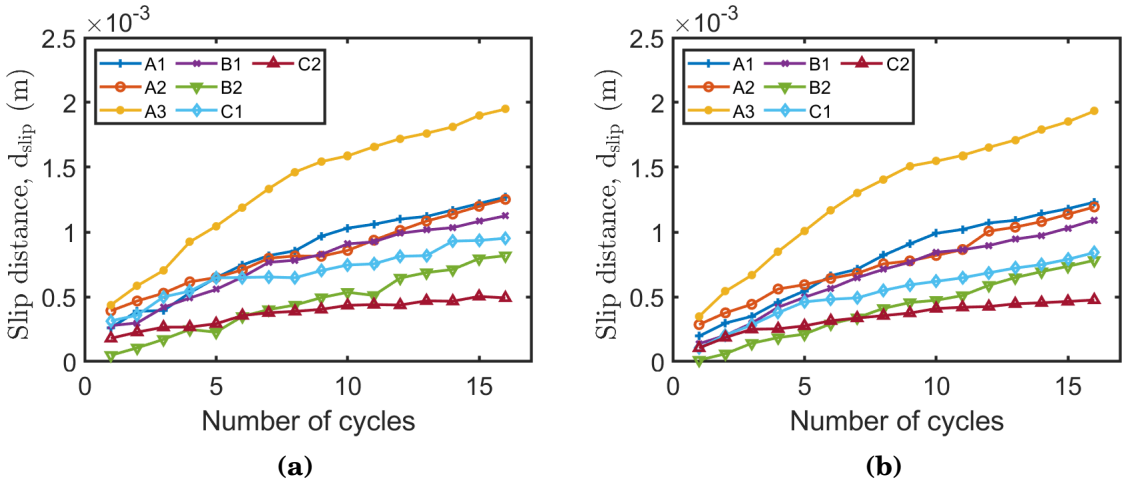

Figure 4-22: Evolution of the slip distance computed, for different crack configurations and for $\Delta K = 2$ MPa$\sqrt{\text{m}}$. (a) at maximum load ($K_{max} = 2$) and (b) at minimum load ($K_{min} = 0$). The cumulative plastic slip in the crack-tip region increases during cyclic loading.

impede the backwards motion of mobile dislocations. Cross-slip inducing dislocation annihilation can be also evoked to explain the plastic irreversibility. Experiments focusing on plastic irreversibility in ductile metals under cyclic loading allowed the evaluation of plastic irreversibility factor in various conditions. The well-known EGM model ([Essmann and Mughrabi, 1979, Essmann et al., 1981, Differt et al., 1986]) which describes the surface slip irreversibility in PSBs allows the evaluation of the total irreversibility factor. It amounts to about 0.6 in cyclically deformed copper by taking into account only screw dislocations. This value falls to 0.3 when edge dislocations are also taken into account. Furthermore, recently, Fan *et al.* [Fan et al., 2016], by coupling models from the literature based on bulk mechanisms and molecular dynamics simulations, accounting for the surface effects, estimated the irreversibility factor to be between 0.4 and 0.7. As pointed out by Chen and Laird [Cheng and Laird, 1983], the plastic irreversibility in the case of a stage II crack (thus loaded in mode I) is higher than the irreversibility observed in stage I. The mean values over the 16 cycles computed in this study varies between 0.25 for orientation C1 which exhibits the lowest slip irreversibility factor and 0.69 for orientation A3 which exhibits the highest slip irreversibility factor. This may be explained by the dislocation density remaining after unloading due to dislocation interactions and maybe by plastic deformation mechanisms. Indeed as noticed previously the crack configurations A3 exhibits the highest dislocation density while crack configurations C1 and C2 exhibit the lowest densities.

During cyclic loading, the dislocations remaining in the vicinity of the crack-tip impede the glide back of other dislocations towards the crack-tip and therefore lead to plastic irreversibility at the crack-tip. Furthermore, these dislocations remaining close to the crack-tip induce internal stresses in the near crack-tip zones

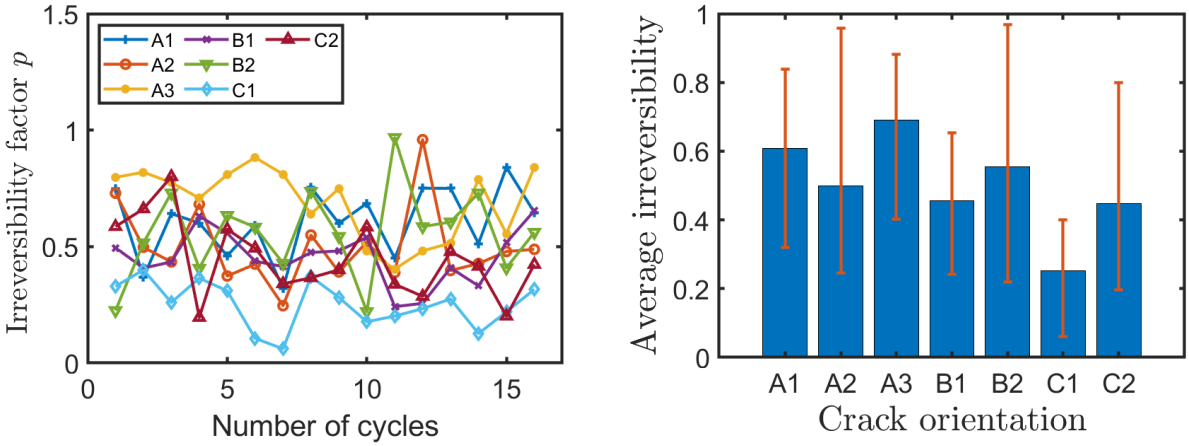

(a) **(b)**

Figure 4-23: (a) Evolution of the slip irreversibility factor computed for each crack configuration during cyclic loading. One can see that slip irreversibility fluctuate around a mean value. (b) Mean slip irreversibility factors for different crack configurations. Values are computed for $\Delta K = 2\ \mathrm{MPa}\sqrt{\mathrm{m}}$

(Fig. 4-24 and Fig. 4-25). More precisely, Fig. 4-24 shows the stress isovalues, σ_{xx} and σ_{yy} and Fig. 4-25 shows the evolution of stress fields along crack axis (axis [OX), Fig. 2-1) after unloading and for a maximum applied SIF of 2 $\mathrm{MPa}\sqrt{\mathrm{m}}$ at the 10th cycle. Compressive stresses prevail ahead of the crack-tip after unloading. As shown in Fig. 4-25, these two stresses (σ_{xx} and σ_{yy}) are compressive ones along crack axis for a distance of about 20 to 40 nm from the crack-tip, and tend towards 0 beyond. These internal stresses have the effect of reducing during cyclic loading, the mean stress and thus reducing the effective local driving force (at the crack-tip) for crack propagation. It was found that these internal stress fields over a distance of about 20 nm ahead of the crack-tip could be described analytically by a logarithmic expression of the form:

$$\sigma = \beta_1 \log(r) + \beta_2 \tag{4.37}$$

In this example, it was found that β_1 was approximately 1.9 for σ_{yy} and 1.44 for σ_{xx}. The coefficient β_2 was estimated at -6.08 for σ_{yy} while for σ_{xx}, β_2 was approximately -5.2.

In addition, the evolution of stress fields along the axis ahead of crack-tip at maximum load has also been analyzed. Fig. 4-26 shows as an example the isovalues of stress fields at the maximum load of the 10th cycle. Fig. 4-27 shows the evolution of the stress fields along the axis ahead of crack-tip at the maximum load of the 10th cycle. First of all, obviously, the stress fields at this level are not compressive stresses as in the previous case but tensile stresses. And it has been found that these stress fields, can be described analytically by the following

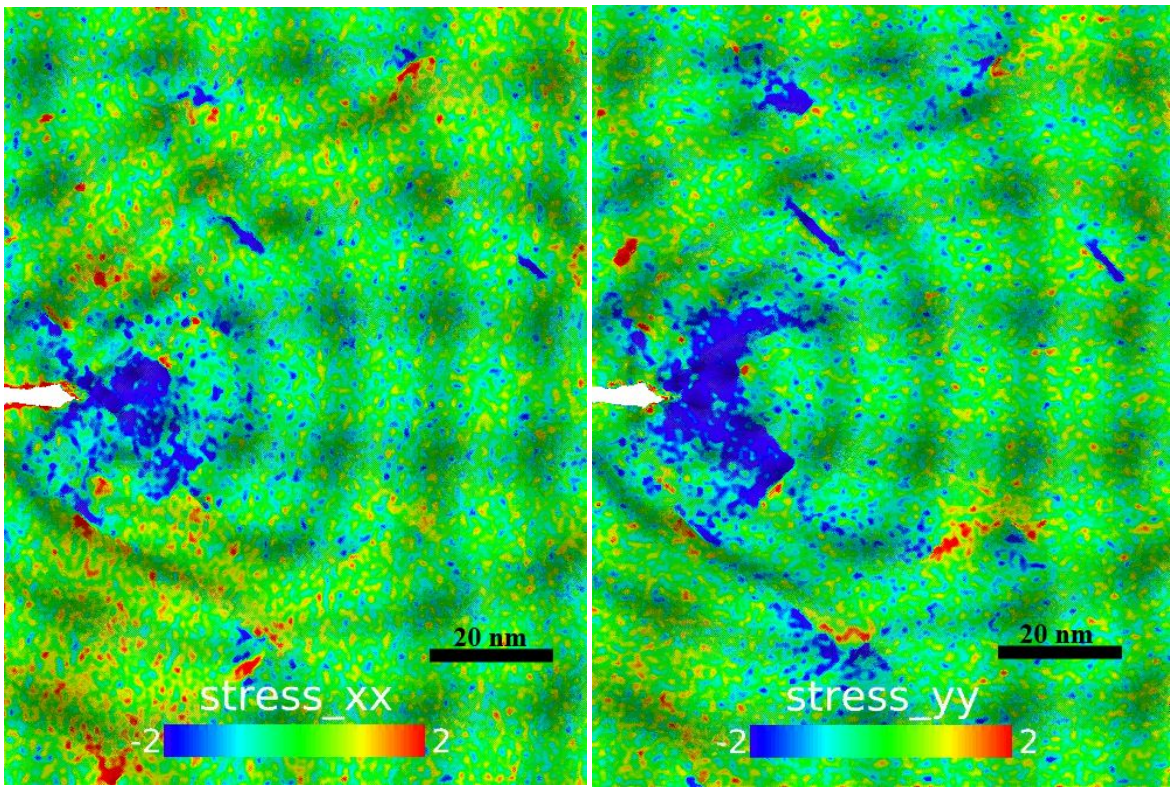

(a) **(b)**

Figure 4-24: Isovalues of residual stress fields for the crack configuration A1 at the end of the 10th cycle, $\Delta K = 2\ \mathrm{MPa}\sqrt{\mathrm{m}}$. (a) σ_{xx} and (b) σ_{yy} (unit GPa)

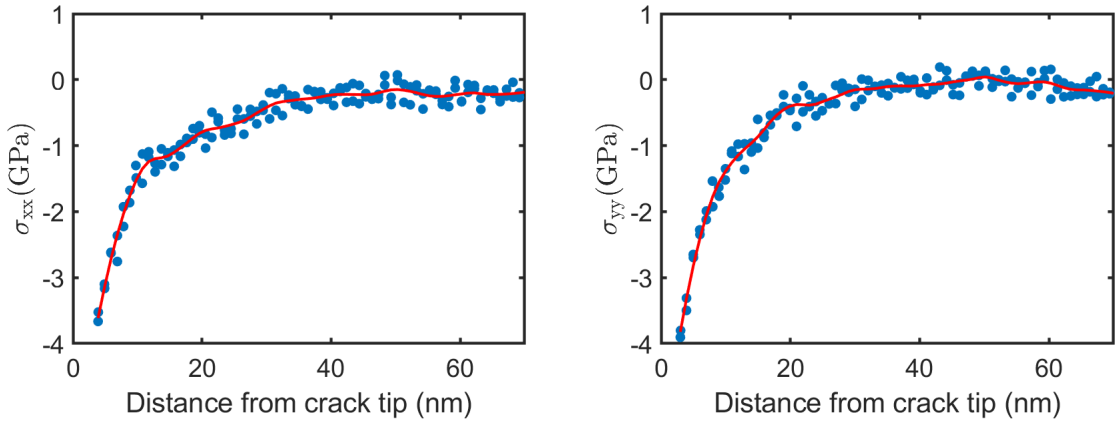

(a) **(b)**

Figure 4-25: Evolution of residual stress fields, after unloading along the axis ahead of fatigue crack. Crack configuration A1, cycle 10, $\Delta K = 2\ \mathrm{MPa}\sqrt{\mathrm{m}}$

expression, provided the distance to the crack-tip is lower than $20\ \mathrm{nm}$:

$$\sigma = \frac{k}{r^{\alpha}} \tag{4.38}$$

with α the stress singularity exponent. In this precise case, α was found to be approximately 0.91 for σ_{yy} and approximately 0.87 for σ_{xx}. As for the value of k, the latter was estimated at about 16.67 for σ_{yy} and 14.2 for σ_{xx}.

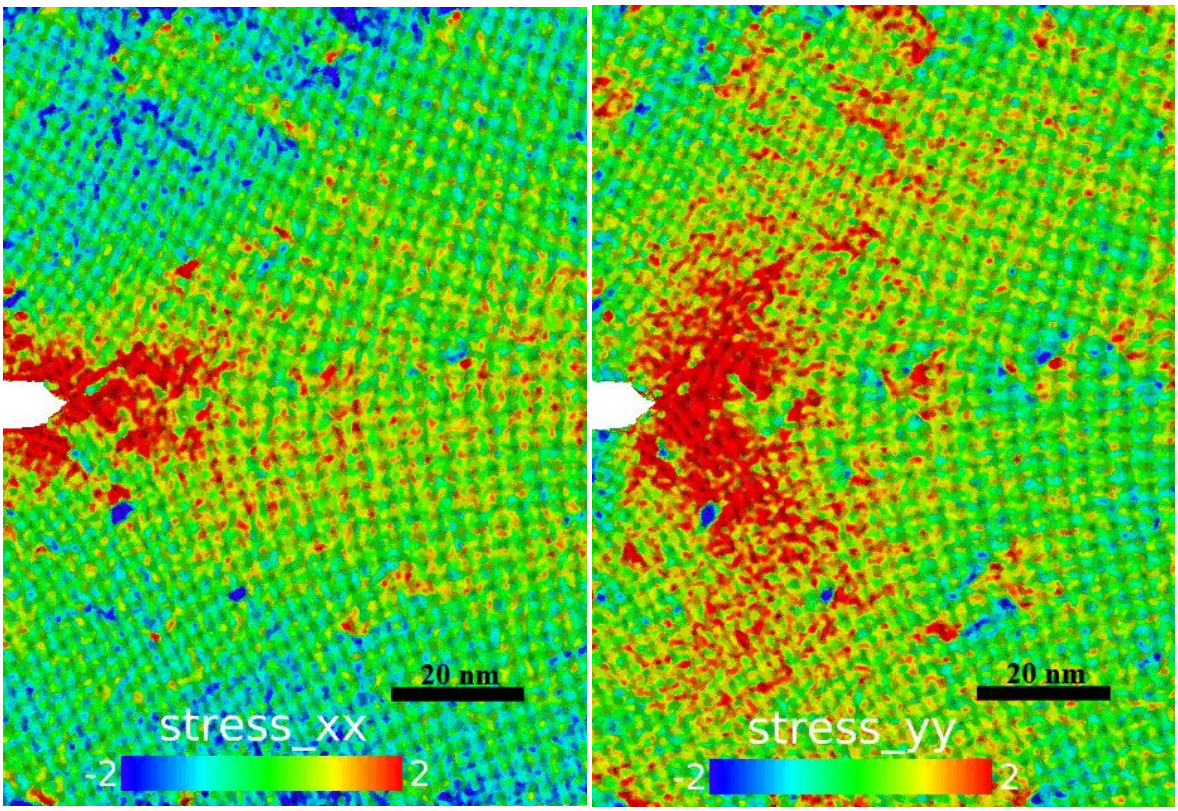

(a) **(b)**

Figure 4-26: Isovalues of stress fields at the 10th cycle maximum loading for orientation A1, $\Delta K = 2\ \mathrm{MPa}\sqrt{\mathrm{m}}$. (a) σ_{xx} and (b) σ_{yy}

4.6 Conclusion

The plastic deformation in the vicinity of crack-tips in cyclically deformed copper single crystals was studied. And its consequences in terms of microstructure was described. The slip patterns around crack-tips for different crack configurations was found to be in agreement with the available experimental observations. Depending on the crack orientation, two main mechanisms of plastic deformation are observed: the dislocation slip process and mechanical twinning. While some

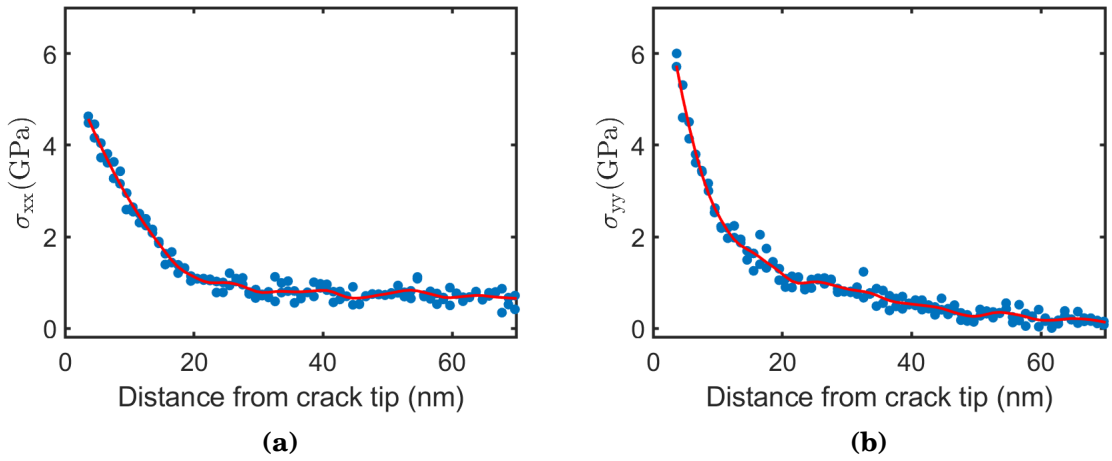

Figure 4-27: Evolution residual stress fields along fatigue crack axis at maximum loading. Orientation A1, cycle 10, $\Delta K = 2\ \mathrm{MPa}\sqrt{\mathrm{m}}$

crack configurations lead only to dislocations slip process, other crack configurations proceed both by mechanical twinning and dislocations slip. But, further during cyclic loading, the amount of twinning was found to decrease gradually and dislocation slip became the only plastic deformation mechanism. The interactions between dislocations are analyzed and different dislocation structures are observed close to the crack-tips: entanglements, Hirth locks, Lomer-Cottrell locks, jogs and superjogs, etc. With the formation of barriers around crack-tips, the motion of mobile dislocations becomes a little more difficult. Cross-slip observed in this study remain a possibility of dislocation motion. Numerous vacancies are produced during cyclic loading. They are created by cross-slip and then jog and superjog dragging, which is a non-conservative movement requiring the production of vacancies. These vacancies have been quantified and their density is in agreement with experimental measurements. These vacancies often agglomerate in the form of clusters leading to the formation of stacking fault tetrahedra, as observed experimentally. As shown in previous studies, these stacking fault tetrahedra may significantly impedes dislocation gliding. Plastic irreversibility in the vicinity of crack-tips, consequence of interactions between dislocations (locks, entanglements, SFTs, cross-slip, etc.) is also analyzed. The plastic irreversibility factor is evaluated for each crack configuration. Finally, the stress fields at the crack-tip are analyzed. It is shown that the dislocations remaining close to crack-tips after each unloading can induce internal compressive stresses near crack-tip zones. These internal compressive stresses can affect the local (near crack-tip) effective driving force for crack propagation.

The plastic irreversibility at atomic scale, highlighted in this chapter, could play an important role in the propagation of fatigue cracks. The following chapter is devoted to fatigue crack propagation.

Chapter 5

Fatigue crack growth in copper single crystals at room temperature

Between two groups of people who want to make inconsistent kinds of worlds, I see no remedy but force.

Oliver Wendell Holmes.

Abstract

Fundamental fatigue crack growth mechanisms are analyzed at nanoscale. It is shown that fatigue crack grows by blunting-resharpening and slip irreversibility. This slip irreversibility is induced by different dislocation locks, entanglements, cross-slip events, etc. Fatigue crack propagation is found to occur even at low rates such as 10^{-11} $\mathrm{m.cycle}^{-1}$ *and Fatigue crack growth rate found to obey the Paris' power law, with an exponent of approximately 4. This is in agreement with experimentally reported values under inert environment. Fatigue crack closure is also observed and analyzed. Fatigue crack front geometry analysis brings further evidences on fatigue crack growth mechanisms while fracture surface analysis does not exhibit striations, generally reported experimentally under air environment, but rarely in inert environment.*

Contents

5.1 Introduction

For some years now, atomistic simulations have been widely performed in order to predict material properties or to make the link between the atomistic theories and those of the continuum mechanics. Many studies of crack propagation under monotonic loading, deformation mechanisms near crack-tip, dynamic instability and subsequent failure via MD simulations [Abraham et al., 1994, Buehler et al., 2004, Knap and Sieradzki, 1999, Komanduri et al., 2001, Sieradzki et al., 1988, Zhang and Ghosh, 2013, Zhou et al., 1997, Zhu et al., 2004] have been successfully used to model these phenomena. However, there are only few studies focusing on crack propagation and near crack-tip plastic deformation mechanisms under cyclic loading. This can be explained by the expensive computational cost of such simulations that limits the physical time and the accessible system size. Indeed, the sizes of the simulated systems are on the order of a few hundred nanometers and the physical times range between picoseconds to few nanoseconds.

Recently, studies on surface slip irreversibility and nanocrack initiation have been carried out by Fan *et al.* [Fan et al., 2016, Fan et al., 2017]. It was observed that surface steps formed by the glide of dislocations subjected to cyclic loading could be reconstructed by different mechanisms. This surface reconstruction can induce surface irreversibility damage that accumulates cycle after cycle and forms a notch from which a crack could initiate. Nishimura and Miyazaki [Nishimura and Miyazaki, 2004] performed MD simulations to investigate mechanical behavior and microstructure around the crack-tip in α-iron. Phase transition and dislocation emission and annihilation were observed and therefore, vacancies were produced. They proposed that fatigue crack grows by coalescence of vacancies. Considering Lennard-Jones potential and a collection of 960 atoms, Chang and Fang [Chang and Fang, 2003] observed in nanoscale copper numerical fatigue tests, a ductile fracture configuration as low stress was applied; a fatigue limit of 10^5 cycles was deduced. Farkas and co-authors [Farkas et al., 2005] investigated fatigue crack growth mechanisms in nanocrystalline nickel and showed that the main mechanism of crack advance in this material was the formation of nanovoids ahead of crack-tip and their absorption by the blunting tip. A same mechanisms was reported by Zhou *et al.* [Zhou et al., 2015] for nanotwinned copper. For both studies, the fatigue crack growth was found to obey Paris' law. But while in simulations carried out on nanocrystalline metals lead to an exponent of 2 [Farkas et al., 2005], those on nanotwinned materials provide a Paris' law exponent of 4 [Zhou et al., 2015], which is in agreement with theoretical model of damage accumulation. Many other studies reported the similar mechanisms [Potirniche and Horstemeyer, 2006, Potirniche G.P et al., 2006]. In addition, other mechanisms were suggested such as cleavage of atomic bounds in the crack plane [Potirniche and Horstemeyer, 2006, Potirniche G.P et al., 2006, Potirniche et al., 2005, Baker and Warner, 2014]. Baker and Warner

[Baker and Warner, 2014] investigate by the means of a 2D multiscale coupled atomistic-discrete dislocation dynamics method, the crack growth mechanisms in aluminum near threshold. They reported three mechanisms of fatigue crack growth such as cleavage along the primary slip plane, crack extension by dislocation emission, and crack extension by opening along lattice defects. Horstemeyer *et al.* [Horstemeyer et al., 2010] revealed also that crack propagation mechanism depends on crystal orientation. They observed that, in the case of orientations resulting in double slip at crack-tip, the plastic slip was localized on two slip bands and crack propagates along one of the two slip bands leading to a mixed mode (mode I + Mode II) crack propagation. Cracks were found to grow by nanovoid absorption when crystals were oriented for multiple slip at crack-tip. Qiu *et al.* [Qiu et al., 2018] performed molecular dynamics simulations using a quasi-continuum method based on Embedded Atom Method (EAM) potential to investigate crack growth characteristics of single crystal iron and nickel under cyclic loading in terms of stress fields and force-distance curves. They observed that the variations of the force–distance curve become steady after a certain number of cycles. Liu and Zhou [Liu and Zhou, 2018] analyzed fatigue crack growth in polycrystalline metals with nanotwinned structures. They found that fatigue crack growth along twin plane during plastic deformation can be prevented by the presence of a hierarchically nanotwinned structures. By the means of cohesive zone representation in molecular dynamics simulations, Wu and co authors [Wu et al., 2015] analyzed crack growth mechanisms under two different cyclic loading regimes. Their simulations revealed that under increasing strain amplitude fatigue loading, the crack propagates rapidly after several cycles, finally crack-tip experiences a large plastic deformation which retardates crack propagation. Under constant strain amplitude, it was found that crack propagates by the linkage of voids formed ahead of crack-tip. Crack growth through grain boundaries was also investigated [Horstemeyer et al., 2010]. It revealed that for high misorientation angle grain boundaries, fatigue crack path deviates from one grain to another. However, for low crystal misorientation crack does not deviate significantly. Large misorientations were found to promote void nucleation at grain boundaries. Other studies on fatigue crack growth in single crystals [Ma et al., 2014, Sung and Chen, 2015, Tang et al., 2010] or on transgranular fatigue crack growth [Mao et al., 2018], or fatigue crack growth in nanocrystalline alloy [Chowdhury et al., 2013] or hydrogen effect [Zamora et al., 2015] can be pointed.

Overall, fatigue crack behavior at atomic scale has revealed different mechanisms of crack growth. Cleavage and void formation are the widely observed mechanisms in the MD literature in FCC metals under inert environment and are not in agreement with experimental observations in single crystals. If there is no doubt that plastic deformation plays an important role in fatigue crack growth, the exact contribution of plasticity remain unclear. In the following, we analyze the role of dislocations in fatigue crack growth in relationship with the microstructures described in chapter 4. Single crystals deformation at different

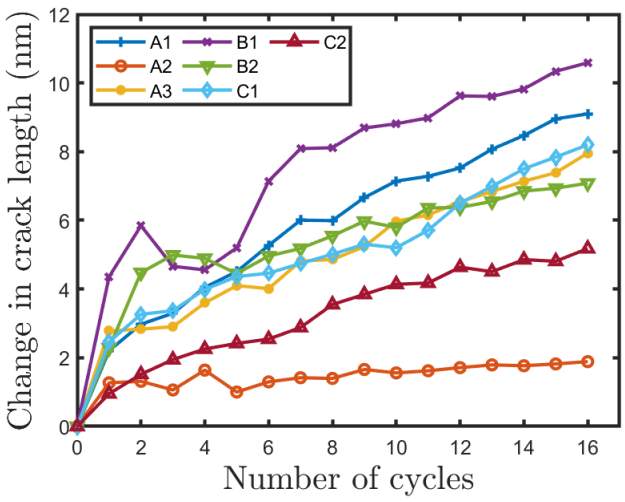

Figure 5-1: Change in crack length during cyclic loading for different crack orientations applying $\Delta K = 2.5\ \mathrm{MPa}\sqrt{\mathrm{m}}$ and $R = 0$. Whatever the orientation, two main regimes are observed: a transient regime at the beginning then a quasi steady regime.

load levels (stress intensity factor amplitudes) and for different crack configurations (Table 4.1, chapter 4) are carried out by the means of molecular dynamics simulations. Fatigue crack growth mechanisms as well as fatigue crack growth rates (FCGR) are analyzed in copper single crystals at room temperature (RT). The effects of crystal orientation are also highlighted. To achieve these objectives, large simulation boxes containing almost 18 - 20 millions of atoms is used.

The computational methods used in this chapter are the same as those used in the previous chapter. The reader can therefore refer to the previous chapter 4. Nevertheless, mention will be made of new features that will be introduced.

5.2 Fatigue crack growth rates

During cyclic loading, the crack-tip is deformed and propagates incrementally. Fig. 5-1 displays the change in crack length during cyclic loading. One can notice a non-steady crack growth during the first cycles. This short transient regime is due to the fact that, the initial state is a defectless state, namely without dislocations. This induces the crack to advance faster during the first loading cycles. Subsequently, with the emission of dislocations at the crack-tip, a steady regime appears and quasi-stable FCP develops. The number of cycle involved in this transient regime varies randomly between 1 and about 3 cycles depending on the crystal orientation and even up to $6 - 7$ cycles in the case of orientation B1. Hence, these first cycles where this transient regime prevails are not taken into account when estimating the FCGR. The FCGR is estimated by taking the slope of the quasi-steady linear regime.

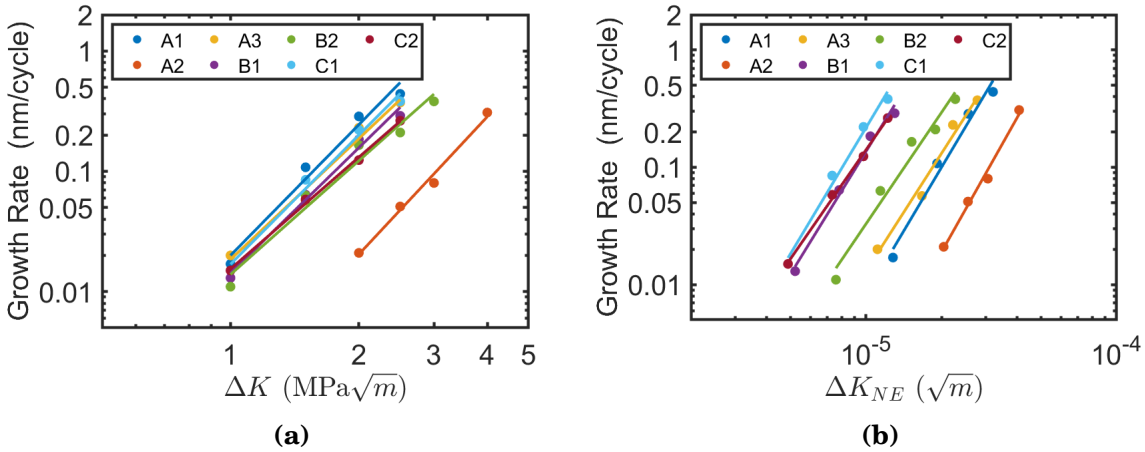

(a) **(b)**

Figure 5-2: FCGR as function of (a) SIF amplitude (b) normalized SIF amplitude.

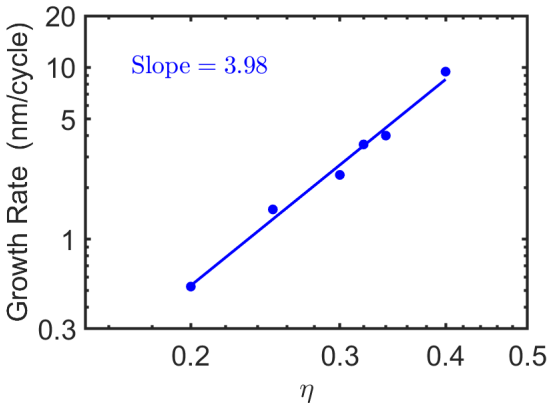

Figure 5-3: Experimental data of FCGR as function of $\eta = \frac{P}{P(COD=50\ \mu m)}$. Tests performed at 300 K under vacuum with a long axis along [1 0 0] and crack front oriented along [0 1 1] [Neumann et al., 1978] (Orientation A2)

The dependence of fatigue crack growth rate on SIF amplitude and on orientation is shown in Fig. 5-2. The fatigue crack growth data seems to obey reasonably well to Paris law [Paris and Erdogan, 1963]:

$$\frac{da}{dN} = C_1 \times (\Delta K)^{m_1} \tag{5.1}$$

where C_1 and m_1 are adjusted parameters that depend on the metal and crack orientation. Their values are reported in table 5.1. In Fig. 5-2, the dots are data from the present atomistic simulations and the solid lines represent the adjusted Paris law.

As previously evoked, we can notice a conformity with the Paris law. The exponents of the Paris law found in our simulations ranges between

3.08 for orientation C1 to 3.79 for orientations A2 (Table 5.1) Previous MD computations predicted a wide range for this exponent. Horstemeyer *et al.* [Horstemeyer et al., 2010] found a value of approximately 2 for different crack orientations in copper and nickel single crystals. For nanocrystalline nickel, Farkas *eet al.* [Farkas et al., 2005] reported an exponent of 2. Baker and Warner [Baker and Warner, 2014] investigated the mechanisms associated with fatigue crack growth in aluminium alloys single crystals and reported values of m_1 ranging between 3.5 and 6.7 according to the loading ratio. For $R = 0$, the exponent was found to be about 6.4-6.7 whereas it ranges between 3.5-5.0 for $R = 0.25$. Dislocation dynamics simulations by Deshpande *et al.* [Deshpande et al., 2002] provided power law exponents of 6.33 for $R = 0.1$, 6.46 for $R = 0.3$ and 8.55 for $R = 0.5$. Experimentally, the values often reported are generally between 3 [Frost et al., 1971] and 4 [Suresh, 1998] for metals and alloys, which is in agreement with our simulations.

Copper single crystals of various orientations were subjected to cyclic crack propagation at RT, under air environment by Ishii and Weertmann [Ishii and Weertman, 1971b]. The authors showed an orientation dependence of the Paris law exponent. They show that, the more the crystals were oriented towards $(1\,0\,0)$ - $(1\,1\,1)$ symmetry boundary, the larger was the value of the Paris law exponent. Experiments carried out in liquid nitrogen ($\mathrm{T} = 77\,\mathrm{K}$), display no orientation dependence of the power law exponent. Moreover, in liquid nitrogen experiments the exponents are approximately equal to 4 for all crystallographic orientations. The Neumann experiments [Neumann et al., 1978] carried out at RT under vacuum with copper single crystal oriented $(1\,0\,0)$ show also an exponent of the order of 4 (Fig. 5-3). The Paris law exponents obtained from our atomistic computations are therefore in close agreement with the experimental predictions of Neumann [Neumann et al., 1978] and Ishii and Weertmann [Ishii and Weertman, 1971b].

The propagation rates measured from our MD simulations show a fairly low scatter with respect to the crystalline orientation. Almost all of the crack orientations tested except for the A2 crack configuration appear to exhibit the same propagation rate. The Orientation A2 is the one which has the lowest propagation rate for the same ΔK. Moreover, crack orientation A1 exhibits the highest FCGR followed by the orientation C1, A3 then orientations B1, B2 and C2. With the exception of orientation A2, it can be observed that the closer the loading axis is oriented along the crystallographic direction $\langle 1\,0\,0 \rangle$ the higher the propagation rate, even if the difference is not so high. This is a priori in agreement with the experimental data of Ishii and Weertmann [Ishii and Weertman, 1971a].

This direct comparison can nevertheless be misleading due to the dependence of the crystal elasticity with the crystal orientation. We are now interested in the effect of the normalization of the SIF by the Young's modulus along each tensile crystallographic direction. Since Copper elasticity shows anisotropy it is also convenient to modify the Paris law with the normalized SIF. The normalized

SIF is defined by:

$$\Delta K_{NE} = \frac{\Delta K}{E^*_{ijk}} \tag{5.2}$$

where ΔK is the SIF amplitude and E^*_{ijk} is the plane strain Young's modulus. As expected, the MD FCGR data obey the Paris' law but using different parameters:

$$\frac{da}{dN} = C_2 \times (\Delta K_{NE})^{m_2} \tag{5.3}$$

Fig. 5-2b shows the fatigue crack growth rate vs normalized SIF ΔK_{NE}. C_2 and m_2 are adjusted parameters and as expected $m_1 = m_2$. These values can be found in table 5.1. The method of calculating the plane strain Young's modulus for cubic crystals was proposed by Knowles [Knowles, 2017]. Due to the dependence of the tensile elastic behavior of the crystal with respect to the crystal orientation, the normalization of the stress intensity factor with respect to the Young's modulus makes it possible to discuss the crack growth rate as a function of each crystal orientation without taking into account the anisotropy of cubic elasticity.

As can be seen from Fig. 5-2b or table 5.1 after the normalization of the SIF, the crack propagation rates is higher in the case of orientations C1, C2 and B1 while orientation A2 always exhibits the lowest FCGR. Orientations A1 and A3 are quite close in terms of FCGR while orientation B2 is somewhat detached from orientation B1. Considering the effect of the the crack front orientation, one can realize that the effect is more or less pronounced according to the loading axis considered. First configurations A1, A2 and A3, for which tensile stress axis is the same ($\langle 1\,0\,0 \rangle$) but different crack front orientations ($[0\,0\,1]$ for orientation A1, $[0\,1\,1]$ for orientation A2 and $[0\,2\,1]$ for orientation A3), are considered. The FCGR of crack configuration A1 and A3 are very close to each other while the orientation A2 stands out a little more with a lower FCGR. The fundamental difference observed between orientation A2 and orientations A1 and A3 concerns the plastic deformation mechanism at crack-tips. Indeed, for the orientations A1 and A3 the main plastic deformation mechanism observed around the crack-tip is the dislocation emission and gliding while in the case of orientation A2, an association of dislocation emission and gliding and deformation twinning is observed. Moreover, considering the orientations B1 and B2 for which the loading axis is a $\langle 1\,1\,0 \rangle$ axis, one also observes for a crack front parallel to axis $\langle \bar{1}\,1\,0 \rangle$ (crack configuration B2), the FCGR is lower than in the case of orientation B1 for which the crack front is aligned along the axis $\langle 0\,0\,1 \rangle$ axis. The same observation can be made for orientations C1 and C2 although the difference in FCGR is not very marked in this case compared to the effects observed for crack configurations A2 and B2. It seems therefore that, if the mechanical twinning offers an additional possibility of plastic deformation, it does not necessarily enhance crack front advance because deformation twinning implies both a huge plastic slip and large lattice rotation. These large and local transformation do not allow the crack front advance as in the case of dislocation emission.

Table 5.1: Paris law adjusted parameters C_i and m_i of Eq. 5.1, Eq. 5.3 respectively.

Orientation	$C_1 \left(\frac{nm.cycle^{-1}}{(MPa)^{m_1}}\right)$	m_1	$C_2 \left(\frac{nm.cycle^{-1}}{(\sqrt{m})^{m_2}}\right)$	m_2
A1	0.02	3.61	8.21×10^{15}	3.61
A2	0.0015	3.79	1.32×10^{16}	3.79
A3	0.018	3.34	6.00×10^{14}	3.34
B1	0.0143	3.46	3.03×10^{16}	3.46
B2	0.0139	3.14	3.03×10^{16}	3.14
C1	0.0169	3.57	1.50×10^{17}	3.57
C2	0.0154	3.08	3.76×10^{14}	3.08

5.3 Fatigue crack growth mechanisms at nanoscale

Cyclic crack growth often involves a certain number of damage phenomena at microstructure scale. Ritchie [Ritchie, 1999] classified the mechanisms involved in fatigue crack propagation (FCP) into two categories namely: the mechanisms causing the advance of the crack, which are called intrinsic mechanisms and the mechanisms delaying the propagation of the crack coined extrinsic mechanisms.

In the category of intrinsic mechanisms, two main mechanisms of fatigue crack propagation are generally reported in the literature as ductile metals and alloys are concerned. Firstly, the production and coalescence of cavities and secondly the blunting-resharpening mechanism. This last intrinsic mechanism (blunting-resharpening), is the only one observed close to the crack-tip in our MD simulations. Indeed, during the loading half cycle, the activation of the plastic deformation at the crack-tip leads to emission and gliding of dislocations. The plastic slip generated by the gliding of the emitted dislocations at the crack-tip and the gliding causes a crack-tip blunting and an advance of the crack front during the loading half cycle. During unloading, the half cycle dislocations emitted from the crack-tip, glide back to the crack-tip and cause a crack-tip resharpening. However, as we observed in chapter 4, the glide of dislocations emitted from a crack-tip is not fully reversible. Indeed, the various and numerous interactions between the dislocations lead to the formation of jogs, entanglements or dislocation locks (Lomer-Cottrell locks, Hirth locks,...), which impede the motion of mobile dislocations during unloading. Then, some of the dislocations will not be able to glide back to the crack-tip. Therefore, the forward plastic slip that yields to the advance of the crack front during loading is not completely recovered during the unloading half cycle leading to a net advance of the crack front (Fig. 5-4). This net advance of the crack front constitutes the cyclic crack growth. Therefore, fatigue cracks in ductile single crystals grow by blunting-resharpening and slip irreversiblity in near crack-tip zone.

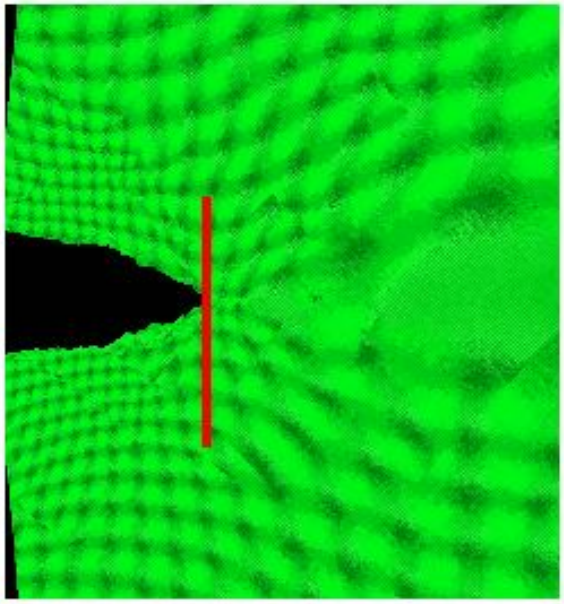

a)

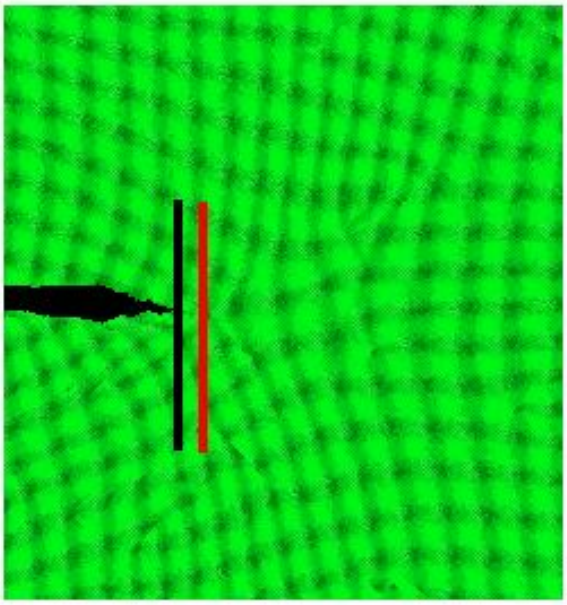

b)

Figure 5-4: Snapshots illustrating the mechanism of crack-tip blunting (a) and resharpening (b). The vertical lines indicate crack tip positions: the red line indicates crack tip position at the maximum loading ($\Delta K = 2.5\ \mathrm{MPa}\sqrt{\mathrm{m}}$) and the black line indicates the crack tip postion at the minimum load ($\Delta K = 0\ \mathrm{MPa}\sqrt{\mathrm{m}}$). The snapshots are taken at the 15th cycle. Crack configuration: A1

As discussed previously, the presence of jogs along dislocations and the presence of stair-rod partials and either Hirth partials in superjogged dislocations increases frictional forces that impede the glide of these jogged dislocations.

Dislocation cross-slip plays a significant role in the FCP. First of all, as pointed out by McEvily and Boettner [McEvily and Boettner, 1963a], in the loading cycle, the screw segments encountering an obstacle such as dislocation junctions for instance in the case of this study, will tend to cross-slip, aided by the pile-up of the following dislocations. By cross-slipping, they may act as source of additional dislocation loops, which would contribute to further blunting and advance of the crack-tip away from obstacles. Also, as shown in copper fatigued at room temperature by Essmann *et al.* [Essmann and Mughrabi, 1979, Essmann et al., 1981], two meeting screw dislocations of opposite signs will annihilate spontaneously by cross-slip, if the distance between their glide planes is smaller than 50 nm. Due to annihilation, the glide back to the crack-tip of annihilated dislocations is impossible. This causes additional plastic irreversibility leading to cyclic crack advance. Cross-slip also induces changes of slip plane. The reversibility of dislocation when gliding back towards crack-tip requires that all the dislocations emitted during the loading half cycle take exactly the opposite path during the unloading half cycle. Due to the frequent change of screw dislocation slip planes caused by cross-slip, this condition is hardly met. As a result, slip irreversibility can be observed at a crack-tip.

The production of vacancies following dislocations interactions and subsequent stacking fault tetrahedra (SFTs) production by low scale vacancy aggregation are all obstacles that will may increase the cumulative plastic irreversibility and help the advance of the crack front cycle after cycle. Indeed, it is well established in our simulations and from the literature that, SFTs can act as hard obstacle, which can impede the glide of dislocations [Wirth et al., 2000b]. And this induces slip irreversibility during unloading. Also as pointed out Baker and Warner [Baker and Warner, 2014], when the crack propagates into a defect such as vacancy, the crack does not return to its original configuration when the load is removed.

Some atomistic studies claimed that fatigue crack propagation is due to the dislocation emission from crack-tip. This is fully true during loading half cycle. The advance of the fatigue crack during loading half cycle is higher than that measured at the end of the full cycle ($\mathrm{R} = 0$). This advance is actually due to the dislocation emission and further gliding. During the unloading half cycle, this advance observed during loading is reduced, due to a partial rewelding, and the unrecovered part of this advance is the cyclic propagation increment. The partial rewelding of fatigue crack has been observed experimentally by Kikukawa *et al.* [Kikukawa et al., 1979]. The FCP is therefore not only due to the dislocation emission and gliding inducing crack advance during loading, but also and especially due to the irreversibility of dislocations glide because of different dislocation substructures and other lattice defects remaining close to the crack-tip in the whole simulation box after unloading.

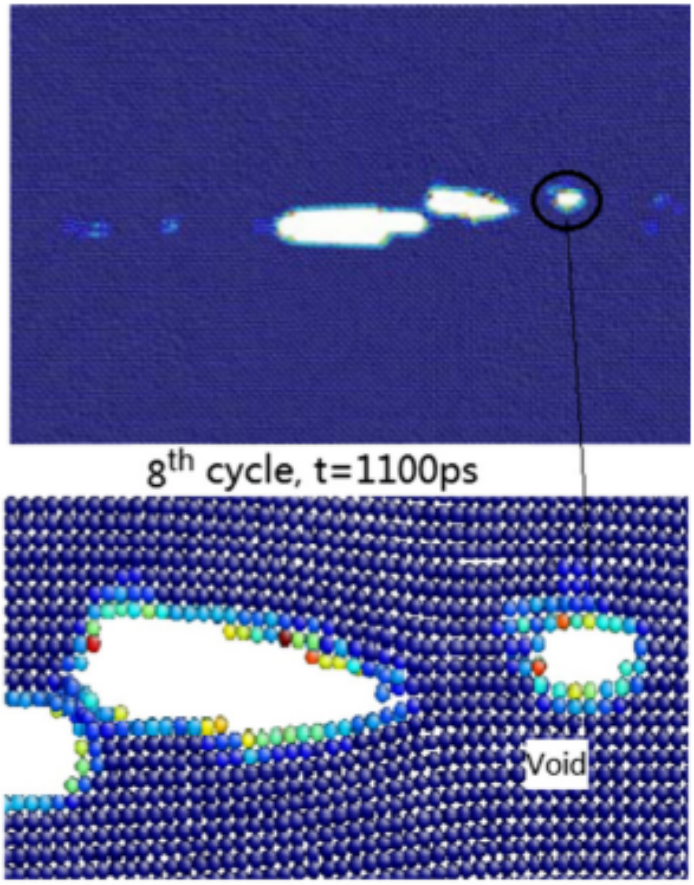

Figure 5-5: Fatigue crack growth by cavity coalescence observed in MD simulations. Quoted by [Wu et al., 2015]

Our simulations are in contradiction with numerous previous atomistic simulations of fatigue crack propagation under inert environment [Farkas et al., 2005, Horstemeyer et al., 2010, Potirniche and Horstemeyer, 2006, Potirniche et al., 2005, Zhou et al., 2015, Wu et al., 2015], which showed widely cavity formation as depicted for example in Fig. 5-5. In these studies the authors conclude that the main mechanism of fatigue crack propagation is the nucleation, growth and coalescence of cavities ahead of fatigue crack-tip.

No cavity formation is predicted in our simulations whatever the conditions (orientation, SIF). This mechanisms, is not reported by experimental observations carried out on pure single FCC crystals provided the specimen thickness is higher than the TEM foil ones. Indeed, the formation of cavities is generally reported in alloys containing second phase particles around which the localization of the plastic deformation can cause the formation of cavities and subsequently their coalescence. The formation of cavities in highly pure metals is prevented or nearly impossible because of the absence of impurities and/or particles of secondary phase. Therefore, we believe that the formation of cavities ahead of crack-

tip reported previously in some MD simulations results from a certain number of artifacts that were introduced by the simulation conditions adopted. This concerns, in particular the choice of the thickness of the simulation box, measured along the crack-front and the loading conditions. The too thin box thicknesses over-constrain the plastic deformation [Zhang and Ghosh, 2013] and reduce the nucleation of dislocation loop which are necessary in the plastic deformation process. This can lead to the formation of the cavities. The application of uniform displacement at the boundaries of the simulation box (or uniform stresses) instead of LEFM displacement fields, leads to an overestimation of the stresses ahead of the crack-tip, resulting in propagation mechanisms that are not consistent with the experimental observations. Other atomistic studies have also reported propagation of fatigue cracks by cleavage, which is not observed in our simulations. The cleavage observed in previous studies is also thought to be an artifact of the effects discussed above.

Since the pioneering work of Laird and Smith [Laird and Smith, 1962] who proposed for the first time the blunting-resharpening mechanism, many researcher as Pelloux [Pelloux, 1970], Neumann and co-workers ([Neumann, 1974, Neumann et al., 1978], Pippan, Riemelmoser and co-workers ([Riemelmoser et al., 1997, Riemelmoser et al., 2001, Pippan et al., 2011]) focussed on cyclic crack propagation mechanisms and a more comprehensive and predictive approach.

Pelloux [Pelloux, 1970] suggested that fatigue crack blunting is the result of high strain concentration. According to the author fatigue crack growth is due to the repeated cyclic crack extension by alternating shear. The experiments of Pelloux were carried out on aluminium alloys and the author observed crack growth by alternating shear and void growth around intermetallic inclusions.

Neuman [Neumann, 1974, Neumann et al., 1978] carried out experiments on copper single crystals. On the basis of his observations, he suggested that the plasticity in near crack-tip zones is carried by two slip planes which originates from the crack-tip. According to Neumann model, strains are reversible at a enough large scale but, the author specifies that this reversibility is imperfect and does not occur at atomic the atomic plane. This would be the reason of the formation of striations on the fracture surfaces and consequently could be the reason of the cyclic crack propagation. Even if two slip planes are indeed sufficient to make advance a crack as suggested by Neumann, it is observed, in our simulations, the activation of plastic slip on more than two $\{1\,1\,1\}$ slip planes. This multiple slip induces the formation of various dislocations locks close to the crack-tip. These dislocation microstructures hinder the forward and backward glide of dislocations inducing plastic strain irreversibility in near crack zones and thus fatigue crack growth. Even if the macroscopic strains are all reversible, the near plastic strain is irreversible as also suggested by the FE computations of Hutar and Sauzay [Hutar and Sauzay, 2006] who showed a ratcheting effect in regions close to the crack-tip, and then crack advance.

Riemelmoser, Pippan and co-workers ([Riemelmoser et al., 1997, Riemelmoser et al., 2001, Pippan et al., 2011]) assumes a 2D array arrangement of dislocations emitted from crack-tip and suggested that these dislocations are reversible during the unloading half-cycle. The cyclic advance of the crack at the end of the cycle is the same as that induced by the emission of dislocations during the loading half cycle. In this model, the authors did not consider the partial crack rewelding as observed in our simulations and as shown experimentally under inert environment [Kikukawa et al., 1979, Neumann et al., 1978]. Indeed, according to the authors when dislocations are emitted from the crack-tip, they cause the formation of steps on crack lips and these steps are irreversible. This is actually only possible in air where the formation of oxide layers could indeed prevent the crack-tip rewelding. Also, the array arrangement of dislocations considered by the authors is not realistic since dislocations structures around crack-tip consist in complex dislocation tangles as shown in by simulations (Fig. 4-14) and by experiments carried out by [Dewald et al., 1990, McEvily and Boettner, 1963b, Awatani et al., 1978].

While the blunting-resharpening mechanism and slip irreversibility inherently cause fatigue crack propagation, crack closure acts as an extrinsic mechanism to delay the advance of the fatigue crack. The pioneering work of Elber *et al.* [Elber, 1970] explain the fatigue crack closure by an elastic unloading causing compressive stresses on the plastic wakes along crack lips: this is the phenomenon of plasticity-induced crack closure (PICC). The PICC was shown to play a role principally under plane stress loading conditions [Suresh and Ritchie, 1983, Lindley and Richards, 1974, McEvily, 1977]. However, many studies including those of Schmidt and Paris [Schmidt and Paris, 1973] showed fatigue crack closure in the case of near threshold crack growth when plane strain conditions prevail. Nevertheless, the numerical investigations of Newman [Newmann Jr, 1983] showed that the modeling of PICC with plane strain conditions was not sufficient to explain the various observations made previously. As pointed out in [Ritchie, 1999, Suresh and Ritchie, 1983], there are several mechanisms of crack closure at near thresholds levels where CTODs are small and approach the distance between the crack lips after unloading. Different mechanisms for fatigue crack closure that are generally reported in the literature apart from the PICC, are roughness-induced crack closure (RICC), oxide-induced crack closure (OICC), viscous fluid-induced crack closure (VICC) and transformation-induced crack closure (TICC). Since this study is carried out under inert environment, we are not concerned by the OICC. No viscous fluid was introduced in our simulations and phase transformation did not occur during cyclic loading. RICC is the most likely mechanism and is the one observed in this study. Indeed, in the current study, by prolonging the cyclic loading beyond 16 cycles in the case of crack configuration C1, one observes a beginning of crack closure from the 20th cycle where the crack surfaces came into contact prematurely during the unloading half cycle before the minimum load $\mathrm{K_{min}} = 0$ was reached. Indeed, at

approximately $0.8\ \mathrm{MPa}\sqrt{\mathrm{m}}$, during unloading half cycle, contact between crack surfaces takes place. Fig 5-6 illustrates this example of evolution of fatigue crack closure with the number of cycles. Indeed, it is observed that during cyclic loading, surface steps formed on fracture surfaces. These surface steps are thought to be the result of the dislocations gliding through the free surface and forming steps on the crack surfaces. These surface steps develop continuously during loading until they come into contact as illustrated on Fig. 5-6. As depicted in Fig. 5-6, no crack closure is observed at cycle 5 (Fig. 5-6a) but one can observe surface steps emerging from the crack surfaces. At cycle 10 (Fig. 5-6b), surface steps grow and lead to the first contact at cycle 20 (Fig. 5-6c) and an almost complete crack closure at cycle 25 (Fig. 5-6d).

Obviously, crack closure has an effect on the propagation of fatigue cracks, in particular by reducing the driving force required to propagate the fatigue crack. That is why Elber proposed to describe the propagation of fatigue cracks not in terms of the amplitude of SIF but in terms of effective SIF, which is defined as the difference between K_{max} and K_{open}, which is the SIF required for the re-opening between the crack lips. In the following section, we present the our MD results in terms of cyclic propagation rates. However, the computed FCGR are measured before crack closure occurs and therefore were not expressed as a function of the Elber effective SIF.

5.4 Crack geometry

5.4.1 Crack front geometry

It is known from previous experimental investigations that, due to the anisotropy of crystal plasticity, the shape of the crack front is often irregular in single crystals [Neumann, 1974]. Fig. 5-7a shows, for example, the crack front geometry for orientation A1 where the initial crack plane and crack front are respectively $(0\,1\,0)$ and $[0\,0\,1]$ (the initial crack front is straight). During fatigue loading, the crack front, which was initially straight evolves and becomes rough. Indeed, considering the blunting-resharpening model, Neumann [Neumann, 1974] shows that in the case of an FCC single crystal, loaded along $\langle 1\,0\,0\rangle$ direction, the crack front should always be parallel to the intersection line of two $\{1\,1\,1\}$ planes, i.e. a $\langle 0\,1\,1\rangle$ direction. Therefore, in the case of orientation A1, the crack front should be orientated at an angle of approximately $45°$ with respect to the initial crack front direction i.e. $\langle 0\,0\,1\rangle$ direction. In the specific case of this study, the crack propagates macroscopically along the $(0\,1\,0)$ plane and the latter contains two $\langle 1\,0\,1\rangle$ directions, which are inclined at $45°$ with respect to the initial crack front direction ($\langle 0\,0\,1\rangle$) and which are contained in the $(0\,1\,0)$ plane. The particular shape of the crack front geometry is shown in Fig. 5-7a. Our prediction agrees with the strong tendency to make the fatigue crack front parallel to the $\langle 0\,1\,1\rangle$ direction as deduced from the blunting-

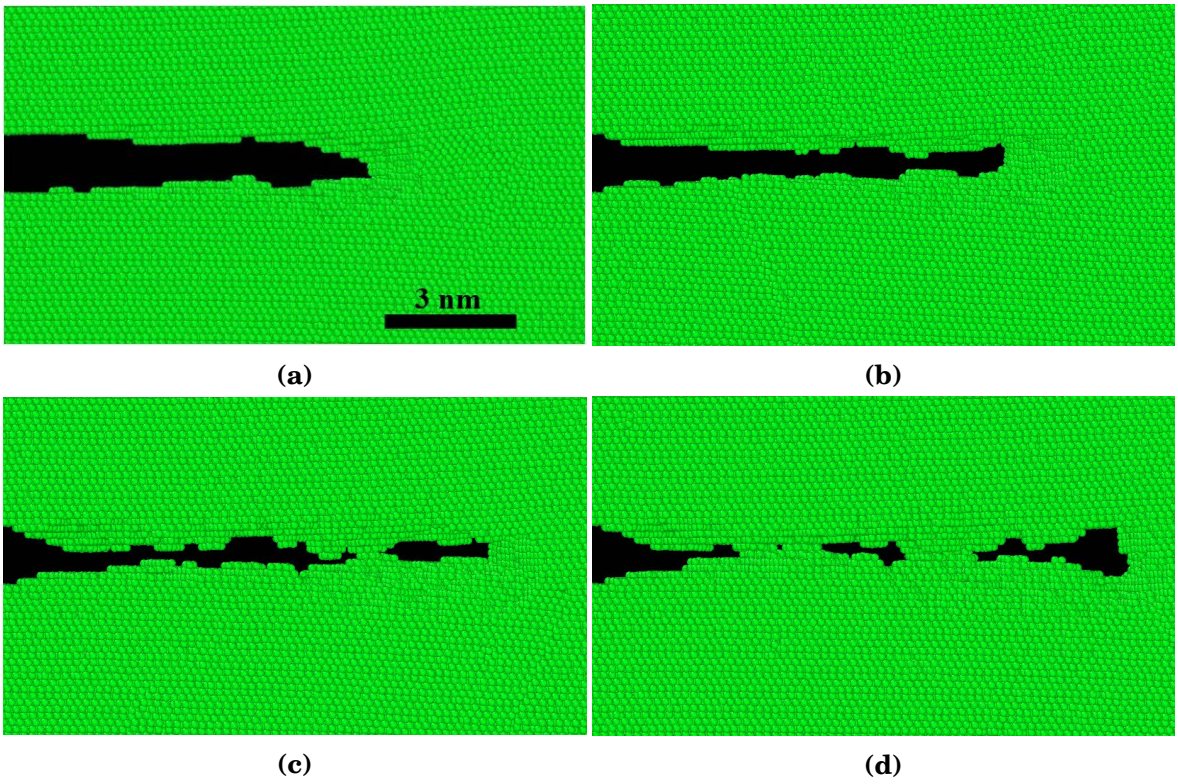

Figure 5-6: Snapshots of fatigue crack closure during cycling for crack configuration C1, $\Delta K = 2.5\ \mathrm{MPa}\sqrt{\mathrm{m}}$; (a) cycle 5; (b) cycle 10; (c) cycle 20 ; (d) cycle 25. Fatigue crack closure occurs from the 20^{th} cycle. Roughness on crack surfaces comes into contact leading to crack closure.

resharpening model [Laird and Smith, 1962] and shown experimentally by Neumann [Neumann, 1974]. As pointed out by Neumann [Neumann, 1974], by a suitable macroscopic force distributions, the crack front forms a zigzag line on a microscopic scale. This is observed in our simulations as illustrated in Fig. 5-7a, with segments being parallel to $\langle 0\,1\,1\rangle$ directions. These segments form angles ranging between 32 and $44°$ with respect to the initial front direction. As stated by Neumann [Neumann, 1974], multiple slip at crack-tip can lead to deviations up to $10°$ from the theoretical value of $45°$. It should also be reminded that in the context of this study thermal vibrations can also induce additional deviations.

Neumann [Neumann, 1974] observed experimentally that, in the case of orientation A2 where the initial crack front lie along the $[0\,1\,1]$ direction, the crack front remains straight during cyclic loading. Interestingly, our atomistic simulations lead to the same observations. Fig. 5-7b shows the crack front geometry obtained from crack configuration A2 for which the initial crack plane and crack front axis are $(1\,0\,0)$ and $[0\,1\,1]$, respectively. The crack front remains almost straight throughout the whole cyclic loading as suggested by the blunting-resharpening model [Laird and Smith, 1962] and as was also experimentally observed by Neumann [Neumann, 1974] in his tests on a copper single crystal which crack plane and crack front were respectively $(1\,0\,0)$ and $[0\,1\,1]$.

Therefore, our atomistic investigations agree well with observations and provide additional evidence that the main mechanism of FCP in ductile FCC single crystals is indeed blunting-resharpening and slip irreversibility rather than cavity coalescence or cleavage as reported previously and for which such crack front geometries would be difficult to obtain.

5.4.2 Fracture surface morphology

The analysis of fracture surfaces can be very instructive, in particular with regards to the mechanisms of FCP. In this section, fracture surfaces obtained from some crack configurations are shown. For instance, Fig. 5-8 and Fig. 5-9 shows the appearance of the fracture surfaces for orientations C1 and A1. These fracture surfaces are obtained by constructing a surface mesh using the positions of the surface atoms. We can indeed observe a fairly rough surface with "bumps" and "hollows" and in the form of river pattern running parallel to the direction of crack propagation (Fig. 5-8). This river pattern has been reported in experiments carried out by Forsyth and Ryder [Forsyth and Ryder, 1961] and by Neumann *et al.* [Neumann et al., 1978]. In the literature, the most reported fracture surface geometry under air environment are surfaces with striations running parallel to the crack front. However, it should be noted that for the most part, the studies reporting these types of fracture surfaces are tests carried out in air environment. In the majority of the tests carried out under vacuum or an inert environment, the authors did not observe these striations.

Fig. 5-10 illustrates the differences in fracture surface morphology according to the environment. As can be noticed, well defined striations appear on the

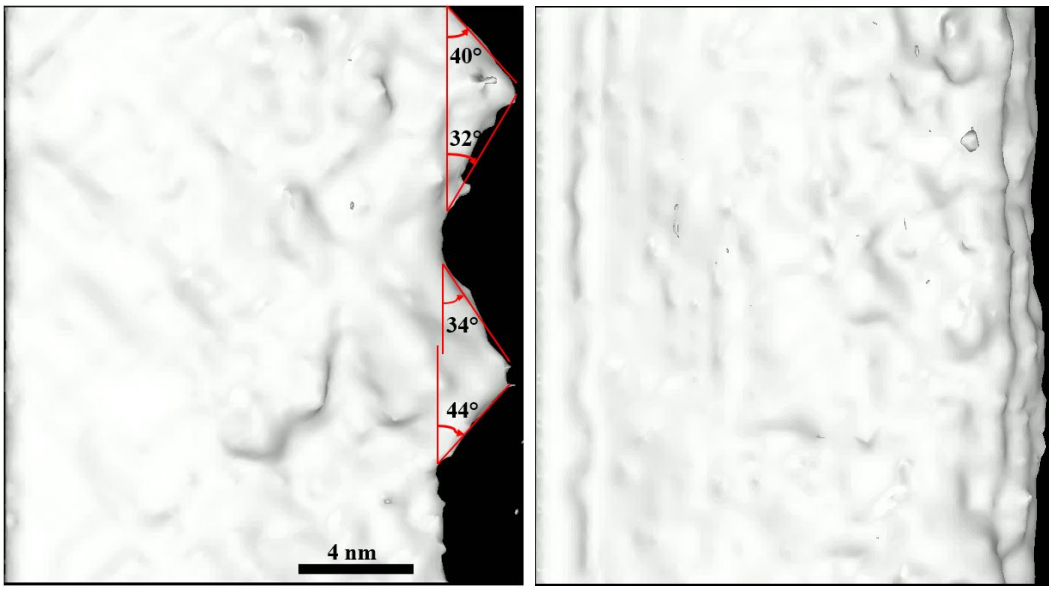

Figure 5-7: Crack front shape for (a) orientation A1 at applied $\Delta K = 2.5\ \mathrm{MPa}\sqrt{\mathrm{m}}, R = 0$ and (b) orientation A2 at applied $\Delta K = 4\ \mathrm{MPa}\sqrt{\mathrm{m}}, R = 0$.

fracture surfaces when the test environment is air whereas under vacuum, no striations are observed.

According to Neumann [Neumann, 1974], these striations are the result of the imperfect slip reversal. The spacing between these striations is often considered as the cyclic propagation increment in a well defined propagation regime.

The absence of fatigue striations under inert environment or under vacuum has also been widely reported in the literature as well as in the near-threshold regime. For instance, Stanzl-Tchegg and co-workers (Stanzl-Tchegg and Schönbauer [Stanzl-Tschegg and Schönbauer, 2010], Stanzl-Tchegg and Mayer [Stanzl-Tschegg and Mayer, 2001], Schönbauer and Stanzl-Tchegg [Schönbauer and Stanzl-Tschegg, 2013], Sarrazin-Baudoux *et al.* [Sarrazin-Baudoux et al., 2016]) investigated near threshold fatigue crack propagation in steels. They reported that, near the threshold regime, in vacuum as well as in ambient air mainly relatively smooth surface with no striations is visible. By increasing stress intensity, fracture appearance becomes rougher but still no striation is observed. The reasons for the absence of striations in an inert environment are still unclear. Some authors try to explain these observations. The experimental investigations of Davidson and Lankford (Davidson and Lankford [Davidson and Lankford, 1981, Davidson and Lankford, 1983], Lankford and Davidson [Lankford and Davidson, 1983, Lankford et al., 1983]) and of McEvily and Velasquez [McEvily and Velasquez, 1992] showed that the CTOD is much higher under vacuum than under moist air environment at the same K_{max} and according to McEvily and Velasquez [McEvily and Velasquez, 1992], this extent of crack-tip blunting in vacuum is responsible for removing stria-

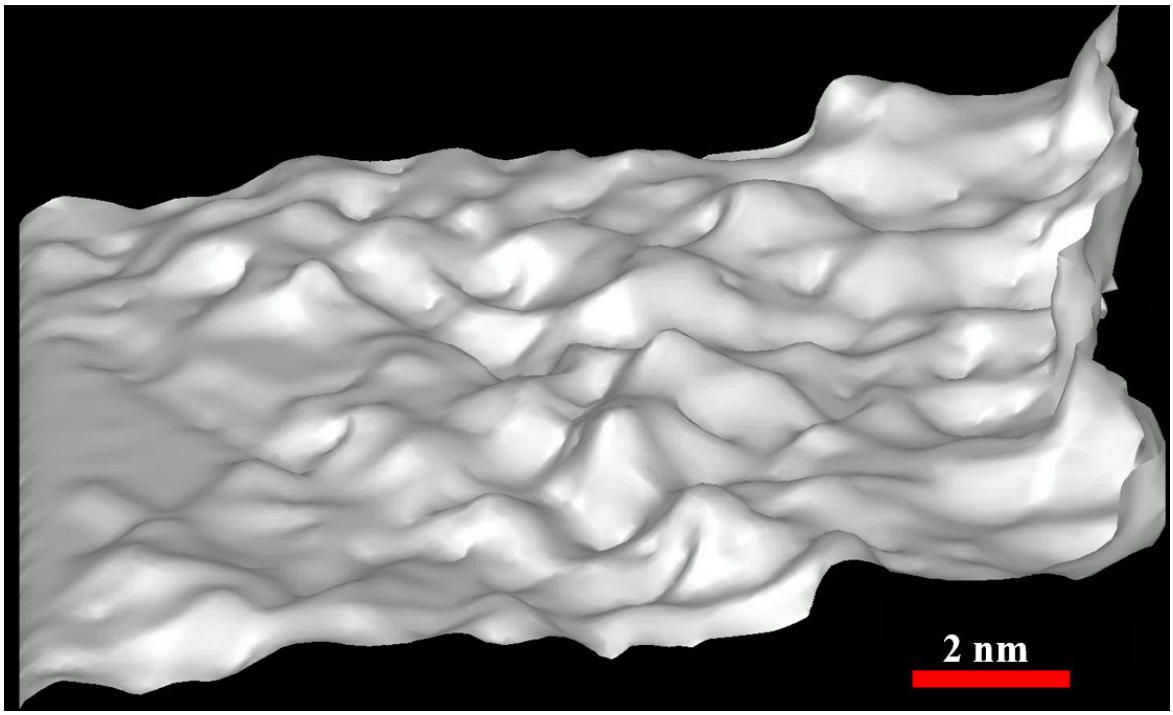

Figure 5-8: Fracture surface morphology for crack configuration C1. Applied loading $\Delta K = 2.5\mathrm{MPa}\sqrt{\mathrm{m}}, R = 0$. The fracture surface displays a relief with "bumps" and "hollows" and a river pattern. Crack propagation direction: from left to right

tions. According to Neumann, the rewelding observed under vacuum or inert environment should be the reason of the absence of striations. According to Laird [Laird, 1967b] the opening of holes in steels containing secondary phase particles completely suppresses the formation of striations, and such fracture surfaces appear like the ordinary fracture surfaces.

5.5 Conclusion

In this chapter, we have studied the mechanisms of crack propagation under inert environment in copper single crystals for various crystallographic orientations. It was initially shown that contrary to what some previous atomistic studies predicted, the mechanism of fatigue crack propagation in copper single crystals and more generally in pure metals with FCC structure, is blunting-resharpening following the emission of dislocations and plastic irreversibility. Moreover, It has been shown that this plastic irreversibility results from interactions between dislocations giving rise to the formation of junctions between dislocations, entanglements, different locks such as Lomer-cottrell locks, Hirth locks, etc. The cross-slip, which results in the change of slip planes and under certain conditions and the annihilation of the dislocations could induce an additional plastic irreversibility. The formation of jogs, the production of vacancies follow-

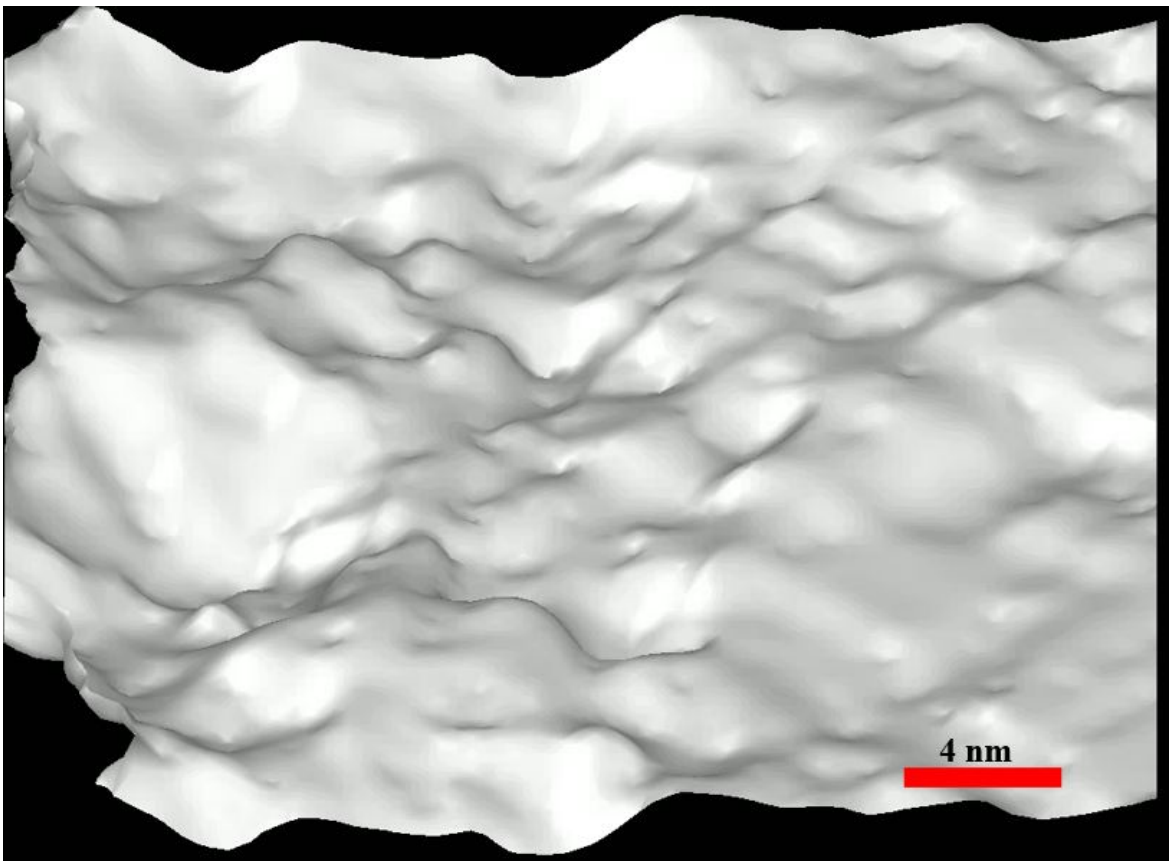

Figure 5-9: Fracture surface morphology for crack orientation A1. Applied loading $\Delta K = 2.5\mathrm{MPa}\sqrt{\mathrm{m}}, R = 0$. Crack propagation direction: from right to left

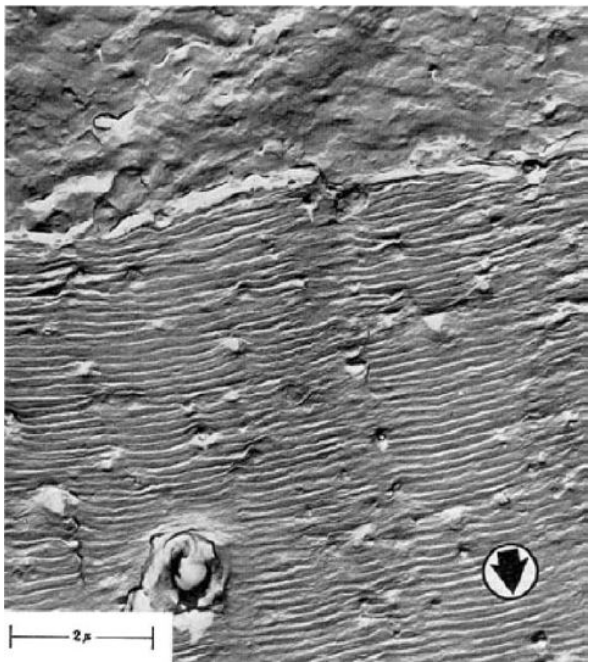

Figure 5-10: Fracture surface morphology of 2024 Aluminium tested in fatigue in vacuum (top) and in air (bottom) [Meyn, 1968]

ing the jogs dragging lead to the formation of stacking fault tetrahedra, which could also lock the motion of mobile dislocations and induce additional plastic irreversibility. The fatigue crack propagation rates were also analyzed. It was observed that the propagation could take place at rates lower than $10^{-10}\mathrm{m.cycle}^{-1}$ as reported experimentally. The propagation rate data are adjusted on the well-known Paris law and exponent between 3.1 to 3.7 have been predicted, which is in agreement with the experimental measurements. It was also observed that for the same stress axis, the influence of the crack front orientation on the propagation rate occurs through the crack-tip deformation mechanisms. More precisely, for crack front orientations favoring mechanical twinning at the crack-tip (which is thought to be an artifact of strain rate), the predicted propagation rates was lower than those without twinning for the same stress axis and for the same amplitude of the normalized stress intensity factor. The geometry of the crack front for example for orientations A1 and A2 are in agreement with the experimental observations and in agreement with the deductions of the theoretical model of Laird and Smith. Indeed, the particular shape of the crack front observed suggests that it is located along the intersection of the $(1\,1\,1)$ planes which are the slip planes in an FCC crystal. This therefore confirms the propagation mechanism observed previously. Analysis of the fracture surfaces does not reveal the striations generally reported on the fracture surfaces with tests carried out in air environment, which is also in agreement with the experimental observations in vacuum and/or inert environment. A particular fracture has been observed with "bumps", "hollows" and river pattern running parallel to the direction of crack

propagation, a geometry which is in agreement with the experimental observations under vacuum and in the near-threshold regime. Finally, an extrinsic crack propagation mechanism has been observed: crack closure. Indeed, it is observed that during cyclic loading, surfaces steps form on the fracture surface develop continuously until they come into contact, inducing in the process, a premature closure of the crack during unloading.

Based on these results, in particular the role of dislocations, cross-slip and other crack-tip phenomena observed in the two previous chapters, we have investigated the influence of temperature and stacking fault energy on fatigue crack propagation and this is what will be discussed in the next chapter.

THIS PAGE INTENTIONALLY LEFT BLANK

Chapter 6

Effect of temperature and stacking fault energy on fatigue crack propagation

Man verdirbt einen Jüngling am sichersten, wenn man ihn anleitet, den Gleichdenkenden höher zu achten, als den Andersdenkenden.

Friedrich Wilhelm Nietzsche, *Morgenröte. Gedanken über die moralischen Vorurteile*

Abstract

*In this chapter, we investigate the influence of temperature and stacking fault energy on the propagation of fatigue cracks, via molecular dynamics. First, simulations considering different copper single crystals are carried out at different temperatures (*77 K, 300 K *and* 600 K*) in order to study the impact of the temperature on the plastic deformation around crack-tip. The effect of temperature on crystal defects resulting from plastic deformation, the fatigue crack propagation mechanisms and rates are also investigated. A weak influence of temperature on the dislocation structures and on the other crystal defects is observed. Only slight effects can be attributed mainly to the temperature dependence of materials parameters. This weak influence of temperature on crystal defects leads to a weak influence on propagation rates; which is in agreement with the experimental observations. The propagation rates obtained are used to adjust the parameters of Paris law, and an exponent of approximately 4 is obtained, still in agreement with experimental observations. Secondly, the effect of the stacking fault energy on fatigue propagation is investigated through simulations carried out on different FCC single crystals presenting a wide variety of stacking fault energies (Ag, Al, Cu, Ni). An influence of the stacking fault energy is observed both on the dislocation microstructures and on the other crystal defects. Even if the mechanism of propagation is not fundamentally affected, the propagation rates are. And an attempt of explanation is proposed based on the crystal defects observed around the crack-tip in our simulations. The computed propagation rates in these different metals still provide an adjusted exponent of the Paris law of approximately 4, in agreement with experiments. Finally, a propagation model taking into account the normalized stacking fault energy is proposed and the latter allows to qualitatively reproduce the effect of the stacking fault energy observed experimentally.*

Contents

6.1 Introduction

From a practical point of view, the study of the fatigue of materials is very important because this damage mechanism represents about 80% of the causes of failure of mechanical devices in service. Many studies since the second half of the 20^{th} century have shed light or (at least partially) on the initiation and especially the propagation of fatigue cracks. These studies allowed considerable progress in understanding this phenomenon from both physical and mechanical point of view. But many questions remain concerning the comprehensive understanding of propagation mechanisms. This may allow the proposal of physically based model and quantitative predictions.

Fatigue of metals and alloys is characterized by the microstructure effects as evidenced by the studies [Ishii and Weertman, 1971a, Carlson and Koss, 1978, Rieux et al., 1979] which have shown the importance of the crystallographic orientation on fatigue crack growth rates in fatigued metals and alloys. Fatigue is also strongly affected by the physical properties of metals and alloys, in particular the stacking fault energy. Some investigations [Awatani et al., 1979, Miller, 1966, Ishii and Weertman, 1971a, Avery and Backofen, 1963, McEvily and Boettner, 1963b, McEvily and Johnston, 1967, Avery and Backofen, 1962] show the influence of the stacking fault energy in fatigue damage. More specifically, some of these studies show that metals and alloys with low stacking energy exhibit a higher resistance to fatigue crack propagation than metals with high stacking energy. Two main reasons were put forward to explain these observations. First, according to some authors such as Avery and Backofen [Avery and Backofen, 1962], Miller [Miller, 1966], Miller *et al.* [Miller et al., 1966], Awatani *et al.* [Awatani et al., 1979] the cell structure produced in high SFE metals influence the crack growth rate by offering a preferential crack path through cell boundaries. Second, according to Laird [Laird, 1967b], the high capacity of hardening of low SFE metals is the most important parameter controlling the fatigue crack-tip deformation and propagation. To shed light on the influence of the normalized SFE on the crack-tip plastic deformation and crack propagation, we carry out MD simulations of FCC metals with various normalized SFE.

Also, some investigations in literature was devoted to the effect of temperature on fatigue crack growth. These experimental investigations reveal a weak influence of temperature on fatigue crack propagation under vacuum or inert environment. This weak influence of temperature on fatigue crack propagation highlighted previously [Sarrazin et al., 1997, Petit et al., 2003, Cotterill and Knott, 1992] should also be understood in relation to the microstructure.

As stated by Dewald *et al.* [Dewald et al., 1990], the predictive modeling of the macroscopic response to load requires information on the microstructural response of the material. Therefore, it seems very relevant from a scientific point of view to understand the behavior of FCC metals subjected to cyclic loading, at

the microstructure scale, accounting for a large range of temperature and SFE. This is why, in this chapter, in order to shed light on the influence of temperature and stacking fault energy on fatigue crack propagation, we carry out, atomistic computations (molecular dynamics), to study at the atomic scale, the fundamental mechanisms of plastic deformation and propagation of fatigue cracks with respect to the temperature and stacking fault energy. Different pure single crystals with a face-centered cubic structure of various normalized stacking fault energies, namely, silver, aluminum, copper and nickel are subjected to cyclic mode I loading. The crack-tip dislocation structures are studied as function of temperature and the normalized stacking fault energy. The consequences in terms of fatigue cracks growth mechanisms and rates are also investigated.

6.2 Computational methodology

Classical molecular dynamics simulations are carried out with the LAMMPS (Large scale Atomic/Molecular Massively Parallel Simulator) software [Plimpton, 1995]. To investigate the effect of temperature, three different temperatures are tested: $77\,\mathrm{K}$, $300\,\mathrm{K}$, $600\,\mathrm{K}$ on three crack orientations: A1 $(0\,1\,0)[0\,0\,1]$, B1 $(1\,1\,0)[0\,0\,\bar{1}]$ and C1 $(1\,1\,1)[1\,1\,\bar{2}]$. Four pure single crystals are considered in the following (Ag, Al, Cu, Ni) in order to study the effect of stacking fault energy (SFE) on crack orientation A1.

Embedded Atom Method (EAM) type potentials are used. These potentials are known to reproduce well physical and mechanical properties of metals and alloys. The total potential energy in the framework of EAM formalism is given by:

$$E_{tot} = \sum_i F\left(\bar{\rho}_i\right) + \frac{1}{2}\sum_{ij} V(r_{ij}) \tag{6.1}$$

where $V\left(r_{ij}\right)$ is a pair potential; r_{ij} is the distance between the atoms i and j; F is the embedding energy as a function of the host electron density $\bar{\rho}_i$. The latter is given by:

$$\bar{\rho}_i = \sum_{j \neq i} \rho_j\left(r_{ij}\right). \tag{6.2}$$

All parameters in the mathematical functions are metal dependent.

- ***Embedded Atom Method Potentials for Ag***
  The interatomic potential of Ag is adjusted almost in the same way as the Cu interatomic potential used previously since the potential of Ag developed by Williams *et al.* [Williams et al., 2006] has been set up, based on the mathematical descriptions used for Cu [Mishin et al., 2001]. The pair

potential is taken as a superposition of two Morse potentials.

$$V(r) = \left[E_1 M(r, r_0^{(1)}, \alpha_1) + E_2 M(r, r_0^{(2)}, \alpha_2) + \delta\right] \psi\left(\frac{r - r_c}{h}\right) - \sum_{n=1}^{3} H\left(r_s^{(n)} - r\right) S_n \left(r_s^{(n)} - r\right)^4 \tag{6.3}$$

where M is a Morse function given by :

$$M(r, r_0, \alpha) = \exp\left[-2\alpha(r - r_0)\right] - 2\exp\left[-\alpha(r - r_0)\right] \tag{6.4}$$

and $H(x)$ is a unit step function.
The electron density function is described by :

$$\rho(r) = \left[a\exp(-\beta_1(r - r_0^{(1)})^2 + \exp(-\beta_2(r - r_0^{(2)}))\right] \psi\left(\frac{r - r_c}{h}\right) \tag{6.5}$$

where ψ is the cutoff function and is given by:

$$\psi(x) = \begin{cases} 0 & \text{if } x \geqslant 0 \\ \frac{x^4}{1+x^4} & \text{if } x < 0 \end{cases} \tag{6.6}$$

E_1, E_2, $r_0^{(1)}$, $r_0^{(2)}$, α_1, α_2, δ, r_c, h, $\left(r_s^{(n)}, S_n\right)_{n=1,2,3}$ are parameters to be adjusted. The values of the adjusted parameters can be found in [Williams et al., 2006] for Ag and in [Mishin et al., 2001] for Cu

- ***Aluminium potential parameterization*** ([Mishin et al., 1999])
In the case of Al, the pair potential and the electron density function are respectively represented by:

$$V(r) = V_s(r) - V_s'(r_c)\,\psi(r - r_c)), \tag{6.7}$$

$$\rho(r) = \rho_s(r) - \rho_s'(r_c)\,\psi(r - r_c)), \tag{6.8}$$

where ψ is a cutoff function defined by :

$$\psi(x) = \frac{x}{1 + \beta^n x^n} \tag{6.9}$$

with $\beta = 2$ and $n = 4$.
V_s and ρ_s are cubic splines through a given set of points (r_i, V_i) $(i = 1, ..., N_1)$ and (r_i, ρ_i) $(i = 1, ..., N_2)$

The embedding function $F(\bar{\rho})$ was represented by a cubic spline through a set of points $(\bar{\rho}_i, F_i)$; $(i = 1, ..., N_3)$

- ***Ni potential parameterization*** ([Mishin, 2004])
  For Ni, the pair potential is taken in a generalized Lennard-Jones form

$$V(r) = \left[\frac{V_0}{b_2 - b_1}\left(\frac{b_2}{z^{b_1}} - \frac{b_1}{z^{b_2}}\right) + \delta\right]\psi\left(\frac{r - r_c}{h}\right) \tag{6.10}$$

  with $z = {}^{r}/_{r_1}$. The electron density field is formulated as:

$$\rho(r) = \left[A_0 z^y e^{-\gamma z}\left(1 + B_0 e^{-\gamma z}\right) + C_0\right]\psi\left(\frac{r - r_c}{h}\right) \tag{6.11}$$

  with $z = r - r_0$.
  ψ function is taken as :

$$\psi(x) = \begin{cases} 0 & \text{if } x \geqslant 0 \\ \frac{x^4}{1+x^4} & \text{if } x < 0 \end{cases} \tag{6.12}$$

The embedding function is taken by inverting the universal equation of state [Zope and Mishin, 2003, Rose et al., 1984] of the FCC structure which is given by:

$$E(a) = E_0\left[1 + \alpha x + \beta\alpha^3 + x^3\frac{2x+3}{(x+1)^2}\right]e^{-\alpha x} \tag{6.13}$$

where $x = a/a_0 - 1$ and

$$\alpha = \left(-\frac{9\Omega_0 B}{E_0}\right)^{1/2} \tag{6.14}$$

Ω_0 is the equilibrium atomic volume, B the bulk modulus and E_0 the cohesive energy. V_0, b_1, b_2, δ, γ, δ, y, B_0, C_0, r_0 and r_1 are adjusted parameters.

For the study of the effect of temperature, the computations are carried out on copper single crystals. As stated previously, the orientations chosen are the A1, B1, and C1 orientations.

The orientation A1 is the only one used in the investigation of the effect of the stacking fault energy. Otherwise, the computational methodology of the previous chapters is still valid with regard to the simulation setup and post-processing.

6.3 Effect of temperature on fatigue crack behavior

6.3.1 Crack-tip plasticity

In this section, the effect of temperature on dislocation nucleation from crack-tip, plastic deformation mechanisms and crystal defects are investigated. Three different temperatures: 77 K ($\approx 0.05\ T_m$), 300 K ($\approx 0.22\ T_m$) and 600 K ($\approx 0.44\ T_m$,

T_m is the melting temperature), are investigated. Generally it is reported that the increase in temperature causes a decrease in yield stress. Our simulations showed a slight temperature effect on crack-tip dislocation emission. In fact, Fig. 6-1a shows that there is a slight decrease in the stress intensity factor required for dislocation emission from crack-tip (measure during the first loading half cycle). Another way to look at this effect is to consider the Fig. 6-1b, Fig. 6-1c and Fig. 6-1d where the critical stress intensity factor required for dislocation emission is normalized with the shear modulus, Young's modulus and unstable stable stacking fault energy to take into account the change in elasticity constants and unstable stacking fault energy with temperature. Thus one can see in Fig. 6-1b, Fig. 6-1c and Fig. 6-1d, that the dependence of K_{Ie} with temperature is not obvious. This agrees with some previous computations. Indeed as shown by Warner and Curtin [Warner and Curtin, 2009], the temperature-dependence of the energy barrier for dislocation nucleation is essentially driven by the change in elastic constants and stable and unstable stacking fault energy with respect to the temperature.

(i) For orientation A1 for example, the dislocation emission from the crack-tip occurs for a SIF of about $0.812\ \mathrm{MPa}\sqrt{\mathrm{m}}$ at $77\ \mathrm{K}$ while at $300\ \mathrm{K}$ the first dislocations are emitted for a SIF of about $0.752\ \mathrm{MPa}\sqrt{\mathrm{m}}$ and about $0.574\ \mathrm{MPa}\sqrt{\mathrm{m}}$ at $600\ \mathrm{K}$.

(ii) In the case of orientation B1, the emission of dislocations can be estimated to approximately $0.75\ \mathrm{MPa}\sqrt{\mathrm{m}}$ at $77\ \mathrm{K}$ and to approximately $0.692\ \mathrm{MPa}\sqrt{\mathrm{m}}$ at $300\ \mathrm{K}$, and $0.574\ \mathrm{MPa}\sqrt{\mathrm{m}}$ at $600\ \mathrm{K}$.

(iii) Finally, for orientation C1, the SIF requires for dislocation emission from the crack-tip at $77\ \mathrm{K}$ is about $0.6\ \mathrm{MPa}\sqrt{\mathrm{m}}$. This SIF is estimated at $0.516\ \mathrm{MPa}\sqrt{\mathrm{m}}$ at $300\ \mathrm{K}$ and to $0.41\ \mathrm{MPa}\sqrt{\mathrm{m}}$ at $600\ \mathrm{K}$.

If temperature modifies slightly the SIF required for dislocation emission from crack-tip, it does not however modify the mechanism of plastic deformation at crack-tip. Indeed, whether the computation temperature is $77\ \mathrm{K}$, $300\ \mathrm{K}$ or $600\ \mathrm{K}$, only dislocation emission and gliding processes are observed as plastic deformation mechanism. As previously, no deformation twinning is observed for these orientations whatever the temperature tested in this investigation.

Since plastic deformation proceeds by dislocation emission and gliding from crack-tip, it is interesting to investigate the effect of temperature on dislocation density evolution during cyclic loading. Fig. 6-2 shows the evolution of the total dislocation density during cyclic loading for the three crack orientations under study at the three temperatures investigated. In general, we observe the same trends in the evolution of dislocation density whatever the temperatures for a given crack orientation: the dislocation density increases with the number of cycles. After the first cycles for example (1st - 5th or 6th cycle depending on the orientation), the increase in the dislocation density can be considered to be linear and the increasing rate for crack orientation A1 can be estimated at about $6 \times 10^{14}\ \mathrm{m}^{-2}.\mathrm{cycle}^{-1}$ at $77\ \mathrm{K}$, $4 \times 10^{14}\ \mathrm{m}^{-2}.\mathrm{cycle}^{-1}$ at $300\ \mathrm{K}$, and $5 \times 10^{14}\ \mathrm{m}^{-2}.\mathrm{cycle}^{-1}$ at $600\ \mathrm{K}$. For orientation B1, this increasing rate is estimated at approximately $2 \times 10^{14}\ \mathrm{m}^{-2}$ at $77\ \mathrm{K}$ and $600\ \mathrm{K}$ and at about $5 \times 10^{14}\ \mathrm{m}^{-2}$ at $300\ \mathrm{K}$. For orientation

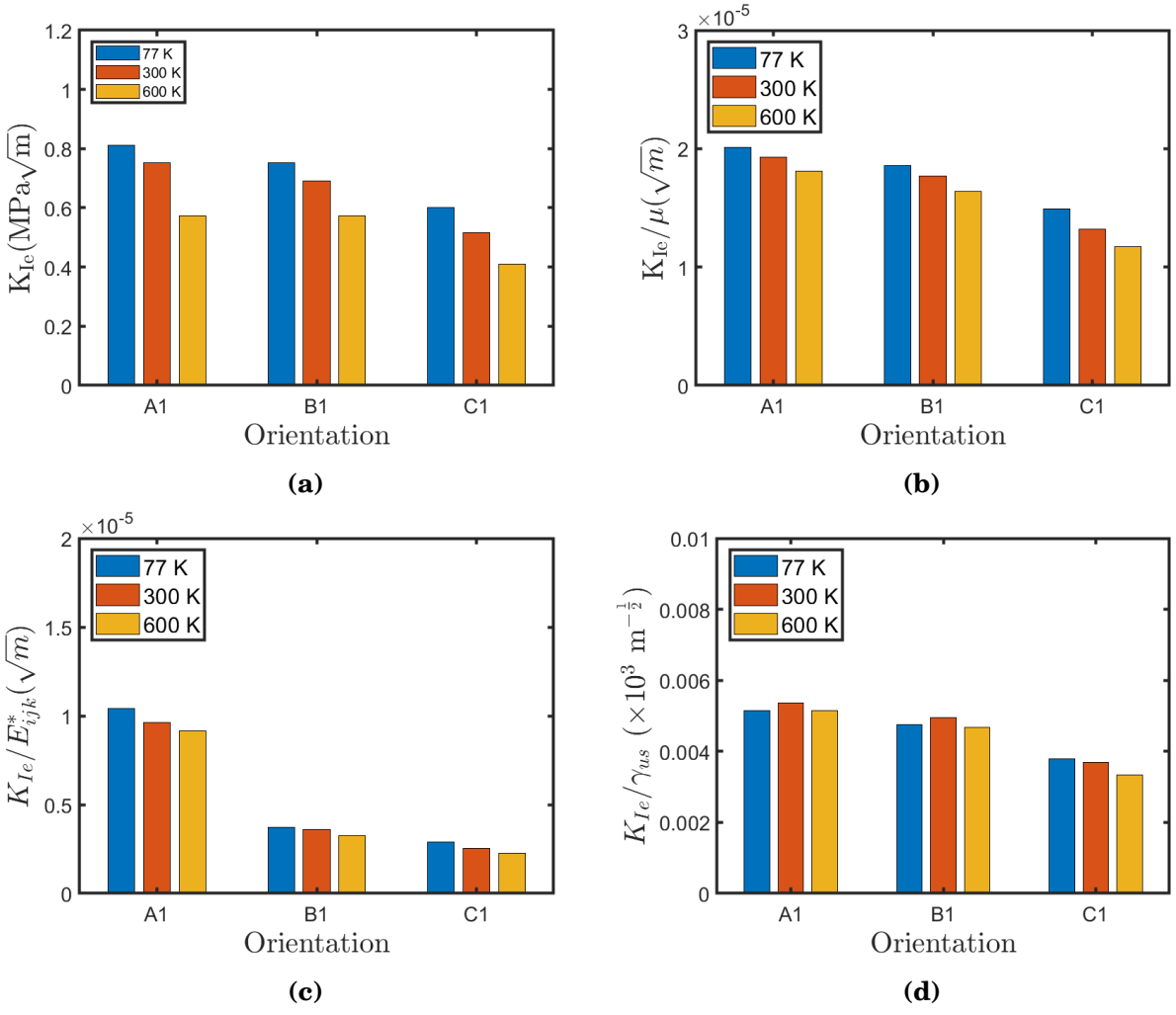

Figure 6-1: Effect of temperature on crack-tip dislocation emission. (a) Critical SIF K_{Ie} for dislocation emission (b) Normalized critical SIF K_{Ie}/μ (c) Normalized critical SIF K_{Ie}/E^*_{ijk} (d) Normalized critical SIF K_{Ie}/γ_{us} One can observe that the dependence of dislocation emission SIF on temperature is driven by the dependence of materials parameters on temperature.

C1, the increasing rate is about 1.5×10^{14} m^{-2} at $77\,\mathrm{K}$ and $300\,\mathrm{K}$, and about 4×10^{14} m^{-2} at $600\,\mathrm{K}$.

To summarize, for orientation A1 and B1, the dislocation density evolution at $77\,\mathrm{K}$, $300\,\mathrm{K}$ and $600\,\mathrm{K}$ appear to be parallel and rather close. But for orientation C1, it is rather the total dislocation densities at $77\,\mathrm{K}$ and $300\,\mathrm{K}$ increases slowly and are close. However, the differences in the total dislocation densities predicted at the three different temperatures are not significant with regard to the temperatures tested. Indeed, after neglecting some fluctuations during the first cycles, the ratio between the maximum dislocation density among the three temperatures and the minimum dislocation density among the three temperatures amounts to about 1.3 for the orientation A1, and 1.5 for the orientation B1. For orientation C1, this ratio reaches approximately 1.75. We could therefore conclude that in the range of temperatures studied, temperature display a moderate effect on the total density of dislocations. Moreover, in terms of dislocation structuring near crack-tip, no significant difference can be reported as depicted in Fig. 6-3. Indeed, Fig. 6-3 shows a close-up of dislocation networks around crack-tip in copper for orientation C1 at different temperatures and at the 15^{th}. As one can notice, dislocation networks around crack-tip seem similar and no clear effect can be reported.

In addition, the proportion of each type of dislocation does not vary significantly with temperature. One can observe in Figs. D-2, D-3, D-4, D-5, and D-6 of Appendix D, that the proportions of Shockley partials, stair-rod partials, Hirth partials, perfect dislocations, and Frank partials are only slightly affected by the temperature in the range $77\,\mathrm{K}$-$600\,\mathrm{K}$.

In Figs. D-2, D-3, D-4, D-5, and D-6, one can see that whatever the applied temperature, Shockley partials proportions decrease during cyclic loading. The stair-rod partials proportions are found to increase during cycling and Hirth partials proportions decrease slightly. Whether the applied temperature is $77\,\mathrm{K}$, $300\,\mathrm{K}$ or $600\,\mathrm{K}$, perfect dislocations and Frank partials proportion is found to be constant during fatigue loading.

Shockley partials proportions decrease from $82\% - 87\%$ at the end of the first cycle to $72 - 74\%$ at the end of the 16^{th} for orientation A1. For orientation B1, Shockley partials proportions decrease from approximately 80% to approximately $61 - 70\%$. And for orientation C1, Shockley partials proportions decrease from $83 - 86\%$ to approximately $67 - 72\%$.

Stair-rod partials proportions are found to increase from about $8 - 10\%$ to 25% for orientation A1. for orientation B1, the stair-rod partials proportions increase from $13 - 17\%$ up to approximately $27 - 35\%$. As orientation C1 is concerned, the stair-rod partials proportions increase from $10 - 12\%$ to $25 - 30\%$.

The Hirth partials proportions decrease from $2 - 3\%$ to $1 - 2\%$ for orientations A1 and B1 while for orientation C1 their proportions seem to be constant during cyclic loading.

Perfect dislocations proportions seem to be constants between 0.5% and 1.5% during for orientation A1 and between 1% and 2% for orientations B1 and C1.

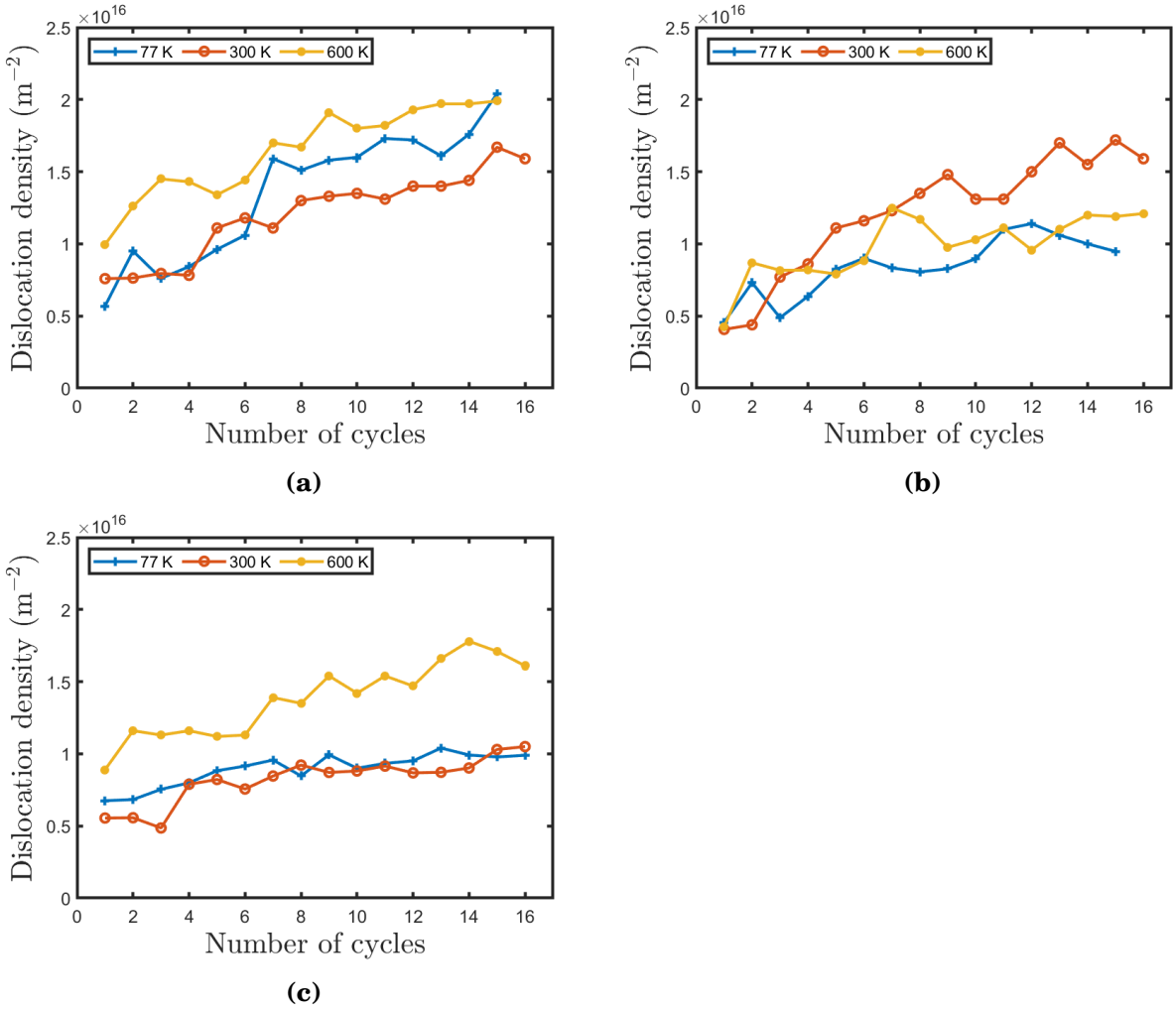

Figure 6-2: Evolution of the dislocation density for orientation (a) A1, (b) B1 and (c) C1 as a function of number of cycles for different temperature in copper.

Finally, Frank partials proportions are also found to be constant between 0 and 0.5% for orientation A1, whereas for orientations B1 and C1, Frank partials proportions are constant and fluctuate between 0 and 1%.

Interactions between dislocations generally result in the formation of various dislocation structures. In chapter 4, we state that the dislocation structures observed near crack-tip zones are not so different whatever the crystal orientation considered. In this investigation of temperature effect, it is also observed that whatever the applied temperature, the same dislocation structures are observed near the crack-tip(Fig. 6-3).

Point defects such as vacancies and vacancy clusters in the form of stacking fault tetrahedra are also observed. Fig. 6-6 shows for example the evolution of the vacancy concentration as a function of the number of cycles for each applied temperature and for orientation A1 (Fig. 6-6a), B1 (Fig. 6-6b) and C1 (Fig. 6-6c).

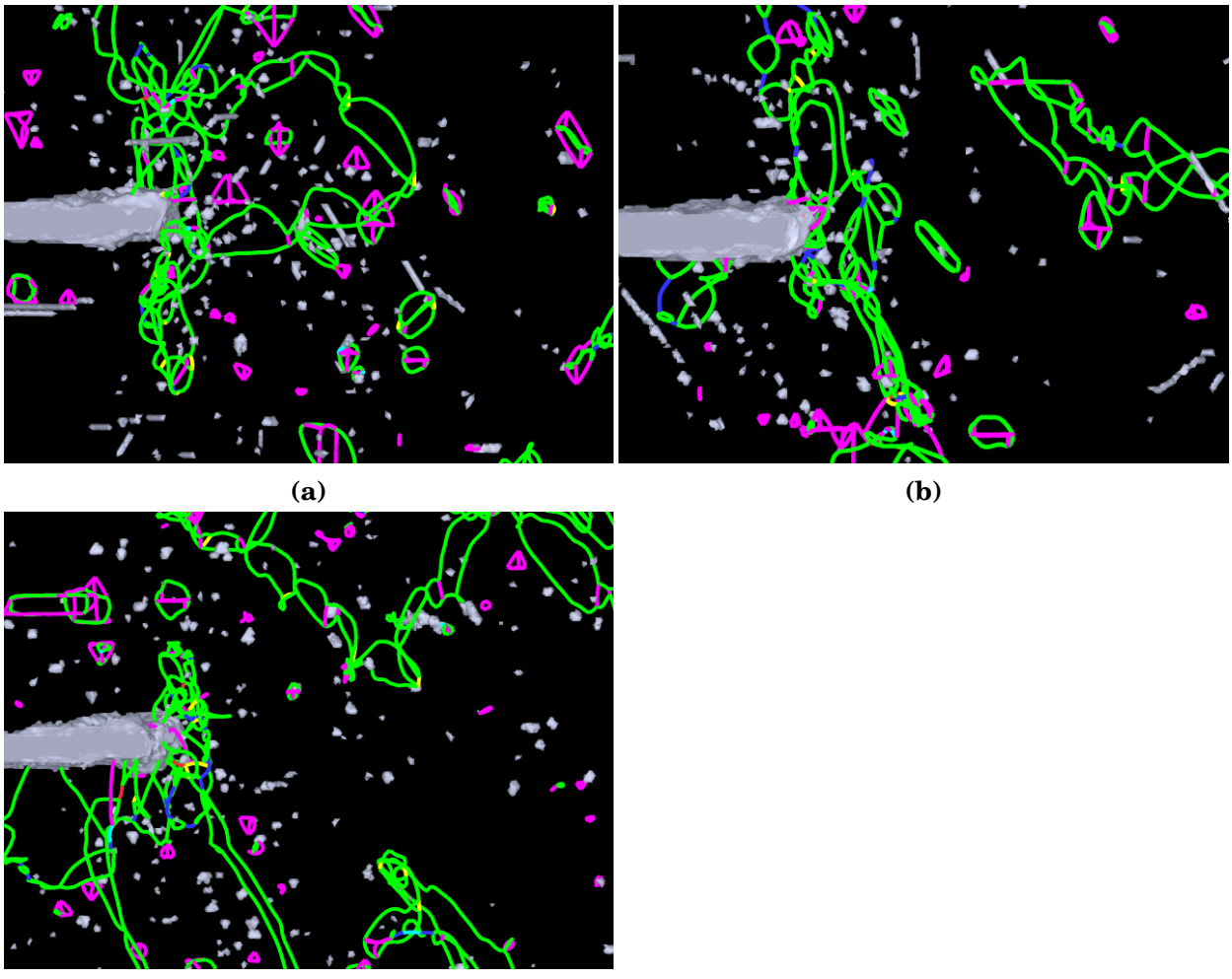

(a) **(b)**

(c)

Figure 6-3: Effect of temperature on dislocation network around fatigue crack-tip at the 15^{th} cycle in crack configuration C1 at (a) $77\,\mathrm{K}$, $300\,\mathrm{K}$ and (c) $600\,\mathrm{K}$.

Whatever the temperature or crack orientation, we clearly observed an increase in vacancy concentration with the number of cycle. The trends in vacancy concentration versus temperature follow almost the same trend as that in dislocation density versus temperature. We can estimate the vacancy production rate per cycle.

(i) For orientation A1 the vacancy production rate can be estimated to 4×10^{-5} $\mathrm{at}^{-1}\mathrm{cycle}^{-1}$ at $77\,\mathrm{K}$ and 2×10^{-5} $\mathrm{at}^{-1}\mathrm{cycle}^{-1}$ at $300\,\mathrm{K}$ and at $600\,\mathrm{K}$.

(ii) For orientation B1, the vacancy production rate at $77\,\mathrm{K}$ and $300\,\mathrm{K}$ is estimated to be around 2×10^{-5} $\mathrm{at}^{-1}\mathrm{cycle}^{-1}$ and 10^{-5} $\mathrm{at}^{-1}\mathrm{cycle}^{-1}$ at $600\,\mathrm{K}$.

(iii) The vacancy production rate for orientation C1 is approximately 10^{-5} $\mathrm{at}^{-1}\mathrm{cycle}^{-1}$ at $77\,\mathrm{K}$ and $300\,\mathrm{K}$ while at $600\,\mathrm{K}$, it reaches about 2×10^{-5} $\mathrm{at}^{-1}\mathrm{cycle}^{-1}$.

These data show no clear trend with temperature and the effect of temperature on vacancy production is considered weak (within a factor two, whithout clear effect).

More interestingly, some mechanisms such as cross-slip or jogs dragging, which are thought to be thermally activated are also observed at low temperatures such as $77\,\mathrm{K}$. Fig. 6-4 and Fig. 6-5 show respectively examples of cross-slip and jog dragging observed at $77\,\mathrm{K}$. Fig. 6-4 shows a cross-slip mechanism occurring with constriction formation at $77\,\mathrm{K}$, the original glide plane being the $(1\,\bar{1}\,\bar{1})$ plane and the cross-slip plane being the $(1\,1\,1)$ plane. Fig. 6-5 shows an example of jogs dragging at $77\,\mathrm{K}$ with a row of vacancies produced since the glide of a jogged screw dislocation is non conservative. A test carried out at $4\,\mathrm{K}$ reveals also these mechanisms of cross-slip and jogs dragging. The appearance of these mechanisms at all temperatures even at low temperatures can be evoked to explain this weak influence of temperature on the vacancy concentration near the crack-tip zones. These mechanisms seem to be rather stress driven close to crack-tip because of high local stresses.

However, some particular points should be noted. While temperature does not have a great effect on vacancy concentration, differences are observed in vacancy clustering. As shown in Fig. 6-7 at low temperature ($77\,\mathrm{K}$) and medium temperature ($300\,\mathrm{K}$), the number of rows of vacancies is higher than at $600\,\mathrm{K}$, at which there are fewer rows of vacancies despite the fact that jogs dragging is observed at all temperatures. Therefore, this clustering difference should probably be an effect of short-range vacancy diffusion, which is higher for high temperatures. As a consequence of this effect, higher number of stacking fault tetrahedra was observed at $600\,\mathrm{K}$ than at $77\,\mathrm{K}$ or $300\,\mathrm{K}$

Finally, the plastic irreversibility induced by various dislocation interactions and lattice defects is evaluated according to the temperature for each crack configuration. Fig. 6-8 shows the evolution of the plastic irreversibility factor during cyclic loading. In Fig. 6-8a, we can observe that the plastic irreversibility factor for orientation A1 fluctuates around a mean value (computed over the 16 cycles) of approximately 0.67 at $77\,\mathrm{K}$, 0.55 at $300\,\mathrm{K}$ and around 0.6 at $600\,\mathrm{K}$. For crack orientation B1, the irreversibility factor is established around a mean value of 0.25

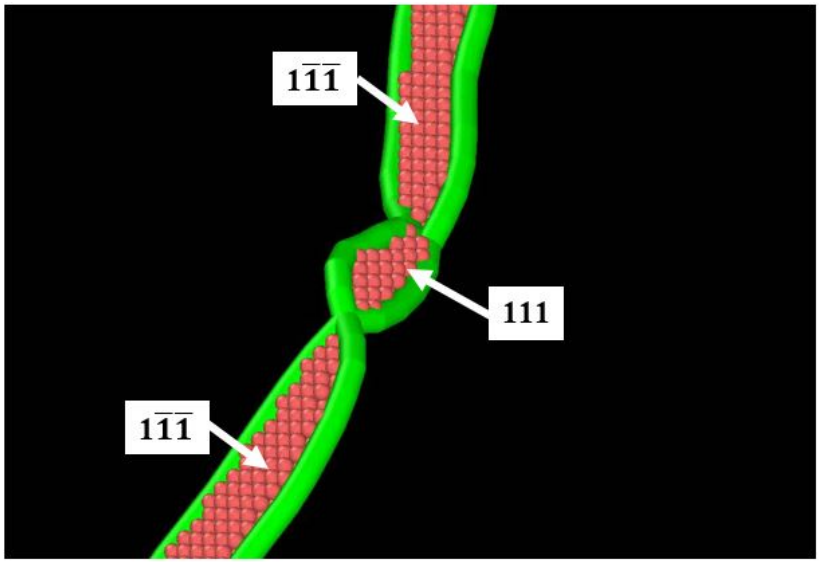

Figure 6-4: Example of the result of cross-slip observed at 77 K in copper allowed by constriction formation. Green lines are Shockley partials with atoms in stacking faults (red spheres). Crack orientation A1

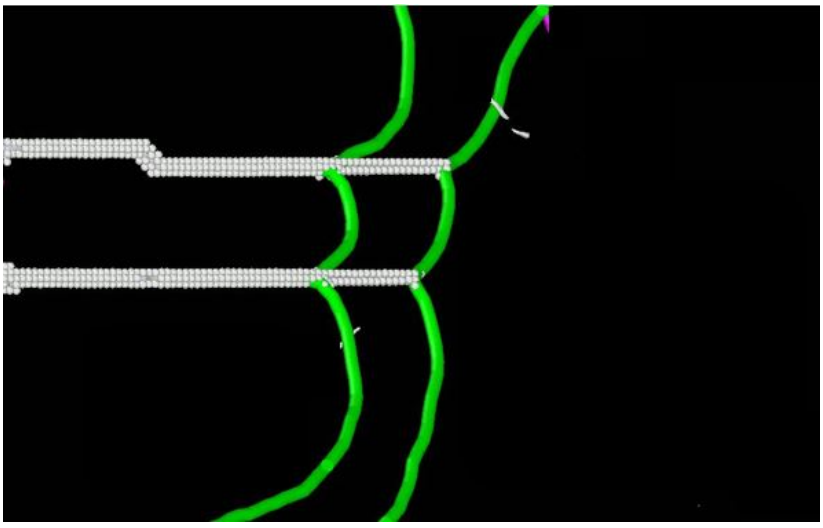

Figure 6-5: Example of jog dragging observed at 77 K in copper. Green lines represent are Shockley leading and trailing partials lines and the white lines are rows of vacancies. Crack orientation A1.

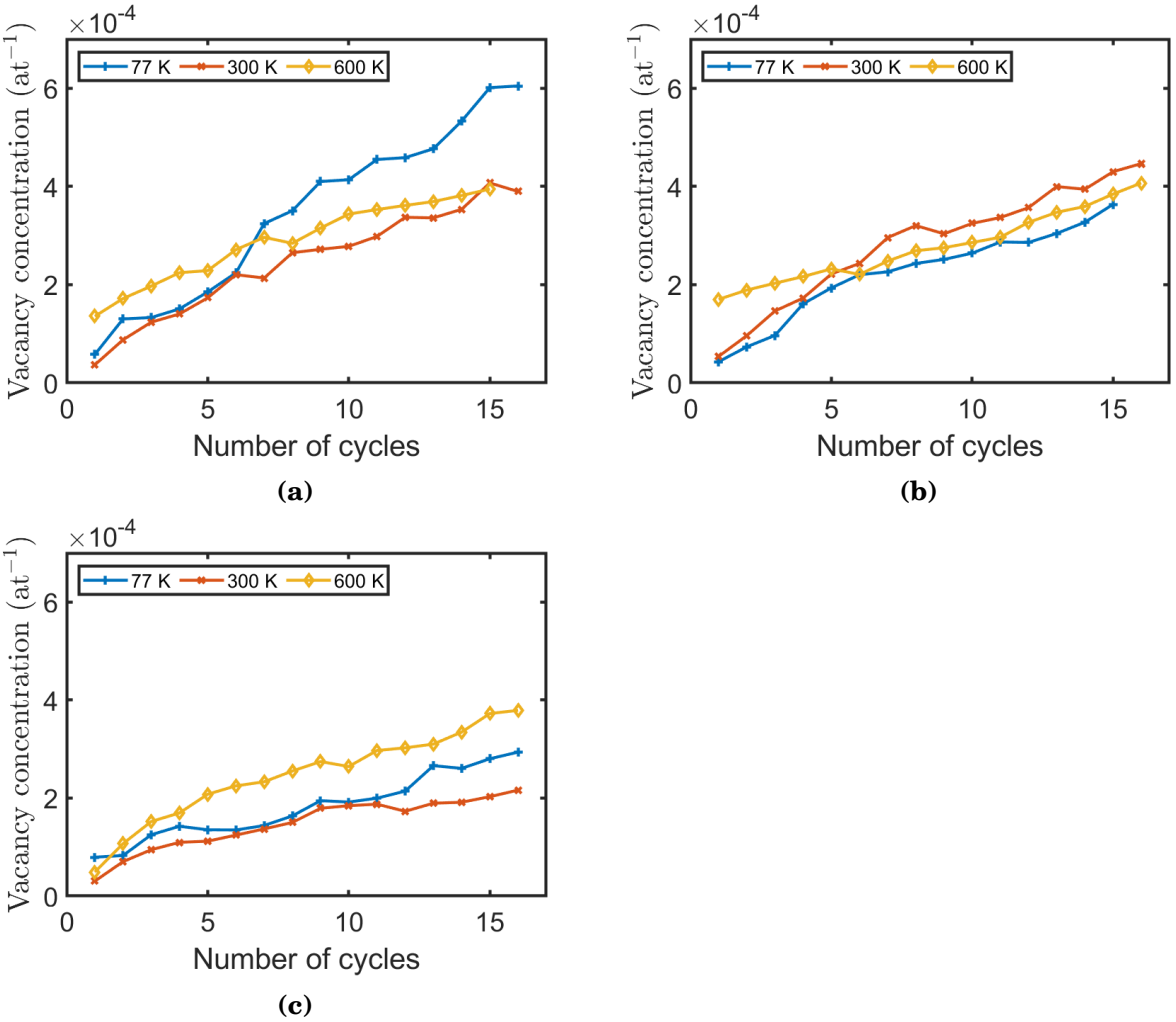

Figure 6-6: Effect of temperature on vacancy concentration for (a) crack orientation A1, (b) crack orientation B1 and (c) crack orientation C1.

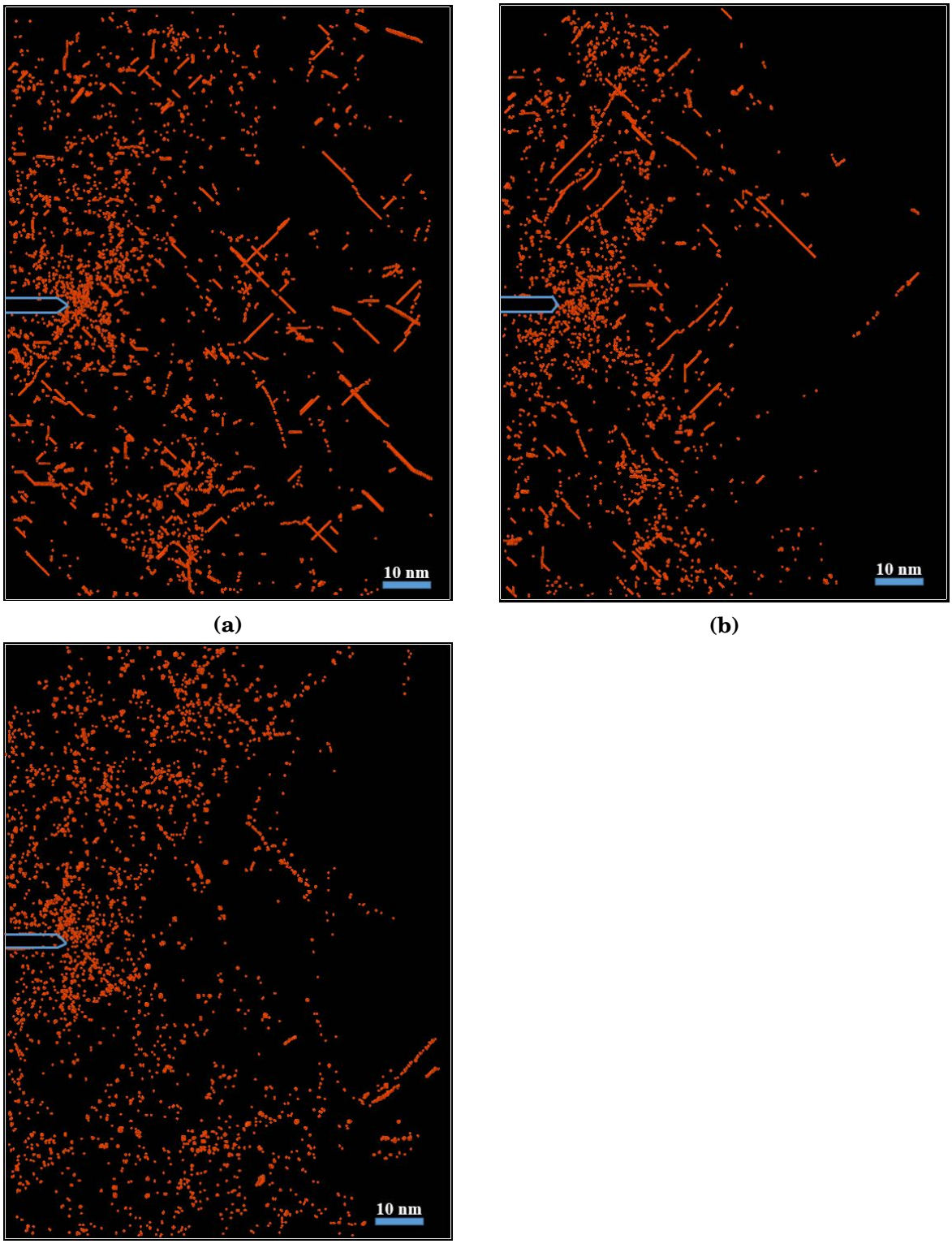

Figure 6-7: Spatial distribution of vacancies for crack orientation A1 at different temperatures (a) $77\,\mathrm{K}$, (b) $300\,\mathrm{K}$ and (c) $600\,\mathrm{K}$. One can observe that at $77\,\mathrm{K}$ and $300\,\mathrm{K}$ there are lot of vacancy rows while at $600\,\mathrm{K}$, the number of vacancy rows vanishes and more low-scale vacancy clusters are observed.

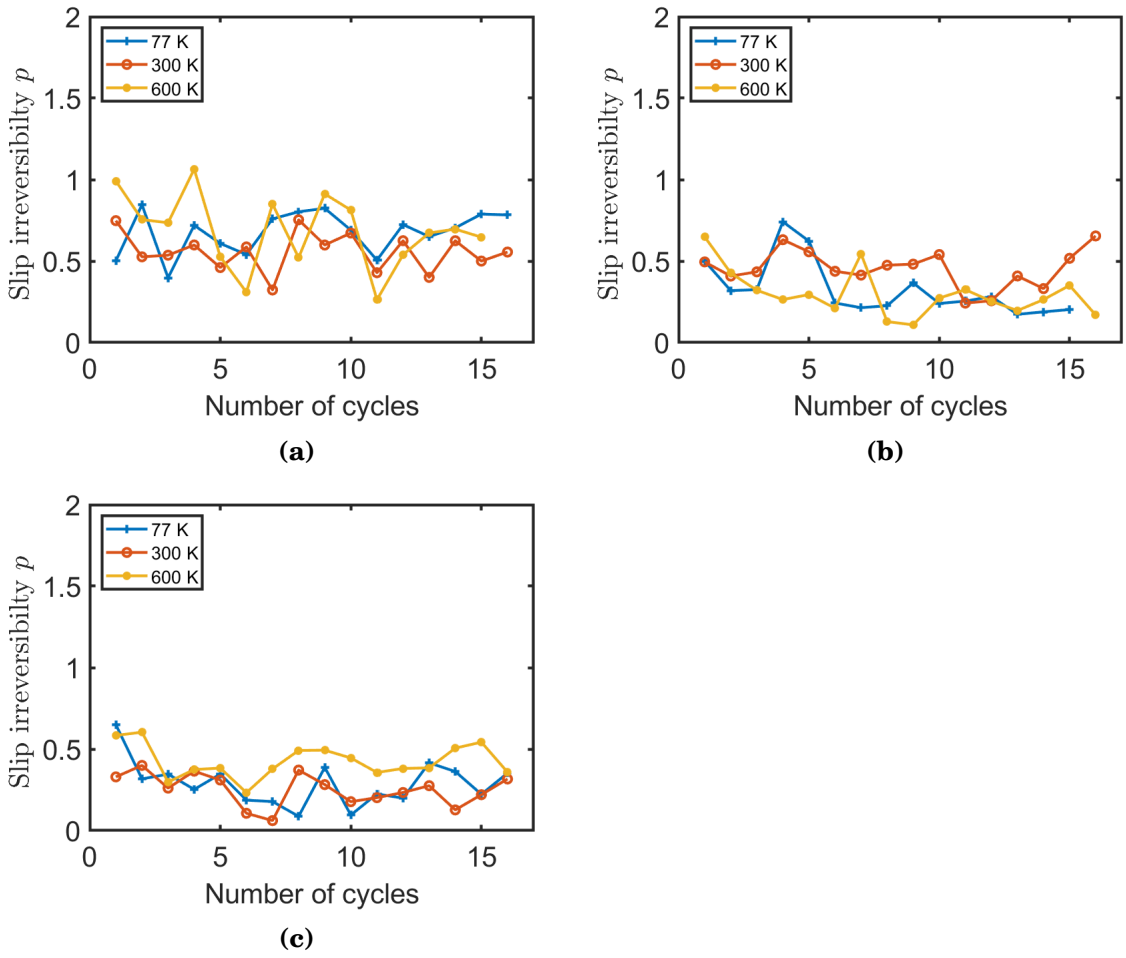

Figure 6-8: Effect of temperature on slip irreversibility factor during cyclic loading for (a) orientation A1, (b) orientation B1 and (c) orientation C1.

at $77\,\mathrm{K}$, 0.45 at $300\,\mathrm{K}$ and around 0.25 and at $600\,\mathrm{K}$. Finally, for orientation C1, the irreversibility factor fluctuates around a mean value of approximately 0.25 at $77\,\mathrm{K}$ and $300\,\mathrm{K}$ while this mean value is established at around 0.47 at $600\,\mathrm{K}$.

In summary, one can conclude to a weak or moderate effect of temperature as well on the mechanisms of plastic deformation as on the crystal defects around crack-tip in the investigated range. In fact, in our simulations, temperature does not change the mechanisms of deformation around crack-tip. And the different dislocation structures observed at crack-tip at $300\,\mathrm{K}$ are also found to be similar to that observed at $77\,\mathrm{K}$ and at $600\,\mathrm{K}$ (Fig. 6-3). Moreover, the dislocation density and the vacancy concentration are found to be only slightly influenced by temperature without a general trend (Fig. 6-6). However, the mobility of vacancies is found to be enhanced, as evidenced by the clustering of vacancies (Fig. 6-7). As a result, at higher temperature, a relative high number of SFTs is observed at $600\,\mathrm{K}$ than at $77\,\mathrm{K}$ or at $300\,\mathrm{K}$, while at $77\,\mathrm{K}$ and $300\,\mathrm{K}$ a higher number of rows of vacancies are observed than at $600\,\mathrm{K}$ (Fig. 6-7). Considering this relatively weak

influence of temperature on plastic deformation around crack-tips, it is now relevant to investigate the influence of temperature on the mechanisms of fatigue crack propagation and on the fatigue crack growth rates.

It is true that the present simulations are carried out at high strain rates which probably does not allow thermal activation to take place for some mechanisms. As a result, the cross-slip observed is mainly induced by the high stresses prevailing around the crack tip. It is important to specify that even for low strain rates, the crack-tip stresses remain high because of the stress singularity. One would then tend to think that the cross-slip observed in these simulations is underestimated and could be even higher for lower strain rates where thermal activation could occur. However, in this study, a large number of cross-slip is observed. Given the very large number of narrowly spaced constrictions on dislocation lines, the author wonders whether there is still the possibility of carrying out more cross-slip in particular by thermoactivation. According to the author, the probability that there is a thermally activated cross-slip remains quite low considering the very large number of cross-slip already occurring around crack-tip.

6.3.2 Effect of temperature on fatigue crack growth

As in chapter 5 when applying room temperature ($300\,\mathrm{K}$), fatigue crack propagation whether at $77\,\mathrm{K}$ or at $600\,\mathrm{K}$ proceeds by plastic blunting and irreversibility. It is stated in chapter 5, that fatigue crack propagation proceeds by a mechanism of plastic blunting and irreversibility which is consequence of the emission of dislocations from crack-tips and of plastic irreversibility. This plastic irreversibility at crack-tip being the result of various dislocation barriers impeding the glide back of mobile dislocations towards the crack-tip. This induces a non-recovery of the matter removed by dislocation emission during the loading half cycle. In our investigations, it is observed that the same mechanisms occur whatever the temperature, that is, the temperature does not influence the fatigue crack growth mechanisms. Considering that the dislocation structures observed near crack-tip zones at room temperature are also found at $77\,\mathrm{K}$ and $300\,\mathrm{K}$, and only slightly affected by temperature (Fig. 6-3, Fig. 6-2), and that, other crystal defects are also only slightly affected by the temperature (Fig. 6-7, Fig. 6-6), it is therefore expected that the fatigue crack propagation mechanisms do not change in the range of temperatures investigated. The fact that the fatigue crack propagation mechanism do not change so much with temperature is in agreement with the experimental results of Ishii and Weertmann [Ishii and Weertman, 1971a] who performed fatigue tests at $300\,\mathrm{K}$ and in liquid nitrogen ($77\,\mathrm{K}$) on single crystals and polycrystals of copper and copper-aluminium alloys. If fatigue crack growth mechanisms are not influenced by temperature, what about fatigue crack growth rates?

Fig. 6-9, Fig. 6-11 and Fig. 6-12 shows the influence of temperature on fatigue

crack propagation rates for different crack orientations. Fig. 6-9a, Fig. 6-9b and Fig. 6-9c show the dependence of the computed FCGR as a function of the applied SIF amplitude for respectively crack orientations A1, B1 and C1. These FCGR data obey to the well-known Paris power law (Equation 5.1) and the adjusted parameters are listed in table 6.1. As can be noticed in Fig. 6-9a, Fig. 6-9b and Fig. 6-9c and in table 6.1, the exponent of the Paris' law is approximately 4 for all the temperatures. This is in agreement with the experimental measurements of Ishii and Weertmann [Ishii and Weertman, 1971a]. The latter reported exponents of Paris law of approximately 4 in tests carried out in liquid nitrogen ($77\,\mathrm{K}$) in copper single crystals with various orientations (Fig. 6-10). Tests carried out at room temperature ($300\,\mathrm{K}$) and under air environment by the same authors still using copper single crystals reveal exponents varying between 3.5 and 6. In the latter case, it would be necessary to take into account the influence of air environment, and particularly O_2 on the propagation rates depending on the crack orientation. Ishii and Weertmann also performed tests on Cu-Al alloy single crystals at room temperature (300 K) and in liquid nitrogen ($77\,\mathrm{K}$) and reported an exponent of approximately 4 for at both temperatures. A similar exponent of 4 was reported by the same authors on polycrystals of copper in tests carried out at room temperature under air and in liquid nitrogen. Neumann [Neumann et al., 1978] investigations on copper single crystals under vacuum at $300\,\mathrm{K}$ showed the existence of a Paris regime on single crystals with an exponent of 4. Therefore, the constancy of the exponent of Paris law with the temperature observed in our atomistic study is in agreement with the various experimental results in literature.

By setting the exponent m of the Paris law to 4 for all tested temperatures and orientations, the prefactor of Paris law is assessed and plotted in Fig. 6-9d. In this figure, one can observe for a given orientation, a dependence of the prefactor C with temperature. Indeed, the prefactor C of Equation 6.16, tends to increase slightly with temperature increasing. Nevertheless, this temperature dependence of FCGR is very moderate as shown in Fig. 6-9d. In fact, on can see that, apart from orientation A1, the temperature effect is very small, if not almost non-existent as can be seen in Fig. 6-9d. Indeed, for orientation A1, there is a factor of approximately 1.7 between the propagation rates at $600\,\mathrm{K}$ and that at $300\,\mathrm{K}$ and a factor of approximately 2 between the propagation rate at $600\,\mathrm{K}$ and that at $77\,\mathrm{K}$. For orientation B1, the propagation rate at $600\,\mathrm{K}$ is only about 2 times higher than that at $77\,\mathrm{K}$. Compared to the propagation rate at $300\,\mathrm{K}$, the propagation rate at $600\,\mathrm{K}$ is only about 1.4 times higher. It the case of orientation C1, propagation rate at $600\,\mathrm{K}$ is only about 1.2 times higher than at $77\,\mathrm{K}$ and only 1.1 times higher than the propagation at $300\,\mathrm{K}$.

Fig. 6-10 shows the propagation rates measured experimentally in liquid nitrogen in copper single crystals with different crystal orientations by Ishii and Weertmann [Ishii and Weertman, 1971a]. These measured propagation

rates obey Paris law and the exponents of the Paris law range between 3.1 and 3.9. Indeed, for an orientation close to the loading axis $\langle 1\,0\,0\rangle$, an exponent of 3.1 was obtained, while for loading axes close to $\langle 1\,1\,0\rangle$ and $\langle 1\,1\,1\rangle$, exponents of 3.9 and 3.5 are respectively obtained. As a reminder, at the same temperature, our simulations provide an exponent of 3.6 for crack orientation A1 (loading axis: $[0\,1\,0]$), 3.7 for orientation B1 (loading axis: $[1\,1\,0]$) and 3.5 for crack orientation C1 (loading axis: $[1\,1\,1]$). Our predictions are therefore in agreement with the experimental investigations of Ishii and Weertmann [Ishii and Weertman, 1971a]. Also, as can be noticed in Fig. 6-10, the propagation rates are higher when the loading axis is close to $\langle 1\,0\,0\rangle$ axis and lower when the loading axis is close to $\langle 1\,1\,0\rangle$ axis. Our simulations are in agreement with these experimental measurements. Indeed, the propagation rates measure in our simulations are higher for crack orientation A1 (loading axis: $[0\,1\,0]$) and lower for crack orientation C1 (loading axis: $[1\,1\,0]$) both at $77\,\mathrm{K}$ and $300\,\mathrm{K}$. By setting the exponent of the Paris' law to 4 and assessing the prefactor with the experimental data of Ishii and Weertmann [Ishii and Weertman, 1971a] at $77\,\mathrm{K}$, the comparisons between experiments and our simulations show a discrepency factor of 2.9 to 10 between the experiments and our simulations depending on the crack orientation. For orientation A1 for example, a factor of 10 is observed, i.e. the propagation rates predicted by the MD are 10 times lower than the experimental data. Likewise, a factor of about 2.9 is found for crack orientation B1 and of about 7 for crack orientation C1.

To take into account the temperature dependence of cubic elasticity constants, with the aim of better understanding the temperature effect, it seems relevant to apply a normalization of ΔK ($K_{max} - K_{min}$) and ΔK_{eff} ($K_{max} - K_{Ie}$), accounting for the variation of the tensile axis Young's modulus with temperature. Fatigue crack grow rates were plotted as a function of the normalized SIF (Equation 6.17 and Fig. 6-11) and as a function of the normalized effective SIF (Equation 6.19 and Fig. 6-12) and the adjusted parameters C_i and m_i are provided in table 6.2 and table 6.3 respectively.

$$\frac{da}{dN} = C_4 \times (\Delta K)^{m_4} \tag{6.15}$$

$$\frac{da}{dN} = C \times (\Delta K)^{4} \tag{6.16}$$

$$\frac{da}{dN} = C_5 \times \left(\frac{\Delta K}{E^*_{ijk}(T)}\right)^{m_5} \tag{6.17}$$

$$\frac{da}{dN} = C_{NE} \times \left(\frac{\Delta K}{E^*_{ijk}(T)}\right)^{4} \tag{6.18}$$

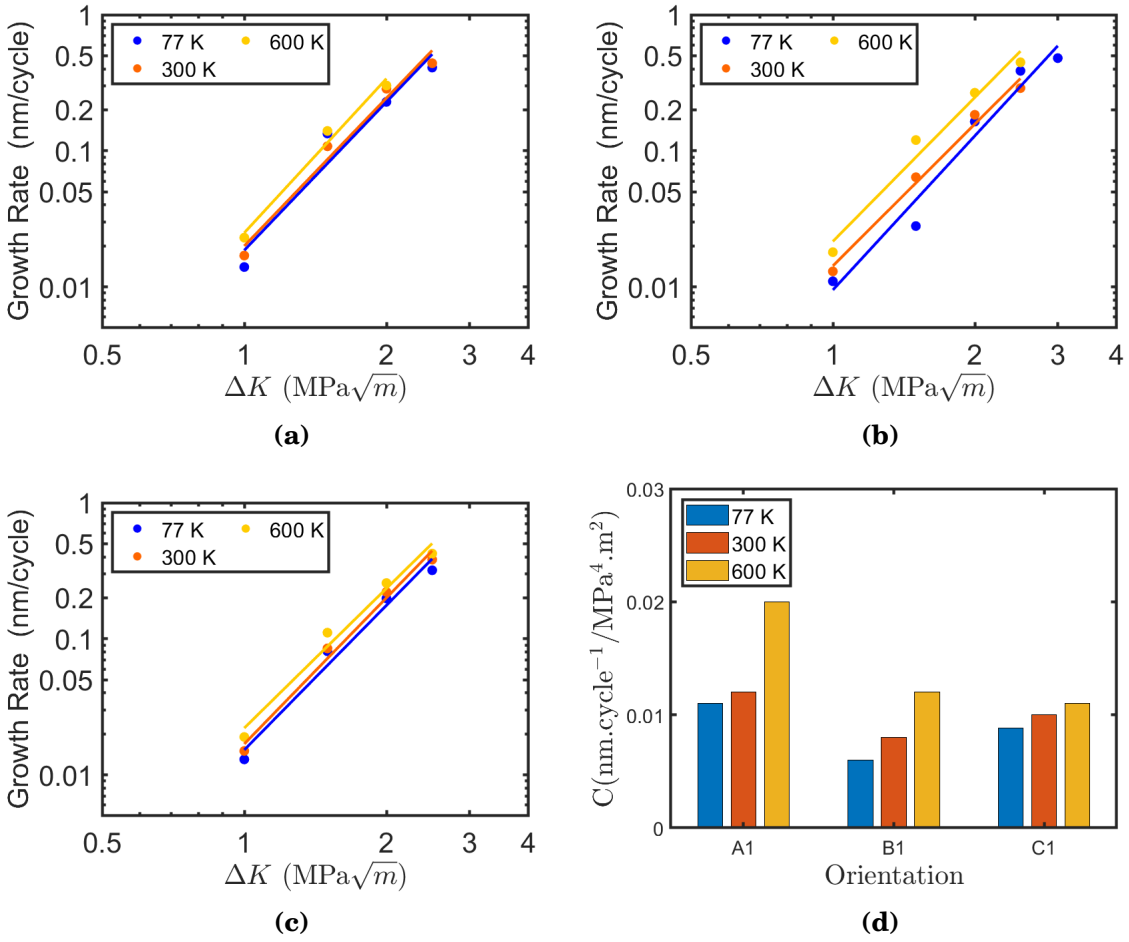

Figure 6-9: Effect of temperature on fatigue crack propagation rates: (a) orientation A1, (b) orientation B1, (c) orientation C1. Dots represent data arising from MD simulations and solid lines are adjusted power law curve (Equation 6.15). The adjusted parameters can be found in Table 6.1. FCGR are plotted vs SIF amplitude (Equation. 6.15) and the slopes observed in (a), (b) and (c) are close to 4. (d) Evolution of the prefactor C of Equation 6.16 with temperature given for different crack orientation.

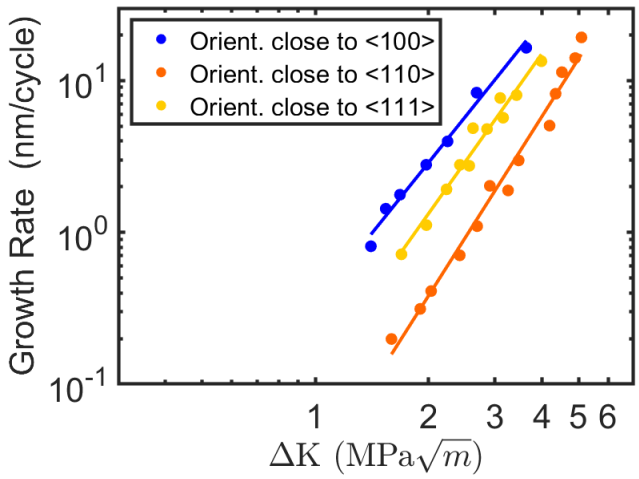

Figure 6-10: Experimental FCGR in copper single crystals for different orientations in liquid nitrogen (77 K). Experiments by Ishii and Weertmann [Ishii and Weertman, 1971a]. The slopes varied between 3.1 and 3.9.

$$\frac{da}{dN} = C_6 \times \left(\frac{\Delta K_{eff}}{E^*_{ijk}(T)} \right)^{m_6} = C_6 \times \left(\frac{(K_{max} - K_{Ie})}{E^*_{ijk}(T)} \right)^{m_6} \tag{6.19}$$

$$\frac{da}{dN} = C^{NE}_{eff} \times \left(\frac{\Delta K_{eff}}{E^*_{ijk}(T)} \right)^{2} \tag{6.20}$$

One can observed that the exponent of the modified Paris law in Equation 6.17 and in Equation 6.19 are close to 4 and 2 respectively. By setting the exponent used in Equation 6.17 to 4 and the exponent m_6 in Equation 6.19 to 2, the prefactors C_{NE} and C^{NE}_{eff} of Equations 6.18 and 6.20 are assessed and plotted in Fig. E-1d and Fig. E-2d respectively (Appendix E).

In Fig. 6-11, Fig. 6-12, Fig. E-1d and Fig. E-2d, for a given crack orientation, the FCGR data plots for different temperatures are almost superimposed, which shows that the small differences observed in Fig. 6-9 are only the result of the temperature dependence of the elasticity constants with temperature. This effect disappears when the applied SIF and effective SIF are normalized by the Young's modulus of the corresponding temperature. One can thus conclude that under inert environment, in the studied temperature range, no temperature effect on FCGR is observed as for main characteristics of crack-tip plasticity.

Some authors have investigated experimentally the effect of temperature on fatigue crack propagation. On can cite some representative but non exhaustive papers (Hénaff *et al.* [Hénaff et al., 2001], Rosenberger *et al.* [Rosenberger et al., 1997], Sarrazin-Baudoux *et al.* [Sarrazin et al., 1997], Cotterill and Knott [Cotterill and Knott, 1992], Petit *et al.* [Petit et al., 2003]).

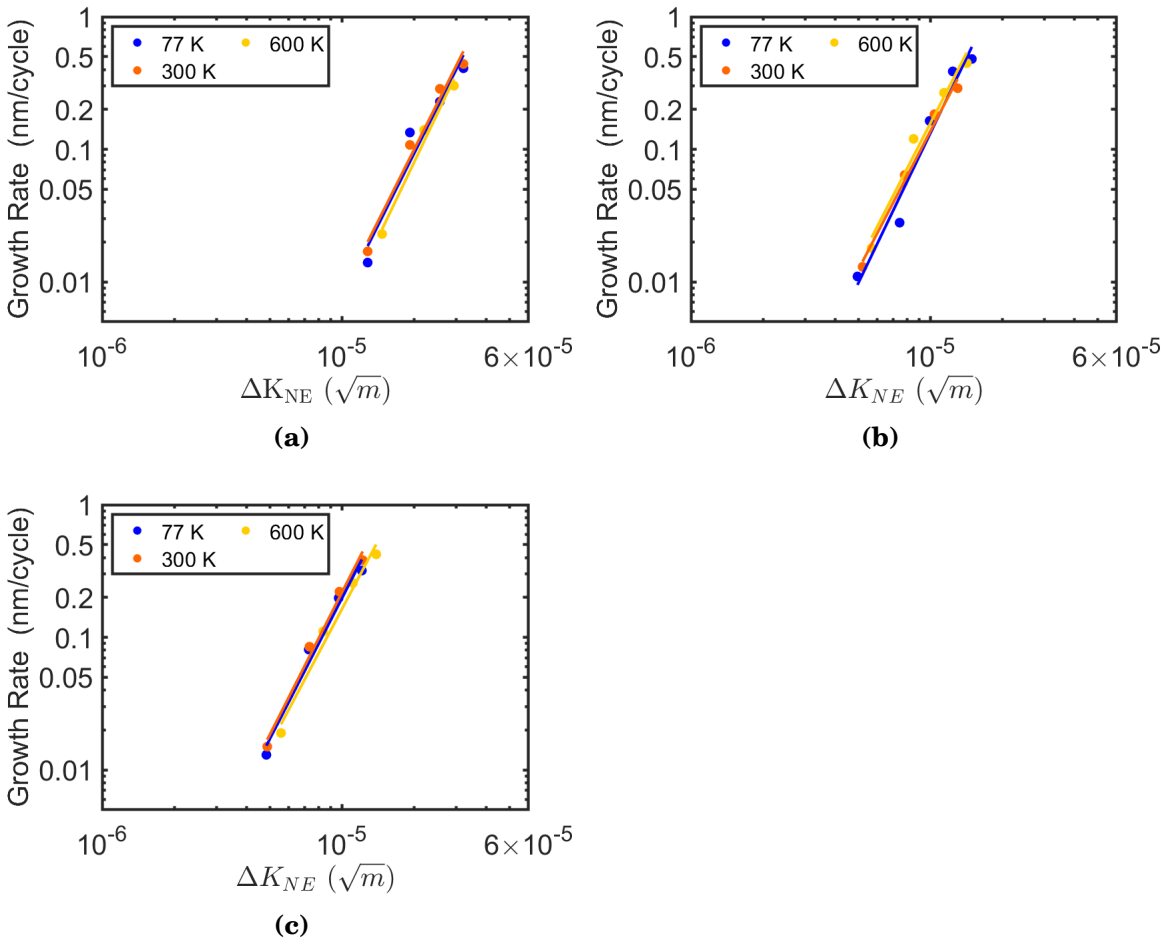

Figure 6-11: Effect of temperature on computed fatigue crack propagation rates: (a) orientation A1, (b) orientation B1, (c) orientation C1. Dots represent data from MD simulation and solid lines are the adjusted power law curves (Equation 6.17). The adjusted parameters can be found in Table 6.2. FCGR are plotted as function of normalized SIF (Equation 6.17 and the slopes in (a), (b) and (c) are approximately 4.)

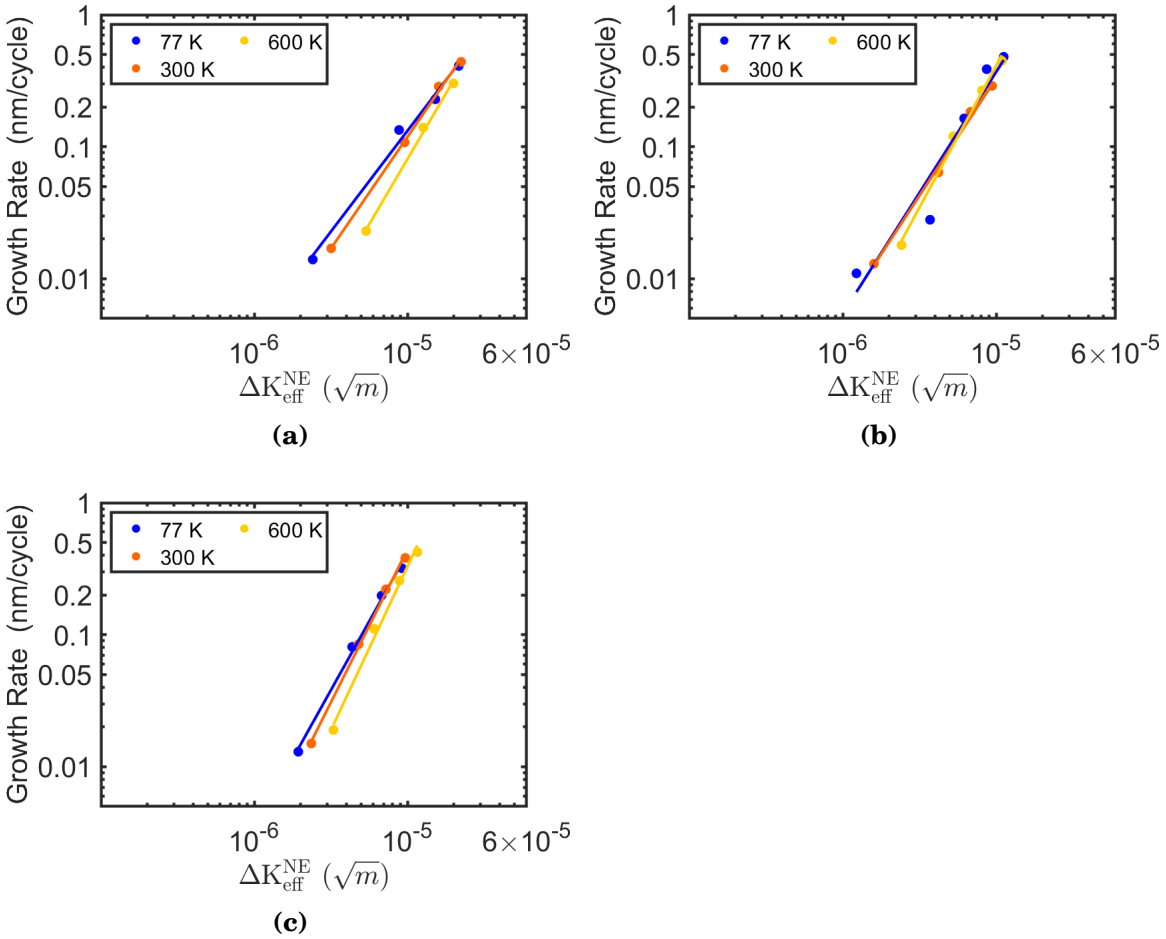

Figure 6-12: Effect of temperature on the fatigue crack propagation rates: (a) orientation A1, (b) orientation B1, (c) orientation C1. Dots represent data from MD simulation and solid lines are the adjusted power law curves (Equation 6.19). The adjusted parameters can be found in Table 6.3. FCGR are plotted as function of normalized effective SIF (Fig. 6.19 and the slopes in (a), (b) and (c) are approximately 2.)

For instance, Cotterill and Knott [Cotterill and Knott, 1992] carried out an experimental study on the effect of temperature and environment on fatigue crack growth in a $9\%Cr - 1\%Mo$ steel. The tests were performed in air and vacuum and at temperatures ranging from room temperature up to $625°C$ $(T/T_m \approx 0.5)$. The authors reported that in vacuum, the fatigue crack growth rates are practically independent of temperature over the whole range of temperatures tested. Under air environment the conclusion was different as reported by the authors. Indeed Cotterill and Knott observed that the fatigue threshold at room temperature is lower in air than in vacuum with an opposite situation for higher temperatures. Experiments carried out in TA6V alloy by Sarrazin-Baudoux *et al.* [Sarrazin et al., 1997] from room temperature up to $300°C$ under various atmospheres suggested that the measured FCGR are independent of temperature, but affected by moisture. The authors reported a marked embrittlement effect of water vapor, which was thought to induce a lower threshold and accelerate fatigue crack growth. Investigations carried out on some intermetallic compounds reveal that the presence of water vapor increases fatigue crack growth rates (Hénaff *et al.* [Hénaff et al., 2001], Rosenberger *et al.* [Rosenberger et al., 1997]) without significant change in fracture mode but this environmental effect was found to decrease as temperature increased above the brittle-to-ductile transition (Rosenberger *et al.* [Rosenberger et al., 1997]).

Table 6.1: Paris' law adjusted parameters where parameters C_4 and m_4 are the adjusted parameters of Equation. 5.1

	77		300 K		600 K	
	C_4	m_4	C_4	m_4	C_4	m_4
A1	0.0186	3.62	0.02	3.61	0.025	3.76
B1	0.0095	3.76	0.0143	3.46	0.02	3.52
C1	0.0153	3.53	0.0169	3.57	0.0221	3.41

Table 6.2: Modified Paris' law adjusted parameters where parameters C_5 and m_5 are the adjusted parameters of Equation. 6.17

	77		300 K		600 K	
	C_5	m_5	C_5	m_5	C_5	m_5
A1	8.47×10^{15}	3.60	8.21×10^{15}	3.61	4.27×10^{16}	3.78
B1	8.00×10^{17}	3.76	3.03×10^{16}	3.47	5.43×10^{16}	3.51
C1	8.67×10^{16}	3.53	1.49×10^{17}	3.57	2.01×10^{17}	3.42

To summarize this section, under inert environment, the influence of temperature on crack-tip plasticity as well as crack propagation mechanisms and

Table 6.3: Modified Paris' law adjusted parameters where parameters C_6 and m_6 are the adjusted parameters of Equation 6.19

	77		300 K		600 K	
	C_6	m_6	C_6	m_6	C_6	m_6
A1	5.78×10^6	1.53	5.55×10^7	1.77	6.39×10^8	1.98
B1	5.29×10^8	1.83	2.62×10^8	1.78	2.25×10^8	2.15
C1	1.08×10^{10}	2.08	1.70×10^{11}	2.32	8.60×10^{11}	2.48

rates is found to be weak under the adopted conditions. The effect is limited to the temperature dependence of elasticity constants with temperature. The temperature effect vanishes when the applied SIF or effective SIF are normalized by the appropriate Young's modulus which is temperature dependent. Considering that fatigue is a damage mechanism which involves microstructural changes, a temperature effect on the microstructures around crack-tips should probably influence the mechanisms of fatigue crack propagation as well as the FCGR. However, it is clear from the previous sections that, the plastic deformation at crack-tip as well as the underlying crystal defects around crack-tip are not significantly affected by temperature. All the mechanisms are identical at all temperatures in the range of temperatures investigated and for the number of cycles applied ($16\ cycles$). Therefore, the weak influence of temperature on the fatigue crack propagation can be explained by the weak effect of temperature on the crack-tip deformation and on the underlying crystal defects. But how can one explain the weak influence of temperature on the plastic deformation and the microstructures at crack-tip ?

One of the reasons could arise from the very high stresses prevailing near crack-tip regions. Phenomena, which are often thermally activated, will be rather governed by these high stresses prevailing near crack-tip such as cross-slip observed at $77\,\mathrm{K}$ or even $4\,\mathrm{K}$. However, under a gaseous environment such as air or hydrogen environment the conclusion could be different. In that case, oxidation kinetics or hydrogen embrittlement (moisture in aluminides) at crack-tip occur and can lead to significant modifications of both plastic deformation and fatigue crack propagation mechanisms and rates.

6.4 Effect of stacking fault energy

In the previous section, the influence of temperature on the mechanics and mechanisms of fatigue crack propagation was investigated. We explain the influence of temperature on fatigue crack propagation under an inert environment by microstructural evolution resulting from the plastic deformation around crack-tip.

Knowing also that stacking fault energy (SFE) is an influencing material pa-

rameter, which affects plastic deformation as well as dislocation microstructures in ductile metals and alloys, we try, in this section to shed light on the effect of stacking fault energy on the propagation of fatigue cracks under inert environment in FCC single crystals.

The influence of SFE on fatigue crack behavior under inert environment is now investigated. Four different FCC materials exhibiting various values of SFE are considered. Silver, copper, nickel and aluminium are used in this study. For more physically-based comparisons between different materials, we used the normalized stacking fault energy (NSFE), which is defined by $\gamma_{sf}/\mu_{slip}b$ where γ_{sf} is the stacking fault energy of the material, b the magnitude of the Shockley partial Burgers vector and μ_{slip} the shear modulus defined as:

$$\mu_{slip} = \frac{C_{11} - C_{12} + C_{44}}{3} \tag{6.21}$$

with C_{ij} the elastic constants.

The computations are carried out at room temperature ($300\,\mathrm{K}$) and the values of different parameters are given in table 6.4. All values used to compute the NSFE are those predicted by the interatomic potentials.

The normalized stacking fault energy is inversely proportional to the equilibrium distance between the leading and trailing of a dissociate full dislocation (Equation 6.22, Equation 6.23).

Table 6.4: Normalized stacking fault energy for different metals. Values are computed using the parameters predicted by the potential

	Ag	Al	Cu	Ni
γ_{sf} $(\mathrm{mJ.m^{-2}})$	11	157	45	137
μ (GPa)	26.33	26.67	40.00	68.00
$b\,(10^{-10}\mathrm{m})$	1.667	1.683	1.476	1.439
$\gamma_{sf}/\mu_{slip}b\,(10^{-2})$	0.137	2.08	0.398	0.681

6.4.1 Fatigue crack-tip deformation

6.4.1.1 Dislocation emission from crack-tip

When they are subjected to mechanical loading, the crystals undergo first of all an elastic deformation, which generally precedes dislocation emission and gliding which characterizes the plastic deformation. The variable which controls the applied loading in this study is the stress intensity factor. Depending on the considered metal, the critical stress intensity factor for emitting crack-tip dislocations varies.

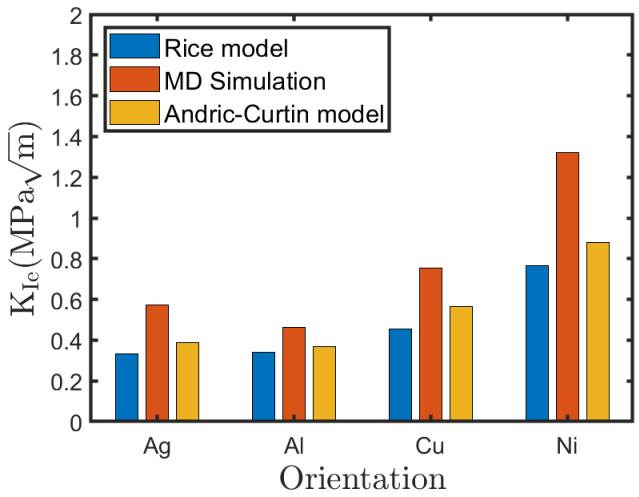

Figure 6-13: Critical stress intensity factor for dislocation emission at crack-tip for different materials. The MD predictions are compared with the predictions of [Rice, 1992] and [Andric and Curtin, 2017]

In our investigation, we compare the critical stress intensity factor required for dislocation emission during the first loading half cycle, derived from our atomistic simulations, to the predictions of Rice [Rice, 1992] and Andric and Curtin [Andric and Curtin, 2017] criteria (chapter 4). It can be observed in Fig. 6-13 that, the critical SIF for dislocation nucleation derived from our simulations differ from the predictions of Andric and Curtin [Andric and Curtin, 2017] by approximately 33% for Ag and Ni, 20% for Al, 25% for Cu. They differ from the predictions of Rice theory [Rice, 1992] by 42% for Ag and Ni, 26% for Al and by 39% for Cu. These differences as stated previously should be due to the fact that for the crack configuration considered, the crack plane does not intersect the slip plane, therefore, the crack front is not contained in the slip plane. As a reminder, the original Rice theory considers a configuration where the slip plane contains the crack front. The anisotropic nature of cubic elasticity should also be pointed out.

It is worth noting that dislocations emitted from crack-tips are Shockley partials. The emission of Shockley partials leads to the formation of stacking faults at the crack-tip. The width of these stacking faults strongly depends on the normalized SFE ($\gamma_{sf}/\mu_{slip}b$) of the metal. For instance, the approximate equilibrium separation between Shockley partials is given by:

For edge partials:

$$d_{SF}^{E} = \frac{\mu_{slip} b^2 \left(2+\nu\right)}{8\pi \left(1-\nu\right) \gamma_{SF}} \tag{6.22}$$

For screw partials:

$$d_{SF}^{S} = \frac{\mu_{slip} b^2 \left(2 - 3\nu\right)}{8\pi \left(1 - \nu\right) \gamma_{SF}} \tag{6.23}$$

The equilibrium separation distances between Shockley partials at room temperature in metals under investigation are provided in Table 6.5.

Table 6.5: Equilibrium separation distances between Shockley partials for metals under investigation (at $300\,\mathrm{K}$)

	Ag	Al	Cu	Ni
d_{sf}^{E} (nm)	11.36	0.70	3.17	1.48
d_{sf}^{S} (nm)	3.25	0.28	1.00	0.60

The higher the normalized stacking fault energy, the lower the width of the stacking fault. Hence, as can be observed in Fig. 6-14, the stacking fault widths are larger in silver, which exhibits the lowest normalized stacking fault energy of the order of 0.137×10^{-2} and much smaller in aluminum for which the normalized stacking fault energy is 2.08×10^{-2}. The cumulative surface of stacking fault is not only related to the SFE but also to the degree of the plastic strain. Thus, for significant plastic deformation, the number of stacking faults is higher as can be observed in Fig. 6-15, which shows the evolution of the fraction of atoms located in stacking fault areas as a function of the number of cycles. The bowing out of dislocations increases the length of dislocation line in the MD simulation box too.

The general trend deduced from Fig. 6-15 suggests that: (i) the stacking fault atoms fraction quantity increases with the number of cycles, (ii) the proportion of atoms in the stacking faults is higher in silver than in all other metals. In particular in aluminum the cumulative surface of stacking fault does not change with the number of cycles, even if the dislocation density in aluminum is higher than in any other metal. It can be noticed that low stacking fault energy materials (Ag, Cu) display the highest proportion of atoms located in stacking fault areas while Ni exhibits the lowest proportion even if the SFE of Nickel is lower than that of Al. This can be explained by the fact that for a stress intensity factor of 2 $\mathrm{MPa}\sqrt{\mathrm{m}}$ the plasticity in nickel remains at an early stage. In fact, it must be reminded that the stress intensity factor for the nucleation of dislocations in nickel is around 1.32 $\mathrm{MPa}\sqrt{\mathrm{m}}$ which is much higher than in the three other metals

6.4.1.2 Lattice defects

Dislocations are one of the most and common lattice defects generated during cyclic plastic deformation in our simulations whatever the metal. The dislocation density depends on the local plastic strain amplitude depending on the applied stress intensity factors. Fig. 6-16 displays the evolution of dislocation density in

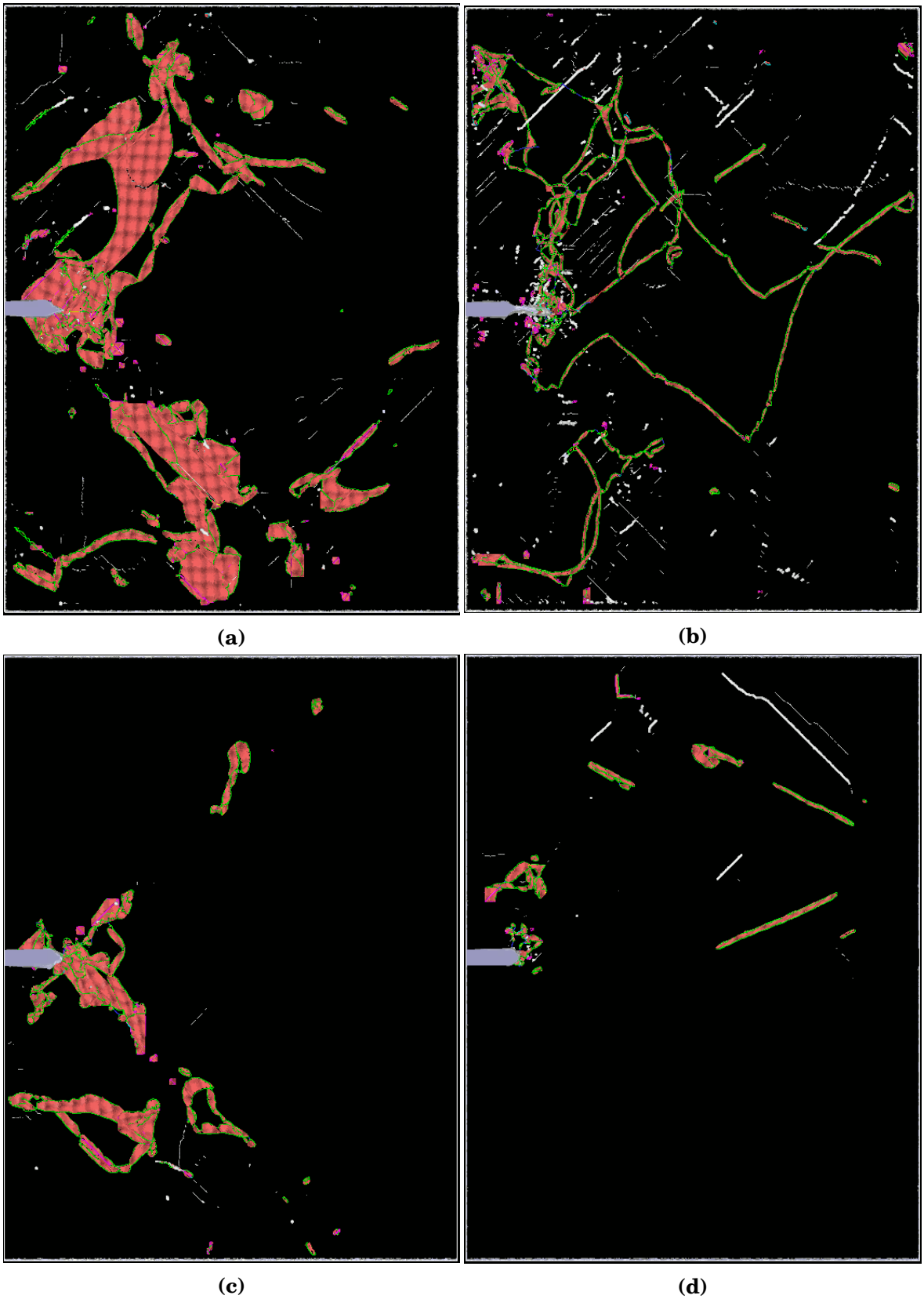

Figure 6-14: Stacking fault areas around crack-tips after the first full cycle with K_{max}=2 $\mathrm{MPa}\sqrt{\mathrm{m}}$ for (a) Ag, (b) Al, (c) Cu, (d) Ni. The stacking fault width varies with the NSFE. Small stacking fault widths are observed for in Al, Ni and large stacking fault widths observed in Ag, Cu

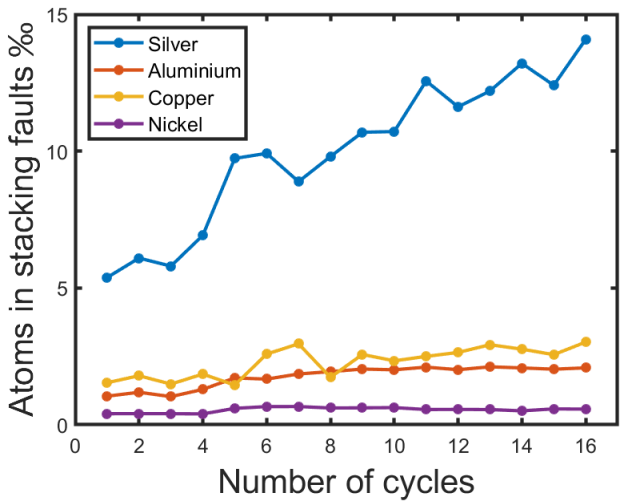

Figure 6-15: Evolution of the proportion of atoms in stacking faults after each cycle for different materials for an applied $K_{max} = 2\ \mathrm{MPa}\sqrt{\mathrm{m}}$

Nickel during cyclic loading for different magnitudes of stress intensity factor. As highlighted in Fig. 6-16, the total dislocation density in Ni increases not only with the applied stress intensity factor but also with the number of cycles. Additionally, the total dislocation density as well as the density of Shockley partials and stair-rod partials increase rapidly with the number of cycles from the first cycles (1^{st} to 5^{th}) then tend to increase almost steadly. Considering the evolution from the 5^{th} cycle, the dislocation density increase rate can be estimated at approximately:

(i) $2 \times 10^{14}\ \mathrm{m}^{-2}.\mathrm{cycle}^{-1}$ for $\Delta K = 2\ \mathrm{MPa}\sqrt{\mathrm{m}}$ and $\Delta K = 2.5\ \mathrm{MPa}\sqrt{\mathrm{m}}$,
(ii) $6 \times 10^{14}\ \mathrm{m}^{-2}.\mathrm{cycle}^{-1}$ for $\Delta K = 3\ \mathrm{MPa}\sqrt{\mathrm{m}}$ and
(iii) $9 \times 10^{14}\ \mathrm{m}^{-2}.\mathrm{cycle}^{-1}$ for $\Delta K = 4\ \mathrm{MPa}\sqrt{\mathrm{m}}$.

Fig. 6-17 show the evolution of dislocation density for different metals for an applied stress intensity factor of 2 $\mathrm{MPa}\sqrt{\mathrm{m}}$. As previously, the total dislocation densities increase with the number of cycles as well as Shockley or stair-rod partials. Considering the evolution of the total dislocation density from the 6^{th} cycle, one can estimate the total dislocation density increase rate at approximately:

(i) $5 \times 10^{14}\ \mathrm{m}^{-2}.\mathrm{cycle}^{-1}$ for silver ($\Delta K = 2\ \mathrm{MPa}\sqrt{\mathrm{m}}$),
(ii) $10^{15}\ \mathrm{m}^{-2}.\mathrm{cycle}^{-1}$ for aluminum ($\Delta K = 2\ \mathrm{MPa}\sqrt{\mathrm{m}}$),
(iii) $6 \times 10^{14}\ \mathrm{m}^{-2}.\mathrm{cycle}^{-1}$ for copper ($\Delta K = 2\ \mathrm{MPa}\sqrt{\mathrm{m}}$).

Considering approximately the same values of ΔK_{eff} ($\Delta K_{eff} = K_{max} - K_{Ie}$) for example, we observe that the increase rate of dislocation density in aluminum ($\Delta K_{eff} = 1.536$) is approximately 2 times higher (around $10^{15}\ \mathrm{m}^{-2}.cycle^{-1}$) than that in silver (with a $\Delta K_{eff} = 1.426$ and around $5 \times 10^{14}\ \mathrm{m}^{-2}.\mathrm{cycle}^{-1}$). However, what about the proportion of each type of dislocation?

As noted previously, the most dislocation type observed are Shockley partials. Other types of dislocation have also been observed and are mostly the result

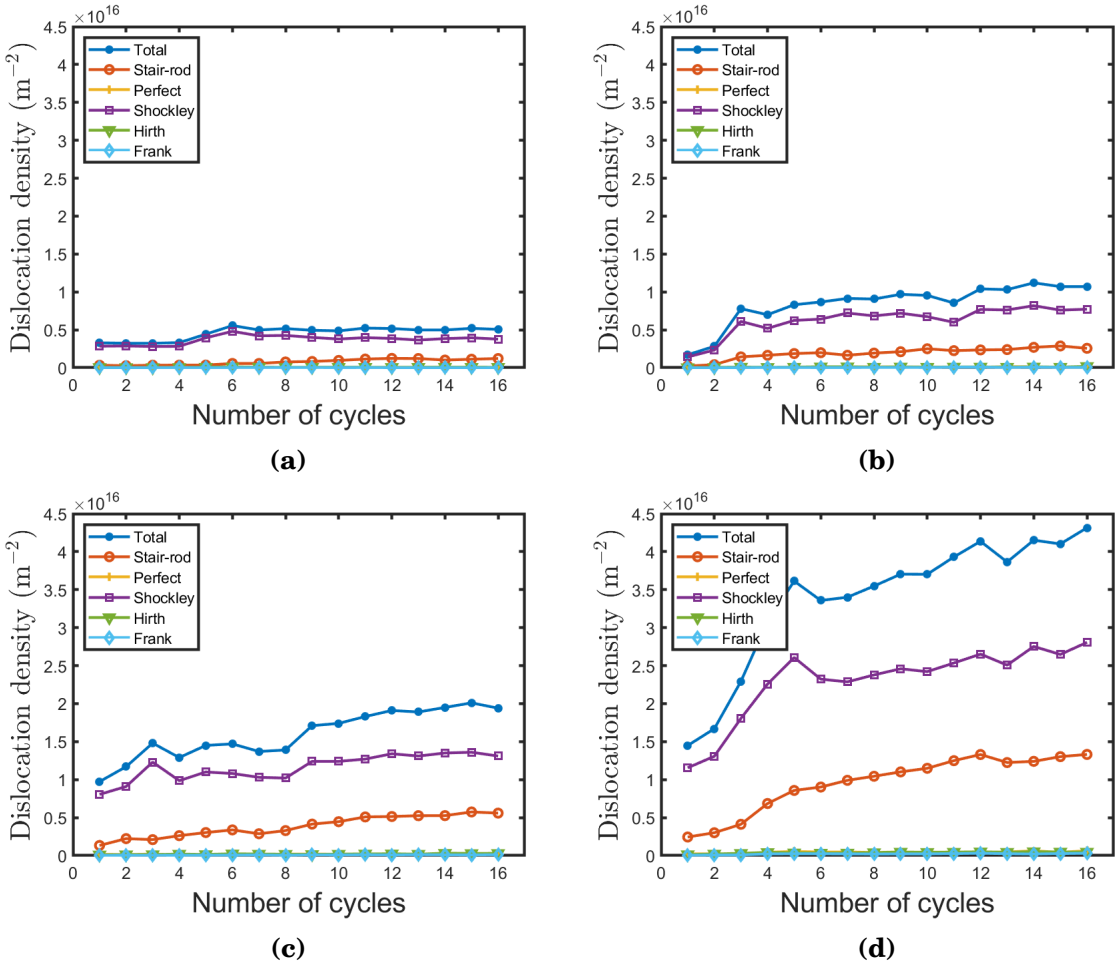

Figure 6-16: Dislocation densities in Ni for different applied stress intensity factor (a) 2 $\mathrm{MPa}\sqrt{\mathrm{m}}$ (b) 2.5 $\mathrm{MPa}\sqrt{\mathrm{m}}$ (c) 3 $\mathrm{MPa}\sqrt{\mathrm{m}}$ (d) 4 $\mathrm{MPa}\sqrt{\mathrm{m}}$. The dislocation density increases with the number of cycles and with the applied stress intensity factor.

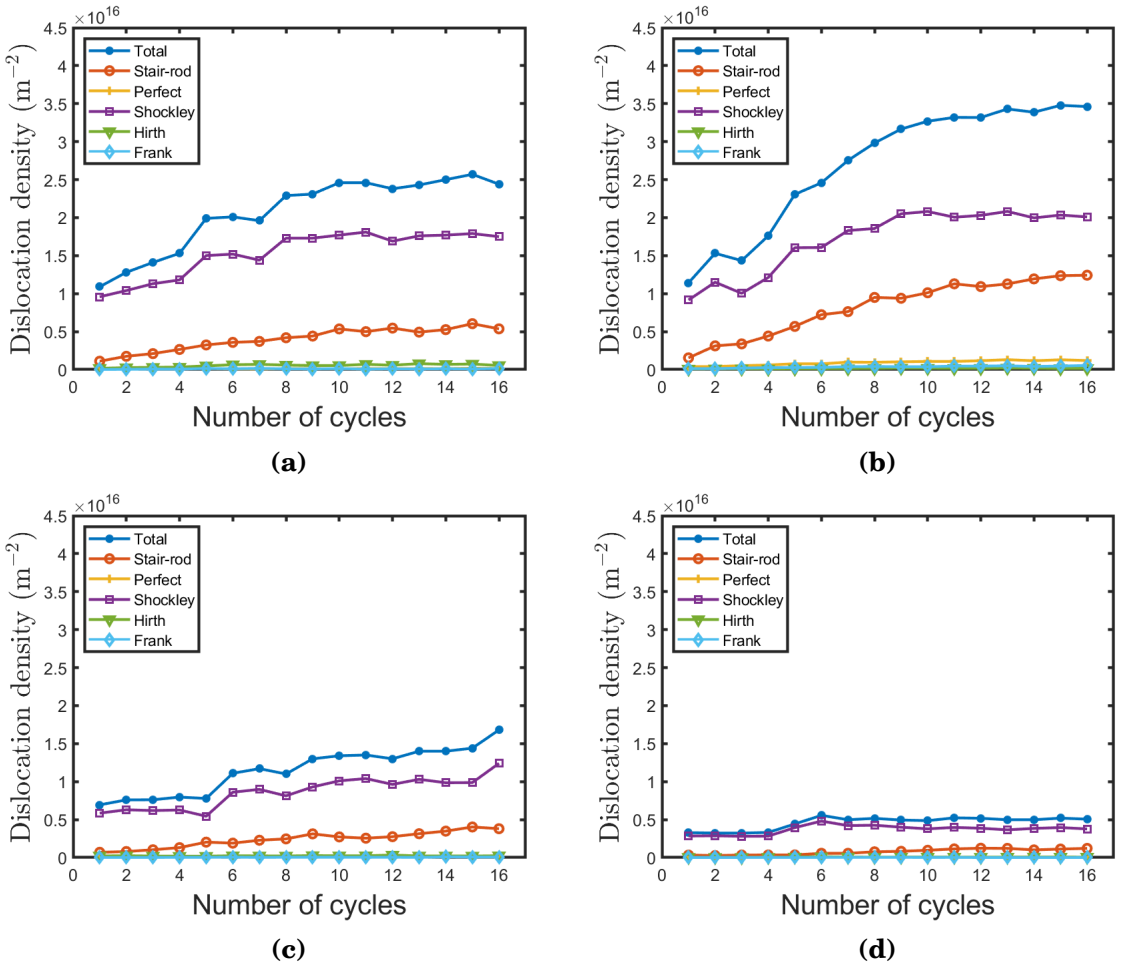

Figure 6-17: Dislocation density at the end of each cycle (after unloading) for (a) Ag, (b) Al, (c) Cu, (d) Ni. Applied $\Delta K = 2\ \mathrm{MPa}\sqrt{\mathrm{m}}$

of interactions between Shockley partials. Indeed, as discussed in chapter 4, given the high density of dislocations emitted at crack-tip, different interactions between slip systems take place and cause the formation of dislocation locks and junctions such as Lomer-Cottrell locks, Hirth locks, entanglements, etc.

Stair-rod partials are dislocation type that are generally involved in the formation of Lomer Cottrell locks, sessile prismatic loops, stacking defect tetrahedra, superjogs and other interactions requiring the presence of a stair-rod partial as a geometrically necessary dislocation [Hull and Bacon, 2011]. These stair-rod dislocations are sessile and constitute barriers, which may prevent the gliding of mobile dislocations as shown in chapter 4. The Hirth locks, which cumulative length is much lower, are also the result of interactions between Shockley partials. These Hirth dislocations are also sessile, and as stair-rod partials, are barriers that may hinder the gliding of mobile dislocations.

Fig. D-7 shows the evolution of the proportion of different types of dislocations during cyclic loading. In general, as depicted on Fig. D-7a and Fig. D-7b,

the Shockley partials proportion decreases during cycling while the stair-rod one increases with the number of cycle as mentioned in chapter 4. It was previously mentioned that the dislocation density is slightly higher in aluminum than in silver for similar values of ΔK_{eff}. Further analysis shows that this difference is partially due to the density of stair-rod partials which is much higher in aluminum than in silver, while the density of Shockley partials is approximately 1.2 times the density of Shockley partials in silver. On the other hand, the proportion of other types of dislocation (perfect dislocations, Hirth partials, Frank partials) in general remains constant throughout the loading cycle.

As can be observed in Fig. D-8 (Appendix D), the loading amplitude does not affect the proportion of certain types of dislocations like perfect dislocations, Hirth partials and Frank partials in nickel. However, certain types of dislocation are more affected, such as Shockley partials or stair-rod partials. Indeed, Fig. D-8 (Appendix D) shows that, the proportion of Shockley partials decreases with the load amplitude increasing. But the inverse situation is observed for stair-rod partials. In fact, for a SIF of $4\ \mathrm{MPa}\sqrt{\mathrm{m}}$, the proportion of Shockley partials at the end of the 16^{th} cycle is established at about 65% while this proportion establishes around 75% for a SIF twice lower ($2\ \mathrm{MPa}\sqrt{\mathrm{m}}$). On the contrary, for stair-rod partials, the proportion at a SIF of $4\ \mathrm{MPa}\sqrt{\mathrm{m}}$, is about 32% and that for a SIF of $2\ \mathrm{MPa}\sqrt{\mathrm{m}}$ is about 24% at the end of the 16^{th} cycle. More generally, one can observe a decrease in the proportion of Shockley partials and at the same time an increase in stair-rod partials proportion as revealed previously (chapter 4) and whatever the metal. The proportion of other types of dislocations (perfect dislocations, Hirth partial, Frank partials) remains almost constant during loading whatever the metal.

The proportions of certain types of dislocations are metal dependent.

(i) For instance, if we consider aluminum ($\Delta K_{eff} = 1.536\ \mathrm{MPa}\sqrt{\mathrm{m}}$) and silver ($\Delta K_{eff} = 1.426\ \mathrm{MPa}\sqrt{\mathrm{m}}$), we notice that the proportion of Shockley partials is higher in aluminum than in silver. This difference is certainly due to the high density of vacancies (due to cross-slip, which seems to be more frequent in aluminium because of the high SFE) leading to the formation of a large number of vacancies because of jogs dragging. Subsequently, these vacancies aggregate either into SFTs and or small vacancy loops with stair-rod partials.

(ii) Nickel shows the same tendency than silver with similar effective SIF, even if its normalized stacking fault energy is 5 times higher than silver. Indeed, for an effective SIF of about $1.68\ \mathrm{MPa}\sqrt{\mathrm{m}}$ ($1.18\ \mathrm{MPa}\sqrt{\mathrm{m}}$) nickel displays a proportion of stair-rod partials of about 29% (25%) against 22% for silver at the end of the 16^{th} cycle for an effective SIF of about $1.426\ \mathrm{MPa}\sqrt{\mathrm{m}}$. Concerning Shockley partials, silver exhibits a proportion of about 71% for an effective SIF of about $1.426\ \mathrm{MPa}\sqrt{\mathrm{m}}$ while nickel displays a proportion of about 68% (72%) for an effective SIF of $1.68\ \mathrm{MPa}\sqrt{\mathrm{m}}$ ($1.18\ \mathrm{MPa}\sqrt{\mathrm{m}}$).

(iii) Copper for example displays a proportion of stair-rod partials of around 23% (75% for Shockley partials) for an effective SIF of $1.248\ \mathrm{MPa}\sqrt{\mathrm{m}}$ while at a slightly lower effective SIF ($1.18\ \mathrm{MPa}\sqrt{\mathrm{m}}$), the proportion of stair-rod partials is

about 25% (72% for Shockley partials) in nickel.

(iv) For the other dislocation types, under an effective SIF of about 1.536 $\mathrm{MPa}\sqrt{\mathrm{m}}$ in aluminum (respectively 1.426 $\mathrm{MPa}\sqrt{\mathrm{m}}$ in silver), the proportion of perfect dislocations remain almost constant during loading and is established to 3.5% in aluminum (respectively 0.5% in silver). Their proportion is approximately 7 times lower than in aluminium. In fact, the high stacking fault energy of aluminium leads to low Shockley partial separation distance. This favors the local recombination between Shockley partials for cross-slip. For other metals with a similar effective SIF the proportion of perfect dislocations ranges between 0.5% and 1.2%.

Otherwise, one can notice in Fig. D-7d (Appendix D) that, the proportion of Hirth partials is higher in low (Ag) and medium (Cu) SFE materials than in high (Al, Ni) SFE materials. For instance, in silver, Hirth partials represents $2.5 - 3\%$ of dislocation density whereas in aluminium this proportion drops to 0.5%, i.e. five times lower than in silver. In fact a low SFE (high partial separation) increases the probability of interaction whith long Hirth partials in Ag than in Al, which exhibits high SFE (low partial separation distance).

A local analysis of dislocation structures in the direct vicinity of the crack-tip (in a radius of 25 nm around the crack-tip) show a number of Hirth junction in and a number of junctions involving stair-rod partials in Ag whereas in Al, these junctions are rare (Fig. 6-24).

As a consequence, a dense dislocation network confined in the direct vicinity of the fatigue crack-tip in Ag compared to Al or Ni (Fig. 6-24). A similar observation was made experimentally by Awatani *et al.* [Awatani et al., 1979] who reported that in brass (low SFE), very dense dislocations accumulated just ahead of crack-tips whereas in copper well defined dislocation cells were observed. As stated previously, since the low SFE materials such as Ag exhibits large separation distance between the leading and trailing Shockley partials, this increases the probability of interactions between dislocations leading to the formation of sessile dislocations such as Hirth locks, Lomer-Cottrell locks, entanglements, inducing obstacles formation and confining dislocations near crack-tip zones. In Al which exhibits high SFE for example, Hirth junctions and junctions involving stair-rod partials and mobile dislocations are rare. Moreover, the relative low number of dislocations in the direct vicinity of crack-tip in high SFE metals such as Al and Ni can be explained by the high mobility of dislocations. Because of easy cross-slip, dislocations may pass obstacles much more easily than in Ag. Cross-slip can also lead to dislocation annihilation and this can also explain the relative low number of dislocation near crack-tip in high SFE metals.

With such dislocation structures made of entanglements, Hirth locks, Lomer-Cottrell locks, etc. the mobility of dislocations can be impeded and cross-slip mechanisms can enhance the overpassing of the obstacles more easily in high SFE metals. In our investigation, cross-slip was more frequently observed in Al than in all other metals. In fact, with the highest SFE, aluminum displays the lowest Shockley screw partial separation distance ($\mathrm{d}_{\mathrm{SF}}^{\mathrm{S}} = 0.28$ nm) which is suffi-

ciently small to facilitate the cross-slip mechanism. A relatively high frequency of cross-slip can be also reported in nickel ($d_{SF}^{S} = 0.59$ nm). This is not the case in silver ($d_{SF} = 3.26$ nm) where this mechanism is not so frequent even if one can report some cross-slips. The relative high stresses near crack-tip zones can also contribute to facilitate the cross slip.

One of the consequences of this cross slip is the production of point defects such as vacancies as shown previously. As plastic deformation intensifies, the dislocation density increases (Fig. 6-16). The glide of dislocations through a forest of dislocations leads to the formation of jogs and superjogs as well as cross-slip of screw dislocations. The glide of these jogs, which is a non conservative movement leads to the production of point defects, mainly vacancies. Fig. 6-18 displays for instance, the spatial distribution of vacancies in the four metals under investigation for an applied SIF of 2 $\mathrm{MPa}\sqrt{\mathrm{m}}$ (for Ag, Al, Cu) and 3 $\mathrm{MPa}\sqrt{\mathrm{m}}$ (for Ni). And as stated previously, vacancies and vacancy clusters in FCC metals such as those observed in our investigation have been widely observed in prior experimental investigation conducted by Kiritani *et al.*, [Kiritani et al., 1999], Matsukawa *et al.* in Al, Cu, Ni [Matsukawa et al., 2003b]. Plastic deformation, as already pointed out by Hull and Bacon [Hull and Bacon, 2001], generally results in a supersaturation of vacancies. Since plastic deformation accumulates with the number of cycles and increases with the load level, the vacancy concentration also follows the same trends.

Fig. 6-19a shows the evolution of vacancy concentration as a function of the number of cycles for the four metals after unloading and for $\Delta \mathrm{K} = 2\ \mathrm{MPa}\sqrt{\mathrm{m}}$. As depicted in Fig. 6-19a in aluminum much more numerous vacancies are produced than in all other metals under study. This measured vacancy concentration is very high and is due to cross-slip jogs formation and dragging. With its high SFE, dislocations in aluminium can easily cross-slip, mechanism during which many jogs are produced on screw dislocations. These jogs dragging leads to the production of vacancies. Values of vacancy concentration ranges from 10^{-4} to $10^{-3}\mathrm{at}^{-1}$ and are in the same order of magnitude as those measured experimentally during severe plastic deformation (see Čížek et al. [Čížek et al., 2019]).

As stated previously, the production of vacancies increases with the loading amplitude. In Fig. 6-19b, one can observe that the vacancy concentration in Nickel increases with the applied SIF. The vacancy production rate can be estimated to be around:

(i) $10^{-5}\ \mathrm{at}^{-1}.\mathrm{cycle}^{-1}$ for an applied SIF of $2\ \mathrm{MPa}\sqrt{\mathrm{m}}$,
(ii) $2 \times 10^{-5}\ \mathrm{at}^{-1}.\mathrm{cycle}^{-1}$ for an applied SIF of $2.5\ \mathrm{MPa}\sqrt{\mathrm{m}}$,
(iii) $3 \times 10^{-5}\ \mathrm{at}^{-1}.\mathrm{cycle}^{-1}$ for an applied SIF of $3\ \mathrm{MPa}\sqrt{\mathrm{m}}$,
(iv) $10^{-4}\ \mathrm{at}^{-1}.\mathrm{cycle}^{-1}$ for a SIF of $4\ \mathrm{MPa}\sqrt{\mathrm{m}}$.

The vacancy production rate is also metal depending:

(i) For a similar applied effective SIF, the vacancy production rate in aluminum (for $\Delta K_{eff} = 1.536\ \mathrm{MPa}\sqrt{\mathrm{m}}$) is about six times higher than in silver (for $\Delta K_{eff} = 1.426\ \mathrm{MPa}\sqrt{\mathrm{m}}$).

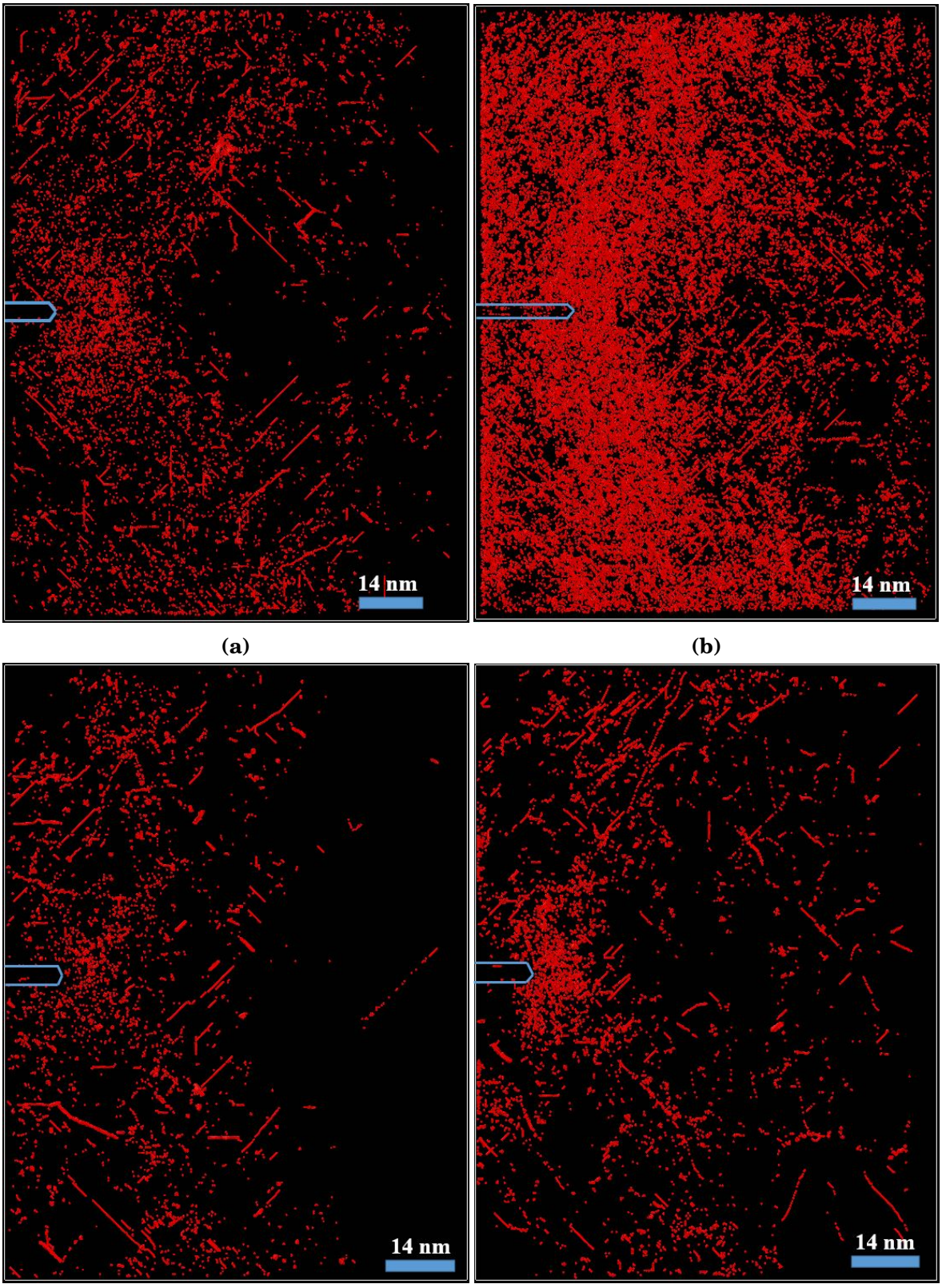

Figure 6-18: Snapshots of vacancy distribution at the 16th cycle for (a) silver (applied $\Delta K = 2\ \mathrm{MPa}\sqrt{\mathrm{m}}$); (b) aluminum (applied $\Delta K = 2\ \mathrm{MPa}\sqrt{\mathrm{m}}$); (c) copper (applied $\Delta K = 2\ \mathrm{MPa}\sqrt{\mathrm{m}}$); (d) nickel (applied $\Delta K = 3\ \mathrm{MPa}\sqrt{\mathrm{m}}$). One can see the high vacancy concentration in aluminum.

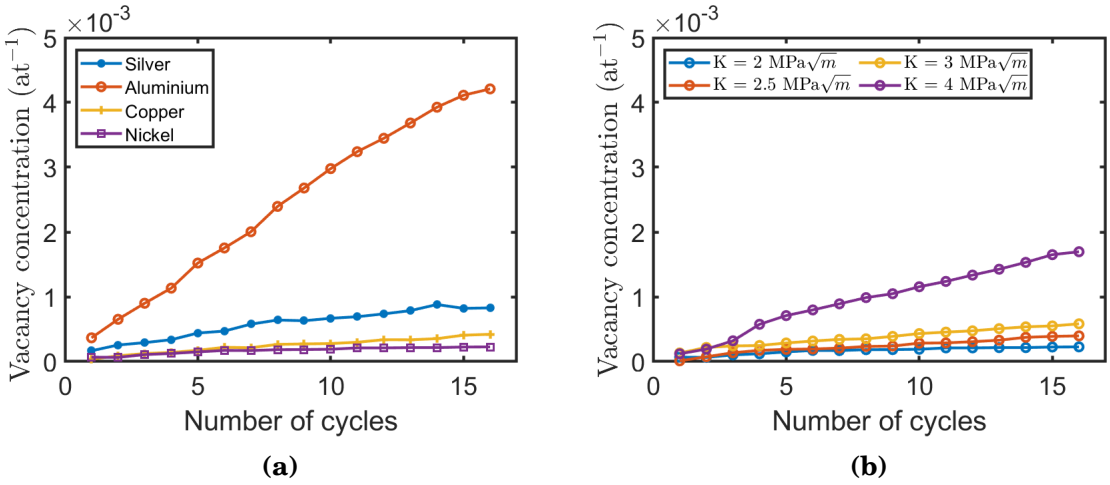

Figure 6-19: Vacancy concentration during cyclic straining measured at the end of each cycle: (a) in the four metals under investigation and an applied $\Delta K = 2\ \mathrm{MPa}\sqrt{\mathrm{m}}$. (b) in nickel for different ΔK.

(ii) In copper, vacancy production rate for an effective SIF of $1.248\ \mathrm{MPa}\sqrt{\mathrm{m}}$ is approximately $2 \times 10^{-5}\ \mathrm{at}^{-1}.\mathrm{cycle}^{-1}$ while that in nickel amount to about $2 \times 10^{-5}\ \mathrm{at}^{-1}.\mathrm{cycle}^{-1}$ (respectively $3 \times 10^{-5}\ \mathrm{at}^{-1}.\mathrm{cycle}^{-1}$) for an effective SIF of $1.18\ \mathrm{MPa}\sqrt{\mathrm{m}}$ (respectively $1.68\ \mathrm{MPa}\sqrt{\mathrm{m}}$). Therefore, copper and nickel behaves similarly.

(iii) At a similar effective SIF, the vacancy production rate is therefore higher in aluminum than in the three other metals which exhibit, at a similar effective SIF, close vacancy production rates. The high production rate of vacancies in aluminum can indeed be explained by the normalized fault stacking energy, which is found to be largely the highest of all the values of other studied metals.

Vacancy clustering can lead to the production of stacking fault tetrahedron. A large number of small stacking fault tetrahedra are widely observed in our investigations. Number of experimental studies have showed the formation of a large number of stacking fault tetrahedra and vacancy-type dislocation loops near crack-tip zones by the means of Transmission Electron Microscopy (Matsukawa *et al.* [Matsukawa et al., 2003b], Kiritani *et al.* [Kiritani et al., 1999]). These stacking fault tetrahedra have been observed in a variety of FCC metals including Al, Cu, Ni, Au. In our investigations, similar observations are made However, the number of SFTs seems fairly low in aluminium in which large number of vacancy-type dislocation loops are produced. The SFTs formation was widely studied in MD simulations (Wang and co-workers [Wang et al., 2011c], [Wang et al., 2011e], [Wang et al., 2011d]), and their interaction with mobile dislocations has been the subject of a number of studies (for instance, [Wirth et al., 2000b], [Chen et al., 2019]). Numerous studies have made it possible to study the influence of SFTs on the mobility of dislocations. In our simulations, it is observed for example that in Ag, mobile disloca-

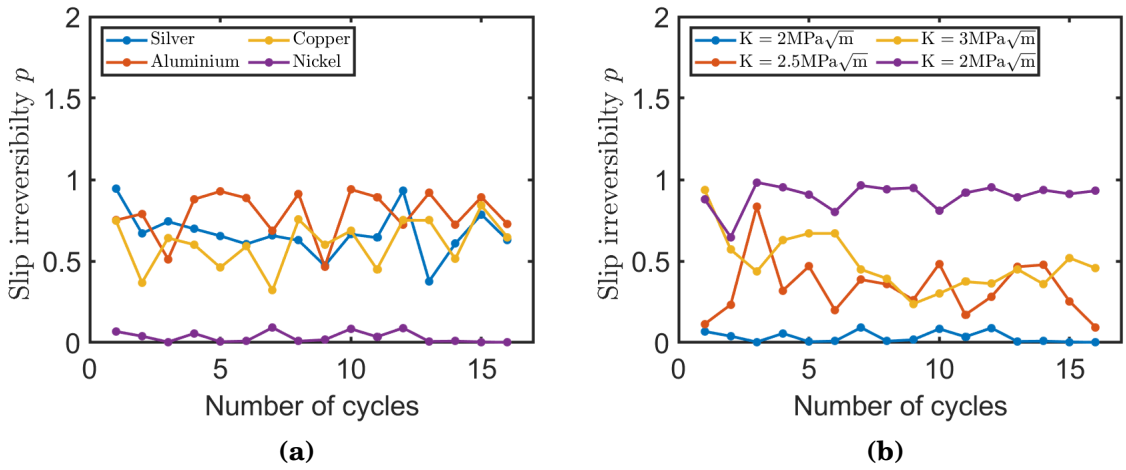

Figure 6-20: (a) Per cycle slip irreversibility factor in the four metals under investigation and for an applied $\Delta K = 2\ \mathrm{MPa}\sqrt{\mathrm{m}}$ (b) Per cycle slip irreversibility factor for nickel for different applied ΔK.

tions can interact with SFTs and since stair-rod partials are sessile dislocations, it impedes the gliding of these mobile dislocations. But in Al, less interactions is observed between SFTs and mobile dislocations.

6.4.1.3 Plastic irreversibility

Plastic slip induced by dislocation gliding can be strongly irreversible because of different dislocation junctions and obstacles as shown previously in chapter 4. Fig. 6-20a shows the evolution of the slip irreversibility factor as a function of the number of cycles in nickel under different loading amplitudes. One can observe in Fig. 6-20a that the slip irreversibility factor increases with the loading amplitude. Hence, the mean slip irreversibility factor over the 16 cycles are the following:

(i) it can be estimated to be 0.033 under $\Delta K = 2\ \mathrm{MPa}\sqrt{\mathrm{m}}$,

(ii) the mean value under $\Delta K = 2.5\ \mathrm{MPa}\sqrt{\mathrm{m}}$ amount to approximately 0.34.

(iii) The computed mean slip irreversibility factor for a $\Delta K = 3\ \mathrm{MPa}\sqrt{\mathrm{m}}$ is estimated to be 0.5

(iv) and finally, under $\Delta K = 4\ \mathrm{MPa}\sqrt{\mathrm{m}}$, the mean slip irreversibility factor amounts to 0.89.

The plastic irreversibility factor is also found to be metal dependent. Hence, as one can observe in Fig. 6-20b, at the same loading amplitude $\Delta K = 2\ \mathrm{MPa}\sqrt{\mathrm{m}}$:

(i) the mean plastic irreversibility factor in silver is approximately 0.67 while the aluminium one reaches 0.8.

(ii) As far as copper is concerned, the mean plastic irreversibility factor under $\Delta K = 2\ \mathrm{MPa}\sqrt{\mathrm{m}}$ equals 0.55.

Considering now the effective SIF applied, one can report for example that, at similar effective SIF, the mean plastic irreversibility factor in aluminium is

0.8 under $\Delta K_{eff} = 1.536\ \mathrm{MPa}\sqrt{\mathrm{m}}$, close to the silver value: 0.67 under $\Delta K_{eff} = 1.426\ \mathrm{MPa}\sqrt{\mathrm{m}}$). Nevertheless, the mean plastic irreversibility irreversibility factor in silver under $\Delta K_{eff} = 1.426\ \mathrm{MPa}\sqrt{\mathrm{m}}$ is approximately 1.4 times higher than that in nickel (0.5 under $\Delta K_{eff} = 1.68\ \mathrm{MPa}\sqrt{\mathrm{m}}$) and approximately 1.1 times than that in copper (under $\Delta K_{eff} = 1.25\ \mathrm{MPa}\sqrt{\mathrm{m}}$). The plastic irreversibility at the crack-tip can be the result of dislocations barriers in the vicinity of the crack-tip, and also the result of cross-slip mechanism leading to the annihilation of screw dislocations. Depending on the stacking fault energy, certain mechanisms may be favored more than other. Thus in metals with low stacking fault energy such as Ag, the dislocations remaining confined close to the crack-tip induce a high plastic irreversibility. In this case, the irreversibility induced by the junctions between dislocations is preponderant. In metals with high stacking energy (such as Al or Ni), the dislocations remaining confined close to the crack-tip are not many as in Ag. Nevertheless, the dislocation annihilation induced by easy cross-slip may become predominant. Large plastic irreverisibility can lead to fatigue crack growth as shown previously in chapter 5. The following section is dedicated to the analysis of crack propagation from both a physical and mechanical point of view.

6.4.2 Fatigue crack growth

As recalled in chapter 2, two main mechanisms of fatigue crack propagation have been highlighted in literature: the propagation by cavity coalescence encountered mainly in alloys containing secondary phase particles and the blunting-resharpening mechanisms. Now examining the influence of the stacking fault energy on fatigue crack propagation, it was found that in general, fatigue crack propagation occurs by plastic blunting and irreversibility whatever the metal under investigation. In other words, the stacking fault energy does not change the fatigue crack growth mechanism which is apparently intrinsic to ductile pure metals. If stacking fault energy does not lead to a change of the FCP mechanisms, the same does not hold for the propagation rates as described in the following paragraph.

Fig. 6-21 shows the computed FCGR data for the metals plotted as a function of the SIF amplitude (Fig. 6-21a), of the SIF normalized by the Young's modulus: $\Delta K_{NE} = \Delta K / E^*_{[1\,0\,0]}$ (Fig. 6-21b), and as a function of the effective SIF normalized by the Young's modulus: $\Delta K^{NE}_{eff} = \Delta K_{eff} / E^*_{[1\,0\,0]}$ (Fig. 6-21c). These data all obey power laws (Equations 6.24, 6.25, 6.26).

$$\frac{da}{dN} = C_7 \times (\Delta K)^{m_7} \tag{6.24}$$

$$\frac{da}{dN} = C_8 \times (\Delta K_{NE})^{m_8} = C_8 \times \left(\frac{\Delta K}{E^*_{[0\,1\,0]}} \right)^{m_8} \tag{6.25}$$

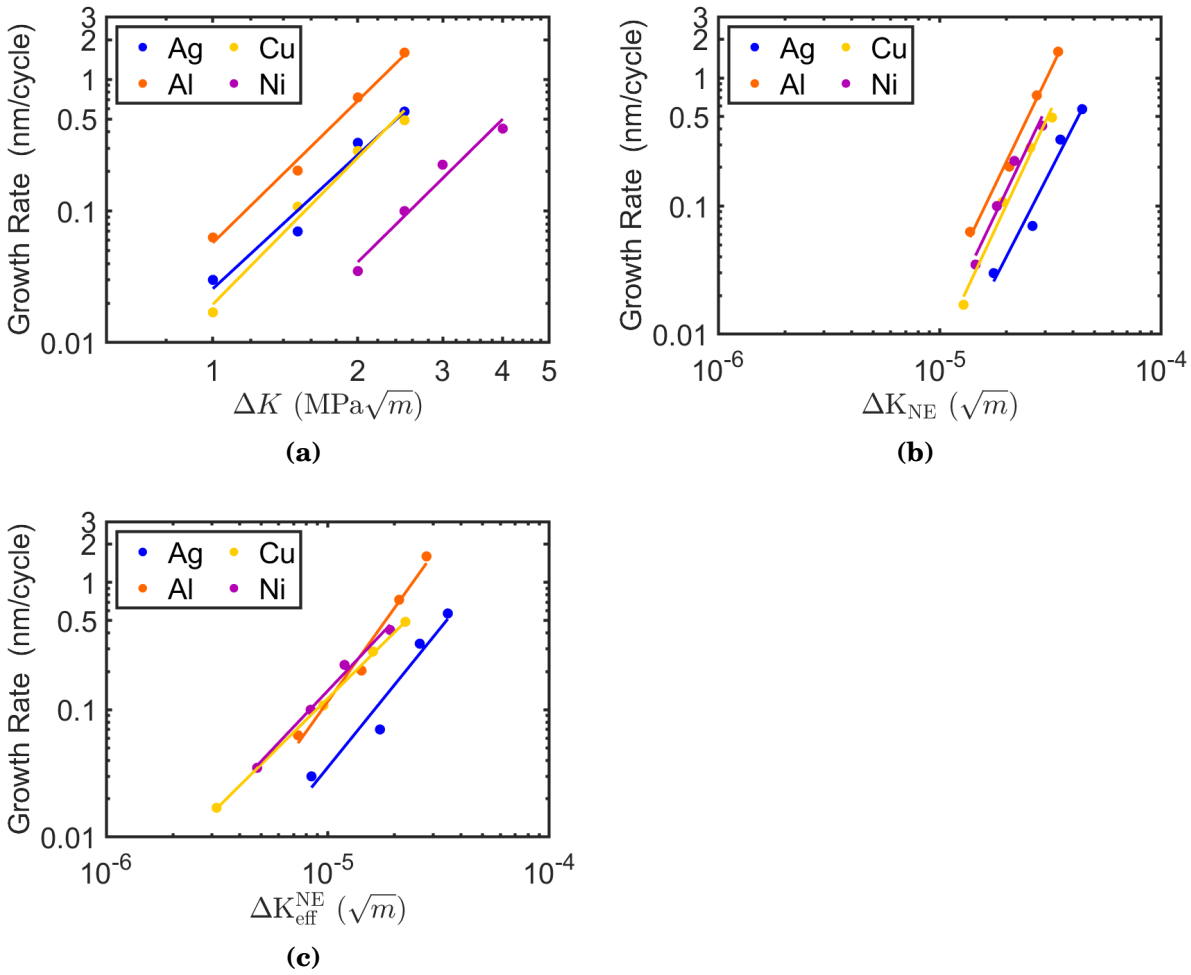

Figure 6-21: Fatigue crack growth rate as function of (a) SIF amplitude (b) Normalized SIF ΔK_{NE} (c) Normalized effective SIF ΔK_{eff}^{NE}. Dots represent fatigue crack growth rate data from MD simulation and solid lines represent the adjusted Paris law curves.

$$\frac{da}{dN} = C_9 \times \left(\Delta K_{eff}^{NE}\right)^{m_9} = C_9 \times \left(\frac{\Delta K_{eff}}{E^*_{[0\,1\,0]}}\right)^{m_9} \tag{6.26}$$

The adjusted parameters, are displayed in tables 6.6, 6.7 6.8. We observe that the exponent of the Paris law and modified Paris law characterized by Equations 6.24 and 6.25 varies between 3 and 4 (3.38 for silver, 3.59 for aluminum, 3.60 for copper and 3.61 for nickel). These exponents are approximately 4 and are in agreement with reported experimental values in ductile single crystals ([Ishii and Weertman, 1971a]). The exponents adjusted using Equation 6.26 vary between 1.7 and 2.44 (i.e. approximately 2). Fig. 6-21a shows that the highest propagation rates occur in aluminum, followed by silver, copper and fi-

Table 6.6: Adjusted parameters of Equation 6.24

	Ag	Al	Cu	Ni
$C_7 \left(\frac{\text{nm.cycle}^{-1}}{(\text{MPa}\sqrt{\text{m}})^{\text{m}_7}}\right)$	0.0257	0.0574	0.0196	0.003
m_7	3.38	3.59	3.60	3.61

Table 6.7: Adjusted parameters of Equation 6.25

	Ag	Al	Cu	Ni
$C_8 \left(\frac{\text{nm.cycle}^{-1}}{(\sqrt{\text{m}})^{\text{m}_8}}\right)$	2.7×10^{14}	1.67×10^{16}	8.22×10^{15}	1.17×10^{16}
m_8	3.38	3.59	3.60	3.61

nally nickel. Fig. 6-21b shows the propagation rates as a function of the SIF normalized by the Young's modulus. It still suggests a higher propagation rate in aluminum, but now followed by nickel, copper and silver, which recalls the order of the four stacking fault energies, or normalized stacking fault energies. Since the modified Paris law exponents in Equation 6.25 and Equation 6.26 are approximately 4 and 2 respectively, by fixing the exponent of the modified Paris law to 4 in the Equation 6.25 and to 2 in Equation 6.26, the values of $1/C_{NE}$ (Equation 6.27) and $1/C_{NE}^{eff}$ (Equation 6.28) are obtained for each of the four metals. The metal-dependent parameter $1/C_{NE}$ is plotted as a function of the normalized stacking fault energy (Fig. 6-22). A similar plot is shown in Fig. 6-23 and is dedicated to the metal-dependent parameter $1/C_{NE}^{eff}$.

Closed-form expressions describing the evolution of these parameters, C_{NE} and C_{eff}^{NE}, as a function of the normalized stacking fault energy is proposed are Equations 6.29 and 6.30. They are based on the evolution observed in Equation 6-22 and Equation 6-23. The three parameters related to each analytical formula are identified and displayed in table 6.9. The Paris law can therefore be enriched to take into account the influence of the normalized stacking fault energy (as shown in Equations 6.31 and 6.32).

$$\frac{da}{dN} = C_{NE} \times (\Delta K_{NE})^4 = C_{NE} \times \left(\frac{\Delta K}{E^*_{[0\,1\,0]}}\right)^4 \tag{6.27}$$

Table 6.8: Adjusted parameters of Equation 6.26

	Ag	Al	Cu	Ni
$C_9 \left(\frac{\text{nm.cycle}^{-1}}{(\sqrt{\text{m}})^{\text{m}_8}}\right)$	2.018×10^9	1.797×10^{11}	5.037×10^7	2.24×10^8
m_9	2.15	2.44	1.72	1.84

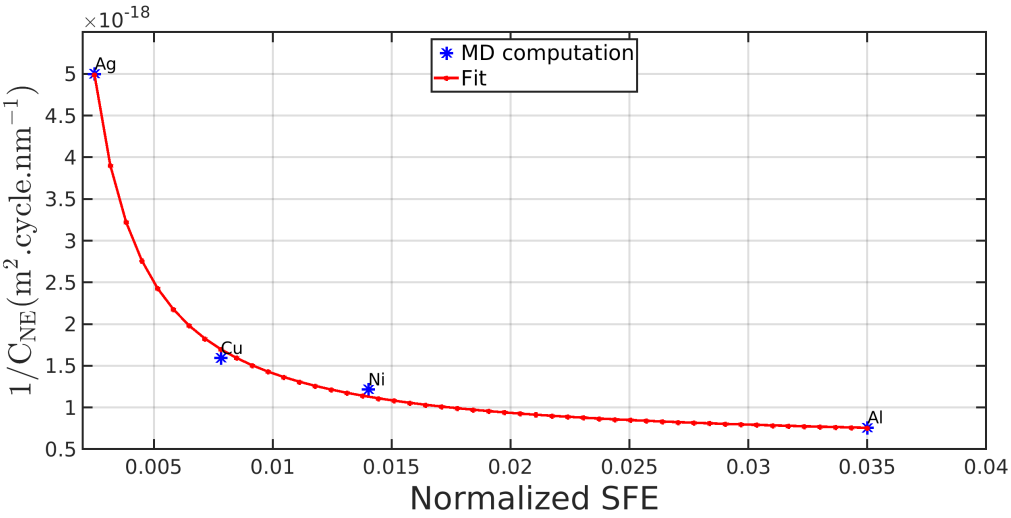

Figure 6-22: Evolution of $1/C_{NE}$ as function of the normalized stacking fault energy. Adjustment of the three parameters of Equation 6.29

$$\frac{da}{dN} = C_{eff}^{NE} \times \left(\Delta K_{eff}^{NE}\right)^2 = C_{eff}^{NE} \times \left(\frac{\Delta K_{eff}}{E^*_{[0\,1\,0]}}\right)^2 \tag{6.28}$$

$$\frac{1}{C_{NE}} = \chi_1 \times \left(\frac{\gamma_{sf}}{\mu_{slip} b}\right)^{\phi_1} + \psi_1 \tag{6.29}$$

$$\frac{1}{C_{eff}^{NE}} = \chi_2 \times \left(\frac{\gamma_{sf}}{\mu_{slip} b}\right)^{\phi_2} + \psi_2 \tag{6.30}$$

$$\frac{da}{dN} = \left(\frac{1}{\chi_1 \times \left(\frac{\gamma_{sf}}{\mu_{slip} b}\right)^{\phi_1} + \psi_1}\right) \times \left(\frac{\Delta K}{E^*}\right)^4 \tag{6.31}$$

$$\frac{da}{dN} = \left(\frac{1}{\chi_2 \times \left(\frac{\gamma_{sf}}{\mu_{slip} b}\right)^{\phi_2} + \psi_2}\right) \times \left(\frac{\Delta K_{eff}}{E^*}\right)^2 \tag{6.32}$$

Table 6.9: Fitted parameters of Equation 6.29 and Equation 6.30

$1/C$	χ_i	ϕ_i	ψ_i
$1/C_{NE}$ $(i=1)$	4.554×10^{-21}	**-1.15**	5.190×10^{-19}
$1/C_{eff}^{NE}$ $(i=2)$	1.192×10^{-14}	**-2.00**	6.404×10^{-10}

In agreement with numerical results, these analytical formulas suggest that FCGR increases with increasing normalized stacking fault energy. Knowing that

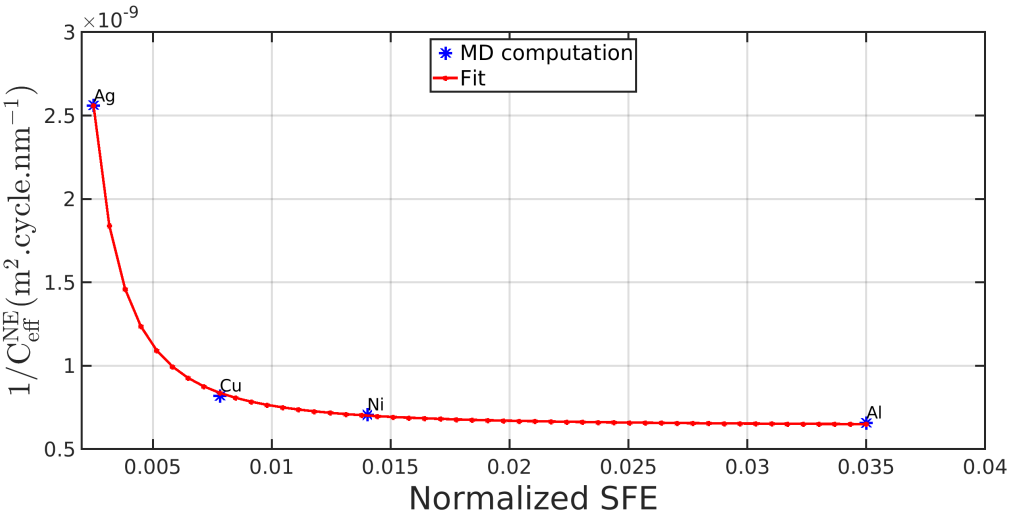

Figure 6-23: Evolution of $1/C_{eff}^{NE}$ as function of the normalized stacking fault energy. Adjustment of the three parameters of Equation 6.30

there is a relationship between the normalized stacking fault energy and the separation distance d_{SF} between Shockley partials of a dissociated full dislocation (Equation 6.22, 6.23), we can use the dislocation structures to explain this variation in the propagation rates as a function of normalized stacking fault energy. Indeed, these formulas present two asymptotes:

(i) when $\gamma_{sf}/\mu_{slip}b$ tends toward 0 (i.e. $d_{SF} \rightarrow \infty$), the value of $1/C_{NE}$ (respectively $1/C_{eff}^{NE}$) tends toward ∞ i.e. C_{NE} and C_{eff}^{NE} tend towards 0. Therefore, $da/dN \rightarrow 0$. This purely theoretical case, corresponds physically to the case where the emission of a first leading Shockley partial is not followed by a trailing partial. The difficulty of emitting dislocations impede the advance of the crack which occurs by material removal induced by dislocation emission during the loading half cycle, and therefore hinder the cyclic crack propagation. In the case where the emission of the first leading partial is not followed by a trailing partial but rather by another leading partial on an adjacent plane, twinning occurs and it offers increased resistance to the fatigue crack propagation (chapter 5).

(ii) When $\gamma_{sf}/\mu b \rightarrow \infty$ (i.e. $d_{SF} \rightarrow 0$), the values of $1/C_{NE}$ and $1/C_{eff}^{NE}$ tends towards finite values of respectively $\psi_1 = 5.190 \times 10^{-19}$ $[\mathrm{m}^{-2}.\mathrm{nm}^{-1}.\mathrm{cycle}]$ and $\psi_2 = 6.404 \times 10^{-10}$ $[\mathrm{m}^{-1}.\mathrm{nm}^{-1}.\mathrm{cycle}]$. It is interesting to note that these finite values are close to the aluminum ones, which amount to approximately 7.604×10^{-19} and 6.596×10^{-10} respectively. Knowing that in aluminum the separation distance of Shockley partials equals approximately $d_{SF}^{S} = 0.28$ nm for screw partials and $d_{SF}^{E} = 0.70$ nm for edge partials, the closed-form expressions predict that the effect of these small d_{SF} would affect FCGR. The propagation rates therefore seems to be intrinsically linked to the separation distance of the Shockley partials, which depends on the normalized stacking fault energy of each FCC metal. Hence, to understand the influence of the normalized stacking fault energy on

the propagation rates, it would be interesting to understand the influence of the separation distance of Shockley partials on the microstructures around the crack-tip.

As mentioned previously, the separation distances between Shockley partials depend on the normalized stacking fault energy. In metals with low stacking fault energy such as silver, the separation distance between Shockley partials is large and smaller in high stacking fault energy metals such as aluminum (Table 6.5). The higher the separation distance between Shockley partials, the higher the probabilities of interactions and formation of junctions. This leads to a complex and dense cluster of dislocations confined to close crack-tip volume (Fig. 6-24a). Also, one can observe in Fig. 6-24a, interactions between dislocations involving stair-rods and Hirth partials which are sessile dislocations. This hinders the dislocations gliding away from the crack tip. This complex and dense cluster of dislocations close to the crack-tip in low SFE metals induces a hardening of the material in the surroundings close to the crack-tip hindering deformation and cyclic propagation difficult. The dislocations remaining confined at the crack-tip also induce back-stresses which are exerted on the crack-tip and prevent the emission of additional dislocations. The difficulty of emitting dislocations prevents crack-tip advance since crack advance by material remove from crack-tip due to dislocation emission. In metals with high normalized stacking energy, the separation distance between Shockley partials being small, there is less junctions and locks and thanks to the easy cross-slip, mobile dislocations can pass beyond the obstacles (other dislocation locks, SFTs, etc.). The dislocation are then highly mobile and fewer dislocations remains close to the crack-tip (Fig. 6-24b). The annihilation of the dislocations by cross-slip is also one of the reasons for the low number of dislocations near crack-tip. The metal close to the crack-tip is therefore softer than in the previous case and the back-stresses acting on the crack-tip are reduced. Therefore, the metal is a more ductile compared to the previous case and the plastic deformation is a more larger as the propagation rates are. It should be added that the annihilation of the dislocations during cross-slip, more frequent at small d_{SF} values, triggers an additional plastic irreversibility. Consequently, an increase in propagation rates is expected. Finally, as can be noticed in Fig. 6-24b, the high vacancy concentration around crack-tip in high SFE metals, may also increase slightly propagation rates.

The predictions of the analytical formula proposed in Equation 6.28 are now compared to experimental data of Ishii and Weertman [Ishii and Weertman, 1971a]). Based on previous computations described in chapter 5 and dedicated to the effect of crystal orientation, a closed-form expression for orientation B1 ($[1\,1\,0]$) is derived. Fig. 6-25 shows the comparison between the predictions and the experimental data. These experiments were carried out using copper and Cu-13.5%Al alloy ($\gamma_{sf} = 8.5\ \mathrm{mJ.m^{-2}}$ [Bonnet and Youssef, 2006]) with a tensile axis close to $\langle 1\,1\,0\rangle$ in liquid nitrogen ($77\,\mathrm{K}$). We can observe in Fig. 6-25 a gap between the proposed model and the experimental results. As stated previously in chapter 5, the fatigue crack

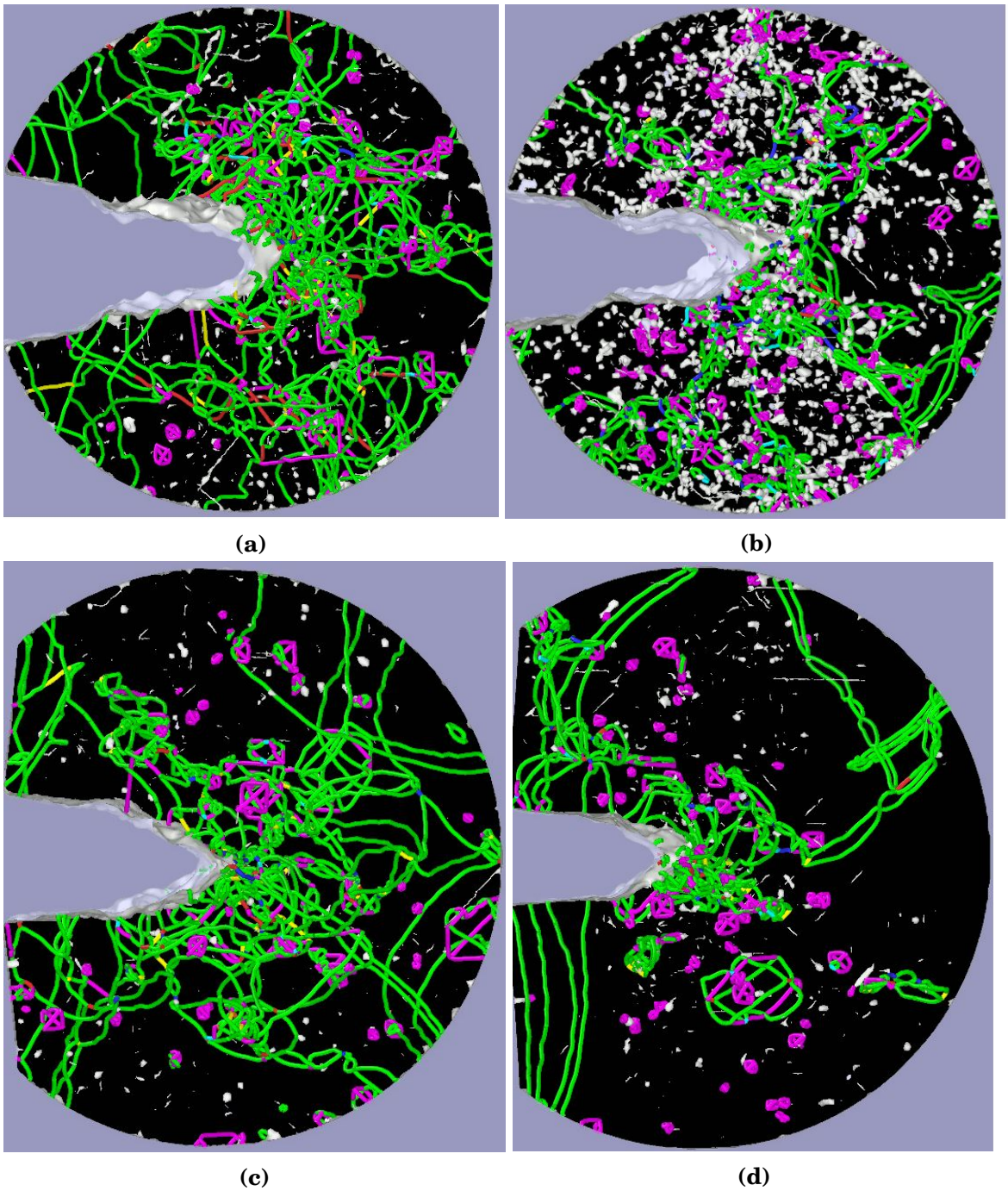

Figure 6-24: Dislocation microtructures in the vicinity of the crack tip within a radius of 25 nm for (a) silver (applied effective SIF: 1.43 $\mathrm{MPa}\sqrt{\mathrm{m}}$); (b) aluminum (applied effective SIF: 1.53 $\mathrm{MPa}\sqrt{\mathrm{m}}$); (c) copper (applied effective SIF: 1.75 $\mathrm{MPa}\sqrt{\mathrm{m}}$); (d) nickel (applied effective SIF: 1.68 $\mathrm{MPa}\sqrt{\mathrm{m}}$). The small white spots represent vacancies. One can observe the high dislocation length (an low vacancies) in Ag and the low dislocation length (high vacancies) in Al.

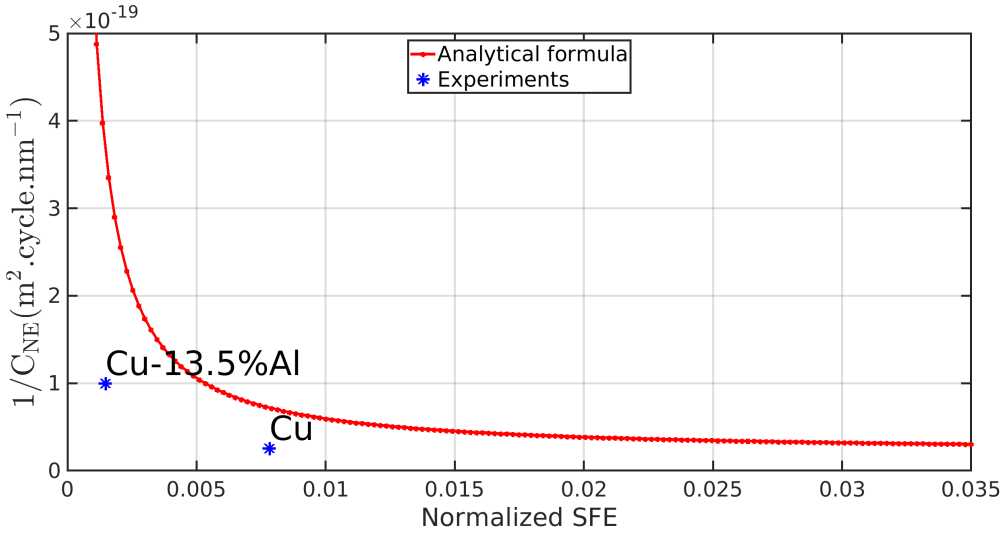

Figure 6-25: Comparison between the proposed model and the experiments. The comparison is made without correction.

growth rates predicted by MD computations are three times lower the ones measured by Ishii and Weertman [Ishii and Weertman, 1971a] for orientation B1.(tensile axis along $[1\,1\,0]$). This gap is reproduced by the model proposed. As one can notice in Fig. 6-25, the model prediction for the Cu-13.5%Al is also three times lower than the measure values. The proposed model is therefore in qualitative agreement with the available experimental data.

In this study we limited ourselves to low stress intensity factors in order to limit the activity of dislocations and confine them in the simulation box. These SIF values are in the same orders of magnitude as those observed in the near threshold regime (between $1.5 - 2.9\ \mathrm{MPa}\sqrt{\mathrm{m}}$ for copper; $0.9 - 1.9\ \mathrm{MPa}\sqrt{\mathrm{m}}$ for aluminum for example [Riemelmoser et al., 1998]). The SIF threshold values are often defined by considering the moment when the propagation rates become lower than $10^{-10}\ \mathrm{m.cycle}^{-1}$. However, some experiments such as those carried out on ARMCO iron by Pippan [Pippan, 1991] have shown propagation rates of the order of $10^{-12}\ \mathrm{m}$ and which obey Paris law. Experiments carried out on copper single crystals by Ishii and Weertmann [Ishii and Weertman, 1971a] show fatigue crack propagation for stress intensity factors as low as $1.5\ \mathrm{MPa}\sqrt{\mathrm{m}}$ with propagation rates of approximately $10^{-9}\ \mathrm{m.cycle}^{-1}$. We can therefore affirm that the values given experimentally are not the "real" propagation thresholds and one can even define a theoretical propagation threshold. In fact, it is understood that the propagation of fatigue cracks in ductile metals and alloys first requires the emission of dislocations from crack-tip. The stress intensity factor necessary to emit a crack tip dislocation (K_{Ie}) can therefore be considered as the fatigue crack propagation threshold. Defined in this way, the theoretical threshold stress intensity factors are those displayed in the Fig. 6-13, Fig. 6-

1, Fig. 4-4. One can also wonder if the propagation mechanisms observed in these near threshold regime are valid at higher SIFs. Although this question can not be answered with complete confidence, the author thinks that the observed propagation mechanism, that is to say the emission of dislocations and the plastic irreversibility at a crack-tip remains valid at higher stress intensity factors since some features such as crack front geometry, fracture surface appearance agree with experimental observations made for higher stress intensity factors in vacuum.

With these low SIFs and short number of cycles applied, it is difficult to address the effects dislocation cell structures on fatigue crack propagation mechanisms. The effect of these dislocation cell structures could not be therefore investigated in this work. However, there is controversy in the literature concerning the effect of these dislocation cells on the propagation of fatigue cracks. Some authors, such as [Avery and Backofen, 1962, Miller et al., 1966, Miller, 1966] believe that cell boundaries constitute a preferential propagation path for fatigue cracks. For Laird [Laird, 1967a] for example, the analysis of the fracture surface shows the same morphology, and therefore, one cannot expect a change in the propagation mechanism between metals with high SFE (containing cell structures) and low SFE (with no cell structure). Nevertheless, let us note that in this study, in spite of the absence of these cell structures due probably to the low values of the SIFs and the short number of cycles applied, the orders of magnitude of fatigue crack propagation could be reproduced. This effect of dislocation cells still remains to be investigated if and when such simulations can someday be undertaken with much more computing power.

6.5 Conclusion

In this chapter, we highlighted the effect of temperature and stacking fault energy on fatigue crack growth.

Effect of temperature

The emission of crack-tip dislocations is found to be slightly influenced by temperature. In fact, the more the temperature increases, the more the stress intensity factor required for the emission of dislocations at a crack-tip decreases. The drop is on the other hand was not significant and could be a simple thermoelastic effect coupled with a thermal agitation effect. The dislocation microstructures from a qualitative point of view were not affected by temperature. Entanglements, junctions, locks were observed at different temperatures. Quantitatively, the dislocation densities are found to be slightly affected by temperature. Mechanisms such as cross slip, jogs movement with vacancy production are observed even at low temperatures. The mechanisms of fatigue crack propagation is also not affected by temperature. Indeed, the only propagation mechanism observed is blunting resharpening, whatever the

simulation temperature or the orientation but a slight effect is observed on propagation rates. However, this effect is purely thermoelastic since when the stress intensity factor is normalized by the appropriate Young's modulus, this effect disappears and a master curve is obtained. The FCGR provided an exponent of Paris' law of approximately 4. These observations are in agreement with the experimental results. However, it should be noted that in the case of a gaseous environment (air for example), the influence of temperature could be more marked, for example due to the oxidation at the crack-tip, the kinetics of which could be accelerated with temperature. The weak influence of the temperature under inert environment can be explained by the high stresses which prevails at the crack-tip. Indeed, given these high stresses, the phenomena which could have been thermally activated (cross slip, movement of the jogs, ...) will be stress driven.

Effect Stacking fault energy

The study of the influence of the stacking fault energy was made through the study of different materials presenting a wide range of stacking fault energies (Ag, Al, Cu, Ni). The plastic deformation mechanisms at the crack-tip are not affected by the stacking fault energy and the dislocation microstructures are identical with a few exceptions. Indeed, whatever the material, the various locks, entanglements, junctions and other dislocation structures evidenced previously have been observed. However, a strong presence of dislocations in silver was observed in the direct vicinity of the crack-tip compared to other materials. The production rate of vacancies is found to be highest in aluminum while it is substantially the same in other materials at equivalent strain level. This strong presence of dislocations at the crack-tip hardens the material in the vicinity of crack-tip making plastic deformation at the crack-tip difficult and consequently reducing the rate of propagation. The increased mobility of dislocations at the crack-tip thanks to the cross slip in materials with high stacking fault energy and the annihilation of dislocations following the cross slip leads to a high production of vacancies at the crack-tip and the presence of dislocations less marked than in the case of silver which has a high stacking fault energy. As a consequence, the crack-tip material is a little softer than in the case of silver. The deformation of the crack-tip is made easy and the propagation is increased. The propagation rates fit the Paris' law well and provide an exponent of approximately 4 which is in agreement with the experimental data on ductile FCC single crystals. Closed form expression describing the influence of the stacking fault energy (or normalized stacking fault energy) on fatigue crack propagation rates is proposed and it is in qualitative agreement with the experimental results.

THIS PAGE INTENTIONALLY LEFT BLANK

Chapter 7

Fatigue crack growth under mixed mode loading

Don't you try and go through life worrying about if somebody like you or not. You best be making sure they doing right by you.
August Wilson, *Fences* .

Abstract

Fatigue crack growth under mixed mode loading is studied in this chapter. As in previous chapters, the crack tip deformation and the mechanisms of fatigue crack growth are studied. It is found that fatigue crack growth proceeds also by plastic blunting and irreversibility. The effect of the ratio between mode I and mode II stress intensity factors is also studied.

Contents

7.1 Introduction

Materials subjected to cyclic loading can display different behaviours according to a certain number of parameters such as the loading amplitude, the loading frequency, the environment but also and especially the loading mode. Nowadays, it is widely accepted that the majority of cracks initiate along persistent slip bands (PSBs). At stage I, cracks generally propagate in mixed mode manner (Mode I+II). Then under certain conditions, after rather long stage I the crack can change its plane and propagates in pure mode I but also sometimes in mode II manner. As Wang *et al.* [Wang et al., 1995] pointed out, in practice, structural components fail in mixed mode manner. Since mode I fatigue crack growth is considered to be the most damaging, it is also the most loading mode investigated even if some authors investigated other loading modes such as mode II, mode III and mixed mode (I+II).

Otsuka *et al.* [Otsuka et al., 1975] studied the condition of fatigue crack growth in mixed mode conditions on three low carbon steels. The authors reported that crack growth was either shear mode or tensile mode. They found that the shear mode growth was controlled by a critical maximum shear stress whereas the critical condition for tensile mode growth is given by a critical maximum tensile stress. The authors suggested also that the transition from the shear growth mode to tensile growth mode is driven by a maximum critical tensile stress. Wang and Mughrabi [Wang and Mughrabi, 1984a] showed that transitions from stage I (mixed mode) to stage II (pure mode I) and inversely can be obtained by increasing or reducing the loading amplitude in appropriate manner. The authors suggested also that in single crystal, activation of plasticity on the secondary system could induce a transition because of the activation of a secondary slip system. The crystal orientation was also found to be a factor that could ensure the transition. Roberts and Kibler [Roberts and Kibler, 1971] carried out tests on 2024-T3 aluminium alloy under mode II loading with static mode I loading and observed mode II crack growth. The authors reported that fatigue crack growth rates under mode II was similar than the one under mode I loading for the same levels of mode I and mode II stress intensity factors. Contrary to Roberts and Kibler, Smith [Smith, 1984] showed that without mode I static loading, mode II growth still exists. Mode I static loading was found to induce only branched crack growth. Crack deflection and branching were also observed in experiments carried out by Qian [Qian, 1995] who performed mode II and mixed mode fatigue crack propagation in Stainless steel under biaxial loading. The investigations of Hua *et al.* [Hua et al., 1985] revealed that once branched, cracks followed a path that has the maximum tensile stress intensity factor, even under combined mode I and mode II loading. In Kitagawa *et al.* [Kitagawa et al., 1985] experiments on a structural steel, the authors reported that the propagation of the branched crack occurs in mode I without mode II stress intensity factor. The crack growth rate for the branched crack was found to be similar to that for pure mode I growth. Tests carried out on

7076-T6 and 2017-T4 aluminium alloy by Otsuka *et al.* [Otsuka et al., 1981] revealed that mode II crack growth rates for the 7076-T6 alloy was 10 ten times higher than mode I growth rates while for the 2017-T4 alloy, mode II cracks grew 7 times faster than mode I cracks. Wang *et al.* [Wang et al., 1995] measured fatigue crack growth rates in a low and a medium carbon steels, an austenitic stainless steel and an aluminium alloy under mode II loading. The authors reported that depending on the material, three possibilities for fatigue crack propagation under mode II could occur: bifurcation into two branches, propagation along the original Mode II direction and a mixture of both situations. The crack growth rate vs mode II stress intensity factor ($\mathrm{K_{II}}$) was found to obey Paris' law. The fractographic analysis revealed striations parallel to crack front in the case of branched crack and many frictional marks parallel to the crack propagation direction in the case where crack grew along the original mode II direction. Experiments by Neumann *et al.* [Neumann et al., 1978] revealed that stage I crack growth (mixed mode manner) could be obtained only in air environment (not in vacuum) for any crack length provided that the growth rate was lower than $10\,\mathrm{nm/cycle}$. However, Wang and Mughrabi [Wang and Mughrabi, 1984a] reported that irrespective to the environment, fatigue crack growth in stage I could be obtained in copper single crystal oriented for single slip. According to the authors, the crystal orientation in Neumann experiments favours multiple slip and therefore is suitable for stage II (pure mode I) crack growth. Some differences in crack behaviour was highlighted by Tong *et al.* [Tong et al., 1986a, Tong et al., 1986c, Tong et al., 1986b] depending on whether the specimen is a single crystal or a polycrystal. Indeed, according to the authors, in polycrystals, fatigue crack is essentially a pure mode I crack whereas in single crystals it was shown that crack follows slip planes and fatigue crack can achieve mode II provided that the crack plane coincide with a $\{1\,1\,1\}$ plane. But Cheng and Laird [Cheng and Laird, 1983] found a change of crack plane after a long stage I propagation of a few millimeters, and the final propagation occurs in mode I manner.

These different studies allows to better understand and model the propagation of fatigue cracks under shear and mixed mode loading but also the transition between different crack growth stages even if some contradictory results can be pointed out. However, as before, more detailed studies at the atomic scale are necessary in order to understand the physical mechanisms governing crack propagation in relation with the microstructure. In this preliminary study, we investigate via molecular dynamics computations, the plastic deformation mechanisms at the crack-tip as well as the crystal defects, which are related under mixed mode loading in copper. We highlight the influence of the loading ratio, $\mathrm{K_I/K_{II}}$, on the fatigue crack propagation mechanisms and rates.

7.2 Computational methods

Our simulations intend to expand the MD simulations of mode I propagation (chapters 4, 5) to fatigue crack propagation under mixed mode loading through the LAMMPS software. The computational methods remain the same as the one applied to investigate mode I propagation mechanisms. The modelled material is copper single crystal and investigations are carried out at room temperature (RT). The interatomic potential of Mishin *et al.* [Mishin et al., 2001] is still used. The crack plane lie in $(1\,\bar{1}\,1)$ plane and crack front is parallel to $[1\,\bar{1}\,\bar{2}]$ direction. The crack propagates in $[1\,1\,0]$. One of the main differences lies in the loading conditions. The loading applied as previously results from linear elastic fracture mechanics (LEFM) formalism. In order to take into account the anisotropy of copper cubic elasticity for mode II loading, we refer once more the work of Sih [Sih et al., 1965]. The displacement field applied to the boundaries of the simulation box is given by Sih *et al.* [Sih et al., 1965]:

$$\begin{cases} u_x = K_{II}\sqrt{\dfrac{2r}{\pi}}\Re\left[\dfrac{1}{a_1-a_2}\left(p_2\sqrt{\cos\theta+a_2\sin\theta}-p_1\sqrt{\cos\theta+a_1\sin\theta}\right)\right] \\ u_y = K_{II}\sqrt{\dfrac{2r}{\pi}}\Re\left[\dfrac{1}{a_1-a_2}\left(q_2\sqrt{\cos\theta+a_2\sin\theta}-q_1\sqrt{\cos\theta+a_1\sin\theta}\right)\right] \end{cases} \tag{7.1}$$

This displacement field is valid under plane strain assumptions and the different parameters of Equation 7.1 are defined in chapter 4, section 4.2.3.

In the case of mixed mode loading, owing to the fact that we make the assumption of linear fracture mechanics, the whole applied displacement field is a superposition of mode I and mode II displacement fields, by specifying the factor of intensity of the stresses in mode I (K_I) and in mode II (K_{II}). As a reminder, the mode I displacement field is given by Equation 4.11.

7.3 Plastic deformation

The plastic deformation occurs by dislocation emission and gliding. Even if the dislocation slip occurs mainly on the crack plane, certain planes inclined with respect to the axis ahead of crack are also activated but with little slip compared to the crack plane. Number of dislocations emitted at the at crack-tip glide towards the boundaries of the MD box where they are pilled-up (Fig. 7-2). Compared to the mode I case, an imperfect dislocation free zone near crack tip is observed, and some dislocation loops interactions at the boundaries of the simulation box are observed as can be seen in Fig. 7-2. Fig. 7-3 shows the evolution of the total dislocation density with the number of cycles. As can be noticed in Fig. 7-3, the total dislocation density seems to be stable from the 4^{th} cycle and the dislocation density is found to increase with the ratio $\Delta K_I/\Delta K_{II}$ even for the same

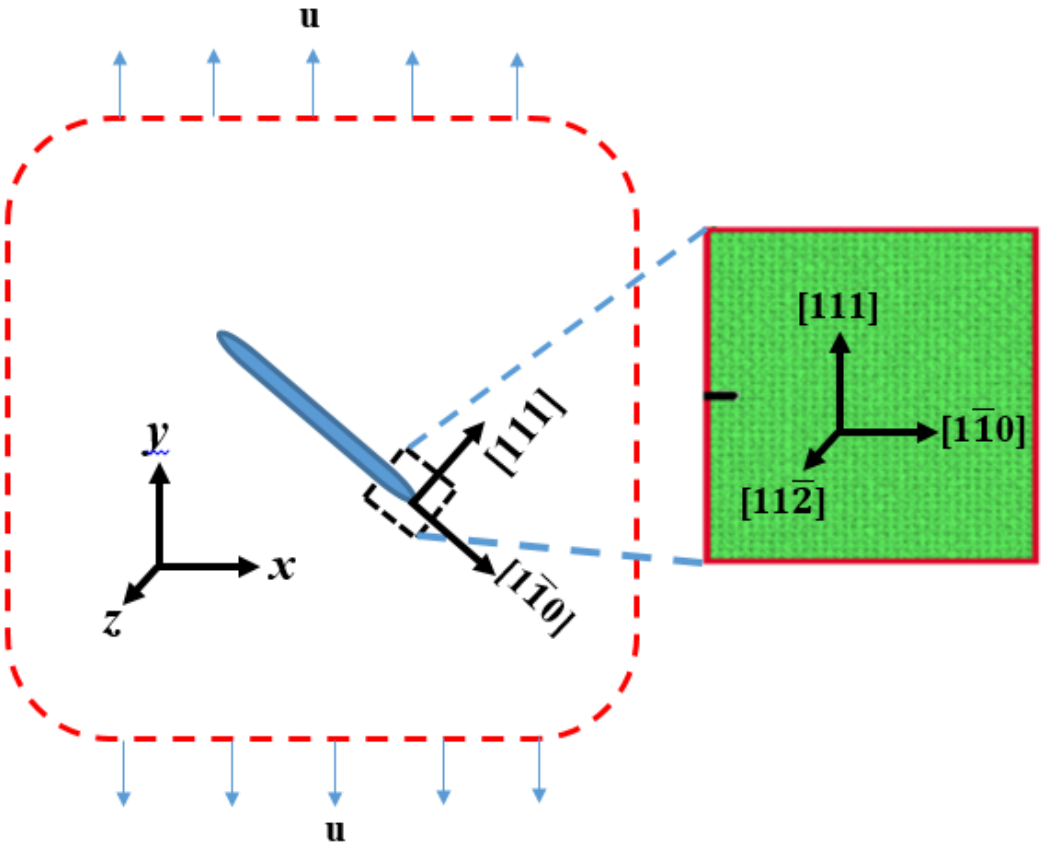

Figure 7-1: Representation of the whole solid and the embedded MD simulation box located in the vicinity of the crack-tip. The LEFM displacement field applied at the boundaries of this MD simulation box (the red zones at the boundaries) is a superposition of mode I and mode II displacement field.

equivalent SIF defined by:

$$\Delta K_{eq} = \sqrt{\Delta K_I^2 + \Delta K_{II}^2} \tag{7.2}$$

The dislocation density stabilizes at approximately 10^{16} m^{-2} for $\Delta K_I/\Delta K_{II} = 1.74$, while the stabilized density amounts to approximately 5×10^{15} m^{-2} for $\Delta K_I/\Delta K_{II} = 1$ and finally 3×10^{15} m^{-2} for a $\Delta K_I/\Delta K_{II} = 0.57$. Compared to mode I loading ($\Delta K = 2$ $\mathrm{MPa}\sqrt{\mathrm{m}}$), the dislocations density seems lower in stage I fatigue crack propagation (mixed mode $\Delta K_I = \Delta K_{II} = 1$ $\mathrm{MPa}\sqrt{\mathrm{m}}$). For example, under mixed mode loading, for $\Delta \mathrm{K_I} = \Delta \mathrm{K_{II}} = 1$ $\mathrm{MPa}\sqrt{\mathrm{m}}$, the dislocation density is about 5×10^{15} $\mathrm{m}{-2}$ while under pure I mode, the dislocation density for $\Delta \mathrm{K} = 2$ $\mathrm{MPa}\sqrt{\mathrm{m}}$ is approximately 10^{16} m^{-2} i.e. 2 times greater than that in mixed mode. However, while under mixed mode the total dislocation densities show saturation, the pure mode I dislocation density shows an increasing tendency beyond the 16^{th} cycle.

Also under mixed mode loading, the total dislocation density depends on the $\Delta K_I/\Delta K_{II}$ ratio. Indeed, the greater the ratio $\Delta K_I/\Delta K_{II}$, the more the total density of dislocations increases. For instance, for a ratio $\Delta \mathrm{K_I}/\Delta \mathrm{K_{II}} = 0.56$ ($\Delta \mathrm{K_I} = 0.73$ $\mathrm{MPa}\sqrt{\mathrm{m}}, \Delta \mathrm{K_{II}} = 1.27$ $\mathrm{MPa}\sqrt{\mathrm{m}}$), the density of dislocations measured seems to stabilize at approximately 3×10^{15} m^{-2} while for $\Delta \mathrm{K_I}/\Delta \mathrm{K_{II}} = 1$ ($\Delta \mathrm{K_I} = 1$ $\mathrm{MPa}\sqrt{\mathrm{m}}, \Delta \mathrm{K_{II}} = 1$ $\mathrm{MPa}\sqrt{\mathrm{m}}$), the total density of dislocations measured is approximately 5×10^{15} m^{-2} and for $\Delta \mathrm{K_I}/\Delta \mathrm{K_{II}} = 1.74$ ($\Delta \mathrm{K_I} = 1.27$ $\mathrm{MPa}\sqrt{\mathrm{m}}, \Delta \mathrm{K_{II}} = 0.73$ $\mathrm{MPa}\sqrt{\mathrm{m}}$) the total dislocation density amount to approximately 10^{16} m^{-2}.

The different interactions between emitted dislocations generate different types of dislocations as mentioned in previous chapters (chapter 4, 5, 6). The proportion of the different dislocation types generated during interactions are shown in Fig. D-9 of Appendix D.

As for mode I, the majority of dislocations are Shockley partials (Fig. D-9) which proportions seem to decrease with the number of cycles followed by stair-rod partials which proportions seem to increase with the number of cycles. The other types of dislocations (Frank, Hirth, perfect) are in small proportion (between 1 and 8 % for perfect dislocations, 8% when shear loading dominates; between 0.5% and 2% for Hirth partials and for Frank partials).

The different interactions taking place between dislocations lead to the formation of junctions, tangles and locks which are mainly piled up at against the box boundary ahead of crack tip as depicted in Fig. 7-2. This can lead to a plastic irreversibility since the dislocation glide back will be difficult. The cross-slip allowing screw dislocations to overcome obstacles was observed. Vacancies production which concentration evolution is depicted in Fig. 7-4, is also observed. The vacancy concentration is found to increase with the number of cycles and the vacancy production rate can be estimated at 4×10^{-6} $\mathrm{at}^{-1}.\mathrm{cycle}^{-1}$ for $\Delta K_I/\Delta K_{II} = 0.57$. For $\Delta K_I/\Delta K_{II} = 1.74$, the vacancy concentration is found to increase from the 1st cycle until the 8th cycle (at a production rate of ap-

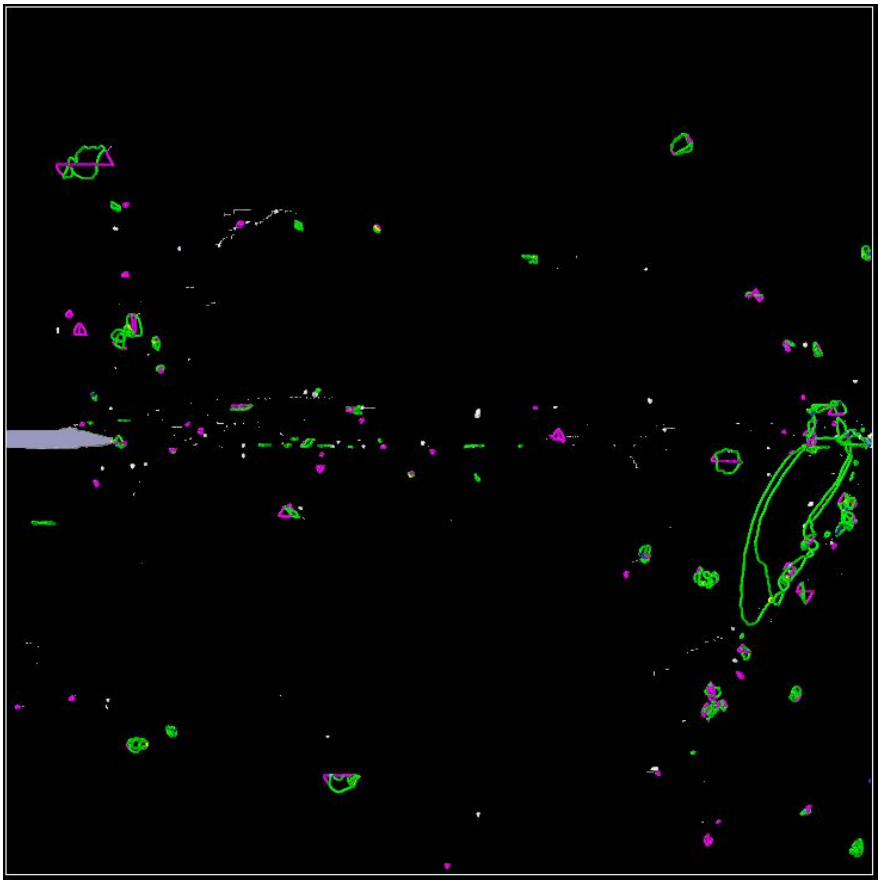

Figure 7-2: Dislocation network under mixed mode loading at the 17^{th} cycle (Applied SIF : $\Delta K_I = \Delta K_{II} = 1\ \mathrm{MPa}\sqrt{\mathrm{m}}$). One can observe an imperfect dislocation free zone near crack-tip and dislocation lines pilled-up against the box boundary ahead of the crack. Some small prismatic loops and other defects such as SFTs can be also observed

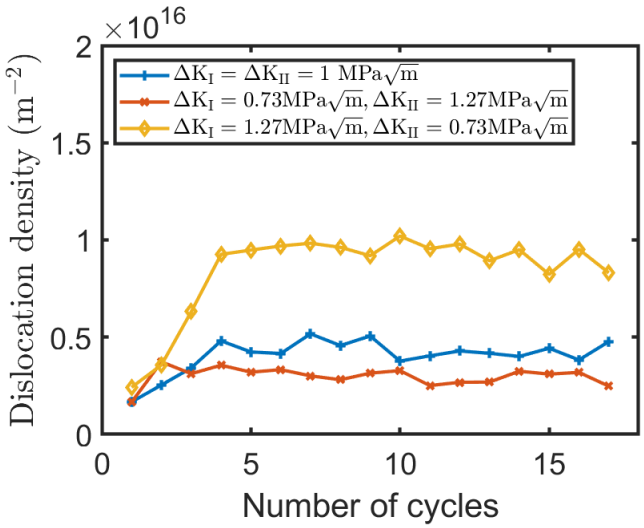

Figure 7-3: Evolution of the total dislocation density with he number of cycles for different loading amplitude. A stabilization of the dislocation density can be observed from the 4^{th} cycle and the dislocation density increases with the increasing ratio $\Delta K_I/\Delta K_{II}$

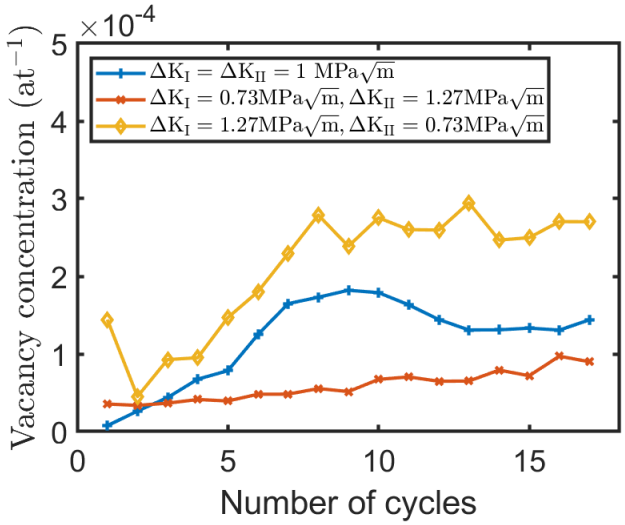

Figure 7-4: Evolution of the vacancy concentration with the number of cycles for different loading ratios $\Delta K_I/\Delta K_{II}$.

proximately 4×10^{-5} $\text{at}^{-1}.\text{cycle}^{-1}$ and then stabilizes at around 2.75×10^{-4} at^{-1}. For $\Delta K_I/\Delta K_{II} = 1$, the vacancy concentration is found also to increase from the first cycle until the 7th cycle at a production rate of approximately 3×10^{-5} $\text{at}^{-1}.\text{cycle}^{-1}$. Then it decreases slightly until the 12^{th} cycle before stabilization at around 1.3×10^{-4} at^{-1}. As with the dislocation densities, the production of vacancies, therefore, depends on the $\Delta K_I/\Delta K_I I$ ratio and vacancy concentration increases with the $\Delta K_I/\Delta K_I I$ ratio. Under stage I propagation, the vacancy concentration also appears to be lower than that observed for pure mode I. Indeed, for $\Delta K_I/\Delta K_{II} = 1$ ($\Delta \text{K}_\text{I} = \Delta \text{K}_\text{II} = 1$ $\text{MPa}\sqrt{\text{m}}$), the vacancy concentration stabilizes around 1.3×10^{-4} at^{-1} cycle^{-1} while under pure I mode for $\Delta K_I = 2$ $\text{MPa}\sqrt{\text{m}}$, vacancy concentration after 16 cycles is about 2×10^{-4} at^{-1}, and the general trend suggests a continuous increase in dislocation density beyond the 16^{th} cycle under mode I loading.

The vacancy production leads also to the formation of stacking fault tetrahedra as one can observe in Fig. 7-2.

The plastic irreversibility induced by various dislocation interactions, pilling-up and dislocation annihilation via cross-slip is evaluated in terms of irreversibility factor (Equation 4.36) and depicted in Fig. 7-5. Clearly, the plastic irreversibility factor fluctuates during cyclic loading. For $\Delta K_I/\Delta K_{II} = 0.57$, the mean irreversibility factor over the 17 cycles is estimated to be about 0.29, and about 0.33 when $\Delta K_I/\Delta K_{II} = 1$. For $\Delta K_I/\Delta K_{II} = 1.74$, the mean plastic irreversibility factor over the 17 cycles is estimated at 0.45. For instance, the mean plastic irreversibility factor over 16 cycles for the similar orientation but under pure mode I loading is estimated at approximately 0.25 for $\Delta K_I = 2$ $\text{MPa}\sqrt{\text{m}}$ (chapter 4, Fig. 4-23). This value is slightly lower than that computed in this section. The dependence of the plastic irreversibility on the loading ratio ($\Delta K_I/\Delta K_{II}$) can be explained by the amount of mode I loading proportion which is higher when the loading ration increases. Indeed with higher mode I proportion, more slip systems are activated inducing dislocation tangles around crack-tip and therefore higher plastic irreversibility. For low ratios (shear loading dominating), dislocations on the primary slip plane dominate. Few interactions occur and as a result the plastic irreversibility factor is low.

7.4 Propagation

The mechanisms of propagation observed previously remains valid under mixed loading. Indeed, it is observed an advance of the crack-tip due to dislocation emission from the crack-tip during the loading half cycle. These dislocations for a number of reasons (interactions with the other dislocations pilled-up against simulation box boundary ahead of the crack-tip (Fig. 7-2), dislocation cross-slip, etc.), are not all reversible Then, we witness a propagation induced by plastic blunting and irreversibility. For example, Fig. 7-6 shows an example of crack-tip blunting under mixed mode loading. One can observe in Fig. 7-6a the crack

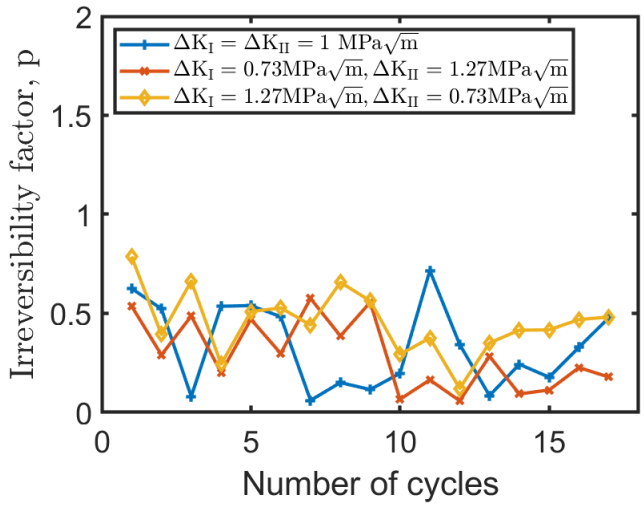

Figure 7-5: Per full cycle plastic irreversibility factor for different loading ratios $\Delta K_I/\Delta K_{II}$.

tip blunting (induced by dislocation emission) during the loading half cycle and in Fig. 7-6b, a crack-tip geometry after unloading. The mechanism remains the same regardless of the $\Delta K_I/\Delta K_{II}$ ratio. However, as stated previously, for higher loading ratios ($\Delta K_I/\Delta K_{II}$), more slip systems are activated and some dislocations tangles are observed in the vicinity of the crack and inducing higher irreversibility and therefore, higher propagation rates. Indeed, at the same SIF, the FCGR depends on the ratio $\Delta K_I/\Delta K_{II}$. For a ratio $\Delta K_I/\Delta K_{II} = 0.57$, the FCGR was estimated at around 0.19 nm/cycle while for $\Delta K_I/\Delta K_{II} = 1.0$, the FCGR was estimated at approximately 0.22 nm/cycle. The assessed FCGR for $\Delta K_I/\Delta K_{II} = 1.74$, is approximately 0.34 nm/cycle.

Keeping the same loading ratio ($\Delta K_I/\Delta K_{II} = 1$, stage I crack growth), different loading amplitudes are applied and the FCGR are plotted in Fig. 7-7. The data obey the Paris law with an adjusted exponent of approximately 3.04, which is close to the exponent obtained in agreement with the value obtained by Wang *et al.* [Wang et al., 1995] under pure mode II loading (3.25).

7.5 Conclusion

Fatigue crack propagation during stage I generally takes place under mixed mode. In this preliminary study, we use molecular dynamics to simulate the propagation of fatigue cracks under mixed mode loading. Plastic deformation around crack-tip occurs by dislocation emission and gliding. For the same SIF, the total dislocation density, the vacancy concentration and the irreversibility factor depend on the ratio $\Delta K_I/\Delta K_{II}$. The higher the mixed mode ratio $\Delta K_I/\Delta K_{II}$ the higher the total density of dislocations, vacancy concentration and irreversibility factor. It is also observed that the mechanism of propagation

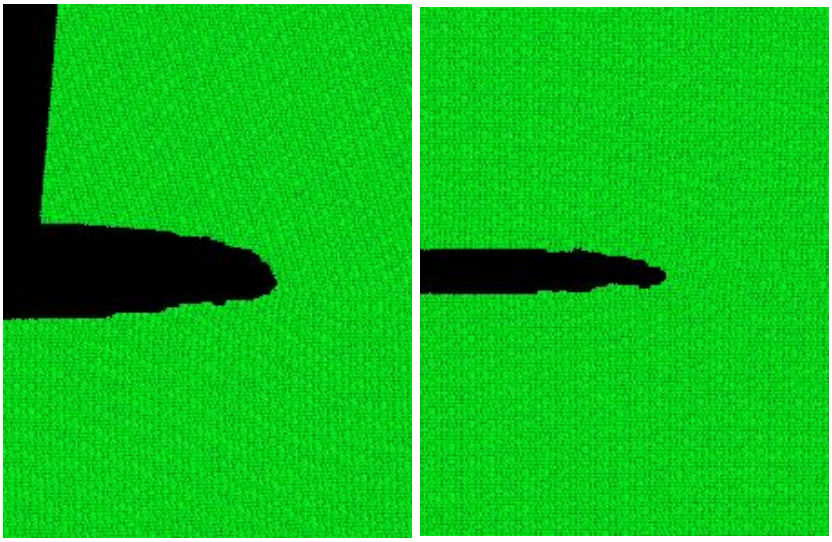

(a) **(b)**

Figure 7-6: (a)Crack tip geometry at the maximum loading ($\mathrm{K_I} = \mathrm{K_{II}} = 1\ \mathrm{MPa}\sqrt{\mathrm{m}}$) and (b) at the minimum loading ($\mathrm{K_I} = \mathrm{K_{II}} = 0\ \mathrm{MPa}\sqrt{\mathrm{m}}$).

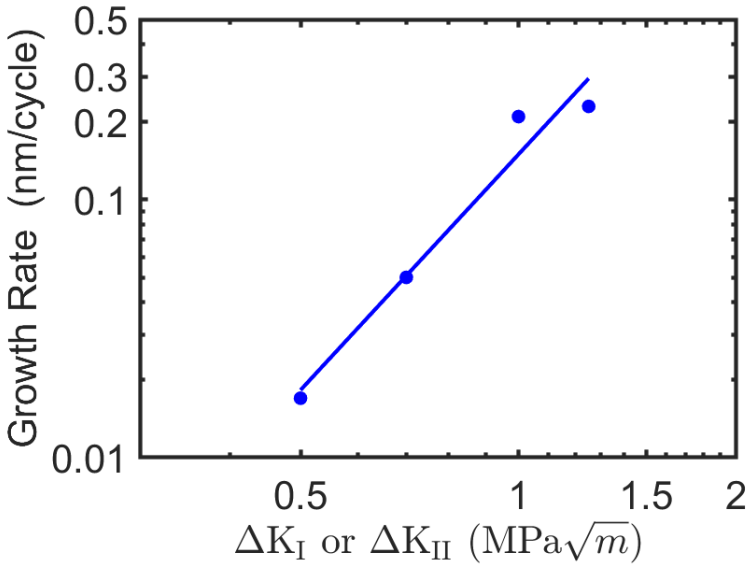

Figure 7-7: FCGR as function of mode I or mode II SIF for fatigue crack loaded under mixed mode. Dots represent MD results and solid line represnts Paris law fit. The slope is approximately 3.04.

under mixed mode is the same as that observed under pure mode I loading, which is characterized by plastic blunting and irreversibility. The propagation rates depend on the ratio $\Delta K_I/\Delta K_{II}$ as expected and vary in the same way as the dislocation density, the vacancy concentration and the irreversibility factor. For $\Delta K_I/\Delta K_{II} = 1$ (stage I crack propagation), the higher SIF, the higher FCGR. The FCGR obey Paris' law with an exponent of 3.04.

As stated previously, unlike some previous atomistic studies, which claimed that the main mechanism of fatigue crack propagation in ductile metals is cavity nucleation, growth and coalescence ahead of fatigue crack-tip, the fatigue crack propagation mechanism observed in this study is the plastic blunting and irreversibility. indeed, the emission of dislocations from the crack-tip and their gliding induces a matter removal from the crack tip and leads to plastic slip during the loading half cycle. During the unloading half cycle, due to different interactions between dislocations and other crystal defects leading to the formation of different locks, some of the emitted dislocations do not return back to the crack-tip. This induces a plastic irreversibility characterized by the non-recovery of the matter removed which occured during previous emission of dislocations. Therefore, this net partial matter removal induces cyclic crack propagation. It is also important to specify that, at this level, there are two types of plastic irreversibilities: a plastic irreversibility at the scale of atomic planes and an irreversibility at the scale of a volume around the crack-tip (at the scale of the simulation box in MD). The first (plastic irreversibility at atomic plane scale) is not fully effective in inducing fatigue crack propagation. The consequence of the latter will generally be the formation of small roughness on the crack front. The irreversibility on the scale of a volume around the crack-tip, characterized by a ratchetting effect and by a partial irreversibility of the matter removal which occured during the emission of the dislocations, is considered to be the most efficient mechanism for inducing effective crack propagation.

Chapter 8

Conclusions and future research directions

Once you eliminate the impossible, whatever remains, no matter how improbable must be the truth.

Arthur Conan Doyle, *Sherlock Holmes* .

Fatigue of metals and alloys is characterized by strong environmental effects and a large scatter in lifetimes that should be understood and predicted. This requires a detailed understanding fatigue cracks initiation and propagation mechanisms. In this Ph.D. thesis, we studied fatigue crack initiation and propagation under inert environment via crystal plasticity finite element and via molecular dynamics computations. The effects of crystal orientation, temperature, stacking fault energy, and loading mode were investigated in different fcc single crystals.

The cyclic deformation of single crystals and polycrystals generally causes the strain localization in persistent slip bands (PSBs) along which fatigue cracks may initiate. Before, crack initiation is preceded by PSBs extrusion formation and growth, which was the subject of chapter 3 of this manuscript, after a short literature review presented in chapter 2 and industrial context description in chapter 1.

In chapter 3, we simulated the extrusion growth in metals and alloys subjected to cyclic loading via crystal plasticity finite element computations. In agreement with experimental observations, an elastic-plastic persistent slip band embedded in an elastic matrix is modelled. Persistent slip bands extrusion induced by vacancies production is modeled by a free thermal expansion. Our simulations showed that the extrusion height above type B PSBs is higher than that of type A PSBs. This effect, which can be explained by an easier plastic accommodation in the direction of the burgers vector in type B PSBs, is in agreement with the experimental observations [Holste and Schwab, 2006, Obrtlík et al., 1997]. A linear evolution of the extrusion height as a function of the number of cycles was also found. This is also in agreement with experimental observations [Man et al., 2003]. Our conclusions disagree with the ones of the models based on the cumulative plastic slip irreversibilities. Based on the central limit theorem, they indeed lead to the dependence of extrusion height with the number of cycles of the square root type [Essmann et al., 1981, Differt et al., 1986]. The influences of the extrusion height on PSB thickness and length were also investigated. Closed form expressions are deduced from the numerous FE computations. Their predictions agrees fairly well with experimental measurements [Man et al., 2002, Hunsche and Neumann, 1986]. Additionally, our simulations show that extrusions height evolve linearly with PSB inclination angle with respect to the loading axis (tilt rotation) still in agreement with experimental investigations [Man et al., 2002]. Otherwise, the effect of the modelling and computational hypotheses was assessed. No significant effect was observed concerning cubic elasticity versus isotropic elasticity, large versus small displacements assumptions, and accounting for lattice rotation. In addition, surface stress field and PSB/matrix interface stress fields in copper were investigated. It was shown that the stress values assessed after a few thousand of cycle were not sufficient to induce fatigue crack initiation as proposed earlier by some authors [Brown and Ogin, 1985] based on purely thermoelastic computations. Therefore other types of stress concen-

trators than those induce by the PSB extrusion only, are required to reach the theoretical [Černý and Pokluda, 2009, Pokluda et al., 2015] or experimental [Kobayashi and Hiki, 1973, Macmillan, 1983] cleavage tensile strength along $\{1\,1\,1\}$ crystallographic direction in copper.

The next step following fatigue crack initiation is its propagation. Because of the available mode I experimental data, and their simplicity, mode I loading (stage II crack propagation) was first investigated and then, mixed mode loading (stage I crack propagation).

The propagation of fatigue cracks was studied at the atomic scale via molecular dynamics simulations. First, the plastic deformation near crack-tip zones and the underlying crystal defects were studied in chapter 4 in copper single crystals cyclically deformed at room temperature. Depending on the seven crack orientations considered, different strain localization patterns are observed. Furthermore they are in agreement with available SEM experimental observations [Flouriot et al., 2003, Crone and Shield, 2001, Vinogradov et al., 1995]. Two plastic deformation mechanisms are observed: dislocations emission and deformation twinning depending on the crack orientation but the latter is thought to be an artefact induced by the high strain rate used in MD simulations. Due to multiple slip at crack-tip, different interactions between dislocations occur leading to a complex dislocation network close to the crack-tip. This 3D dislocation network around the crack-tip is in agreement with various experimental investigations [Dewald et al., 1990, Awatani et al., 1978, McEvily and Boettner, 1963a] who observed similar 3D dislocation networks made of tangles. But this contradicts the theories based on 2D array dislocation arrangement aiming to explain fatigue crack propagation mechanisms [Riemelmoser et al., 2001, Riemelmoser et al., 1997, Pippan et al., 2011]. Different dislocation barriers such as Lomer-Cottrell locks, Hirth locks, entanglements, jogs, are observed in our simulations and can impede dislocation forward and backward gliding. However, screw dislocations very frequently change glide plane via cross-slip. The movement of jogged screw dislocations and screw dislocation cross-slip lead to the production of vacancies, the evolution of which was studied as a function of the number of cycles and of the crack orientation. Vacancies production are observed experimentally around crack-tips in some f.c.c. metals [Kiritani et al., 1999, Matsukawa et al., 2003a]. The vacancy concentration computed was in the same order of magnitude of those measured experimentally in copper single crystals cyclically deformed at $4\,\mathrm{K}$ [Polák, 1969] or under severe plastic deformation [Čížek et al., 2019]. The aggregation of vacancies was found to induced the formation of stacking fault tetrahedra in accordance with some experiments [Matsukawa et al., 2003a, Kiritani et al., 1999]. The various barriers due to dislocations interactions and other defects such as stacking fault tetrahedra impede the glide back of dislocations and induce a plastic irreversibility, which was found to be responsible for fatigue crack propagation as discussed in chapter 5.

Chapter 5 is dedicated to fatigue crack propagation in copper single crystals

at room temperature. In chapter 5, we revisited some previous models with regard to the dislocation microstructures observed around crack-tips in chapter 4. It was observed that fatigue cracks grow by plastic blunting and irreversibility inducing a ratchetting effect around fatigue crack-tip. Indeed, the activation of plasticity on different slip systems causes crack-tip blunting with dislocation emission from crack-tip. Dislocation emission induces material removal from crack-tip leading to plastic slip and crack advance. During unloading, all the dislocations emitted during the loading half cycle do not return back to the crack-tip after unloading as shown by many pictures. This non-reversible part of plastic slip induced by the numerous dislocation locks, SFTs, entanglements and also cross-slip lead to the non-reversibility of the matter removed by dislocation emission and gliding during loading half cycle. Therefore a cyclic crack propagation occurs. Fatigue crack growth rates data obtained from our simulations obey the Paris' law with an exponent of approximately 4 in agreement with experimental observations on copper single crystals [Ishii and Weertman, 1971b, Neumann et al., 1978] and various ductile alloys [Ishii and Weertman, 1971b]. The analysis of the geometry of crack front provides further evidence that the propagation of fatigue cracks occurs in pure fcc metals by plastic blunting rather than by cleavage or cavity coalescence as concluded from previous atomistic simulations [Farkas et al., 2005, Horstemeyer et al., 2010, Potirniche et al., 2005, Potirniche et al., 2006, Zhou et al., 2015, Wu et al., 2015].

The weak influence of temperature generally observed experimentally under inert environment and the effect of stacking fault energy on fatigue crack propagation were reproduced by our atomistic simulations in chapter 6. They are explained in the light of the microstructures observed around fatigue crack-tips in our simulations. Whatever the temperature, fatigue crack propagation rates were found to obey Paris law with still an exponent of approximately 4. This is in agreement with the experimental measurements [Ishii and Weertman, 1971b]. The plot of the computed propagation rates as a function of the temperature showed a weak influence of temperature. It is explained by the temperature dependence of the elasticity constants with temperature. Our findings agree well with various observations in the literature and concerning more complex engineering alloys cyclically deformed under inert environment [Sarrazin et al., 1997, Rosenberger et al., 1997, Hénaff et al., 2002, Cotterill and Knott, 1992, Hénaff and Tonneau, 2001, Petit et al., 2003]. This negligible temperature dependence of FCGR predicted by our simulations is explained by the weak effect of temperature on dislocation microstructures and on other crystal defects observed in our simulations. Indeed, dislocation microstructures and other crystal defects were found to be almost temperature-independent. Chapter 6 also focused on the influence of normalized stacking fault energy. To be the most exhaustive as possible, four metals (Ag, Al, Cu, Ni) with different normalized stacking fault energies were studied. It was observed that for the same normalized stress intensity factor, the propagation rates in aluminum, the most wavy metal, is approximately 5 times higher than that

in silver. This difference is explained by dislocation microstructures predicted by our simulations. Indeed, a high dislocation density close to crack-tips is observed in silver whereas in aluminum dislocation density close to crack-tip is lower than that in silver. In fact, in silver number of junctions between dislocations involving sessile dislocations such as Hirth partials and stair-rod partials were observed whereas in aluminum theses junctions were rare. This makes the gliding of mobile dislocations away from crack-tip difficult in silver. As a consequence, it leads to a strong hardening near crack-tip regions in silver and high backstresses, which renders crack-tip plastic deformation dislocation emission difficult. In aluminum, the high stacking fault energy favors numerous dislocation cross-slip events that makes dislocation glide away from the crack tip easier. The annihilation of screw dislocation due to cross-slip is also one the reasons of low dislocation number around crack-tip in aluminum. Therefore the metal located in the direct vicinity of the crack-tip is much softer and ductile than in silver. This favors an easier plastic deformation and dislocation emission and gliding. As a consequence, higher propagation rates occur. The effect of high vacancy concentration around crack-tip in high SFE metals which can increase slightly the propagation rates should also be pointed out but this effect is limited. Finally, an analytical formula describing the influence of the normalized stacking fault energy was proposed. This formula is in qualitative agreement with some experimental measurements [Ishii and Weertman, 1971b].

Finally, chapter 7 was devoted to fatigue crack propagation under mixed mode loading (stage I fatigue crack growth which occurs after crack initiation and before stage II). As previously, it was observed that, fatigue cracks propagate by plastic blunting and irreversibility. The influence of the K_I/K_{II} ratio was studied and it was shown that the higher the K_I/K_{II} ratio, the higher the propagation rate for the same equivalent stress intensity factor. Fatigue crack growth rates were also found to obey the Paris law with an exponent of approximately 3.

In this multi-scale simulation study, we explored the initiation and propagation of cracks by studying subsequently the extrusion of above PSBs, the plastic deformation in the vicinity of a crack-tip, the mechanisms of fatigue crack propagation, the influence of stacking fault energy, temperature and loading mode (mixed mode), all under inert environment. However, our study was unable to cover a number of influent parameters and mechanisms known experimentally. Two of them are discussed in the further outlook.

As perspectives of our research work, two main directions should be envisaged.

On the one hand, concerning the study of fatigue crack initiation, a simulation taking into account the formation of intrusions along persistent slip bands should be considered. As we have noticed previously, the computed surface stresses and stresses along PSB/matrix interface are not sufficiently high to induce fatigue crack initiation. Other types of stress concentrators should be

active. The formation of an intrusion would certainly allow higher stress concentrations allowing possibly crack initiation. This would also help to explain some observations made by Hunsche and Neumann [Hunsche and Neumann, 1986] regarding the evolution of fatigue crack initiation sites (Fig. 3-29). More precisely, it requires the combined solving of the diffusion equation and crystal plasticity laws. The shape and depth of intrusions can be predicted. The extraction of the displacement fields computed by the finite element method can be used as boundary conditions of a MD simulation box containing a notch built using the shape and depth of the predicted intrusion. This could allow to check which fatigue crack initiation mechanism is effective.

On the other hand, the second future direction concerns the atomistic investigation of the environment-assisted fatigue crack propagation by considering O_2, and/or H_2O environment.

As reported previously, fatigue crack propagation could be accelerated under an O_2, H or H_2O environment. Each metal is more or less sensitive to each. Indeed, according to the investigations carried out by Sriram *et al.* [Sriram et al., 1990], oxygen atoms play an important role in surface slip irreversibility (see also the investigation of Fan et al. [Fan et al., 2017] on atomistic simulation of surface slip irreversibility on nickel and copper). The authors studied the effect of oxygen partial pressure on fatigue crack initiation in silver and showed a strong adsorption of ambient oxygen molecules on the slip steps formed at free surface. This adsorption can induce a surface slip irreversibility during fatigue. Also dislocations gliding could be impeded by oxygen atoms and induce slip irreversibility. It can be thought that a similar effect can occur at crack-tip and enhance the irreversibility already existing under inert environment. In addition, surface oxidation could prevent the partial crack rewelding observed in our simulations and under inert environment generally reported experimentally [Kikukawa et al., 1979] and therefore increase propagation rates. By increasing temperature, the adsorption of oxygen atoms on metals surfaces, and steps and their mobility could be enhanced near dislocations and impede the dislocations forward and backward glides. Furthermore oxidation kinetics could be also enhanced by increasing temperature and affect fatigue crack closure.

Moreover, by considering hydrogen atoms, mechanism of hydrogen embrittlement at atomic scale during fatigue could be also better understood. Indeed, it is also known from previous studies [Hénaff et al., 2002, Hénaff and Tonneau, 2001, Stoloff and Duquette, 1993, Liu et al., 1989, Liu and Kim, 1992] that aluminides are prone to environmental embrittlement in the presence of a moist atmosphere. Then a more comprehensive understanding of hydrogen effect on fatigue crack propagation could be obtained from such atomistic simulations.

THIS PAGE INTENTIONALLY LEFT BLANK

Appendix A

Engineering moduli

The values of Young's modulus, shear modulus are shown Table A.1, Table A.2, Table A.3.

Table A.1: Young's modulus and plane strain Young's modulus of copper for different crystal orientation. Values are computed with elastic constants predicted by the used potentials. The plane strain Young's modulus is computed as proposed by Knowles [Knowles, 2017]

Orientation	**77 K**		**300 K**		**600 K**	
	E (GPa)	E^* (GPa)	E (GPa)	E^* (GPa)	E (GPa)	E^* (GPa)
A1	64	78	64	78	56	69
A2	-	-	64	98	-	-
A3	-	-	64	90	-	-
B1	133	202	130	192	113	176
B2	-	-	130	132	-	-
C1	194	207	192	205	168	180
C2	-	-	192	205	-	-

Table A.2: Young's modulus and plane strain Young's modulus for different materials and orientation A1 ($(0\,1\,0)[0\,0\,1]$, loading axis along $[0\,1\,0]$). Values are computed with elastic constants predicted by the used potentials

Material	**300 K**	
	E (GPa)	E^* (GPa)
Ag	46	57
Al	63	73
Cu	64	78
Ni	120	140

Table A.3: Shear modulus μ_{slip} and Poisson ratio

	300 K			
	Ag	Al	Cu	Ni
μ_{slip}(GPa)	26.33	26.67	40	68
ν	0.434	0.359	0.484	0.351

Appendix B

Metals properties

Table B.1 provides some properties of the metals under investigations in this manuscript. These properties are predicted by EAM potentials some of which have been used in this manuscript. The values are those reported by the authors.

Table B.2 show the experimental values of some metals properties as reported by the authors

Table B.1: FCC metals properties predicted by EAM interatomic potentials

	Nickel	**Copper**	**Aluminium**	**Silver**
E_{coh}	4.450[a]; 4.39[b]; 4.46[c]; 4.45[d]	3.28[f]; 3.54[g]	3.36[j]; 3.36[i]	2.85[h]; 2.85[d]
C_{11}	247[a] ; 247.03[b]; 260.69[c]; 235.57[d]	174.48[f]; 170.0[g]	114.0[j] ; 116.8[i]	124.2[h]; 129.07[d]
C_{12}	148[a]; 147.30[b]; 150.55[c]; 153.14[d]	127.84[f]; 122.5[g]	61.90[j]; 60.1[i]	93.9[h]; 91.7[d]
C_{44}	125[a]; 122.77[b]; 131.43[c]; 133.51[d]	84.44[f]; 75.8[g]	31.6[j]; 31.17[i]	46.14[h]; 56.74[d]
γ_{us}	366[a]; 379[b]; 553.6[c]; 235.2[d]	266[f]; 162[g]	168[j]; 151[i]	115[h]; 118.3[d]
γ_{sf}	125[a]; 195.5[b]; 26.9[c]; 16.7[d]	39.2[f]; 45[g]	146[j] ;115[i]	17.8[h]; 2.2[d]
$\gamma_s(100)$	1936[a]	1330[a]	943[j]	940[h]
$\gamma_s(110)$	2087[a]	1475[a]	1006[j]	1017[h]
$\gamma_s(111)$	1629[a]	1239[g]	870[j] ; 601[i]	862[h]
E_f^v	1.60[a]; 1.71[d]	1.27[g] ; 1.33[d]	0.68[j] ; 0.71[i]	1.103[h] ; 0.97[d]
E_m^v	1.29[a]; 1.10[d]	0.689[g] ; 0.69[d]	0.64[j] ; 0.65[i]	0.655[h]; 0.77[d]

a - [Mishin, 2004]
b - [Mendelev et al., 2012]
c - [Ackland et al., 1987]
d - [Adams et al., 1989]
f - [Mendelev et al., 2008]
g - [Mishin et al., 2001]
h - [Williams et al., 2006]
i - [Zope and Mishin, 2003]
j- [Mishin et al., 1999]

Table B.2: FCC metals properties (Experimental data)

	Nickel	**Copper**	**Aluminium**	**Silver**
E_{coh}	4.44^{l}	3.49^{l}	3.39^{l}	2.95^{l}
C_{11}	246.5^{a}	170^{a}	114^{a}	122^{a}
C_{12}	147.3^{a}	122.5^{a}	61.90^{a}	93.4^{a}
C_{44}	124.7^{a}	75.8^{a}	31.6^{a}	46.1^{a}
γ_{sf}	128^{d}; 125^{g}	55^{h}; 41^{i}; 45^{n}	$120 - 144^{s}$	22^{h}; 16^{j}
γ_s(Average orientation)	$2280^{d,e}$	1790^{e}	980^{k}; 1140^{t}; 1160^{e}	1140^{g}
E_f^v	1.60^{b}	1.27^{m} ; 1.28^{c}	0.68^{b}	1.1^{c}
E_m^v	1.3^{c}	0.71^{c}	0.66^{c}	0.66^{c}

a - [Huntington, 1958]
b - [Schaefer et al., 1987]
c - [Balluffi, 1978]
d - [Murr, 1975]
e - [Tyson and Miller, 1977]
g - [Hirth and Lothe, 1982]
h - [Gallagher, 1970]
i - [Stobbs and Sworn, 1971]
j - [Cockayne et al., 1971]
k - [Murr, 1973]
l - [Kittel, 2004]
m - [Tam et al., 1978]
n- [Carter and Ray, 1977]
p - [Smith, 1984]
s - [Westmacott and Peck, 1971]
t - [Boer and etc, 1988]

THIS PAGE INTENTIONALLY LEFT BLANK

Appendix C

LEFM stress fields around crack-tip in anisotropic bodies

The following equation gives the stress fields at the crack tip. This field is written in the general framework of the elastic anisotropic.

$$\begin{cases} \sigma_{xx} = \dfrac{K_I}{\sqrt{2\pi r}} \Re \left[\dfrac{a_1 a_2}{a_1 - a_2} \left(\dfrac{a_2}{\sqrt{\cos\theta + a_2 \sin\theta}} - \dfrac{a_1}{\sqrt{\cos\theta + a_1 \sin\theta}} \right) \right] \\ \sigma_{yy} = \dfrac{K_I}{\sqrt{2\pi r}} \Re \left[\dfrac{1}{a_1 - a_2} \left(\dfrac{a_1}{\sqrt{\cos\theta + a_2 \sin\theta}} - \dfrac{a_2}{\sqrt{\cos\theta + a_1 \sin\theta}} \right) \right] \\ \sigma_{xy} = \dfrac{K_I}{\sqrt{2\pi r}} \Re \left[\dfrac{a_1 a_2}{a_1 - a_2} \left(\dfrac{1}{\sqrt{\cos\theta + a_1 \sin\theta}} - \dfrac{1}{\sqrt{\cos\theta + a_2 \sin\theta}} \right) \right] \\ \sigma_{zz} = \dfrac{1}{s_{33}} \left(s_{13}\sigma_{xx} + s_{23}\sigma_{yy} + s_{26}\sigma_{xy} \right) \\ \sigma_{xz} = \sigma_{yz} = 0 \end{cases} \tag{C.1}$$

These stress fields are of the type that those in isotropy i.e.

$$\sigma_{ij} = \frac{K_I}{\sqrt{2\pi r}} f_{ij} \tag{C.2}$$

where K_I is the mode I stress intensity factor, $\Re$ the real part of a complex number, a_i, and p_i depending on the elastic stiffness of the metals. f_{ij} is a function depending on the position of a point M around the crack-tip.

The evolution of the function f_{ij} around the crack tip is displayed in Fig. C-1

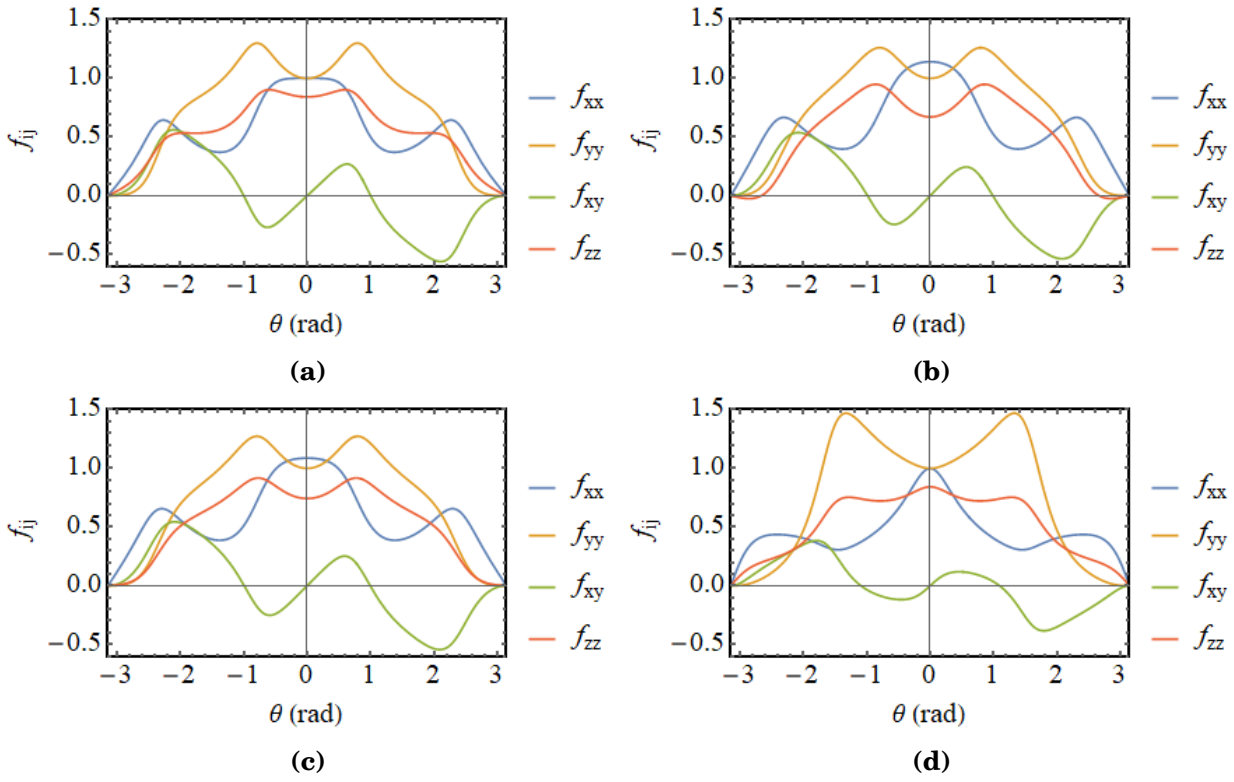

See the next page for complete description ...

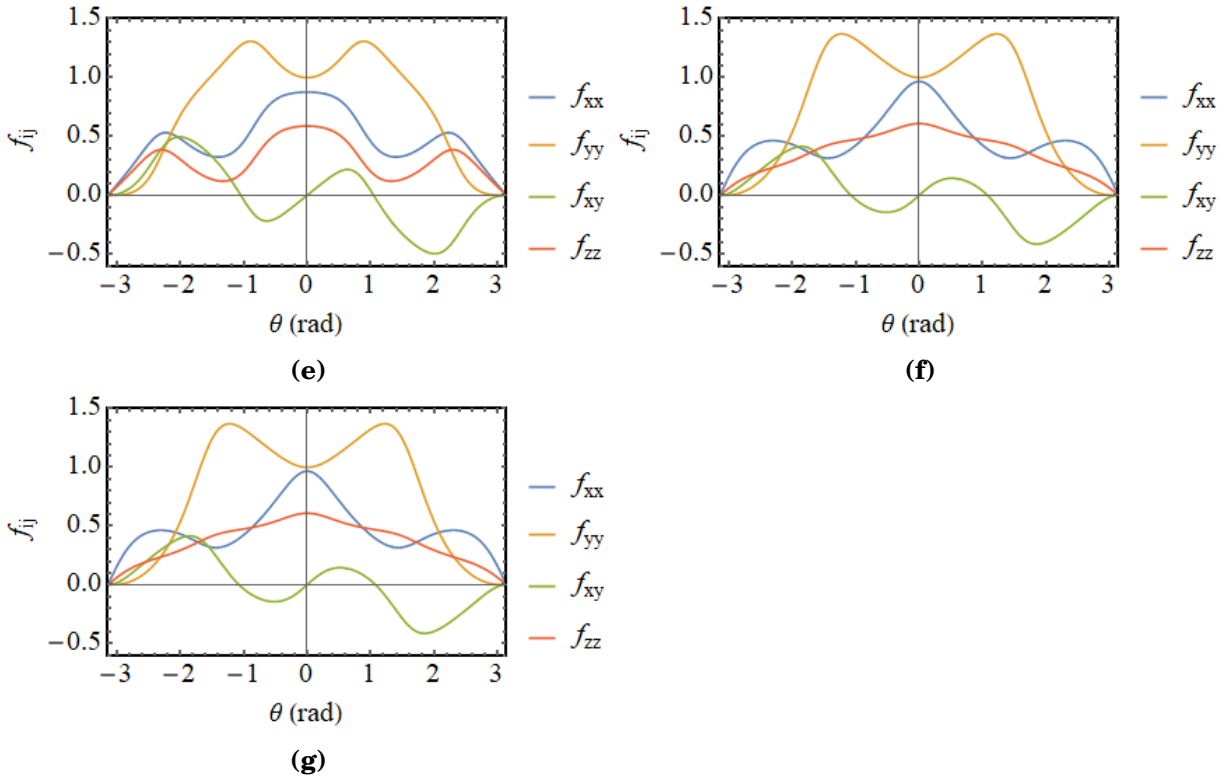

Figure C-1: Near crack tip normalized stress fields for different crack orientation (a) A1, (b) A2, (c) A3, (d) B1, (e) B2, (f) C1, (g) C2

THIS PAGE INTENTIONALLY LEFT BLANK

Appendix D

Proportion of different types of dislocations in copper single crystals

D.1 Effect of crystal orientation

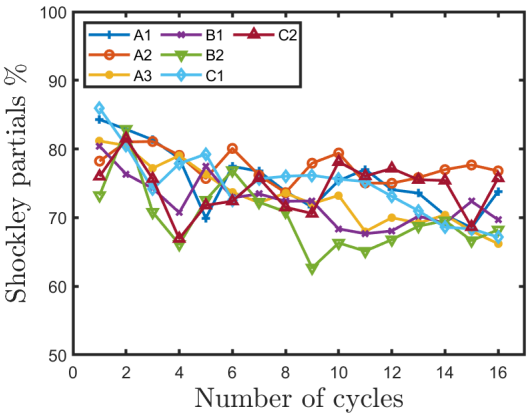

(a)

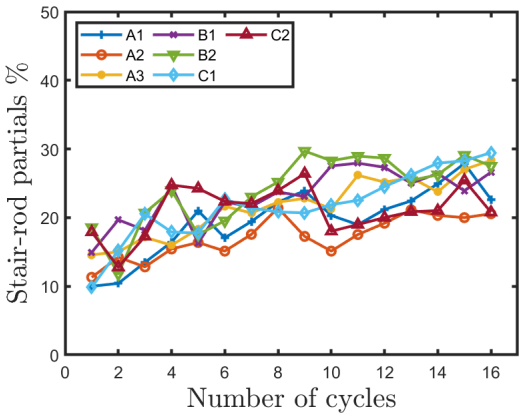

(b)

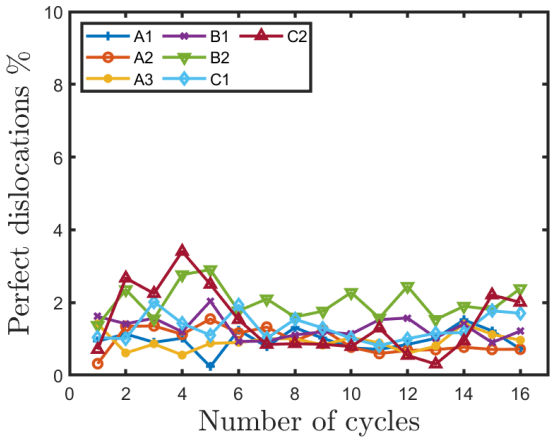

(c)

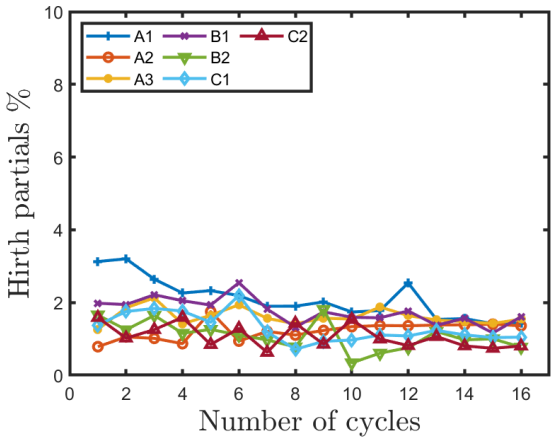

(d)

See the next page for complete description ...

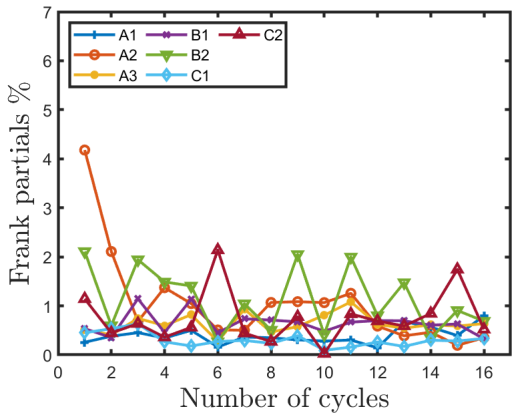

(e)

Figure D-1: Evolution of the proportion of different types of dislocations during cyclic loading for an applied $\Delta K = 2\ \mathrm{MPa}\sqrt{\mathrm{m}}$ for orientations (a) A1, (b) A2, (c) A3, (d) B1, (e) B2, (f) C1, (g) C2. Figures show a slight decrease in Shockley partials proportion and a slight increase in Stair-rod partials proportion whereas other type of dislocations exhibit an almost constant proportion during cyclic loading

D.2 Effect of temperature

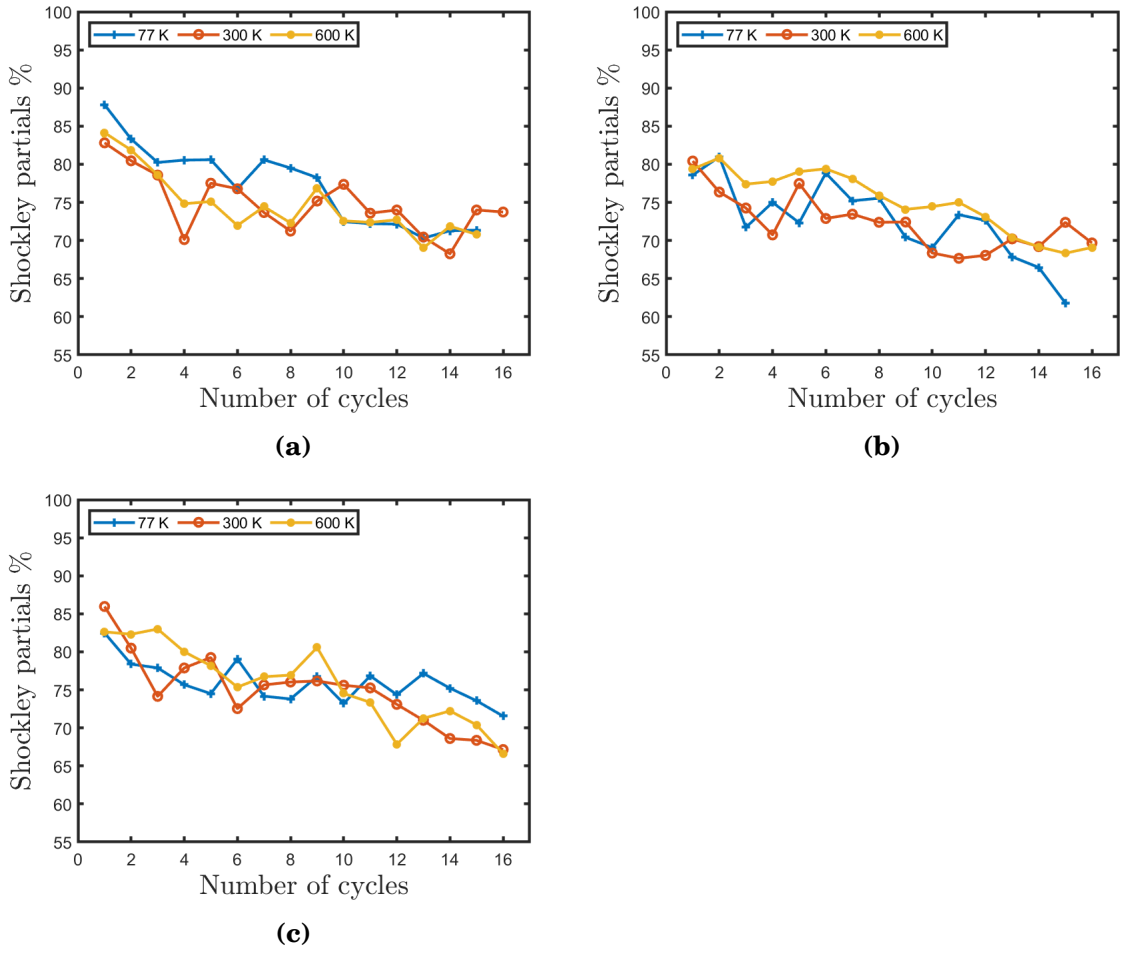

Figure D-2: Evolution of the proportion of Shockley partials during cyclic loading (a) Orientation A1 (b) Orientation B1, (c) Orientation C1. Applied $\Delta K = 2\ \mathrm{MPa}\sqrt{\mathrm{m}}$.

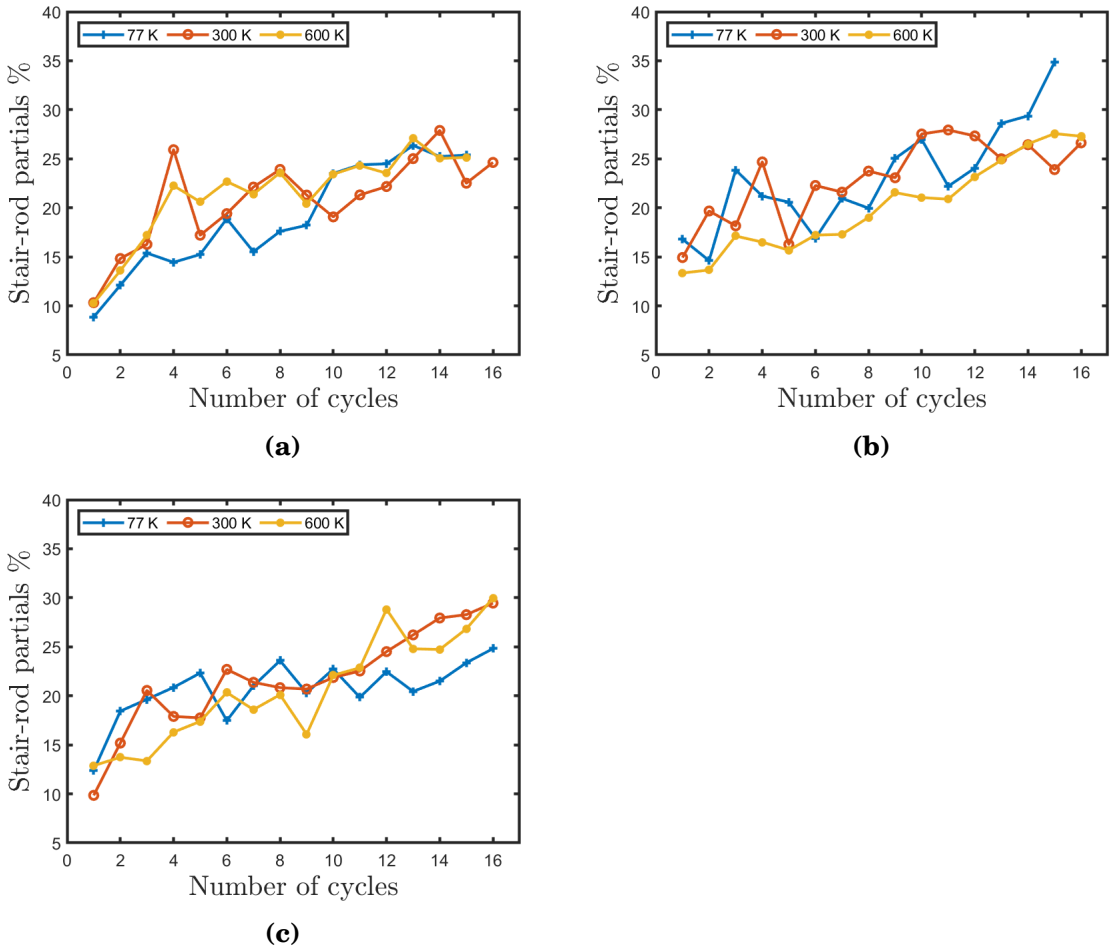

Figure D-3: Evolution of the proportion of Stair-rod partials during cyclic loading (a) Orientation A1 (b) Orientation B1, (c) Orientation C1

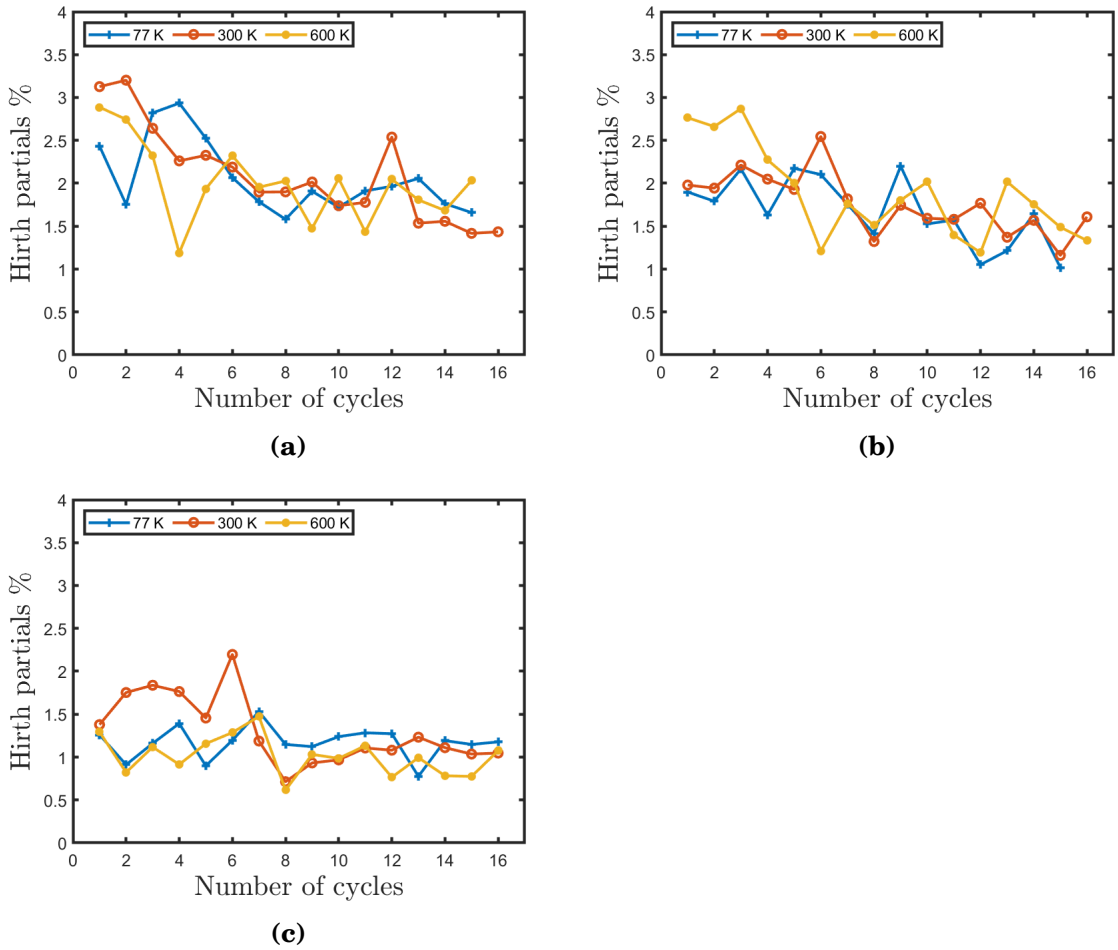

Figure D-4: Evolution of the proportion of Hirth partials during cyclic loading (a) Orientation A1 (b) Orientation B1, (c) Orientation C1

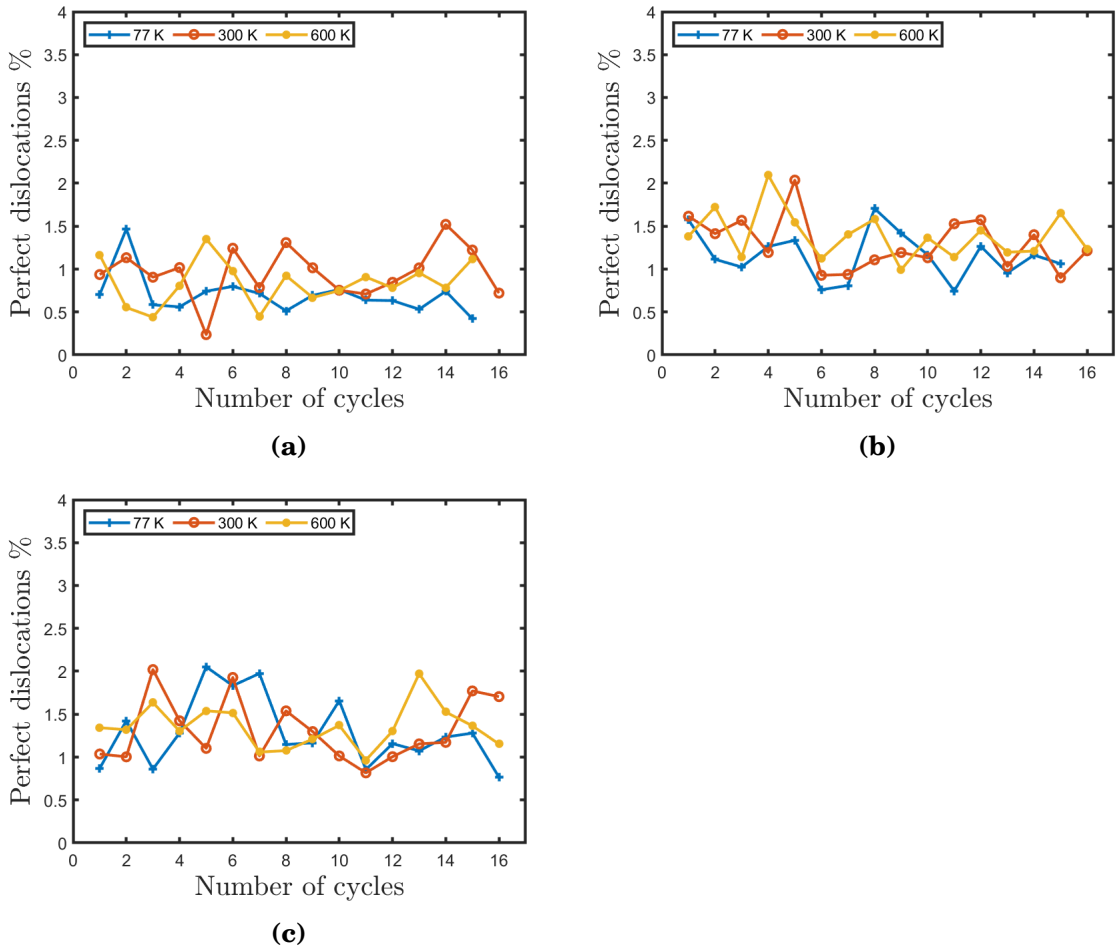

Figure D-5: Evolution of the proportion of perfect dislocations during cyclic loading (a) Orientation A1 (b) Orientation B1, (c) Orientation C1

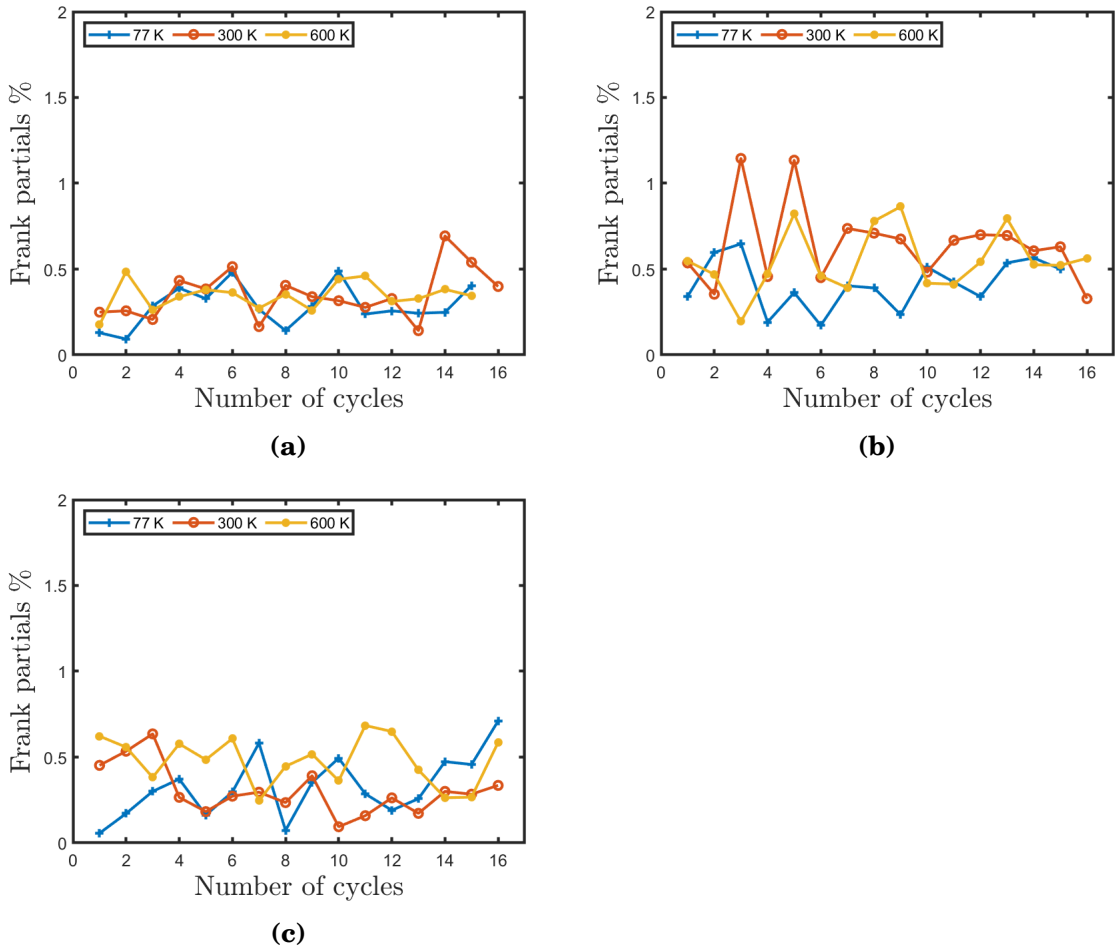

Figure D-6: Evolution of the proportion of Frank partials during cyclic loading (a) Orientation A1 (b) Orientation B1, (c) Orientation C1

D.3 Proportion of different dislocation types in different fcc metals

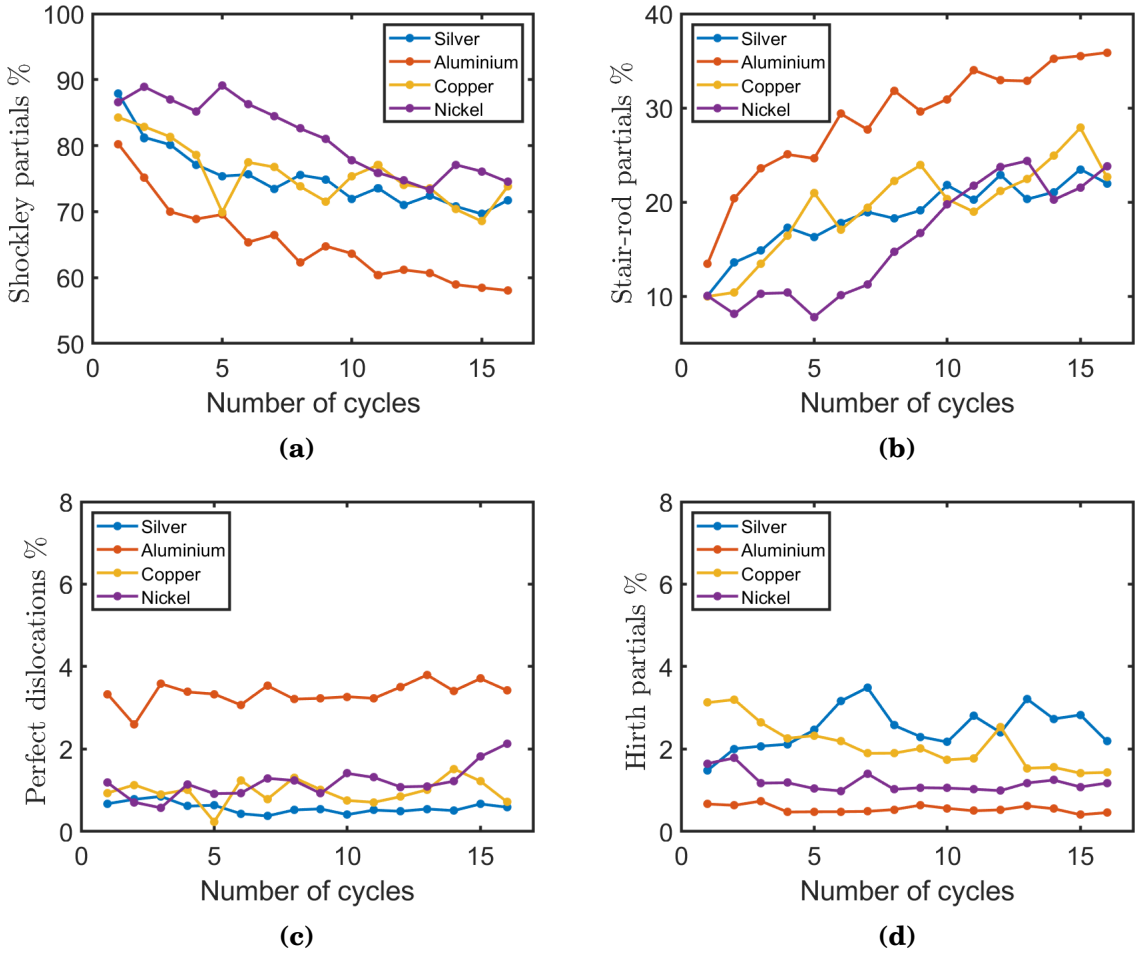

See the next page for complete description ...

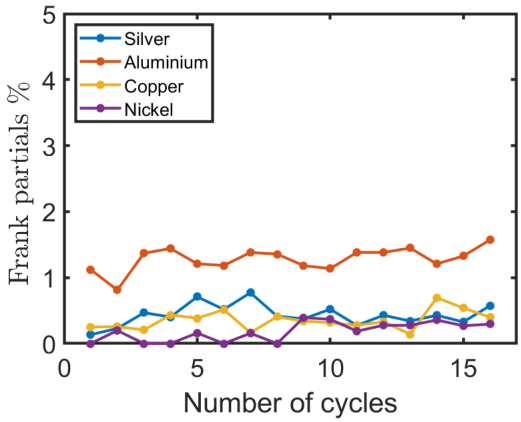

(e)

Figure D-7: Evolution of the proportion of different dislocation types during cyclic loading in different FCC single crystal(a) Shockley partials, (b) stair-rod partials, (c) perfect dislocations, (d) Hirth partials, (e) Frank dislocations. $\Delta K = 2\ \mathrm{MPa}\sqrt{\mathrm{m}}$, crack orientation A1, RT.

D.4 Effect of loading amplitude on the proportion of different dislocation types in nickel

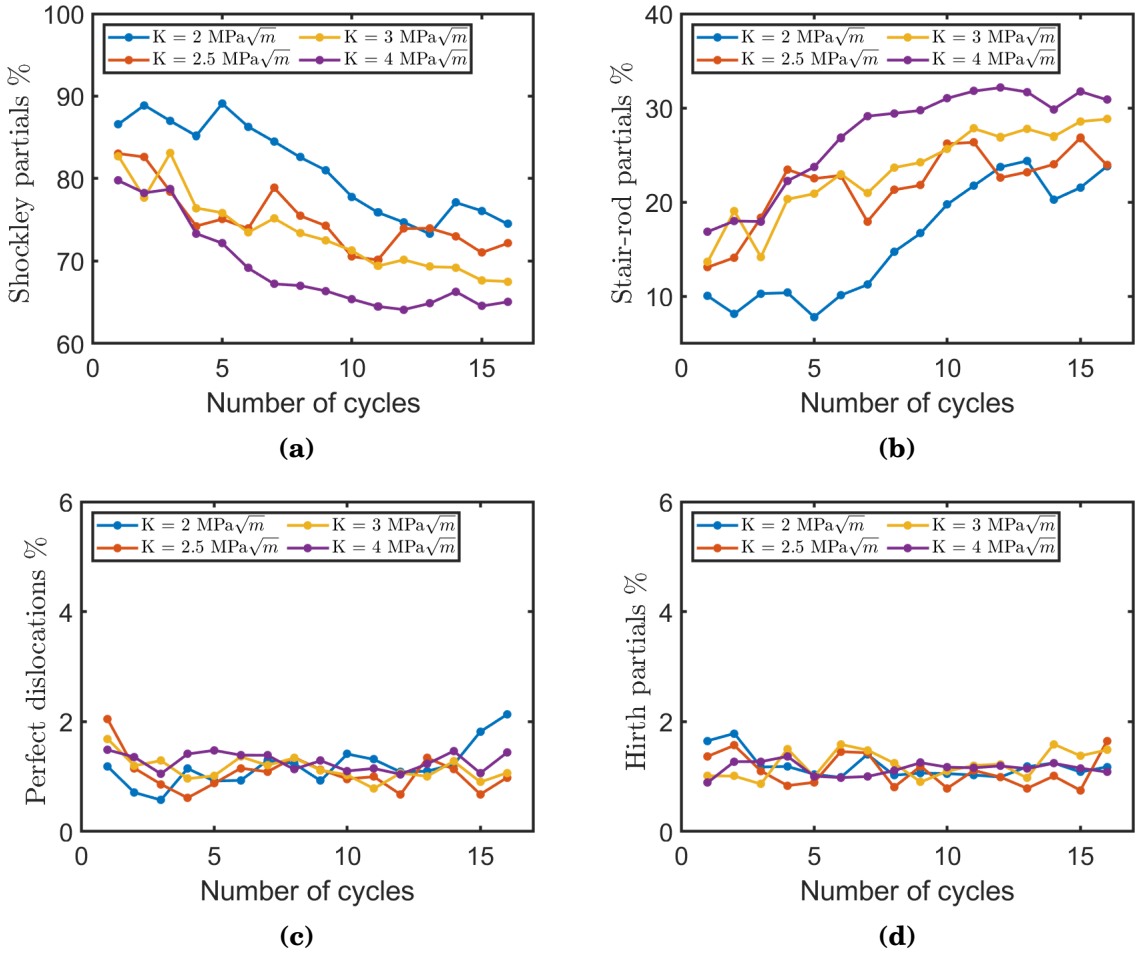

See the next page for complete description ...

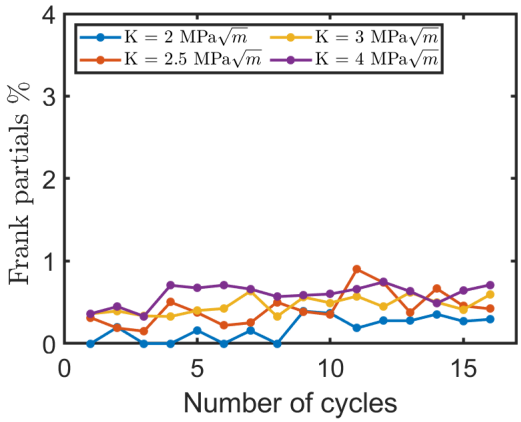

(e)

Figure D-8: Evolution of the proportion of different dislocation types during cyclic loading for nickel and at different loading amplitude (a) Shockley partials, (b) stair-rod partials, (c) perfect dislocations, (d) Hirth partials, (e) Frank dislocations

D.5 Proportion of different dislocation type under mixed mode loading

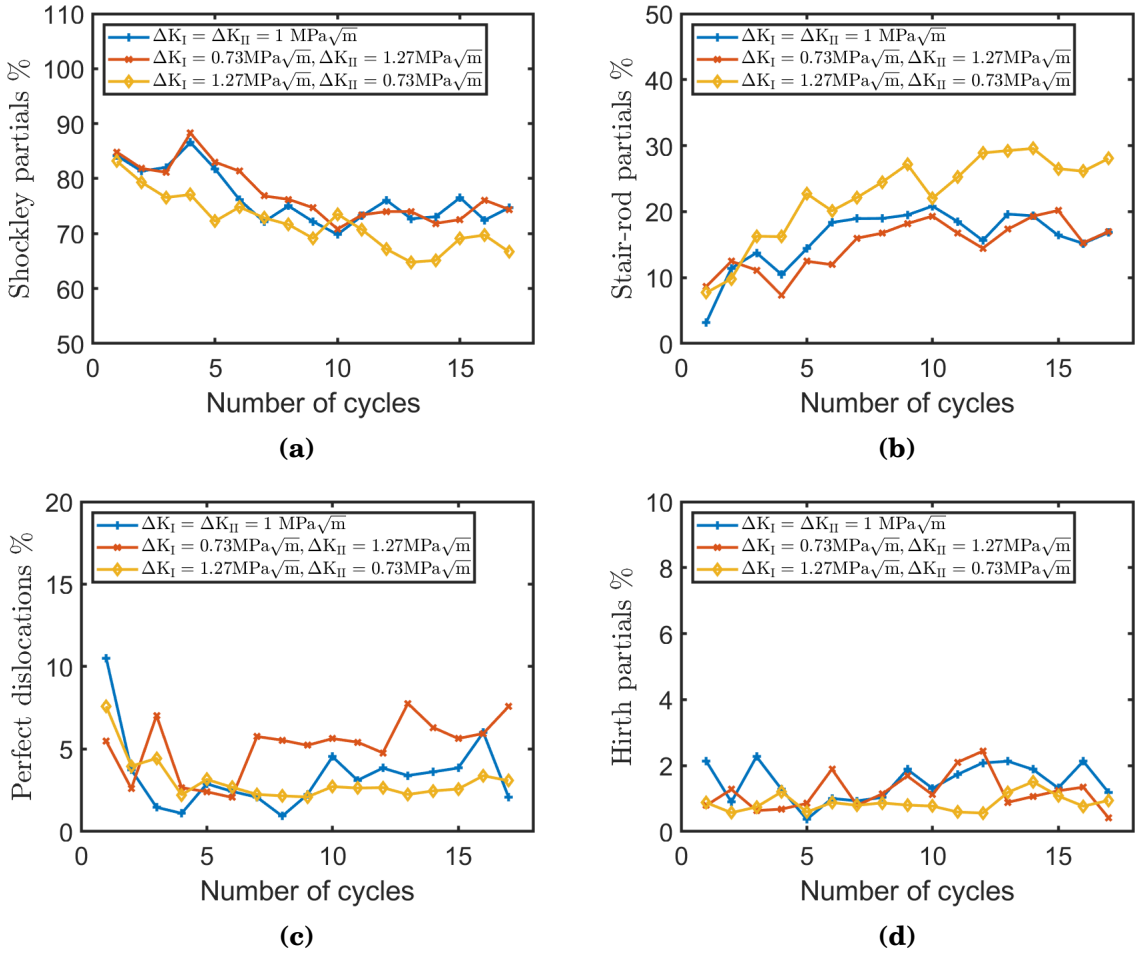

See the next page for complete description ...

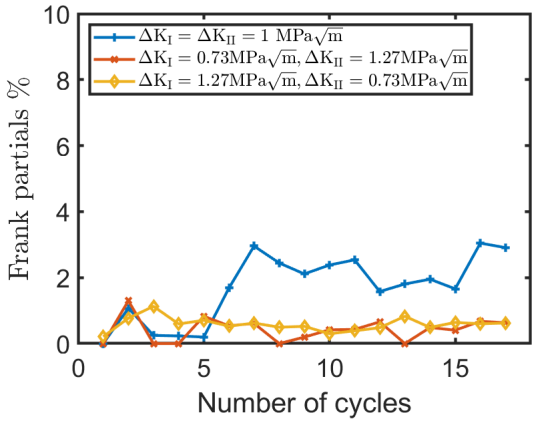

(e)

Figure D-9: Evolution of the proportion of different dislocation type during mixed mode cyclic loading (a) Shockley partials, (b) stair-rod partials, (c) perfect dislocations, (d) Hirth partials, (e) Frank dislocations.

Appendix E

Crack propagation rates

E.1 Effect of temperature

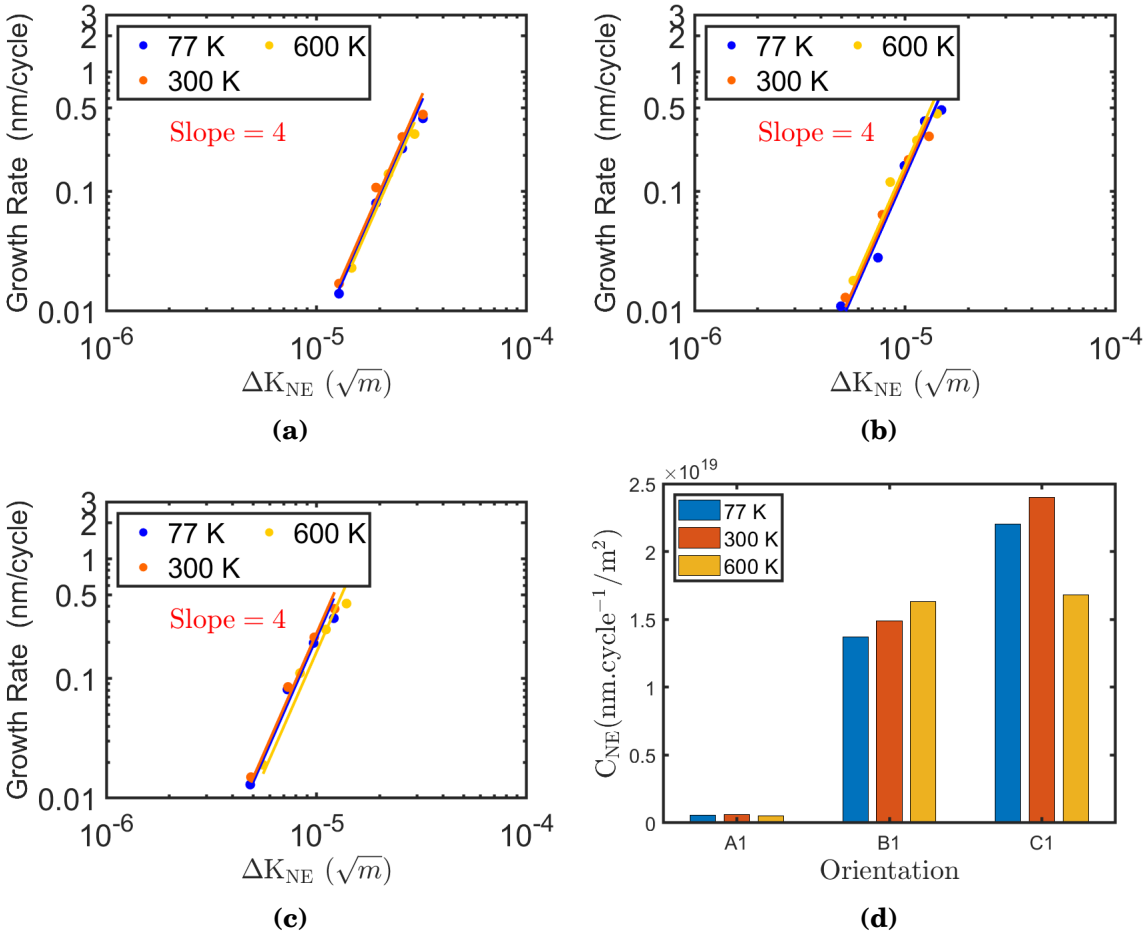

Figure E-1: Effect of temperature on FCGR represented as function of normalized SIF and fitted on Paris law with exponent fixed at 4 (see Equation 6.18). (a) Orientation A1, (b) Orientation B1, (c) Orientation C1. (d) Evolution of the prefactor C_{NE} of Equation 6.18 with temperature for different crystal orientation

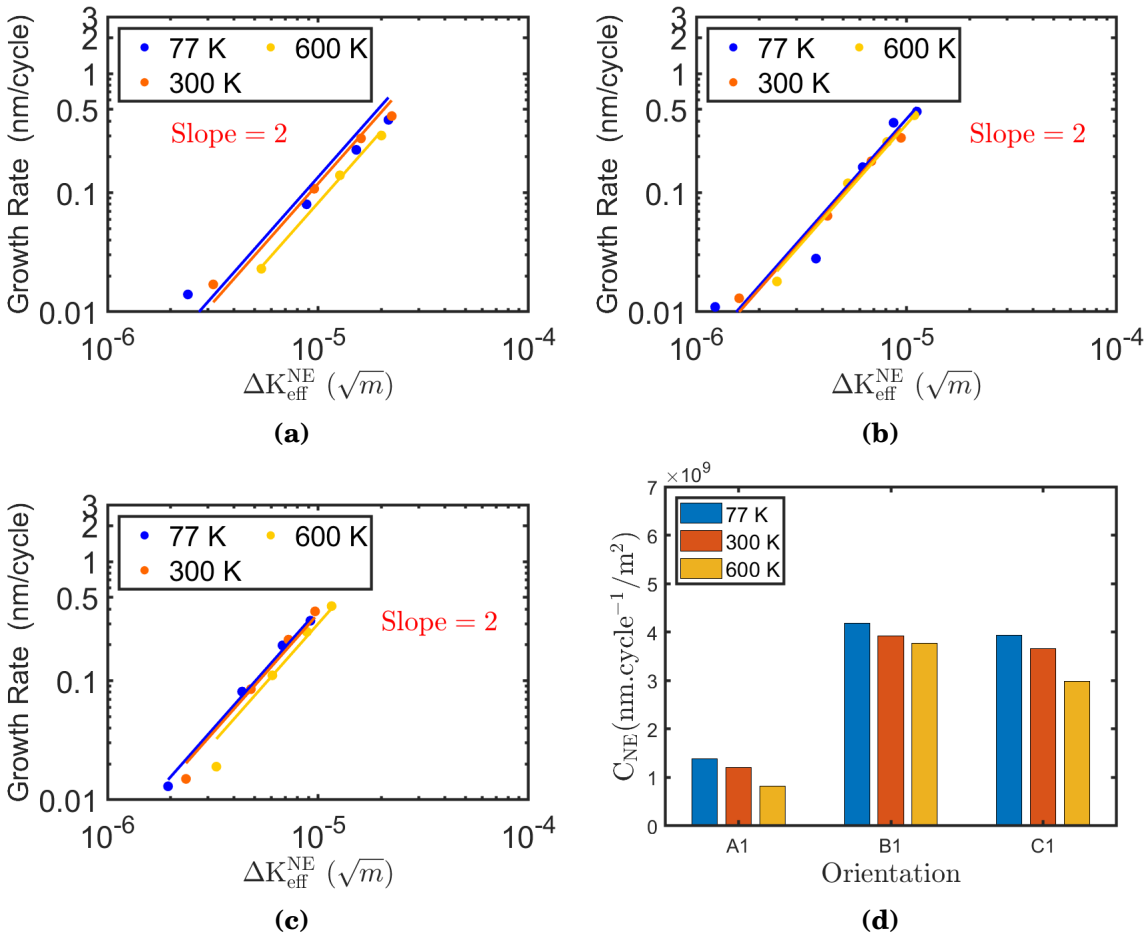

Figure E-2: Effect of temperature on FCGR represented as function of normalized SIF and fitted on Paris law with exponent fixed at 4 (see Equation 6.20). (a) Orientation A1, (b) Orientation B1, (c) Orientation C1. (d) Evolution of the prefactor C_{eff}^{eff} of Equation 6.20 with temperature for different crystal orientation

E.2 Effect of SFE (material)

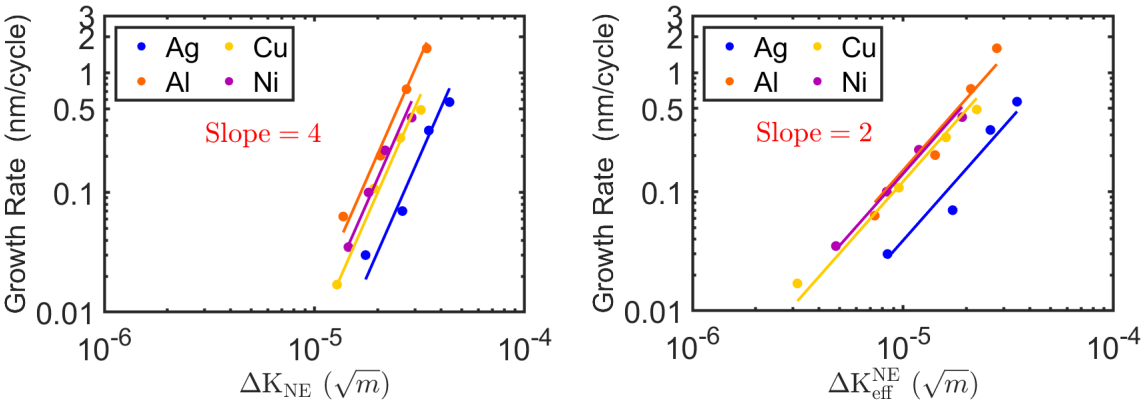

Figure E-3: FCGR as function of (a) normalized SIF and (b) normalized effective SIF.

Appendix F

Dislocation microstructures

F.1 Effect of temperature

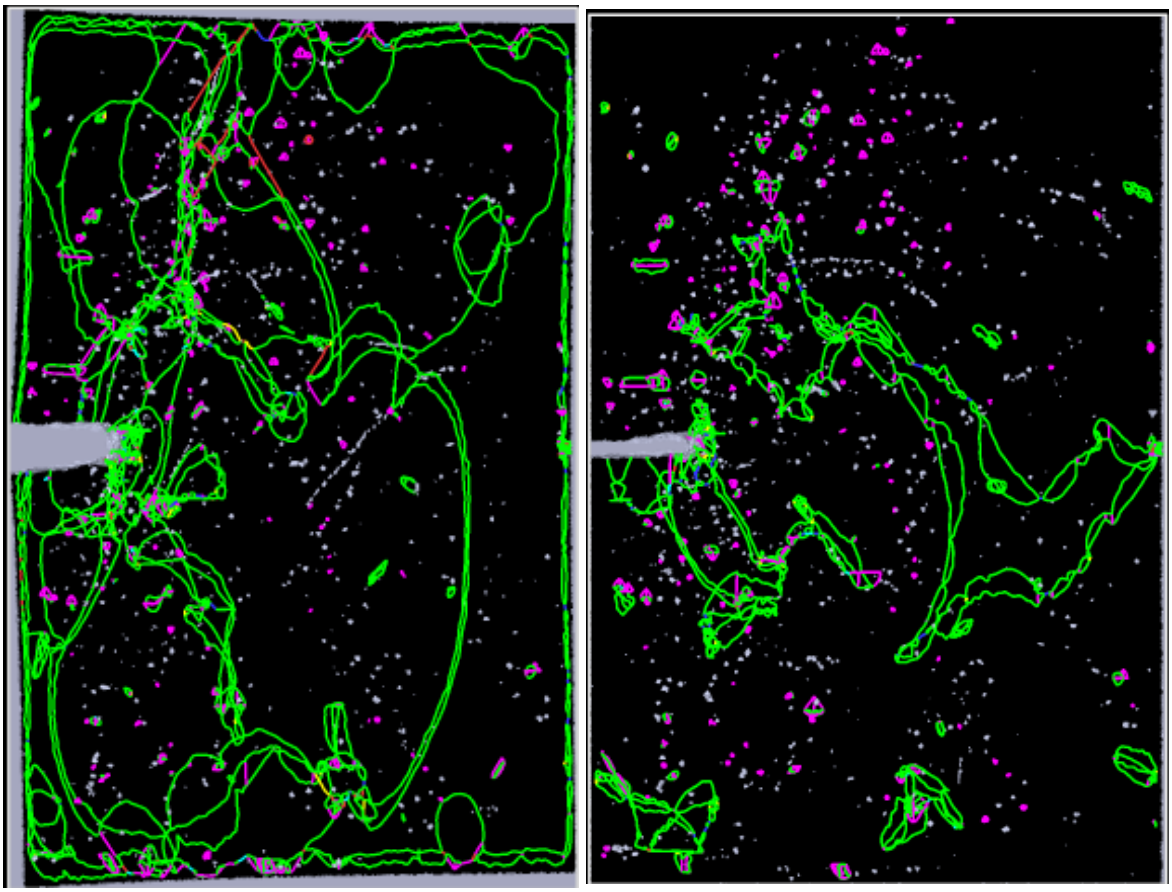

(a) **(b)**

Figure F-1: Dislocation microstructures at the (a) maximum and (b) minimum loading. Applied $\Delta K = 2\ \mathrm{MPa}\sqrt{\mathrm{m}}$, copper, orientation C1, $600\,\mathrm{K}$. The color code for the description of the different types of dislocations is the same as in chapter 4.

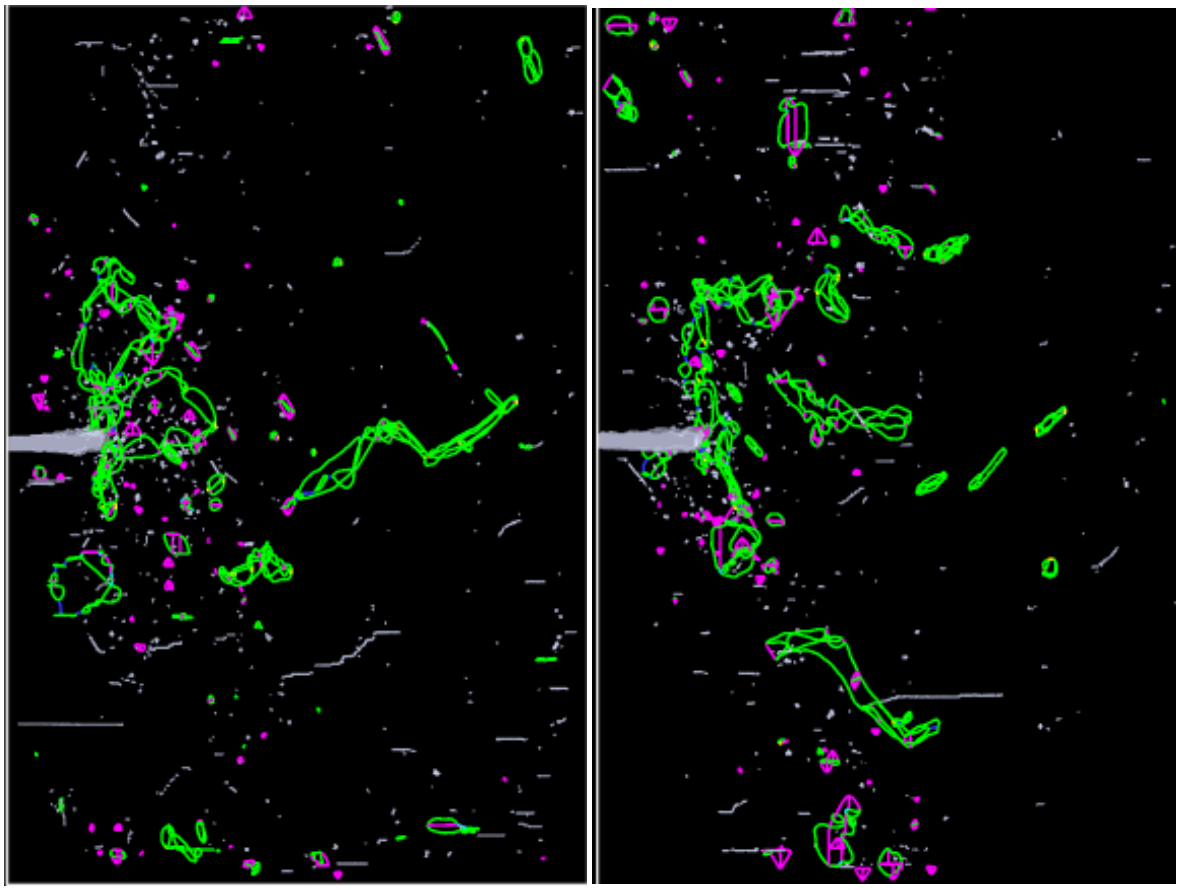

(a) **(b)**

See the next page for complete description ...

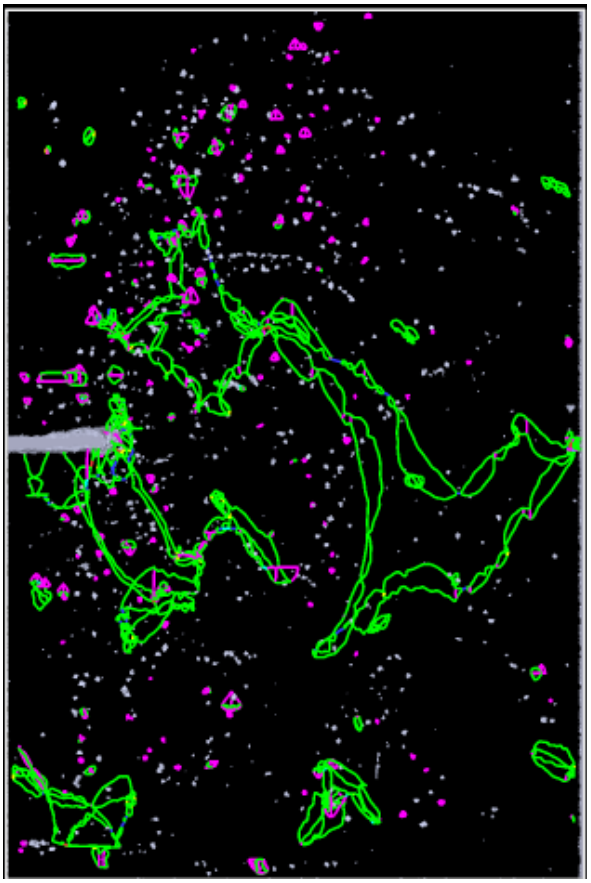

(c)

Figure F-2: Dislocation microtructures around crack tip at different temperatures in copper, crack orientation C1 (a) $77\,\mathrm{K}$; (b) $300\,\mathrm{K}$; (c) $600\,\mathrm{K}$. The color code for the description of the different types of dislocations is the same as in chapter 4.

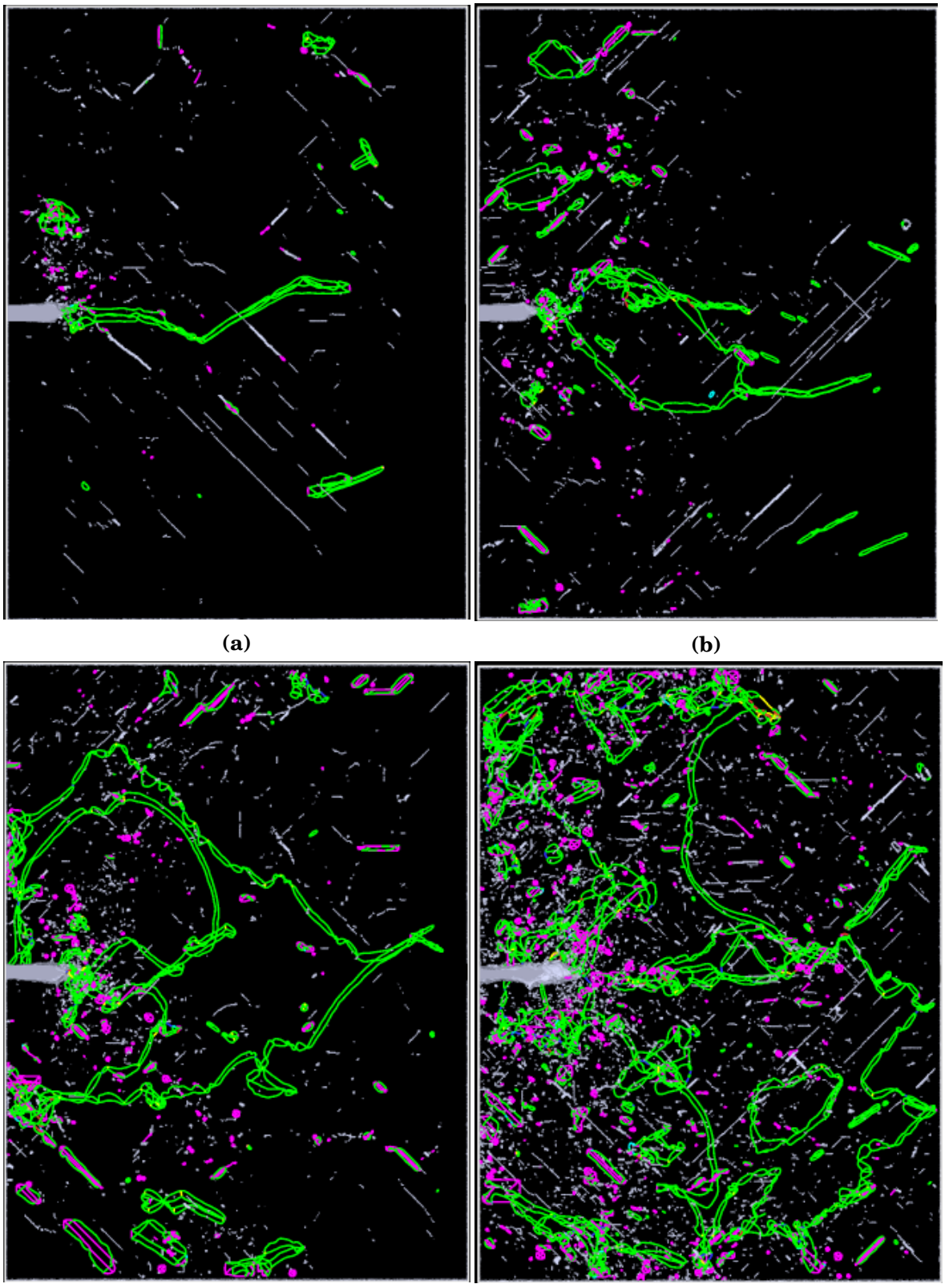

(a) **(b)**

(c) **(d)**

Figure F-3: Dislocation microstructure in nickel for orientation A1 after unloading. (a) $\Delta K = 2\ \mathrm{MPa}\sqrt{\mathrm{m}}$, (b) $\Delta K = 2.5\ \mathrm{MPa}\sqrt{\mathrm{m}}$, (c) $\Delta K = 3\ \mathrm{MPa}\sqrt{\mathrm{m}}$, (d) $\Delta K = 4\ \mathrm{MPa}\sqrt{\mathrm{m}}$.

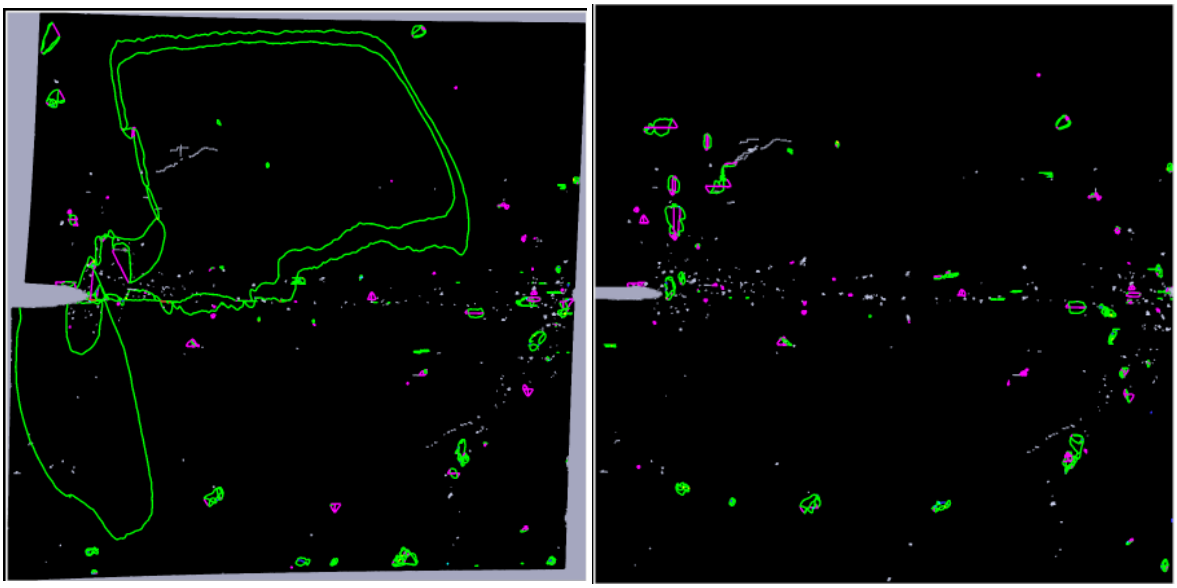

(a) **(b)**

Figure F-4: Dislocation microstructures in copper under mixed mode loading at the 15^{th}. (a) at maximum loading (b) after unloading. The color code for the description of the different types of dislocations is the same as in chapter 4.

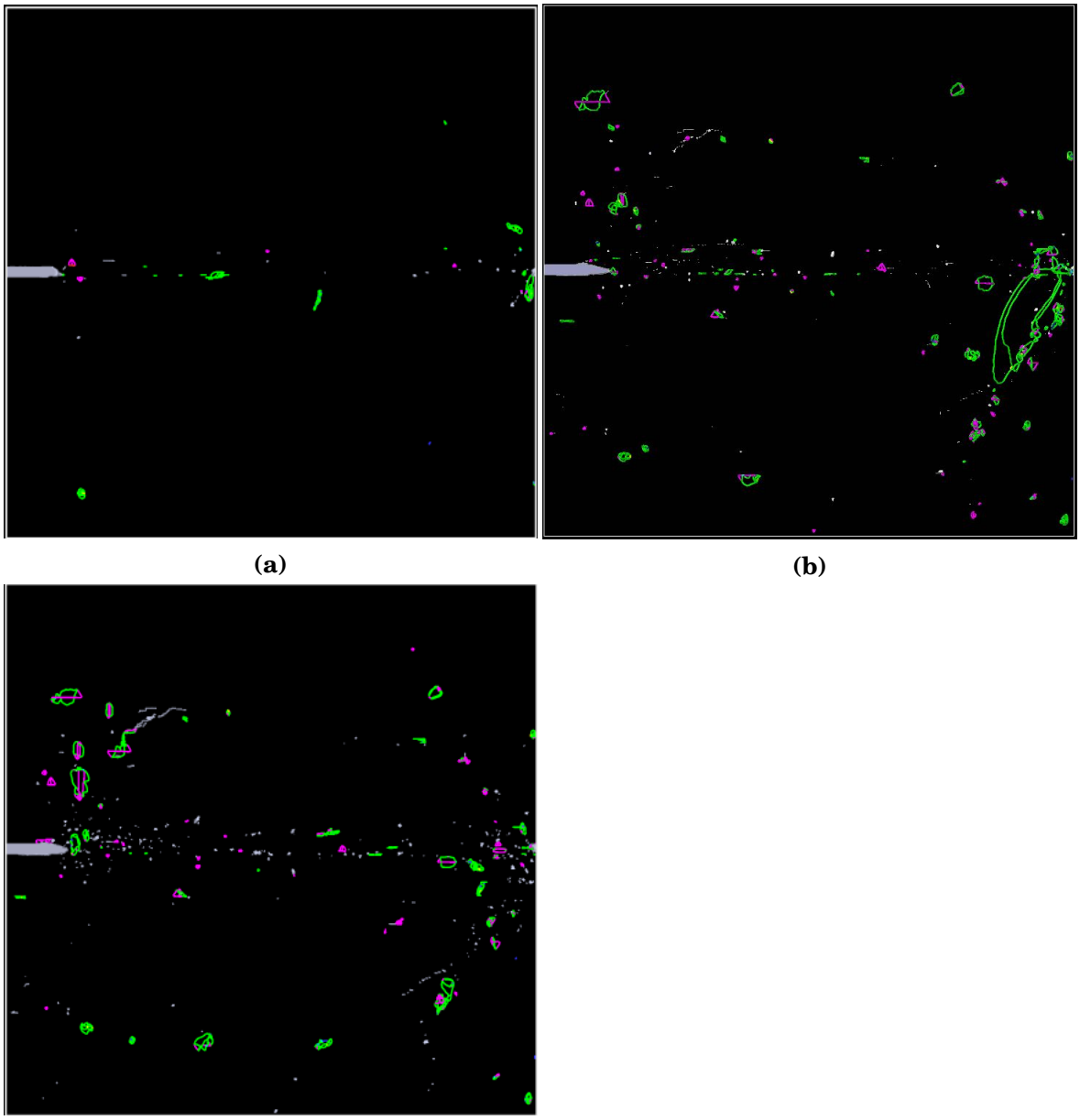

(a) **(b)**

(c)

Figure F-5: Dislocation microstructures in copper under mixed mode loading at the end of the 15^{th} after unloading). (a) $\Delta K_I = \Delta K_{II} = 0.75\ \mathrm{MPa}\sqrt{\mathrm{m}}$ (b) $\Delta K_I = \Delta K_{II} = 1\ \mathrm{MPa}\sqrt{\mathrm{m}}$ (c) $\Delta K_I = \Delta K_{II} = 1.25\ \mathrm{MPa}\sqrt{\mathrm{m}}$. The color code for the description of the different types of dislocations is the same as in chapter 4.

Bibliography

[Abraham et al., 1994] Abraham, F., Brodbeck, D., Rafey, R. A., and Rudge, W. E. (1994). Instability dynamics of fracture: A computer simulation investigation. Physical Review Letters, 73(2):272–275.

[Ackland et al., 1987] Ackland, G. J., Tichy, G., Vitek, V., and Finnis, M. W. (1987). Simple N-body potentials for the noble metals and nickel. Philosophical Magazine A, 56(6):735–756.

[Adamesku et al., 1994] Adamesku, R., Grebenkin, S., Yermakov, A., and Panfilov, P. (1994). On mechanical twinning in iridium under compression at room temperature. J Mater Sci Lett, 13(12):865–867.

[Adams et al., 1989] Adams, J. B., Foiles, S. M., and Wolfer, W. G. (1989). Self-diffusion and impurity diffusion of fee metals using the five-frequency model and the Embedded Atom Method. Journal of Materials Research, 4(1):102–112.

[Agbessi, 2013] Agbessi, K. (2013). Approches expérimentales et multi-échelles des processus d'amorçage de fissures en fatigue sous chargements complexes. Thèse de doctorat de l'Ecole Nationale d'Arts et Métiers ENSAM, page 277.

[Anderson et al., 2017] Anderson, P., Hirth, J., and Lothe, J. (2017). Theory of Dislocations. Cambridge University Press.

[Andric and Curtin, 2017] Andric, P. and Curtin, W. A. (2017). New theory for Mode I crack-tip dislocation emission. Journal of the Mechanics and Physics of Solids, 106:315–337.

[Andric and Curtin, 2018] Andric, P. and Curtin, W. A. (2018). Atomistic modeling of fracture. Modelling and Simulation in Materials Science and Engineering, 27(1):013001.

[Avery and Backofen, 1962] Avery, D. and Backofen, W. (1962). Fracture of Solids.

[Avery and Backofen, 1963] Avery, D. H. and Backofen, W. A. (1963). Fatigue hardening in alloys of low stacking-fault energy. Acta Metallurgica, 11(7):653–661.

[Awatani et al., 1979] Awatani, J., Katagiri, K., and Koyanagi, K. (1979). A study on the effect of stacking fault energy on fatigue crack propagation as deduced from dislocation patterns. MTA, 10(4):503–507.

[Awatani et al., 1978] Awatani, J., Katagiri, K., and Nakai, H. (1978). Dislocation structures around propagating fatigue cracks in iron. MTA, 9(1):111–116.

[Baker and Warner, 2012] Baker, K. L. and Warner, D. H. (2012). Extended timescale atomistic modeling of crack tip behavior in aluminum. Modelling and Simulation in Materials Science and Engineering, 20(6):065005. Publisher: IOP Publishing.

[Baker and Warner, 2014] Baker, K. L. and Warner, D. H. (2014). An atomistic investigation into the nature of near threshold fatigue crack growth in aluminum alloys. Engineering Fracture Mechanics, 115:111–121.

[Balluffi, 1978] Balluffi, R. (1978). Vacancy defect mobilities and binding energies obtained from annealing studies. Journal of Nuclear Materials, 69-70:240–263.

[Basinski et al., 1969] Basinski, S. J., Basinski, Z. S., and Howie, A. (1969). Early stages of fatigue in copper single crystals. Philos. Mag. J. Theor. Exp. Appl. Phys., 19(161):899–924. _eprint: https://doi.org/10.1080/14786436908225856.

[Basinski and Basinski, 1989] Basinski, Z. and Basinski, S. (1989). Copper single crystal PSB morphology between 4.2 and 350 K. Acta Metallurgica, 37(12):3263–3273.

[Basinski and Basinski, 1984] Basinski, Z. S. and Basinski, S. J. (1984). Formation and growth of subcritical fatigue cracks. Scripta Metallurgica, 18(8):851–856.

[Basinski and Basinski, 1992a] Basinski, Z. S. and Basinski, S. J. (1992a). Fundamental aspects of low amplitude cyclic deformation in face-centred cubic crystals. Progress in Materials Science, 36:89–148.

[Basinski and Basinski, 1992b] Basinski, Z. S. and Basinski, S. J. (1992b). Surface-related phenomena in low amplitude fatigue of fcc metals. Scripta Metallurgica et Materialia, 26(10):1505–1510.

[Basinski et al., 1983] Basinski, Z. S., Pascual, R., and Basinski, S. J. (1983). Low amplitude fatigue of copper single crystals—I. The role of the surface in fatigue failure. Acta Metallurgica, 31(4):591–602.

[Benzerga and Leblond, 2010] Benzerga, A. A. and Leblond, J.-B. (2010). Ductile Fracture by Void Growth to Coalescence. In Aref, H. and Giessen, E. v. d., editors, Advances in Applied Mechanics, volume 44 of Advances in Applied Mechanics, pages 169–305. Elsevier.

[Benzerga et al., 2016] Benzerga, A. A., Leblond, J.-B., Needleman, A., and Tvergaard, V. (2016). Ductile failure modeling. Int J Fract, 201(1):29–80.

[Bilotta et al., 2017] Bilotta, G., Arzaghi, M., Benoit, G., Halm, D., Henaff, G., and Shinko, T. (2017). Environmentally-Assisted Fatigue Crack Growth in ARMCO Iron Under High Pressure of Gaseous Hydrogen.

[Bílý, 1993] Bílý, M. (1993). Cyclic Deformation and Fatigue of Metals. Elsevier.

[Blochwitz et al., 2008] Blochwitz, C., Jacob, S., and Tirschler, W. (2008). Grain orientation effects on the growth of short fatigue cracks in austenitic stainless steel. Materials Science and Engineering: A, 496(1):59–66.

[Blochwitz and Richter, 1999] Blochwitz, C. and Richter, R. (1999). Plastic strain amplitude dependent surface path of microstructurally short fatigue cracks in face-centred cubic metals. Materials Science and Engineering: A, 267(1):120–129.

[Blochwitz et al., 1997] Blochwitz, C., Richter, R., Tirschler, W., and Obrtlik, K. (1997). The effect of local textures on microcrack propagation in fatigued f.c.c. metals. Materials Science and Engineering: A, 234-236:563–566.

[Blochwitz and Tirschler, 2003] Blochwitz, C. and Tirschler, W. (2003). Influence of texture on twin boundary cracks in fatigued austenitic stainless steel. Materials Science and Engineering: A, 339(1):318–327.

[Boer and etc, 1988] Boer, F. R. d. and etc (1988). Cohesion in Metals: Transition Metal Alloys. Elsevier Science Ltd, Amsterdam.

[Boettner and McEvily, 1965] Boettner, R. C. and McEvily, A. J. (1965). Fatigue slip band formation in silicon-iron. Acta Metallurgica, 13:10.

[Bonnet and Youssef, 2006] Bonnet, R. and Youssef, S. (2006). Équilibre d'une dislocation dissociée placée dans une lame mince élastiquement anisotrope. Comptes Rendus Physique, 7(5):567–572.

[Brinckmann and Van der Giessen, 2003] Brinckmann, S. and Van der Giessen, E. (2003). Stress concentration at the surface of fatigued materials: a discrete dislocation dynamics study. In Advances in Computational and Experimental Engineering and Sciences.

[Brinckmann and Van der Giessen, 2004] Brinckmann, S. and Van der Giessen, E. (2004). A discrete dislocation dynamics study aiming at understanding fatigue crack initiation. Materials Science and Engineering: A, 387-389:461–464.

[Brown, 1981] Brown, L. (1981). Dislocations and the fatigue strength of metals. In Dislocation Modelling of Physical Systems, page 51.

[Brown, 1990] Brown, L. (1990). Deformation mechanisms leading to the initiation and slow growth of fatigue cracks. In Modelling of Material Behavior and Design, page 175.

[Brown and Ogin, 1985] Brown, L. and Ogin, S. (1985). Role of internal stresses in the nucleation of fatigue cracks. In Fundamentals of Deformation and Fracture, page 501.

[Brown, 1977] Brown, L. M. (1977). Dislocation substructures and the initiation of cracks by fatigue. Met. Sci., 11(8-9):315–320.

[Brown and Nabarro, 2004] Brown, L. M. and Nabarro, F. R. N. (2004). The enumeration and transformation of dislocation dipoles II. The transformation of interstitial dipoles into vacancy dipoles in an open dislocation array. Philos. Mag., 84(3-5):441–450.

[Brown and Miller, 1973] Brown, M. W. and Miller, K. J. (1973). A Theory for Fatigue Failure under Multiaxial Stress-Strain Conditions. Proceedings of the Institution of Mechanical Engineers, 187(1):745–755.

[Buehler et al., 2004] Buehler, M. J., Hartmaier, A., Gao, H., Duchaineau, M., and Abraham, F. F. (2004). Atomic plasticity: Description and analysis of a one-billion atom simulation of ductile materials failure. Computer Methods in Applied Mechanics and Engineering, 193(48):5257–5282.

[Cachon et al., 2015] Cachon, L., Vitillo, C., Garnier, C., Jeanningros, X., Rigal, E., Bourdais, F. L., Madeleine, S., Gastaldi, O., and Laffont, G. (2015). Status of the Sodium Gas Heat Exchanger (SGHE) development for the Nitrogen Power Conversion System planned for the ASTRID SFR prototype. In ICAPP 2015 - International Congress on Advances on Nuclear Power Plants, volume ICAPP 2015 Proceedings, page paper 15362.

[Carlson and Koss, 1978] Carlson, J. A. and Koss, D. A. (1978). Fatigue fracture and slip processes in B.C.C. TiV alloy single crystals. Acta Metallurgica, 26(1):123–132.

[Carter and Ray, 1977] Carter, C. B. and Ray, I. L. F. (1977). On the stacking-fault energies of copper alloys. The Philosophical Magazine: A Journal of Theoretical Experimental and Applied Physics, 35(1):189–200.

[Castelluccio and McDowell, 2013] Castelluccio, G. M. and McDowell, D. L. (2013). Effect of annealing twins on crack initiation under high cycle fatigue conditions. Journal of Materials Science, 48(6):2376–2387.

[Castelluccio et al., 2016] Castelluccio, G. M., Musinski, W. D., and McDowell, D. L. (2016). Computational micromechanics of fatigue of microstructures in the HCF–VHCF regimes. International Journal of Fatigue, 93:387–396.

[CEA, 2000] CEA (2000). Online castem notice. http://www-cast3m.cea.fr/.

[Černý and Pokluda, 2009] Černý, M. and Pokluda, J. (2009). The theoretical tensile strength of fcc crystals predicted from shear strength calculations. J. Phys.: Condens. Matter, 21(14):145406.

[Chan, 2010] Chan, K. S. (2010). Roles of microstructure in fatigue crack initiation. International Journal of Fatigue, 32(9):1428–1447.

[Chan et al., 2009] Chan, K. S., Tian, J. W., Yang, B., and Liaw, P. K. (2009). Evolution of Slip Morphology and Fatigue Crack Initiation in Surface Grains of Ni200. Metall Mater Trans A, 40(11):2545–2556.

[Chang and Fang, 2003] Chang, W.-J. and Fang, T.-H. (2003). Influence of temperature on tensile and fatigue behavior of nanoscale copper using molecular dynamics simulation. Journal of Physics and Chemistry of Solids, 64(8):1279–1283.

[Chen et al., 2019] Chen, D., Costello, L. L., Geller, C. B., Zhu, T., and McDowell, D. L. (2019). Atomistic modeling of dislocation cross-slip in nickel using free-end nudged elastic band method. Acta Materialia, 168:436–447.

[Cheng and Laird, 1981] Cheng, A. S. and Laird, C. (1981). The high cycle fatigue life of copper single crystals tested under plastic-strain-controlled conditions. Materials Science and Engineering, 51(1):55–60.

[Cheng and Laird, 1983] Cheng, A. S. and Laird, C. (1983). The transition from stage I to stage II fatigue crack propagation in copper single crystals cycled at constant strain amplitudes. Materials Science and Engineering, 60(2):177–183.

[Chowdhury et al., 2013] Chowdhury, P. B., Sehitoglu, H., Rateick, R. G., and Maier, H. J. (2013). Modeling fatigue crack growth resistance of nanocrystalline alloys. Acta Materialia, 61(7):2531–2547.

[Čížek et al., 2019] Čížek, J., Janeček, M., Vlasák, T., Smola, B., Melikhova, O., Islamgaliev, R. K., and Dobatkin, S. V. (2019). The Development of Vacancies during Severe Plastic Deformation. Mater. Trans., 60(8):1533–1542.

[Cockayne et al., 1971] Cockayne, D. J. H., Jenkins, M. L., and Ray, I. L. F. (1971). The measurement of stacking-fault energies of pure face-centred cubic metals. The Philosophical Magazine: A Journal of Theoretical Experimental and Applied Physics, 24(192):1383–1392.

[Cotterill and Knott, 1992] Cotterill, P. J. and Knott, J. F. (1992). Effects of temperature and environment on fatigue crack growth mechanisms in a 9% Cr 1% Mo steel. Acta Metallurgica et Materialia, 40(10):2753–2764.

[Crone and Shield, 2001] Crone, W. C. and Shield, T. W. (2001). Experimental study of the deformation near a notch tip in copper and copper–beryllium single crystals. Journal of the Mechanics and Physics of Solids, 49(12):2819–2838.

[Crone and Shield, 2003] Crone, W. C. and Shield, T. W. (2003). An experimental study of the effect of hardening on plastic deformation at notch tips in metallic single crystals. Journal of the Mechanics and Physics of Solids, 51(8):1623–1647.

[Crone et al., 2004] Crone, W. C., Shield, T. W., Creuziger, A., and Henneman, B. (2004). Orientation dependence of the plastic slip near notches in ductile FCC single crystals. Journal of the Mechanics and Physics of Solids, 52(1):85–112.

[Davidson and Lankford, 1981] Davidson, D. L. and Lankford, J. (1981). The effect of water vapor on fatigue crack tip stress and strain range distribution and the energy required for crack propagation in low-carbon steel. Int J Fract, 17(3):257–275.

[Davidson and Lankford, 1983] Davidson, D. L. and Lankford, J. (1983). The Effect of Water Vapor on Fatigue Crack Tip Mechanics in 7075-T651 Aluminum Alloy. Fatigue Fract. Eng. Mater. Struct., 6(3):241–256.

[Daw and Baskes, 1983] Daw, M. S. and Baskes, M. I. (1983). Semiempirical, Quantum Mechanical Calculation of Hydrogen Embrittlement in Metals. Physical Review Letters, 50(17):1285–1288.

[Depres et al., 2015] Depres, C., Robertson, C., and Fivel, M. (2015). 3D Discrete Dislocation Dynamics Investigations of Fatigue Crack Initiation and Propagation. AerospaceLab Journal, Issue 9.

[Deshpande et al., 2002] Deshpande, V. S., Needleman, A., and Van der Giessen, E. (2002). Discrete dislocation modeling of fatigue crack propagation. Acta Materialia, 50(4):831–846.

[Devaux et al., 1997] Devaux, J., Gologanu, M., Leblond, J. B., and Perrin, G. (1997). On Continued Void Growth in Ductile Metals Subjected to Cyclic Loadings. In Willis, J. R., editor, IUTAM Symposium on Nonlinear Analysis of Fracture, Solid Mechanics and its Applications, pages 299–310, Dordrecht. Springer Netherlands.

[Dewald et al., 1990] Dewald, D. K., Lee, T. C., Robertson, I. M., and Birnbaum, H. K. (1990). Dislocation structures ahead of advancing cracks. MTA, 21(9):2411–2417.

[Differt et al., 1986] Differt, K., Esmann, U., and Mughrabi, H. (1986). A model of extrusions and intrusions in fatigued metals II. Surface roughening by random irreversible slip. Philosophical Magazine A, 54(2):237–258. Publisher: Taylor & Francis.

[Déprés, 2004] Déprés, C. (2004). Modelisation physique des stades précurseurs de l'endommagement en fatigue dans l'acier inoxydable austenitique 316l. These de doctorat de l'insititut national polytechnique de Grenoble, page 200.

[Déprés et al., 2004] Déprés, C., Robertson, C. F., and Fivel, M. C. (2004). Crack initiation in fatigue: experiments and three-dimensional dislocation simulations. Materials Science and Engineering: A, 387-389:288–291.

[Déprés et al., 2006] Déprés, C., Robertson, C. F., and Fivel, M. C. (2006). Low-strain fatigue in 316L steel surface grains: a three dimension discrete dislocation dynamics modelling of the early cycles. Part 2: Persistent slip markings and micro-crack nucleation. Philosophical Magazine, 86(1):79–97.

[Elber, 1970] Elber, W. (1970). Fatigue crack closure under cyclic tension. Engineering Fracture Mechanics, 2(1):37–45.

[English and Chin, 1965] English, A. T. and Chin, G. Y. (1965). On the variation of wire texture with stacking fault energy in f.c.c. metals and alloys. Acta Metallurgica, 13(9):1013–1016.

[Eshelby et al., 1951] Eshelby, J. D., Frank, F. C., and Nabarro, F. R. N. (1951). XLI. The equilibrium of linear arrays of dislocations. Lond. Edinb. Dublin Philos. Mag. J. Sci., 42(327):351–364.

[Essmann et al., 1981] Essmann, U., Gösele, U., and Mughrabi, H. (1981). A model of extrusions and intrusions in fatigued metals I. Point-defect production and the growth of extrusions. Philosophical Magazine A, 44(2):405–426.

[Essmann and Mughrabi, 1979] Essmann, U. and Mughrabi, H. (1979). Annihilation of dislocations during tensile and cyclic deformation and limits of dislocation densities. Philosophical Magazine A, 40(6):731–756.

[Ewing and Humfrey, 1903] Ewing, J. A. and Humfrey, J. C. W. (1903). VI. The fracture of metals under repeated alternations of stress. Philosophical Transactions of the Royal Society of London. Series A, Containing Papers of a Mathematical or Physical Character, 200(321-330):241–250.

[Faken and Jónsson, 1994] Faken, D. and Jónsson, H. (1994). Systematic analysis of local atomic structure combined with 3D computer graphics. Computational Materials Science, 2(2):279–286.

[Fan, 2016] Fan, Z. (2016). Atomistic simulation of fatigue in face centred cubic metals. phdthesis, Université Paris Saclay (COmUE).

[Fan et al., 2017] Fan, Z., Duparc, O. H., Sauzay, M., Diawara, B., and van Duin, A. C. T. (2017). Molecular dynamics simulations of surface oxidation and of surface slip irreversibility under fatigue in oxygen environment. Journal of Materials Research, 32(23):4327–4341.

[Fan et al., 2016] Fan, Z., Hardouin Duparc, O., and Sauzay, M. (2016). Molecular dynamics simulation of surface step reconstruction and irreversibility under cyclic loading. Acta Materialia, 102:149–161.

[Farkas et al., 2005] Farkas, D., Willemann, M., and Hyde, B. (2005). Atomistic Mechanisms of Fatigue in Nanocrystalline Metals. Physical Review Letters, 94(16):165502.

[Favier et al., 2016] Favier, V., Blanche, A., Wang, C., Phung, N. L., Ranc, N., Wagner, D., Bathias, C., Chrysochoos, A., and Mughrabi, H. (2016). Very high cycle fatigue for single phase ductile materials: Comparison between α-iron, copper and α-brass polycrystals. International Journal of Fatigue, 93:326–338.

[Finney and Laird, 1975] Finney, J. M. and Laird, C. (1975). Strain localization in cyclic deformation of copper single crystals. Philos. Mag. J. Theor. Exp. Appl. Phys., 31(2):339–366. _eprint: https://doi.org/10.1080/14786437508228937.

[Finney and Laird, 1982] Finney, J. M. and Laird, C. (1982). The development of slip offsets within persistent slip bands during a single fatigue cycle. Materials Science and Engineering, 54(1):137–141.

[Flouriot et al., 2003] Flouriot, S., Forest, S., Cailletaud, G., Köster, A., Rémy, L., Burgardt, B., Gros, V., Mosset, S., and Delautre, J. (2003). Strain localization at the crack tip in single crystal CT specimens under monotonous loading: 3D Finite Element analyses and application to nickel-base superalloys. International Journal of Fracture, 124(1):43–77.

[Forsyth and Ryder, 1961] Forsyth, P. and Ryder, D. (1961). Some results of the examination of aluminium alloy specimen fracture surfaces. Metallurgia, 63:117–124.

[Forsyth, 1953] Forsyth, P. J. E. (1953). Exudation of Material from Slip Bands at the Surface of Fatigued Crystals of an Aluminium–Copper Alloy. Nature, 171(4343):172–173.

[Fortes and Ralph, 1970] Fortes, M. A. and Ralph, B. (1970). Deformation twinning and double twinning in iridium. Journal of the Less Common Metals, 22(2):201–208.

[Frost et al., 1971] Frost, N. E., Pook, L. P., and Denton, K. (1971). A fracture mechanics analysis of fatigue crack growth data for various materials. Engineering Fracture Mechanics, 3(2):109–126.

[Gallagher, 1970] Gallagher, P. C. J. (1970). The influence of alloying, temperature, and related effects on the stacking fault energy. Metallurgical Transactions, 1(9):2429–2461.

[Guo et al., 2014] Guo, Y., Britton, T. B., and Wilkinson, A. J. (2014). Slip band–grain boundary interactions in commercial-purity titanium. Acta Materialia, 76:1–12.

[Gupta, 1993] Gupta, V. (1993). Tensile crack-tip fields in elastic-ideally plastic hexagonal crystals and layered materials. Acta Metallurgica et Materialia, 41(11):3223–3236.

[Hahn and Duquette, 1978] Hahn, H. N. and Duquette, D. J. (1978). The effect of surface dissolution on fatigue deformation and crack nucleation in copper and copper 8% aluminum single crystals. Acta Metallurgica, 26(2):279–287.

[Hazan, 2019] Hazan, J. (2019). Etude de la durée de vie et de l'endommagement intergranulaire par fatigue des métaux cubiques à faces centrées: influence de la taille des grains et de l'épaisseur d'éprouvette. These de doctorat de Sorbonne Université.

[Heinz and Neumann, 1990] Heinz, A. and Neumann, P. (1990). Crack initiation during high cycle fatigue of an austenitic steel. Acta Metallurgica et Materialia, 38(10):1933–1940.

[Hénaff et al., 2007] Hénaff, G., Odemer, G., and Tonneau-Morel, A. (2007). Environmentally-assisted fatigue crack growth mechanisms in advanced materials for aerospace applications. International Journal of Fatigue, 29(9):1927–1940.

[Hirth and Lothe, 1982] Hirth, J. P. and Lothe, J. (1982). Theory of dislocations. Wiley, New York. OCLC: 7875656.

[Hirth and Lothe, 1992] Hirth, J. P. and Lothe, J. (1992). Theory of Dislocations. Krieger Pub. Co, Malabar, FL, 2nd ed edition.

[Hollmann et al., 2000] Hollmann, M., Bretschneider, J., and Holste, C. (2000). Dislocation Structure and Strain Localisation in Nickel Single Crystals Cyclically Deformed at 77 K. Cryst. Res. Technol., 35(4):479–492.

[Holste, 2004] Holste, C. (2004). Cyclic plasticity of nickel, from single crystals to submicrocrystalline polycrystals. Philosophical Magazine, 84:299–315.

[Holste and Schwab, 2006] Holste, C. and Schwab, A. (2006). Cyclic plasticity of soft oriented NiAl single crystals at 600K. Materials Science and Engineering: A, 418(1):1–10.

[Holzwarth and Essmann, 1994] Holzwarth, U. and Essmann, U. (1994). Temperature-induced rearrangement of the dislocation pattern of Persistent Slip Bands in copper single crystals. Appl. Phys. A, 58(3):197–210.

[Horstemeyer et al., 2001] Horstemeyer, M. F., Baskes, M. I., and Plimpton, S. J. (2001). Computational nanoscale plasticity simulations using embedded atom potentials. Theoretical and Applied Fracture Mechanics, 37(1):49–98.

[Horstemeyer et al., 2010] Horstemeyer, M. F., Farkas, D., Kim, S., Tang, T., and Potirniche, G. (2010). Nanostructurally small cracks (NSC): A review on atomistic modeling of fatigue. International Journal of Fatigue, 32(9):1473–1502.

[Hua et al., 1985] Hua, G., Alagok, N., Brown, M. W., and Miller, K. J. (1985). Growth of Fatigue Cracks Under Combined Mode I and Mode II Loads. Multiaxial Fatigue.

[Hull and Bacon, 2001] Hull, D. and Bacon, D. (2001). Introduction to Dislocations. Elsevier Science.

[Hull and Bacon, 2011] Hull, D. and Bacon, D. (2011). Chapter 7 - Jogs and the Intersection of Dislocations. In Hull, D. and Bacon, D., editors, Introduction to Dislocations (Fifth Edition), pages 137–155. Butterworth-Heinemann, Oxford, fifth edition edition.

[Hunsche and Neumann, 1986] Hunsche, A. and Neumann, P. (1986). Quantitative measurement of persistent slip band profiles and crack initiation. Acta Metallurgica, 34(2):207–217.

[Huntington, 1958] Huntington, H. B. (1958). The Elastic Constants of Crystals. In Seitz, F. and Turnbull, D., editors, Solid State Physics, volume 7, pages 213–351. Academic Press.

[Hutar and Sauzay, 2006] Hutar, P. and Sauzay, M. (2006). Simulation of Fatigue Crack Growth by Crack Tip Blunting. In Gdoutos, E. E., editor, Fracture of Nano and Engineering Materials and Structures, pages 147–148, Dordrecht. Springer Netherlands.

[Hénaff et al., 2002] Hénaff, G., Mabru, C., Tonneau, A., and Petit, J. (2002). Influence of temperature on fatigue crack propagation micromechanisms in TiAl alloys. In Rémy, L. and Petit, J., editors, European Structural Integrity Society, volume 29 of Temperature-fatigue Interaction, pages 277–286. Elsevier.

[Hénaff and Tonneau, 2001] Hénaff, G. and Tonneau, A. (2001). Environment-sensitive fracture of iron aluminides under monotonic tensile loading. Metallurgical and Materials Transactions A, 32(3):557–567.

[Hénaff et al., 2001] Hénaff, G., Tonneau, A., and Mabru, C. (2001). In Structural Intermetallics, 2001. Minerals, Metals & Materials Society.

[Irwin, 1957] Irwin, G. R. (1957). Analysis of stresses and strains near the end of a crack traversing a plate. Journal of Applied Mechanics.

[Ishii and Weertman, 1971a] Ishii, H. and Weertman, J. (1971a). Fatigue crack propagation in copper and Cu-Al single crystals. Metall and Materi Trans B, 2(12):3441–3452.

[Ishii and Weertman, 1971b] Ishii, H. and Weertman, J. (1971b). Fatigue crack propagation in copper and cual single crystals. Metallurgical and Materials Transactions B, 2(12):3441–3452.

[Kaplan, 1967] Kaplan, H. I. (1967). On the mechanism of stage I crack propagation in fatigue. Trans Met Soc AIME, 239:1017–1025.

[Katagiri et al., 1977] Katagiri, K., Omura, A., Koyanagi, K., Awatani, J., Shiraishi, T., and Kaneshiro, H. (1977). Early stage crack tip dislocation morphology in fatigued copper. Metall Mater Trans A, 8(11):1769–1773.

[Kikukawa et al., 1979] Kikukawa, M., Jono, M., and Adachi, M. (1979). Direct Observation and Mechanism of Fatigue Crack Propagation. Fatigue Mechanisms.

[Kim et al., 1991] Kim, G.-H., Kwon, I.-B., and Fine, M. E. (1991). The influence of loading methods on fatigue crack initiation in polycrystalline copper at ambient temperature. Materials Science and Engineering: A, 142(2):177–182.

[Kiritani et al., 1999] Kiritani, M., Satoh, Y., Kizuka, Y., Arakawa, K., Ogasawara, Y., Arai, S., and Shimomura, Y. (1999). Anomalous production of vacancy clusters and the possibility of plastic deformation of crystalline metals without dislocations. Philos. Mag. Lett., 79(10):797–804. _eprint: https://doi.org/10.1080/095008399176616.

[Kitagawa et al., 1985] Kitagawa, H., Yuuki, R., Tohgo, K., and Tanabe, M. (1985). ΔK-Dependency of Fatigue Growth of Single and Mixed Mode Cracks Under Biaxial Stress. Multiaxial Fatigue.

[Kittel, 2004] Kittel, C. (2004). Introduction to Solid State Physics. John Wiley & Sons, Hoboken, NJ, 8th edition edition.

[Knap and Sieradzki, 1999] Knap, J. and Sieradzki, K. (1999). Crack Tip Dislocation Nucleation in FCC Solids. Physical Review Letters, 82(8):1700–1703.

[Knowles, 2017] Knowles, K. M. (2017). The Plane Strain Young's Modulus in Cubic Materials. J Elast, 128(2):147–173.

[Kobayashi and Hiki, 1973] Kobayashi, H. and Hiki, Y. (1973). Anharmonicity in Noble Metals; Nonlinear Elasticity in Whiskers. Phys. Rev. B, 7(2):594–601.

[Komanduri et al., 2001] Komanduri, R., Chandrasekaran, N., and Raff, L. M. (2001). Molecular dynamics (MD) simulation of uniaxial tension of some single-crystal cubic metals at nanolevel. International Journal of Mechanical Sciences, 43(10):2237–2260.

[Kwon et al., 1989a] Kwon, I. B., Fine, M. E., and Weertman, J. (1989a). Fatigue damage in copper single crystals at room and cryogenic temperatures. Acta Metallurgica, 37(11):2937–2946.

[Kwon et al., 1989b] Kwon, I. B., Fine, M. E., and Weertman, J. (1989b). Microstructural studies on the initiation and growth of small fatigue cracks at 298, 77 and 4.2 K in polycrystalline copper. Acta Metallurgica, 37(11):2927–2936.

[Kysar and Briant, 2002] Kysar, J. W. and Briant, C. L. (2002). Crack tip deformation fields in ductile single crystals. Acta Materialia, 50(9):2367–2380.

[Lacroix et al., 2016] Lacroix, R., Leblond, J.-B., and Perrin, G. (2016). Numerical study and theoretical modelling of void growth in porous ductile materials subjected to cyclic loadings. European Journal of Mechanics - A/Solids, 55:100–109.

[Laird, 1967a] Laird, C. (1967a). in fatigue crack propagation. American Society for Testing and Materials.

[Laird, 1967b] Laird, C. (1967b). The Influence of Metallurgical Structure on the Mechanisms of Fatigue Crack Propagation. Fatigue Crack Propag.

[Laird and Smith, 1962] Laird, C. and Smith, G. C. (1962). Crack Propagation in High Stress Fatigue. Philosophical Magazine, 7(77):847–857.

[Lankford et al., 1983] Lankford, J., Davidson, D., Morris, W., and Wei, R., editors (1983). Fatigue Mechanisms: Advances in Quantitative Measurement of Physical Damage. ASTM International, 100 Barr Harbor Drive, PO Box C700, West Conshohocken, PA 19428-2959.

[Lankford and Davidson, 1983] Lankford, J. and Davidson, D. L. (1983). Fatigue crack micromechanisms in ingot and powder metallurgy 7xxx aluminum alloys in air and vacuum. Acta Metallurgica, 31(8):1273–1284.

[Laufer and Roberts, 1966] Laufer, E. E. and Roberts, W. N. (1966). Dislocations and persistent slip bands in fatigued copper. The Philosophical Magazine: A Journal of Theoretical Experimental and Applied Physics, 14(127):65–78.

[Li et al., 2013] Li, L. L., Zhang, P., Zhang, Z. J., and Zhang, Z. F. (2013). Effect of crystallographic orientation and grain boundary character on fatigue cracking behaviors of coaxial copper bicrystals. Acta Materialia, 61(2):425–438.

[Li et al., 2011] Li, P., Li, S. X., Wang, Z. G., and Zhang, Z. F. (2011). Fundamental factors on formation mechanism of dislocation arrangements in cyclically deformed fcc single crystals. Progress in Materials Science, 56(3):328–377.

[Li et al., 2009] Li, P., Zhang, Z. F., Li, X. W., Li, S. X., and Wang, Z. G. (2009). Effect of orientation on the cyclic deformation behavior of silver single crystals: Comparison with the behavior of copper and nickel single crystals. Acta Materialia, 57(16):4845–4854.

[Lindley and Richards, 1974] Lindley, T. C. and Richards, C. E. (1974). The relevance of crack closure to fatigue crack propagation. Materials Science and Engineering, 14(3):281–293.

[Liu et al., 1994] Liu, C. D., Bassim, M. N., and You, D. X. (1994). Dislocation structures in fatigued polycrystalline copper. Acta Metallurgica et Materialia, 42(11):3695–3704.

[Liu and Kim, 1992] Liu, C. T. and Kim, Y. W. (1992). Room temperature environment embrittlement in a tial alloy. Scripta Metallurgica and Materialia, 27(5):5.

[Liu et al., 1989] Liu, C. T., McKamey, C. G., and Lee, E. H. (1989). Environment effects on room temperature ductility and fracture in fe3al. Scripta Metallurgica and Materialia, 24(2):5.

[Liu, 2013] Liu, J. (2013). Prédictions multiéchelles de l'initiation des microfissures de fatigue. These de doctorat de l'Université Pierre et Marie Curie.

[Liu and Zhou, 2018] Liu, Y. and Zhou, J. (2018). The fatigue crack growth in hierarchically nano-twinned materials. Engineering Fracture Mechanics, 204:63–71.

[Loretto et al., 1965] Loretto, M. H., Clarebrough, L. M., and Segall, R. L. (1965). Stacking-fault tetrahedra in deformed face-centred cubic metals. The Philosophical Magazine: A Journal of Theoretical Experimental and Applied Physics, 11(111):459–465.

[Lukáš et al., 1968] Lukáš, P., Klesnil, M., and Krejčí, J. (1968). Dislocations and Persistent Slip Bands in Copper Single Crystals Fatigued at Low Stress Amplitude. Phys. Status Solidi B, 27(2):545–558.

[Lukáš and Klesnil, 1971] Lukáš, P. and Klesnil, M. (1971). Dislocation structures in fatigued single crystals of Cu-Zn system. physica status solidi (a), 5(1):247–258.

[Ma and Laird, 1989] Ma, B. and Laird, C. (1989). Overview of fatigue behavior in copper single crystals—I. Surface morphology and stage I crack initiation sites for tests at constant strain amplitude. Acta Metallurgica, 37(2):325–336.

[Ma, 2006] Ma, J. (2006). Nanoscale study of cyclic deformation behaviour and mechanism of annealing twin. Materials Science and Engineering: A, 427(1):282–288.

[Ma, 2007] Ma, J. (2007). AFM study of the morphology and micro-strain of slip bands in twin under cyclic deformation. Materials Science and Engineering: A, 457(1):63–68.

[Ma et al., 2014] Ma, L., Xiao, S., Deng, H., and Hu, W. (2014). Molecular dynamics simulation of fatigue crack propagation in bcc iron under cyclic loading. International Journal of Fatigue, 68:253–259.

[Macmillan, 1983] Macmillan, N. H. (1983). The Ideal Strength of Solids. In Latanision, R. M. and Pickens, J. R., editors, Atomistics of Fracture, pages 95–165. Springer US, Boston, MA.

[Maillot, 2003] Maillot, V. (2003). Amorçage et propagation de fissures de fatigue thermique dans un acier inoxydable austénitique de type X2 CrNi18-09 (AISI 304L). Thèse de doctorat de l'université de Lille, page 238.

[Man et al., 2009a] Man, J., Klapetek, P., Man, O., Weidner†, A., Obrtlík, K., and Polák, J. (2009a). Extrusions and intrusions in fatigued metals. Part 2. AFM and EBSD study of the early growth of extrusions and intrusions in 316L steel fatigued at room temperature. Philosophical Magazine, 89(16):1337–1372.

[Man et al., 2002] Man, J., Obrtlík, K., Blochwitz, C., and Polák, J. (2002). Atomic force microscopy of surface relief in individual grains of fatigued 316L austenitic stainless steel. Acta Materialia, 50(15):3767–3780.

[Man et al., 2003] Man, J., Obrtlík, K., and Polák, J. (2003). Study of surface relief evolution in fatigued 316L austenitic stainless steel by AFM. Materials Science and Engineering: A, 351(1):123–132.

[Man et al., 2009b] Man, J., Obrtlík, K., and Polák, J. (2009b). Extrusions and intrusions in fatigued metals. Part 1. State of the art and history. Philos. Mag., 89(16):1295–1336. _eprint: https://doi.org/10.1080/14786430902917616.

[Man et al., 2012] Man, J., Vystavěl, T., Weidner, A., Kuběna, I., Petrenec, M., Kruml, T., and Polák, J. (2012). Study of cyclic strain localization and fatigue crack initiation using FIB technique. International Journal of Fatigue, 39:44–53.

[Mao et al., 2018] Mao, J., Hu, D., Meng, F., Zhou, X., Song, J., and Wang, R. (2018). Multiscale modeling of transgranular short crack growth during fatigue in polycrystalline metals. International Journal of Fatigue, 116:648–658.

[Matsukawa et al., 2003a] Matsukawa, Y., Yasunaga, K., Komatsu, M., and Kiritani, M. (2003a). Dynamic observation of dislocation-free deformation process in al, cu, and ni thin foils. Materials Science and Engineering: A, 350(1):17 – 24. Symposium on High-Speed Plastic Deformation.

[Matsukawa et al., 2003b] Matsukawa, Y., Yasunaga, K., Komatsu, M., and Kiritani, M. (2003b). Dynamic observation of dislocation-free deformation process in Al, Cu, and Ni thin foils. Materials Science and Engineering: A, 350(1):17–24.

[McClintock and Argon, 1966] McClintock, F. A. and Argon, A. S. (1966). Mechanical behavior of materials. Addison-Wesley Pub. Co., Reading, Mass. OCLC: 577589.

[McDowell and Dunne, 2010] McDowell, D. L. and Dunne, F. P. E. (2010). Microstructure-sensitive computational modeling of fatigue crack formation. International Journal of Fatigue, 32(9):1521–1542.

[McEvily and Boettner, 1963a] McEvily, A. and Boettner, R. (1963a). On fatigue crack propagation in f.c.c. metals. Acta Metallurgica, 11(7):725 – 743. Mechanisms of fatigue in crystalline solids.

[McEvily, 1977] McEvily, A. J. (1977). Current aspects of fatigue. Metal Science, 11(8-9):274–284.

[McEvily and Boettner, 1963b] McEvily, A. J. and Boettner, R. G. (1963b). On fatigue crack propagation in F.C.C. metals. Acta Metallurgica, 11(7):725–743.

[McEvily and Johnston, 1967] McEvily, A. J. and Johnston, T. L. (1967). The role of cross-slip in brittle fracture and fatigue. Int J Fract, 3(1):45–74.

[McEvily and Velasquez, 1992] McEvily, A. J. and Velasquez, G. (1992). Fatigue crack tip deformation processes as influenced by the environment. Metall. Trans. Phys. Metall. Mater. Sci., pages 2211–2221.

[Mecke and Blochwitz, 1982] Mecke, K. and Blochwitz, C. (1982). Saturation Dislocation Structures in Cyclically Deformed Nickel Single Crystals of Different Orientations. Cryst. Res. Technol., 17(6):743–758.

[Mendelev et al., 2008] Mendelev, M. I., Kramer, M. J., Becker, C. A., and Asta, M. (2008). Analysis of semi-empirical interatomic potentials appropriate for simulation of crystalline and liquid Al and Cu. Philosophical Magazine, 88(12):1723–1750.

[Mendelev et al., 2012] Mendelev, M. I., Kramer, M. J., Hao, S. G., Ho, K. M., and Wang, C. Z. (2012). Development of interatomic potentials appropriate for simulation of liquid and glass properties of NiZr2 alloy. Philosophical Magazine, 92(35):4454–4469.

[Meyn, 1968] Meyn, D. A. (1968). The nature of fatigue crack propagation in air and in vacuum for 2024 aluminium. Trans. ASM.

[Miao et al., 2012] Miao, J., Pollock, T. M., and Wayne Jones, J. (2012). Microstructural extremes and the transition from fatigue crack initiation to small crack growth in a polycrystalline nickel-base superalloy. Acta Materialia, 60(6):2840–2854.

[Miller, 1966] Miller, G. (1966). Fatigue-crack growth in some copper-base alloys. PhD Thesis, Massachusetts Institute of Technology.

[Miller et al., 1966] Miller, G., Avery, D., and Backofen, W. (1966). Fatigue-crack growth in some copper-base alloys. Transactions of the metallurgical society of AIME, 236.

[Mineur et al., 2000] Mineur, M., Villechaise, P., and Mendez, J. (2000). Influence of the crystalline texture on the fatigue behavior of a 316L austenitic stainless steel. Materials Science and Engineering: A, 286(2):257–268.

[Mishin, 2004] Mishin, Y. (2004). Atomistic modeling of the γ and Γ'-phases of the Ni–Al system. Acta Materialia, 52(6):1451–1467.

[Mishin et al., 1999] Mishin, Y., Farkas, D., Mehl, M. J., and Papaconstantopoulos, D. A. (1999). Interatomic potentials for monoatomic metals from experimental data and ab initio calculations. Physical Review B, 59(5):3393–3407.

[Mishin et al., 2001] Mishin, Y., Mehl, M. J., Papaconstantopoulos, D. A., Voter, A. F., and Kress, J. D. (2001). Structural stability and lattice defects in copper: Ab initio, tight-binding, and embedded-atom calculations. Physical Review B, 63(22):224106.

[Monchiet and Kondo, 2013] Monchiet, V. and Kondo, D. (2013). Combined voids size and shape effects on the macroscopic criterion of ductile nanoporous materials. International Journal of Plasticity, 43:20–41.

[Morin and Michel, 2018] Morin, L. and Michel, J.-C. (2018). Void coalescence in porous ductile solids containing two populations of cavities. European Journal of Mechanics - A/Solids, 72:341–353. Publisher: Elsevier.

[Mughrabi, 1999] Mughrabi (1999). On the life-controlling microstructural fatigue mechanisms in ductile metals and alloys in the gigacycle regime. Fatigue & Fracture of Engineering Materials & Structures, 22(7):633–641.

[Mughrabi, 1978] Mughrabi, H. (1978). The cyclic hardening and saturation behaviour of copper single crystals. Materials Science and Engineering, 33(2):207–223.

[Mughrabi, 1979] Mughrabi, H. (1979). Plateaus in the cyclic stress-strain curves of single- and polycrystalline metals. Scripta Metallurgica, 13(6):479–484.

[Mughrabi, 1984] Mughrabi, H. (1984). Dislocations and properties of real materials. In proceedings of the conference to celebrate the fiftieth anniversary of the concept of dislocation in crystals, Institute of metals, pages 244–304.

[Mughrabi, 1985] Mughrabi, H. (1985). Dislocations and properties of real materials: Proc. of the conference to celebrate the 50. anniversary of the concept of dislocation in crystals ... held in London on 11 - 12 December 1984. London. Inst. of Metals.

[Mughrabi, 1988] Mughrabi, H. (1988). Cycle stress strain response and high cycle fatigue behaviour of copper polycrystals. In Proceedings of the International Colloquium "Basic mechanisms in fatigue of metals".

[Mughrabi, 2006] Mughrabi, H. (2006). Specific features and mechanisms of fatigue in the ultrahigh-cycle regime. International Journal of Fatigue, 28(11):1501–1508.

[Mughrabi, 2009] Mughrabi, H. (2009). Cyclic Slip Irreversibilities and the Evolution of Fatigue Damage. Metall and Mat Trans A, 40(6):1257–1279.

[Mughrabi et al., 1983] Mughrabi, H., Wang, R., Differt, K., and Essmann, U. (1983). Fatigue Crack Initiation by Cyclic Slip Irreversibilities in High-Cycle Fatigue. Fatigue Mechanisms: Advances in Quantitative Measurement of Physical Damage. Publisher: ASTM International.

[Murr, 1973] Murr, L. (1973). Twin boundary energetics in pure aluminium. Acta Metallurgica, 21(6):791–797.

[Murr, 1975] Murr, L. E. (1975). Interfacial Phenomena in Metals and Alloys. Addison-Wesley Educational Publishers Inc, Reading, Mass.

[Neumann, 1974] Neumann, P. (1974). New experiments concerning the slip processes at propagating fatigue cracks—I. Acta Metallurgica, 22(9):1155–1165.

[Neumann, 1999] Neumann, P. (1999). Analytical solution for the incompatibility stresses at twin boundaries in cubic crystals. In Proc of the seventh international fatigue congress (FATIGUE '99), volume 1/4, pages 107–114.

[Neumann and Tönnessen, 1987] Neumann, P. and Tönnessen, A. (1987). Cyclic deformation and crack initiation. In Proc third int conf on fatigue and fatigue thresholds (FATIGUE '87), volume 1, pages 3–22.

[Neumann et al., 1978] Neumann, P., Vehoff, H., and Fuhlrott, H. (1978). On the mechanisms of fatigue crack growth. In Taplin, D. M. R., editor, Advances in Research on the Strength and Fracture of Materials, pages 1313–1324. Pergamon, Amsterdam.

[Newmann Jr, 1983] Newmann Jr, J. C. (1983). A nonlinear fracture mechanics approach to the growth of small cracks. In Behaviour of Short Cracks in Airframe Components, Neuilly-sur-Seine,France.

[Nishimura and Miyazaki, 2004] Nishimura, K. and Miyazaki, N. (2004). Molecular dynamics simulation of crack growth under cyclic loading. Computational Materials Science, 31(3):269–278.

[Obrtlík et al., 1997] Obrtlík, K., Man, J., and Polák, J. (1997). Orientation dependence of surface relief topography in fatigued copper single crystals. Materials Science and Engineering: A, 234-236:727–730.

[Osterstock, 2013] Osterstock, S. (2013). Vers la prédiction de l'apparition de réseaux de fissures : influence des paramètres microtructuraux sur la dispersion à l'amorçage. Thèse de doctorat de l'université de Lille, page 227.

[Otsuka et al., 1975] Otsuka, A., Mori, K., and Miyata, T. (1975). The condition of fatigue crack growth in mixed mode condition. Engineering Fracture Mechanics, 7(3):429–439.

[Otsuka et al., 1981] Otsuka, A., Mori, K., Okshoma, T., and Tsuyama, S. (1981). Mode ii fatigue crack growth in aluminum alloys and mild steel. Proceedings of the 5th Int. Conf. Fract., pages 1851–1858.

[Pan, 1986] Pan, J. (1986). Plane-strain crack-tip stress field for anisotropic perfectly-plastic materials. Journal of the Mechanics and Physics of Solids, 34(6):617–635.

[Paris and Erdogan, 1963] Paris, P. and Erdogan, F. (1963). A Critical Analysis of Crack Propagation Laws. Journal of Basic Engineering, 85(4):528–533.

[Pelloux, 1970] Pelloux, R. M. N. (1970). Crack extension by alternating shear. Engineering Fracture Mechanics, 1(4):697–704.

[Petit et al., 2003] Petit, J., Hénaff, G., and Sarrazin-Baudoux, C. (2003). 6.05 - Environmentally Assisted Fatigue in the Gaseous Atmosphere. In Milne, I., Ritchie, R. O., and Karihaloo, B., editors, Comprehensive Structural Integrity, pages 211–280. Pergamon, Oxford.

[Petrenec et al., 2006] Petrenec, M., Polák, J., Obrtlík, K., and Man, J. (2006). Dislocation structures in cyclically strained X10CrAl24 ferritic steel. Acta Mater., 13(54):3429–3443.

[Pippan, 1991] Pippan, R. (1991). Threshold and effective threshold of fatigue crack propagation in ARMCO iron II: The influence of environment. Materials Science and Engineering: A, 138(1):15–22.

[Pippan et al., 2011] Pippan, R., Zelger, C., Gach, E., Bichler, C., and Weinhandl, H. (2011). On the mechanism of fatigue crack propagation in ductile metallic materials. Fatigue & Fracture of Engineering Materials & Structures, 34(1):1–16.

[Plimpton, 1995] Plimpton, S. (1995). Fast Parallel Algorithms for Short-Range Molecular Dynamics. Journal of Computational Physics, 117(1):1–19.

[Pokluda et al., 2015] Pokluda, J., Černý, M., Šob, M., and Umeno, Y. (2015). Ab initio calculations of mechanical properties: Methods and applications. Progress in Materials Science, 73:127–158.

[Polák, 1969] Polák, J. (1969). Electrical resistivity of cyclically deformed copper. Czech J Phys, 19(3):315–322.

[Polák, 1970] Polák, J. (1970). The effect of intermediate annealing on the electrical resistivity and shear stress of fatigued copper. Scripta Metallurgica, 4(10):761–764.

[Polák, 1987] Polák, J. (1987). On the role of point defects in fatigue crack initiation. Materials Science and Engineering, 92:71–80.

[Polák et al., 1985] Polák, J., Lepistö, T., and Kettunen, P. (1985). Surface topography and crack initiation in emerging persistent slip bands in copper single crystals. Materials Science and Engineering, 74(1):85–91.

[Polák et al., 2003] Polák, J., Man, J., and Obrtlík, K. (2003). AFM evidence of surface relief formation and models of fatigue crack nucleation. International Journal of Fatigue, 25(9):1027–1036.

[Polák et al., 2017] Polák, J., Mazánová, V., Heczko, M., Petráš, R., Kuběna, I., Casalena, L., and Man, J. (2017). The role of extrusions and intrusions in fatigue crack initiation. Engineering Fracture Mechanics, 185:46–60.

[Polák and Sauzay, 2009] Polák, J. and Sauzay, M. (2009). Growth of extrusions in localized cyclic plastic straining. Materials Science and Engineering: A, 500(1):122–129.

[Polák, 2020] Polák, J. (2020). Production, annihilation and migration of point defects in cyclic straining. Materialia, 14:100938.

[Polák et al., 2013] Polák, J., Kuběna, I., and Man, J. (2013). The shape of early persistent slip markings in fatigued 316L steel. Materials Science and Engineering: A, 564:8–12.

[Polák and Man, 2014a] Polák, J. and Man, J. (2014a). Fatigue crack initiation – The role of point defects. International Journal of Fatigue, 65:18–27.

[Polák and Man, 2014b] Polák, J. and Man, J. (2014b). Mechanisms of extrusion and intrusion formation in fatigued crystalline materials. Materials Science and Engineering: A, 596:15–24.

[Polák et al., 2009] Polák, J., Man, J., Vystavěl, T., and Petrenec, M. (2009). The shape of extrusions and intrusions and initiation of stage I fatigue cracks. Materials Science and Engineering: A, 517(1):204–211.

[Polák et al., 2017] Polák, J., Mazánová, V., Heczko, M., Kuběna, I., and Man, J. (2017). Profiles of persistent slip markings and internal structure of underlying persistent slip bands. Fatigue & Fracture of Engineering Materials & Structures, 40(7):1101–1116.

[Potirniche and Horstemeyer, 2006] Potirniche, G. P. and Horstemeyer, M. F. (2006). On the growth of nanoscale fatigue cracks. Philosophical Magazine Letters, 86(3):185–193.

[Potirniche et al., 2005] Potirniche, G. P., Horstemeyer, M. F., Jelinek, B., and Wagner, G. J. (2005). Fatigue damage in nickel and copper single crystals at nanoscale. International Journal of Fatigue, 27(10):1179–1185.

[Potirniche et al., 2006] Potirniche, G. P., Horstemeyer, M. F., Wagner, G. J., and Gullett, P. M. (2006). A molecular dynamics study of void growth and coalescence in single crystal nickel. International Journal of Plasticity, 22(2):257–278.

[Potirniche G.P et al., 2006] Potirniche G.P, Horstemeyer M.F, Gullett P.M, and Jelinek B (2006). Atomistic modelling of fatigue crack growth and dislocation structuring in FCC crystals. Proceedings of the Royal Society A: Mathematical, Physical and Engineering Sciences, 462(2076):3707–3731.

[Qian, 1995] Qian, C. F. (1995). On mixed-mode fatigue crack growth and dislocation emission from a Mode I crack. Ph.D. Thesis, Nanjing Institute of Chemical Technology.

[Qiu et al., 2018] Qiu, R.-Z., Lin, Y.-C., and Fang, T.-H. (2018). Fatigue crack growth characteristics of Fe and Ni under cyclic loading using a quasi-continuum method. Beilstein Journal of Nanotechnology, 9(1):1000–1014.

[Qu et al., 2008] Qu, S., Zhang, P., Wu, S. D., Zang, Q. S., and Zhang, Z. F. (2008). Twin boundaries: Strong or weak? Scripta Materialia, 59(10):1131–1134.

[Rasmussen and Pedersen, 1980] Rasmussen, K. V. and Pedersen, O. B. (1980). Fatigue of copper polycrystals at low plastic strain amplitudes. Acta Metallurgica, 28(11):1467–1478.

[Repetto and Ortiz, 1997] Repetto, E. A. and Ortiz, M. (1997). A micromechanical model of cyclic deformation and fatigue-crack nucleation in f.c.c. single crystals. Acta Materialia, 45(6):2577–2595.

[Rice, 1987] Rice, J. R. (1987). Tensile crack tip fields in elastic-ideally plastic crystals. Mechanics of Materials, 6(4):317–335.

[Rice, 1992] Rice, J. R. (1992). Dislocation nucleation from a crack tip: An analysis based on the Peierls concept. Journal of the Mechanics and Physics of Solids, 40(2):239–271.

[Rice and Beltz, 1994] Rice, J. R. and Beltz, G. E. (1994). The activation energy for dislocation nucleation at a crack. Journal of the Mechanics and Physics of Solids, 42(2):333–360.

[Rice and Thomson, 1974] Rice, J. R. and Thomson, R. (1974). Ductile versus brittle behaviour of crystals. The Philosophical Magazine: A Journal of Theoretical Experimental and Applied Physics, 29(1):73–97.

[Riemelmoser et al., 2001] Riemelmoser, F. O., Gumbsch, P., and Pippan, R. (2001). Dislocation Modelling of Fatigue Cracks: An Overview. Materials Transactions, 42(1):2–13.

[Riemelmoser et al., 1997] Riemelmoser, F. O., Pippan, R., and Stüwe, H. P. (1997). A comparison of a discrete dislocation model and a continuous description of cyclic crack tip plasticity. International Journal of Fracture, 85(2):157–168.

[Riemelmoser et al., 1998] Riemelmoser, F. O., Pippan, R., and Stüwe, H. P. (1998). An argument for a cycle-by-cycle propagation of fatigue cracks atsmall stress intensity ranges. Acta Materialia, 46(5):1793–1799.

[Rieux et al., 1979] Rieux, P., Driver, J., and Rieu, J. (1979). Fatigue crack propagation in austenitic and ferritic stainless steel single crystals. Acta Metallurgica, 27(1):145–153.

[Ritchie, 1999] Ritchie, R. (1999). Mechanisms of fatigue-crack propagation in ductile and brittle solids. International Journal of Fracture, 100(1):55–83.

[Roberts and Kibler, 1971] Roberts, R. and Kibler, J. J. (1971). Mode II Fatigue Crack Propagation. J. Basic Eng, 93(4):671–680.

[Rose et al., 1984] Rose, J. H., Smith, J. R., Guinea, F., and Ferrante, J. (1984). Universal features of the equation of state of metals. Physical Review B, 29(6):2963–2969. Publisher: American Physical Society.

[Rosenberger et al., 1997] Rosenberger, H., Worth, B. D., and Larsen, J. M. (1997). In Structural Intermetallics, 1997. Minerals, Metals & Materials Society.

[Sangid et al., 2011a] Sangid, M. D., Maier, H. J., and Sehitoglu, H. (2011a). A physically based fatigue model for prediction of crack initiation from persistent slip bands in polycrystals. Acta Materialia, 59(1):328–341.

[Sangid et al., 2011b] Sangid, M. D., Maier, H. J., and Sehitoglu, H. (2011b). The role of grain boundaries on fatigue crack initiation – An energy approach. International Journal of Plasticity, 27(5):801–821.

[Sarrazin et al., 1997] Sarrazin, C., Lesterlin, S., and Petit, J. (1997). In Piascik, R., Gangloff, R., and Saxena, A., editors, Elevated Temperature Effects on Fatigue and Fracture, 100 Barr Harbor Drive, PO Box C700, West Conshohocken, PA 19428-2959. ASTM International.

[Sarrazin-Baudoux et al., 2016] Sarrazin-Baudoux, C., Stanzl-Tschegg, S. E., Schönbauer, B. M., and Petit, J. (2016). Ultra-slow Fatigue Crack Propagation in Metallic Alloys. Procedia Engineering, 160:151–157.

[Sauzay, 2007] Sauzay, M. (2007). Cubic elasticity and stress distribution at the free surface of polycrystals. Acta Materialia, 55(4):1193–1202.

[Sauzay and Gilormini, 2002] Sauzay, M. and Gilormini, P. (2002). Influence of surface effects on fatigue of microcracks nucleation. Theoretical and Applied Fracture Mechanics, 38(1):53–62.

[Sauzay and Jourdan, 2006] Sauzay, M. and Jourdan, T. (2006). Polycrystalline microstructure, cubic elasticity, and nucleation of high-cycle fatigue cracks. Int J Fract, 141(3):431–446.

[Sauzay and Kubin, 2011] Sauzay, M. and Kubin, L. P. (2011). Scaling laws for dislocation microstructures in monotonic and cyclic deformation of fcc metals. Progress in Materials Science, 56(6):725–784.

[Sauzay and Liu, 2014] Sauzay, M. and Liu, J. (2014). Simulation of Surface Crack Initiation Induced by Slip Localization and Point Defect Kinetics. Conference Name: 11th International Fatigue Congress ISBN: 9783038350088 ISSN: 1662-8985 Pages: 542-548 Publisher: Trans Tech Publications Ltd Volume: 891-892.

[Sauzay and Moussa, 2013] Sauzay, M. and Moussa, M. O. (2013). Prediction of grain boundary stress fields and microcrack initiation induced by slip band impingement. International Journal of Fracture, 184(1):215–240.

[Sauzay and Vor, 2013] Sauzay, M. and Vor, K. (2013). Influence of plastic slip localization on grain boundary stress fields and microcrack nucleation. Engineering Fracture Mechanics, 110:330–349.

[Schaefer et al., 1987] Schaefer, H., Gugelmeier, R., and Schmolz, M.and Seeger, A. (1987). Materials science forum.

[Schmidt and Paris, 1973] Schmidt, R. and Paris, P. (1973). Threshold for Fatigue Crack Propagation and the Effects of Load Ratio and Frequency. Prog. Flaw Growth Fract. Toughness Test.

[Schönbauer and Stanzl-Tschegg, 2013] Schönbauer, B. M. and Stanzl-Tschegg, S. E. (2013). Influence of environment on the fatigue crack growth behaviour of 12% Cr steel. Ultrasonics, 53(8):1399–1405.

[Shield, 1996] Shield, T. W. (1996). An experimental study of the plastic strain fields near a notch tip in a copper single crystal during loading. Acta Materialia, 44(4):1547–1561.

[Sicaud, 2020] Sicaud, B. (2020). Multiscale simulation of intergranular fracture inititation in face-centered cubic metals and alloys: influence of localised slip deformation. Private communication.

[Sieradzki et al., 1988] Sieradzki, K., Dienes, G. J., Paskin, A., and Massoumzadeh, B. (1988). Atomistics of crack propagation. Acta Metallurgica, 36(3):651–663.

[Sih et al., 1965] Sih, G. C., Paris, P. C., and Irwin, G. R. (1965). On cracks in rectilinearly anisotropic bodies. International Journal of Fracture Mechanics, 1(3):189–203.

[Smith, 1984] Smith, M. C. (1984). Some aspects of Mode II fatigue crack growth. Ph.D. Thesis, Churchill College, university of Cambridge.

[Sriram et al., 1990] Sriram, T. S., Fine, M. E., and Chung, Y. W. (1990). STM and surface analytical study of the effect of environment on fatigue crack initiation in silver single crystals II: Effects of oxygen partial pressure. Scripta Metallurgica et Materialia, 24(2):279–284. Publisher: Pergamon.

[Stanzl-Tschegg et al., 2007] Stanzl-Tschegg, S., Mughrabi, H., and Schoenbauer, B. (2007). Life time and cyclic slip of copper in the VHCF regime. International Journal of Fatigue, 29(9):2050–2059.

[Stanzl-Tschegg and Schönbauer, 2010] Stanzl-Tschegg, S. and Schönbauer, B. (2010). Near-threshold fatigue crack propagation and internal cracks in steel. Procedia Engineering, 2(1):1547–1555.

[Stanzl-Tschegg and Mayer, 2001] Stanzl-Tschegg, S. E. and Mayer, H. (2001). Fatigue and fatigue crack growth of aluminium alloys at very high numbers of cycles. International Journal of Fatigue, 23:231–237.

[Stobbs and Sworn, 1971] Stobbs, W. M. and Sworn, C. H. (1971). The weak beam technique as applied to the determination of the stacking-fault energy of copper. The Philosophical Magazine: A Journal of Theoretical Experimental and Applied Physics, 24(192):1365–1381.

[Stoloff and Duquette, 1993] Stoloff, N. S. and Duquette, D. J. (1993). Moisture and hydrogen-induced embrittlement of iron aluminides. JOM, 45(12):30–35.

[Stopka and McDowell, 2020] Stopka, K. S. and McDowell, D. L. (2020). Microstructure-sensitive computational multiaxial fatigue of Al 7075-T6 and duplex Ti-6Al-4V. International Journal of Fatigue, 133:105460.

[Stukowski, 2009] Stukowski, A. (2009). Visualization and analysis of atomistic simulation data with OVITO–the Open Visualization Tool. Modelling and Simulation in Materials Science and Engineering, 18(1):015012.

[Stukowski and Albe, 2010] Stukowski, A. and Albe, K. (2010). Extracting dislocations and non-dislocation crystal defects from atomistic simulation data. Modelling and Simulation in Materials Science and Engineering, 18(8):085001.

[Stukowski et al., 2012] Stukowski, A., Bulatov, V. V., and Arsenlis, A. (2012). Automated identification and indexing of dislocations in crystal interfaces. Modelling and Simulation in Materials Science and Engineering, 20(8):085007.

[Sung and Chen, 2015] Sung, P.-H. and Chen, T.-C. (2015). Studies of crack growth and propagation of single-crystal nickel by molecular dynamics. Computational Materials Science, 102:151–158.

[Suresh, 1998] Suresh, S. (1998). Fatigue of Materials. Cambridge University Press, 2 edition.

[Suresh and Ritchie, 1983] Suresh, S. and Ritchie, R. O. (1983). NEAR-THRESHOLD FATIGUE CRACK PROPAGATION: A PERSPECTIVE ON THE ROLE OF CRACK CLOSURE. Concepts of Fatigue Crack Growth Threshold : An international symposium.

[Tadmor and Hai, 2003] Tadmor, E. B. and Hai, S. (2003). A Peierls criterion for the onset of deformation twinning at a crack tip. Journal of the Mechanics and Physics of Solids, 51(5):765–793.

[Tam et al., 1978] Tam, S., Sinha, S., and Siegel, R. (1978). Theory of the temperature dependence of positron bulk lifetimes — implications for vacancy formation enthalpy measurements via positron experiments. Journal of Nuclear Materials, 69-70:596–599. Publisher: North-Holland.

[Tang et al., 2010] Tang, T., Kim, S., and Horstemeyer, M. F. (2010). Fatigue crack growth in magnesium single crystals under cyclic loading: Molecular dynamics simulation. Computational Materials Science, 48(2):426–439.

[Thompson et al., 1956] Thompson, N., Wadsworth, N., and Louat, N. (1956). Xi. The origin of fatigue fracture in copper. Philos. Mag. J. Theor. Exp. Appl. Phys., 1(2):113–126. _eprint: https://doi.org/10.1080/14786435608238086.

[Tong et al., 1986a] Tong, Z.-x., Lin, S., and Hsiao, C.-m. (1986a). The crystallographic characteristics of fatigue crack propagation in pure aluminum single crystals. Scripta Metallurgica, 20(7):971–976.

[Tong et al., 1986b] Tong, Z.-x., Lin, S., and Hsiao, C.-m. (1986b). The mechanism of fatigue crack propagation in pure aluminum single crystals. Scripta Metallurgica, 20(7):977–982.

[Tong et al., 1986c] Tong, Z.-x., Liu, L., Lin, S., and Hsiao, C.-m. (1986c). Kinetic study on the propagation of fatigue crack in pure aluminum single crystals under different modes of loading. Scripta Metallurgica, 20(7):967–970.

[Tucker et al., 2012] Tucker, G. J., Tiwari, S., Zimmerman, J. A., and McDowell, D. L. (2012). Investigating the deformation of nanocrystalline copper with microscale kinematic metrics and molecular dynamics. Journal of the Mechanics and Physics of Solids, 60(3):471–486.

[Tucker et al., 2011] Tucker, G. J., Zimmerman, J. A., and McDowell, D. L. (2011). Continuum metrics for deformation and microrotation from atomistic simulations: Application to grain boundaries. International Journal of Engineering Science, 49(12):1424–1434.

[Tyson and Miller, 1977] Tyson, W. and Miller, W. (1977). Surface free energies of solid metals: Estimation from liquid surface tension measurements. Surface Science, 62(1):267–276.

[Van der Giessen et al., 2001] Van der Giessen, E., Deshpande, V. S., Cleveringa, H. H. M., and Needleman, A. (2001). Discrete dislocation plasticity and crack tip fields in single crystals. Journal of the Mechanics and Physics of Solids, 49(9):2133–2153.

[Vehoff and Neumann, 1979] Vehoff, H. and Neumann, P. (1979). In situ sem experiments concerning the mechanism of ductile crack growth. Acta Metallurgica, 27(5):915–920.

[Vinogradov et al., 1995] Vinogradov, A., Hashimoto, S., and Miura, S. (1995). Crack initiation and propagation in ⟨110⟩ oriented copper single crystals under cyclic deformation. Acta Metallurgica et Materialia, 43(2):675–680.

[Wang et al., 2011a] Wang, H., Xu, D., Yang, R., and Veyssière, P. (2011a). The formation of stacking fault tetrahedra in al and cu: I. dipole annihilation and the nucleation stage. Acta Materialia, 59(1):1 – 9.

[Wang et al., 2011b] Wang, H., Xu, D., Yang, R., and Veyssière, P. (2011b). The formation of stacking fault tetrahedra in al and cu: Ii. sft growth by successive absorption of vacancies generated by dipole annihilation. Acta Materialia, 59(1):10 – 18.

[Wang et al., 2011c] Wang, H., Xu, D. S., Yang, R., and Veyssière, P. (2011c). The formation of stacking fault tetrahedra in Al and Cu: I. Dipole annihilation and the nucleation stage. Acta Materialia, 59(1):1–9.

[Wang et al., 2011d] Wang, H., Xu, D. S., Yang, R., and Veyssière, P. (2011d). The formation of stacking fault tetrahedra in Al and Cu: II. SFT growth by successive absorption of vacancies generated by dipole annihilation. Acta Materialia, 59(1):10–18.

[Wang et al., 2011e] Wang, H., Xu, D. S., Yang, R., and Veyssière, P. (2011e). The formation of stacking fault tetrahedra in Al and Cu: III. Growth by expanding ledges. Acta Materialia, 59(1):19–29.

[Wang et al., 1995] Wang, M. O., Hu, R. H., Qian, C. F., and Li, J. C. M. (1995). Fatigue Crack Growth Under Mode Ii Loading. Fatigue Fract. Eng. Mater. Struct., 18(12):1443–1454.

[Wang and Mughrabi, 1984a] Wang, R. and Mughrabi, H. (1984a). Fatigue of copper single crystals in vacuum and in air II: Fatigue crack propagation. Materials Science and Engineering, 65(2):235–243.

[Wang and Mughrabi, 1984b] Wang, R. and Mughrabi, H. (1984b). Secondary cyclic hardening in fatigued copper monocrystals and polycrystals. Materials Science and Engineering, 63(2):147–163.

[Wang et al., 1984] Wang, R., Mughrabi, H., McGovern, S., and Rapp, M. (1984). Fatigue of copper single crystals in vacuum and in air I: Persistent slip bands and dislocation microstructures. Materials Science and Engineering, 65(2):219–233.

[Warner and Curtin, 2009] Warner, D. H. and Curtin, W. A. (2009). Origins and implications of temperature-dependent activation energy barriers for dislocation nucleation in face-centered cubic metals. Acta Materialia, 57(14):4267–4277.

[Warner et al., 2007] Warner, D. H., Curtin, W. A., and Qu, S. (2007). Rate dependence of crack-tip processes predicts twinning trends in f.c.c. metals. Nature Materials, 6(11):876–881.

[Watt et al., 1968] Watt, D. P., Embury, J. D., and Ham, R. K. (1968). The relation between surface and interior structures in low-amplitude fatigue. Philos. Mag. J. Theor. Exp. Appl. Phys., 17(145):199–203. _eprint: https://doi.org/10.1080/14786436808218194.

[Weertman, 1996] Weertman, J. (1996). Dislocation Based Fracture Mechanics. WORLD SCIENTIFIC.

[Weidner et al., 2008a] Weidner, A., Blochwitz, C., Skrotzki, W., and Tirschler, W. (2008a). Formation of slip steps and growth of extrusions within persistent slip bands in cyclically deformed polycrystals. Materials Science and Engineering: A, 479(1):181–190.

[Weidner et al., 2008b] Weidner, A., Man, J., Tirschler, W., Klapetek, P., Blochwitz, C., Polák, J., and Skrotzki, W. (2008b). Half-cycle slip activity of persistent slip bands at different stages of fatigue life of polycrystalline nickel. Materials Science and Engineering: A, 492(1):118–127.

[Weidner et al., 2011] Weidner, A., Sauzay, M., and Skrotzki, W. (2011). Experimental Evaluation of the Cyclic Slip Irreversibility Factor. https://www.scientific.net/KEM.465.223.

[Westergaard, 1939] Westergaard, H. M. W. (1939). Bearing pressures and cracks. Journal of Applied Mechanics.

[Westmacott and Peck, 1971] Westmacott, K. H. and Peck, R. L. (1971). A rationalization of secondary defect structures in aluminium-based alloys. The Philosophical Magazine: A Journal of Theoretical Experimental and Applied Physics, 23(183):611–622.

[Williams et al., 2006] Williams, P. L., Mishin, Y., and Hamilton, J. C. (2006). An embedded-atom potential for the Cu–Ag system. Modelling and Simulation in Materials Science and Engineering, 14(5):817–833.

[Winter, 1973] Winter, A. T. (1973). Etching studies of dislocation microstructures in crystals of copper fatigued at low constant plastic strain amplitude. Philos. Mag. J. Theor. Exp. Appl. Phys., 28(1):57–64. _eprint: https://doi.org/10.1080/14786437308217433.

[Winter, 1980] Winter, A. T. (1980). Dislocation structure in the interior of a fatigued copper polycrystal. Acta Metallurgica, 28(7):963–964.

[Winter et al., 1981] Winter, A. T., Pedersen, O. R., and Rasmussen, K. V. (1981). Dislocation microstructures in fatigued copper polycrystals. Acta Metallurgica, 29(5):735–748.

[Wirth et al., 2000a] Wirth, B., Bulatov, V., and de la Rubia, T. D. (2000a). Atomistic simulation of stacking fault tetrahedra formation in cu. Journal of Nuclear Materials, 283-287:773 – 777. 9th Int. Conf. on Fusion Reactor Materials.

[Wirth et al., 2000b] Wirth, B., Bulatov, V., and de la Rubia, T. D. (2000b). Dislocation-stacking fault tetrahedron interactions in cu. Journal of Engineering Materials and Technology, 124:329–334.

[Woods, 1973] Woods, P. J. (1973). Low-amplitude fatigue of copper and copper-5 at. % aluminium single crystals. Philos. Mag. J. Theor. Exp. Appl. Phys., 28(1):155–191.

[Wu et al., 2015] Wu, W.-P., Li, Y.-L., and Sun, X.-Y. (2015). Molecular dynamics simulation-based cohesive zone representation of fatigue crack growth in a single crystal nickel. Computational Materials Science, 109:66–75.

[Yamakov et al., 2014] Yamakov, V. I., Warner, D. H., Zamora, R. J., Saether, E., Curtin, W. A., and Glaessgen, E. H. (2014). Investigation of crack tip dislocation emission in aluminum using multiscale molecular dynamics simulation and continuum modeling. Journal of the Mechanics and Physics of Solids, 65:35–53.

[Zamora et al., 2015] Zamora, R. J., Baker, K. L., and Warner, D. H. (2015). Illuminating the chemo-mechanics of hydrogen enhanced fatigue crack growth in aluminum alloys. Acta Materialia, 100:232–239.

[Zepeda-Ruiz et al., 2017] Zepeda-Ruiz, L. A., Stukowski, A., Oppelstrup, T., and Bulatov, V. V. (2017). Probing the limits of metal plasticity with molecular dynamics simulations. Nature, 550(7677):492–495. Number: 7677.

[Zhang and Ghosh, 2013] Zhang, J. and Ghosh, S. (2013). Molecular dynamics based study and characterization of deformation mechanisms near a crack in a crystalline material. Journal of the Mechanics and Physics of Solids, 61(8):1670–1690.

[Zhang et al., 2008] Zhang, P., Duan, Q. Q., Li, S. X., and Zhang, Z. F. (2008). Cyclic deformation and fatigue cracking behaviour of polycrystalline Cu, Cu–10 wt% Zn and Cu–32 wt% Zn. Philos. Mag., 88(16):2487–2503.

[Zhang et al., 2017] Zhang, Z., Li, L., Zhang, Z., and Zhang, P. (2017). Twin boundary: Controllable interface to fatigue cracking. Journal of Materials Science & Technology, 33(7):603–606.

[Zhou et al., 1997] Zhou, S. J., Beazley, D. M., Lomdahl, P. S., and Holian, B. L. (1997). Large-Scale Molecular Dynamics Simulations of Three-Dimensional Ductile Failure. Physical Review Letters, 78(3):479–482.

[Zhou et al., 2015] Zhou, X., Li, X., and Chen, C. (2015). Atomistic mechanisms of fatigue in nanotwinned metals. Acta Materialia, 99:77–86.

[Zhu et al., 2004] Zhu, T., Li, J., and Yip, S. (2004). Atomistic study of dislocation loop emission from a crack tip. Physical Review Letters, 93(2):025503.

[Zimmerman et al., 2001] Zimmerman, J. A., Kelchner, C. L., Klein, P. A., Hamilton, J. C., and Foiles, S. M. (2001). Surface Step Effects on Nanoindentation. Physical Review Letters, 87(16):165507.

[Zope and Mishin, 2003] Zope, R. R. and Mishin, Y. (2003). Interatomic potentials for atomistic simulations of the Ti-Al system. Physical Review B, 68(2):024102.